The Quest for an Improved Solid Oxide Fuel Cell (SOFC) Electrolyte: Exploring Bismuthate Materials

WITS
UNIVERSITY

A thesis submitted to the Faculty of Science of the University of the Witwatersrand, Johannesburg, in fulfilment of the requirements for the degree of Doctor of Philosophy

By

Mathias Ameer Kiefer

June 2022

Declaration

I declare that this thesis is my own, unaided work. It is being submitted for the Degree of Doctor of Philosophy in the University of the Witwatersrand, Johannesburg. It has not been submitted before for any degree or examination in any other university.

Mathias A. Kiefer

13 June 2022

Supervisor: Professor David Gordon Billing

Co-supervisor: Professor Caren Billing

Abstract

In this project, several bismuthate (Bi_2O_3) materials were investigated as improved solid oxide fuel cell (SOFC) electrolytes with the overall aim of uncovering an electrolyte that is superior to the more popular zirconia (ZrO_2) and ceria (CeO_2) varieties. Investigating materials for application as SOFC electrolytes involves considering several criteria which were investigated throughout this thesis. The bismuthates investigated were synthesized using the citrate sol-gel method and the characterization techniques utilized were powder X-ray diffraction (PXRD) with Rietveld refinement, Raman spectroscopy and electrochemical impedance spectroscopy (EIS).

An investigation of the structural stability, ionic conductivity and *in situ* δ-phase formation of yttrium-doped bismuthates showed that the transition from a phase mixture to the δ-phase occurs at ~550-600 °C. For dopant concentrations less than 25%, the cubic phase was found to not be fully stabilized at room temperature. Additionally, the thermal expansion and ionic conductivity of the δ-phase was found to decrease with increasing dopant content.

An investigation of the phase stability of yttrium-doped bismuthates, with emphasis placed on stability criteria which are often overlooked, showed that the cubic and tetragonal polymorphs are metastable under ambient conditions. Additionally, the spontaneous formation of both the rhombohedral and subcarbonate phases was evident. The spontaneous formation of bismuth subcarbonate occurs directly from the reaction of the stabilized bismuthates with atmospheric carbon dioxide and this phenomenon was reported for the first time in this work. Pelletization and additional sintering as well as annealing under an inert atmosphere was found to enhance the long term phase stability characteristics of the cubic phase. Additionally, non-linear thermal expansion behaviour was observed for 27.5% dopant content and for 15% dopant content, and an abrupt increase in cubic phase unit cell volume was observed which indicates the presence of an unidentified phase change during the thermal cycle.

An investigation of the thermal expansion behaviour of yttrium-doped bismuthates using *in situ* total scattering studies revealed that non-linear thermal expansion behaviour observed for 27.5% yttrium content was linked to changes in the state of disorder of the cation sublattice. For 10% yttrium content and for 10% yttrium, 1% aluminium content, abrupt changes in cubic phase unit cell volume were found to be due to the tetragonal-cubic phase transformation and a mechanism for this was proposed. Changes in the cubic phase coefficient of thermal expansion (CTE) during the thermal cycle were also observed for all dopant content levels and these changes were found to be linked to changes in the state of disorder of the cationic sublattice.

The rhombohedral phase of bismuth oxide has recently emerged as a promising SOFC electrolyte material and the phase stability window of this phase was investigated using yttrium, lanthanum and aluminium doping regimes. It was established that the phase stability window is dependent on both the synthetic method and nature of the dopant species utilized. The thermal stability and phase behaviour of the rhombohedral phase, which has been sparsely reported, was investigated *in situ* over 360-656-360 ^{o}C. Complex phase transformation characteristics were evident during the thermal cycle along with abrupt changes in the thermal expansion of both the cubic and rhombohedral phases. These changes were found to be indicative of the rhombohedral-cubic phase transformation and the separation of the (009) and (104) peaks of the rhombohedral phase were identified as an excellent visual marker for this transformation.

Acknowledgements

But thanks be to God! He gives us the victory through our Lord Jesus Christ (1 Corinthians 15:57).

The completion of this thesis was only possible by the grace of God. Thank you Jesus!

The help, support and guidance from countless people and institutions has been instrumental over the years. I would like to sincerely thank:

- The University of the Witwatersrand and the DSI-CoE-SM for financial support.
- The entire School of Chemistry for accommodating me during the studies.
- Jeppe High School for Boys for providing an excellent foundation which readied me for university life.
- My academic supervisors, Prof. Dave Billing and Prof. Caren Billing, for the opportunities provided, advice given, and guidance offered throughout the past years. I am truly thankful for it all.
- Dr. Daniel Olds from NSLS-II for help and guidance with conducting beamline experiments and data acquisition and processing.
- Dr. Rudolph Erasmus for Raman measurements and data interpretation.
- Dr. Stuart Miller for the help and guidance during my honours project.
- Prof. Manuel Fernandes for the helpful discussions, advice, chats about everything automotive and for being very patient with me during my honours project.
- Dr. Ashvir Narrandes for the fantastic guidance, advice and help during my time as a research assistant.
- My entire research group for the helpful discussions, banter and good memories. Thank you to Mr. Sikhumbuzo Masina, Ms. Gugulethu Nkala and Mr. Adam Shnier for the friendship, memories, endless discussions on research and *everything* else. S'khu, thank you for the

wonderful memories in The Kingdom and at BNL – I will always fondly remember Ezulwini and high calcium bread. Adam, thank you for all the advice on side projects and for the wonderful and wild memories at EPDIC in Edinburgh.

- Dr. Michelle Thiebaut for being a truly remarkable friend, confidant and partner-in-crime. It was an absolute privilege to walk this academic path with you and to share office GH810. Amongst *many* other things, I am thankful to you for the excessive pastry eating and coffee drinking, the DMCs in the tea room, the long discussions about life on the windowsill while admiring the birds, the occasional parking lot chats, and naturally all the other shenanigans that we participated in. This time spent will always hold a special place in my heart. Thank you for everything my friend. SODACOVA.

- My mom, May, and brother, Ameen, for all the support and guidance over the years. Mom, thank you for always reminding me that education is essential and for always pushing me to excel. Also, thank you for the space shuttle poster with the partial Karen Ravn quote 'Only as far as we seek can we go, only as much as we dream can we be.' From childhood, that quote made me dream big and I will continue to dream big because of it. Ameen, thank you for all the side-projects, help with fixing the Beetle and *everything* else over the years.

- My mam'khulu Busisiwe Buthelezi, for all the wonderful stories of years gone by, for taking good care of me during several crucial periods of my life and for *everything* else. I am truly thankful.

- My dear friends during my undergraduate studies, Mr. Sam Malebati, Mr. Lehana Makara and Mr. Mandla Khathwayo. Mandla, thank you for your friendship during my very first year at university. It was a privilege to enter a new environment and to find a genuine friend like you. Sam and Lehana, thank you both for the wonderful memories and help during the materials science course. I have many fond memories from those years, and I am thankful for it all.

- My second family, Mr. Jatin Karsen, Mr. Nishaan Karsen, Aunty Lata and Uncle Davie, thank you for everything. Jatin, thank you for the friendship, memories and *missions* over the past 25-odd years – I am truly thankful to you. Nishaan, thank you for the lifts to and from campus during my first year – I cannot emphasize how much I appreciated that. Aunty Lata, thank you for making me lunch during my first year - I will always fondly remember a pasta sandwich.

Uncle Davie, thank you for all the laughs, wonderful stories of Joburg, and the awesome old-school music.

- Mr. Diran Gulumian for the immense help and support over the years and for always motivating me to pursue a PhD. I am truly thankful.
- The late Mr. Stephen Petersen for the immense support and help during my high school years. You are fondly remembered, and I am truly thankful for everything.

Conference and workshop attendance during the duration of this thesis

Poster presentations:

Mathias A. Kiefer, David G. Billing and Caren Billing, Exploring the $Y_xBi_{2-x}O_\delta$ Family for an Improved SOFC Electrolyte, 9th International Conference of the African Materials Research Society (AMRS2017), Gaborone, Botswana. (2017).

Mathias A. Kiefer, David G. Billing and Caren Billing, Exploring the $Y_xBi_{2-x}O_\delta$ Family for an Improved SOFC Electrolyte, Annual Centre of Excellence in Strong Materials (CoE-SM) Student Presentation Workshop, Johannesburg, South Africa. (2018).

Mathias A. Kiefer, David G. Billing and Caren Billing, Cubic phase, where you at? The Search for an Improved SOFC Electrolyte Material: Stabilizing the *F*m$\bar{3}$m Phase of Bismuth Oxide to Lower Temperatures, 16th European Powder Diffraction Conference (EPDIC16), Edinburgh, Scotland. (2018).

Mathias A. Kiefer, David G. Billing and Caren Billing, What The FCC!? The Search for an Improved SOFC Electrolyte Material: Stabilizing the *F*m$\bar{3}$m Phase of Bismuth Oxide to Lower Temperatures, Annual Centre of Excellence in Strong Materials (CoE-SM) Student Presentation Workshop, Johannesburg, South Africa. (2019).

Mathias A. Kiefer, David G. Billing and Caren Billing, The Search for an Improved SOFC Electrolyte Material: Stabilizing the *F*m$\bar{3}$m Phase of Bismuth Oxide to Lower Temperatures, Energy Storage and Industry 4.0: Challenges and Prospects (ENSTIN 2019), Pilanesburg, South Africa. (2019).

Oral presentations:

Mathias A. Kiefer, David G. Billing and Caren Billing, Electrolyte Materials for a Greener Tomorrow, Annual Centre of Excellence in Strong Materials (CoE-SM) Student Presentation Workshop, Johannesburg, South Africa. (2019).

Mathias A. Kiefer, David G. Billing and Caren Billing, The Search for an Improved SOFC Electrolyte Material: Stabilizing the *F*m$\bar{3}$m Phase of Bismuth Oxide to Lower Temperatures, SA-ESRF 2019 Conference, Johannesburg, South Africa. (2019).

Mathias A. Kiefer, David G. Billing and Caren Billing, Steps Towards Fueling a Clean Environment, South African Chemical Institute (SACI) Young Chemists' Symposium, virtual meeting. (2020). (**1st place oral presentation prize**).

Workshop attendance:

Bruker TOPAS Users' Meeting, Edinburgh, Scotland. (2018).

X-ray pair distribution function (XPDF) Analysis Workshop, Diamond Light Source, Didcot, UK. (2019).

Submitted manuscripts

Chapter 3 of this thesis has been submitted for publication to the *South African Journal of Chemistry*. The journal manuscript number is: sajc-002126.

Table of Contents

List of Figures

List of Tables

Chapter 1. Introduction and literature review

1.1. Overview

Global energy demands have been exponentially increasing since the dawn of the technological age. Fossil fuels have been primarily relied on to serve these demands. The use of fossil fuels has, however, severely damaged the environment and fossil fuel reserves are soon to be exhausted. Alternative, clean energy sources are emerging but are marred by material challenges and limitations which have hindered the green energy revolution. Bismuth oxide is an attractive energy material with application as an electrolyte in solid oxide fuel cells (SOFCs). The high temperature δ-polymorph is the best known oxide ion conductor, with a conductivity of ~1 $S.cm^{-1}$ at 1000 K. This makes the conductivity of this material nearly two orders of magnitude higher than that of yttria stabilized zirconia, the current commercial standard electrolyte for SOFCs. This δ-phase is, however, only stable over a narrow and high temperature range, preventing its practical application. The addition of dopants allows for δ-polymorph stabilization to lower temperatures but at the expense of conductivity. This chapter comprises a review of the literature relevant to this project. This includes a look at the global energy sector and the emergence of fuel cells as alternative energy sources. Thereafter bismuth oxide is introduced as an energy material and as a promising solid oxide electrolyte for application in SOFCs. Finally, the aims and objectives of this work are pertinently discussed.

1.2. The global energy sector

Statistical reviews of world energy have been provided by the British multinational oil and gas company BP p.l.c on an annual basis since 1952. These reviews have consistently shown annual increases in global energy production and consumption. In 2018,[1] a 2.9% growth of global energy consumption was observed, the fastest growth seen since 2010 and nearly double the 10-year average growth rate of 1.5%. As such, fossil fuel usage has been increasingly relied on; oil consumption grew by 1.5%, natural gas consumption grew by 5.3% and coal consumption grew by 1.4%. As a direct result, global carbon emissions grew by 2%, the greatest increase since 2012. Renewable power grew by 14.5%, predominantly due to significant increases in both solar and wind power generation. This growth, although below the historical 10-year average growth rate of 16.4%, is promising and indicates continued growth in the renewable sector. In 2019,[2] a promising shift in world energy was observed. The growth of global energy consumption significantly slowed year-on-year to 1.3%. Fossil fuel usage saw significant changes; oil consumption grew by 0.9%, natural gas consumption grew by 2% and coal consumption declined by 0.6%. As a result, global carbon emissions grew by 0.5% which represents a significantly reduced rate compared to that of the

previous year. Renewable power grew by 12.2% and saw a record increase in consumption, again bolstered by strong growth in wind and solar power generation. The consumption of renewable energy increased which resulted in renewables having a 5% share in the global energy sector – a strong increase of 0.5% from the previous year. These changes in world energy are promising and indicate that the world is slowly transitioning towards renewable energy. However, oil, gas and coal are still dominant and hold a combined 84.3% share in the global energy sector.

1.2.1. The rise of renewable energy sources

In a world characterized by an ever-increasing demand for energy and an ever-decreasing abundance of traditional, fossil-fuel based energy,[3,4] an energy crisis is imminent. Fossil fuels are, by definition, finite and are soon to be depleted. Shafiee *et al*[5] have recently calculated that oil, coal and gas have depletion times of 35, 107 and 37 years, respectively. These depletion limitations as well as the vast environmental concerns over the continued usage of fossil fuels[6] have resulted in renewable, environmentally friendly sources of energy becoming more prevalent. Renewables are predicted to become steadily integrated into the global energy grid whilst fossil fuel-based sources are systematically phased out. Renewable energy, although abundant, has seen limited development and implementation due to the ease at which fossil fuels can be utilized and commercialized. Several forms of renewable energy sources are available however, solar and wind sources have garnered the most research, development, and implementation.[1,2] Fuel cells have more recently emerged as a promising source of renewable energy particularly due to the key predicted role of fuel cells in the future hydrogen economy. However, the implementation and commercialization of fuel cells is still in its infancy.

1.3. Overview of fuel cells

Fuel cells are electrochemical conversion devices and have been fundamentally in existence for almost two centuries.[7] All fuel cells share a common design (i.e. comprise of an anode-electrolyte-cathode architecture) and working principle which involves the electrochemical conversion of the chemical energy stored in a fuel into electrical energy with fuel-specific by-products and heat emissions.[8,9] Several different types of fuel cells exist, with key differences in the nature of the electrolyte and underlying chemistry that governs their operation. Brief summaries of five common types of fuel cells are detailed in Sections 1.3.1-1.3.5 and a detailed description of solid oxide fuel cells is found in Section 1.3.6.

1.3.1. Molten carbonate fuel cell (MCFC)

MCFCs are characterized by employing an electrolyte that is commonly composed of a mixture of lithium and potassium carbonate.[7] These fuel cells require oxygen (O_2) and carbon dioxide (CO_2) to be supplied to

the cathode where electrochemical reduction enables the formation of carbonate ions (CO_3^{2-}) which are transported across the electrolyte to the anode. At the anode, the carbonate ions react with a fuel, such as hydrogen (H_2), and this generates electricity along with steam and heat emissions. Key advantages of MCFCs include high efficiencies of between 45-50% and internal reformation capability. The latter is made possible by the high operating temperature range of ~650 ^oC, which eliminates the need for a noble metal catalyst and results in reduced device cost.[7,9] Key disadvantages include slow start up due to the preheating required to reach the operating temperature (~5-7.5 h)[7,9,10], high sulphur intolerance (sulphur content greater than 1.5 ppm significantly decreases the oxygen surface exchange ability of the cathode) and the handling issues resulting from the presence of a liquid electrolyte.[7] MCFCs are mainly used for medium to large power applications; a 1000 kW MCFC power plant has been developed and tested in Kawagoe, Mie prefecture, Japan over an operation time of 5000 h[10] whilst a 2000 kW plant has been similarly tested in Santa Clara, California, USA over an operation time of 4000 h[11]. The minimum operation time envisioned for a large power plant before replacement is ~40000 h (~4-5 years)[7] and hence MCFC technology, whilst promising, is still in need of further development and improvement before reaching commercial viability.

1.3.2. Alkaline fuel cell (AFC)

AFCs are characterized by a molten alkaline electrolyte which is commonly an aqueous solution of either potassium hydroxide (KOH) or sodium hydroxide (NaOH). The electrolyte can be either in a mobile, liquid form or in an immobile, paste form applied to a porous asbestos supporting matrix.[7,9] These fuel cells require oxygen to be supplied to the cathode where electrochemical reduction enables the formation of hydroxide ions (OH^-) which are the mobile ion for this type of fuel cell. The hydroxide ions are transported across the electrolyte layer where, at the anode, these ions react with hydrogen fuel. This reaction generates electricity with steam emissions. Key advantages of AFCs include a low operating temperature range of 50-100 ^oC, which also enables fast start-up times,[7] and high efficiencies of between ~50-70%.[9] Key disadvantages include the intolerance of carbon dioxide (maximum concentration of 350 ppm)[7] and carbon monoxide (CO) which cannot be present in either the oxidant or fuel gases used. These molecules react with hydroxide ions present in the electrolyte and hence degrade the electrolytic ability of the electrolyte. The corrosive nature of the electrolyte additionally results in these fuel cells having short lifespans. Interestingly, AFCs have been used by NASA in the Shuttle program[7,9,12] and ZeTek Power, a UK-based energy company, has used AFCs to power fleet vehicles and boats in Europe.[13]

1.3.3. Proton exchange membrane fuel cell (PEMFC)

PEMFCs are characterized by a nafion solid polymer electrolyte that is a proton (H^+) conductor.[9] These fuel cells require hydrogen to be supplied to the anode where electrochemical oxidation of these ions generates electricity and produces protons which are transported across the electrolyte layer to the cathode. The oxygen supplied to the cathode reacts with these protons to produce water. Key advantages of PEMFCs include a low operating temperature range of 60-110 ^oC, the use of a solid and non-corrosive electrolyte and high CO_2 tolerance (atmospheric air can be used as a source of oxygen).[7] Key disadvantages include the need for external reformation, which increases the device cost, and low tolerance to sulphur and carbon monoxide.[7,9] PEMFCs have seen significant commercialization; Ballard Power Systems, a Canadian energy company, has tested a 250 kW PEMFC power system prototype in Vancouver, Canada and in Crane, Indiana, USA[11] and has more recently announced plans to power Fuel Cell Electric Buses (FCEBs) in Emmen, the Netherlands.[14]

1.3.4. Phosphoric acid fuel cell (PAFC)

PAFCs are characterized by an electrolyte comprised of liquid phosphoric acid within a matrix of silicon carbide.[7] The chemical reaction that occurs during the operation of a PAFC is the same as that of the PEMFC where protons are the mobile ions transported across the electrolyte. Key advantages of PAFCs include high CO_2 tolerance which enables the use of atmospheric air as the oxygen source and the typical operating temperature range of 150-200 ^oC enables high efficiencies of up to 85% to be attained via co-generation methodologies.[7,9] Key disadvantages include the use of a corrosive acidic liquid electrolyte which has various safety and handling issues, the large device size and like PEMFCs, the need for external reformation substantially increases the overall device cost.[7] PAFCs have been successfully commercialized by Fuji Electric, a Japanese electrical equipment company, and over the period of 1998-2009 twenty-five 100 kW PAFC units were delivered to diverse operating sites such as hospitals, universities, and sewerage treatment plants. The PAFC units displayed excellent durability and reliability with operating times achieved in excess of 40000 h.[15]

1.3.5. Direct methanol fuel cell (DMFC)

DMFCs share similar chemistry and operation to that of PEMFCs and also employ a proton-conducting polymer electrolyte. However, DMFCs use liquid methanol or other simple alcohols solutions as fuel instead of hydrogen gas. At the anode, hydrogen is extracted from the alcohol solution by a process of electro-oxidation facilitated by the anode catalyst.[7,9] The extracted hydrogen is electrochemically oxidized which produces electricity and protons, the latter is transported across the electrolyte layer to the

cathode and reacts with oxygen to produce water and heat. Key advantages include that reformation of fuel is unnecessary which reduces device cost, operating temperatures are low at ~60-200 ^{o}C, liquid fuels reduce infrastructure challenges[7,9] and fuel can be derived from renewable sources such as sugar cane.[16] Key disadvantages include low efficiency of around 40% and the need for large amounts of noble metal for the anode catalyst, the latter negates some of the cost saving achieved by reformation being unnecessary.[7,9] DMFCs have been actively researched as an alternative power source to lithium-ion batteries and have found commercial application. Samsung has developed a portable DMFC for military use as an alternative to relatively heavy batteries[17] whilst Toshiba has developed the DMFC product Dynario© as an external power source to power digital consumer products.[18]

1.3.6. Solid oxide fuel cell (SOFC)

Solid oxide fuel cells are the fuel cell type that are the subject of this project. SOFCs are high temperature, solid-state fuel cells consisting of three primary components: porous anode and cathode layers separated by a solid oxide electrolyte, which is most commonly yttria-stabilized zirconia (YSZ).[19,20] The electrolyte can be either an oxygen ion or proton conductor,[20,21] however only the oxide ion conducting variety was considered in this project. This type of fuel cell was first demonstrated by Baur and Preis[22] in 1937 using a yttria-stabilized zirconia electrolyte with a cell operating temperature of 1000 ^{o}C. Although this demonstration was successful, the high operating temperature and various material instabilities dampened the development of this type of fuel cell until the mid-1960s. The 1970s brought about renewed interest in SOFCs, primarily due to the advances in the study of ceramic materials. Subsequent research has shown SOFCs to be an efficient, versatile, and environmentally friendly source of energy. However, these fuel cells are plagued by various limitations which stem primarily from the *nature* of the electrolyte material. The operating principle and cell design of SOFCs is detailed in Section 1.3.6.1, the reasons behind active SOFC research is detailed in Section 1.3.6.2, a comparison of the different types of fuel cells is given in Section 1.3.6.3, a brief overview of the commercialization of SOFCs is given in Section 1.3.6.4, and a critical analysis of the material challenges and device limitations of SOFCs is given in Section 1.3.6.5.

1.3.6.1. Operating principle and cell design

SOFCs, much like the various other types of fuel cells, have a fundamentally simple operating principle (Fig. 1.1). Air is supplied to the cathode where oxygen molecules are reduced to form oxide ions. These ions are then incorporated into the electrolyte lattice and thereafter migrate towards the anode by means of a thermally-activated hopping mechanism[23]. At the anode, oxide ions react with fuel molecules and this process of oxidation generates electricity through the external circuit. In the case of using H_2 as fuel, the only emission is H_2O whilst using hydrocarbon fuel additionally generates CO and CO_2 emissions.

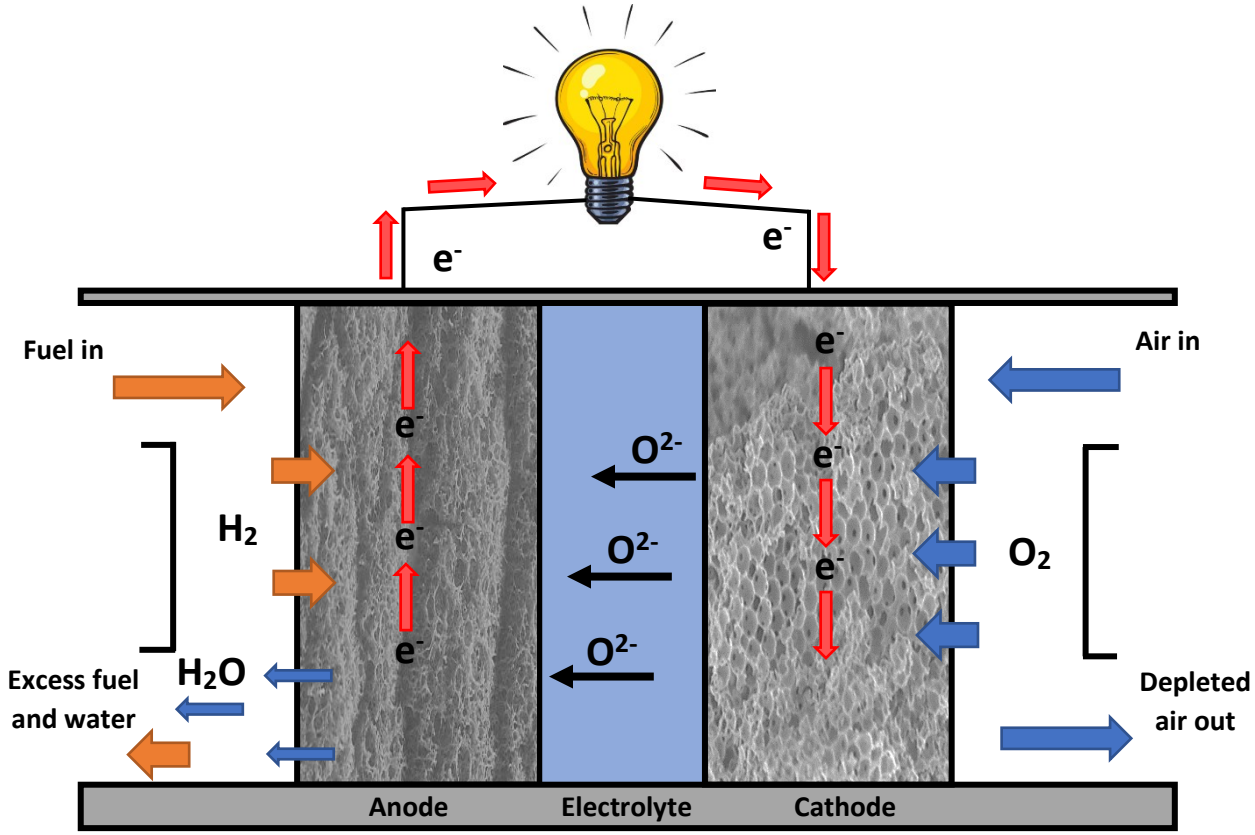

Figure 1.1. Schematic diagram illustrating the operating principles of a solid oxide fuel cell running on hydrogen gas and employing an oxide ion conducting electrolyte. Adapted from Ref. [20].

For practical applications, single SOFC cells are combined to form fuel cell stacks with useable power outputs.[24] This modularity enables SOFC stacks to be designed based on specific power requirements which adds to the versatility of this type of fuel cell. Several cell designs of varying architecture have been investigated[20,24–26] however most research has focused on planar (Fig. 1.2) and tubular (Fig. 1.3) designs.[27]

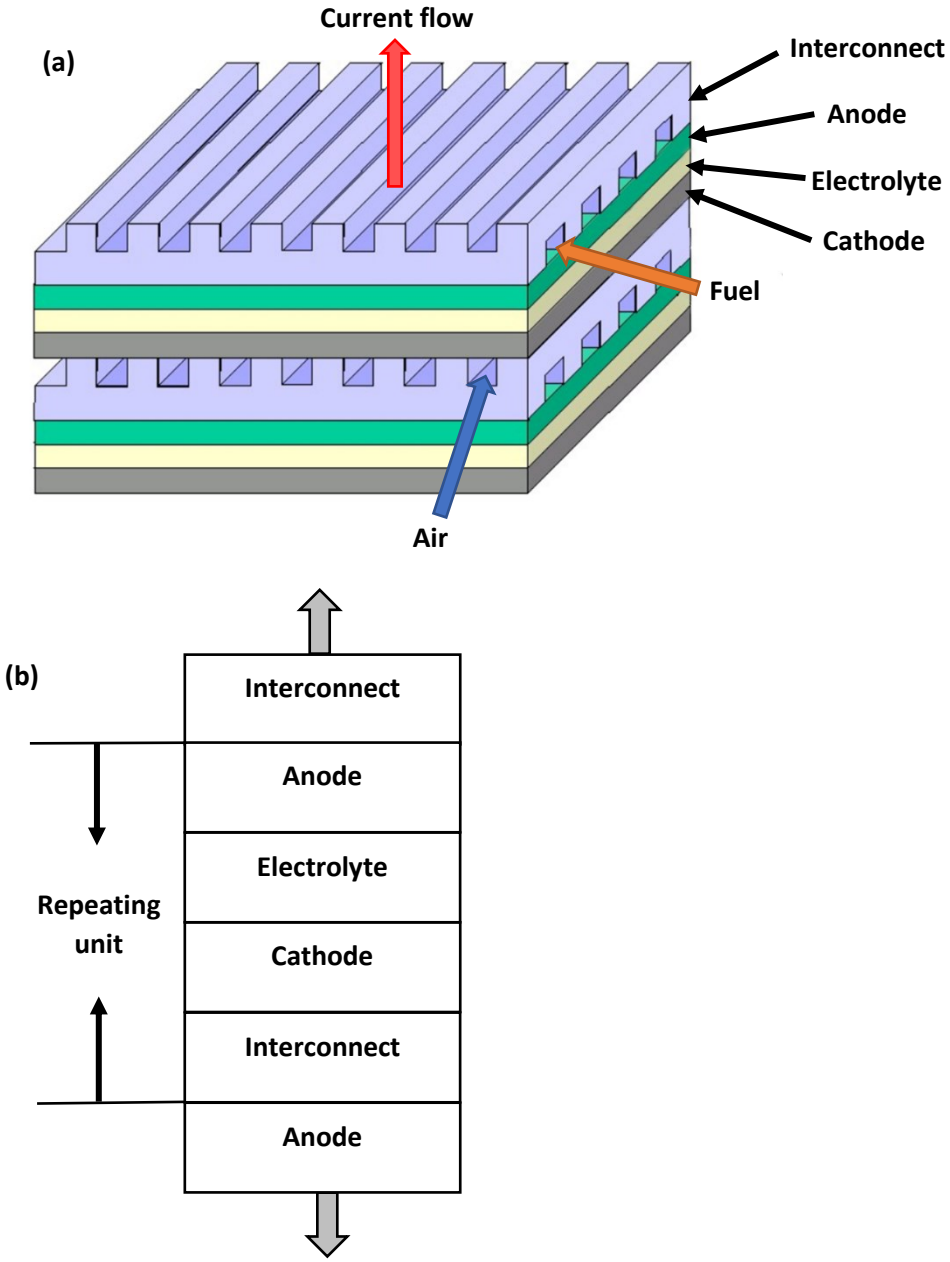

Figure 1.2. (a) Schematic diagram of a planar SOFC and (b) the repeating unit found in the planar SOFC stack. (a) Adapted from Ref. [[28]] and (b) adapted from Ref. [29].

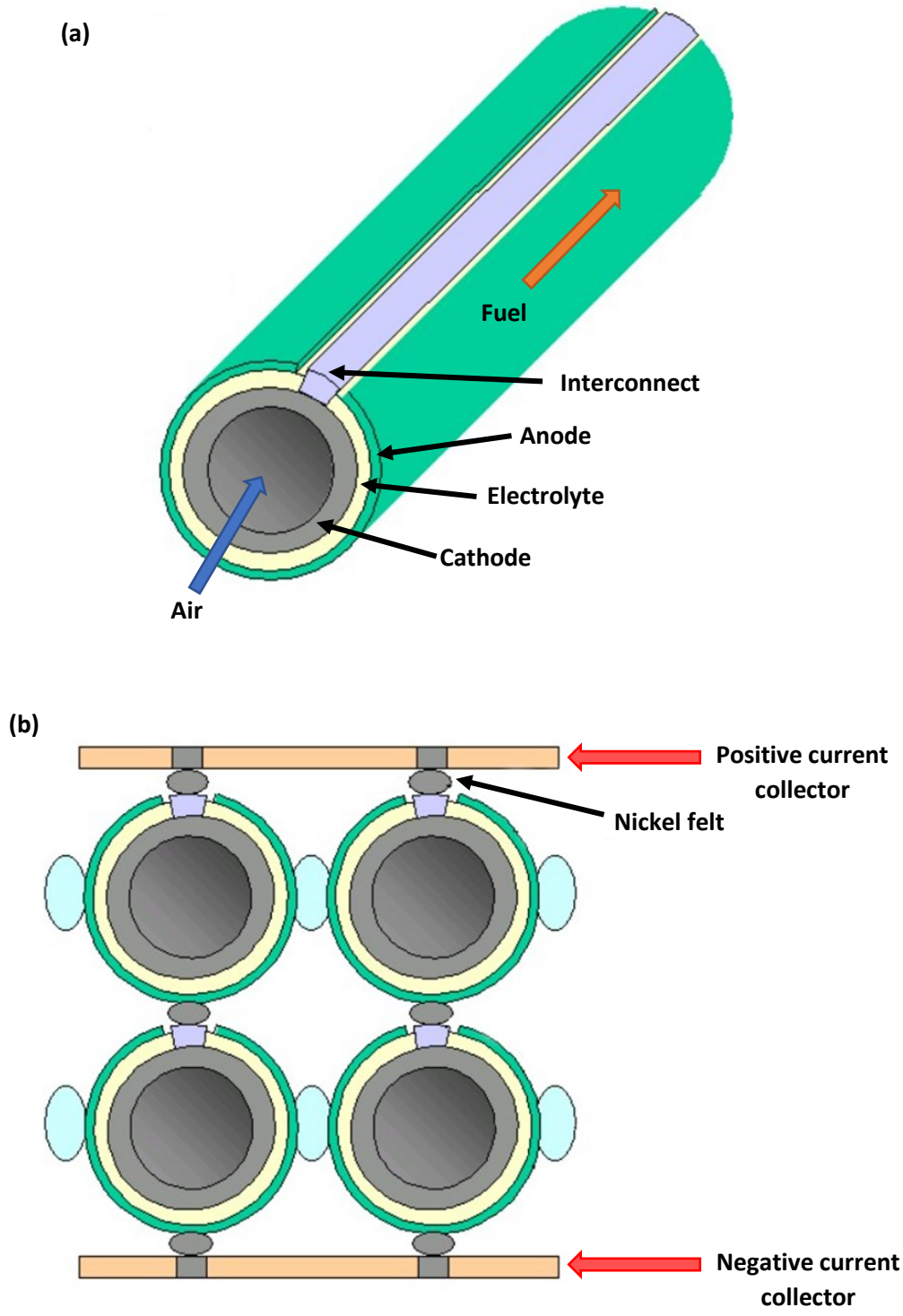

Figure 1.3. (a) Schematic diagram of a tubular SOFC and (b) the typical cell stack arrangement used for tubular cell designs. Adapted from Refs. [28] and [29].

1.3.6.2 Why are SOFCs actively researched?

In recent decades, the need to decrease the reliance on fossil-fuel based energy has directed considerable research towards alternative energy sources and conversion devices.[3] SOFCs have emerged as a leading candidate in the search for an efficient and environmentally friendly source of electrical energy[4,19,30,31] with a significant role to play in the emerging hydrogen economy.[32–34] SOFCs have an array of benefits in comparison to both conventional power sources and other major types of fuel cells. From a device standpoint, these devices have attracted interest due to characteristically high specific energy (energy per unit mass), specific power (power per unit mass), and power density (power per unit volume) (Fig. 1.4) which surpass those of any other energy conversion device. These features make such devices immediately more attractive than competitor devices such as batteries (high specific energy but low specific power) and supercapacitors (high specific power and low specific energy).[35] As a result, SOFCs are ideal for medium to large stationary, portable and transportation applications[9,34] and have notably been touted as the technology to revolutionize the automotive sector[36] by either replacing internal combustion engines completely[37] or, in the more likely scenario, serving as a supplementary energy source in a hybrid powertrain.

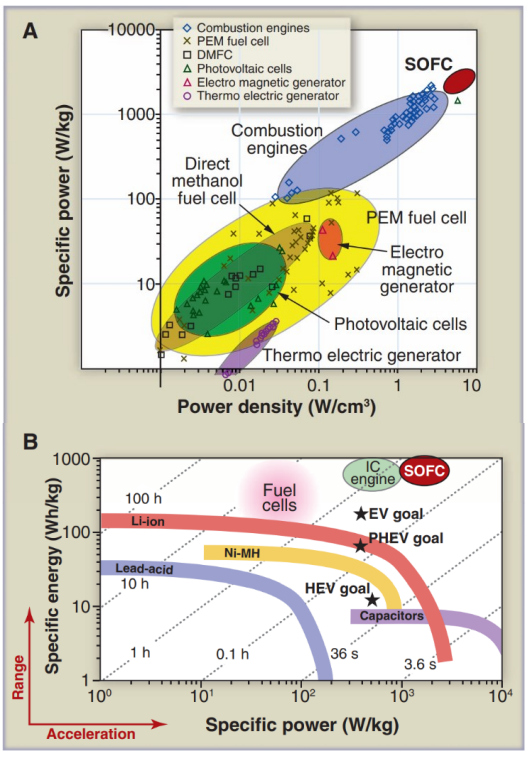

Figure 1.4. (a) Specific power as a function of power density of various energy conversion devices[38] and (b) Ragone plot (specific energy as a function of specific power) for various energy conversion devices.[36]

1.3.6.3. Comparison of SOFCs to conventional energy sources

In comparison to the more traditional and well-known energy generation systems (Table 1.1), fuel cell technologies offer significant benefits; high energy generation efficiencies, significantly reduced operation and maintenance costs, high degrees of fuel flexibility and reduced emissions are among the more prominent advantages. Key drawbacks of fuel cells are high capital costs and limited longevity.

Table 1.1. Comparison of different energy generation systems. Adapted from Ref. [9].

	Reciprocating engine: diesel	Turbine generator	Photo voltaics	Wind turbine	Fuel cells
Capacity range (kW)	500–5000	500-25000	1-1000	10-1000	200-2000
Efficiency (%)	35	29-42	6-19	25	40-80
Capital cost ($/kW)	200-350	450-870	6600	1000	1500-3000
O&M* cost ($/kW)	0.005-0.015	0.005-0.0065	0.001-0.004	0.01	0.0019-0.0153
Emissions	High	Low	Low	Low	Low
Lifespan (years)	~2-5[39]	~25-50[40]	~25-30[41]	>20[42]	~0.23-0.57[43]

*Operation and maintenance

SOFCs are compared to five major types of fuel cells in Table 1.2. The high operating temperature of SOFCs allows for high efficiencies to be obtained; efficiencies of up to 60% are achieved using common fuels such as natural gas.[3,44] These efficiencies can reach up to 90% when the high quality heat generated from the fuel cell is also used to generate electricity[45,46] - this co-generation approach is commonly employed in SOFC devices[19,47,48] and is a significant contributor to the high attainable efficiency of these fuel cells. The high operating temperature also enables internal reformation of fuel which results in a high degree of fuel flexibility and a significant reduction in device cost as no precious metals are needed for the catalytic reformation of fuel.[7–9,20] SOFCs can function successfully using a number of different sources of fuel such as natural gas, hydrogen and even hydrocarbons such as ethanol[3,31,44,49] and additionally show a high tolerance to impurities in fuel. The all solid-state nature of SOFCs additionally eliminates any chance of corrosion or loss of electrolyte – these problems are common in fuel cells that comprise liquid components.[8,9] The most notable disadvantage of SOFCs is the short lifespan. This disadvantage is discussed, along with the additional limitations of SOFCs, in Section 1.3.6.5.

Table 1.2. Comparison of the six major fuel cell types. Adapted from Refs. [9] and [50].

Parameters	Fuel cell type					
	MCFC	AFC	PEMFC	PAFC	DMFC	SOFC
Electrolyte	Lithium and potassium carbonate (Li_2CO_3 and K_2CO_3)	Aqueous solution of NaOH or KOH	Solid polymer (nafion) membrane	Phosphoric acid (H_3PO_4)	Solid polymer membrane	Solid oxide electrolyte
Operating temperature (^oC)	~650	50-100[45]	70-110	~150-200	60-200	800-1000
Fuel	H_2, CH_4 & other hydrocarbons	Pure H_2	Pure H_2	Pure H_2	CH_3OH	H_2,CH_4 & other hydrocarbons
Efficiency	45-60%	~50-70%	35-60%	40%	40%	>50%
Co-generation	Yes	No	No	Yes	No	Yes
Reformer	No	Yes	Yes	Yes	No	No
Installation cost ($/kW)	~2000-3000	~1800	<1500	2100	1650[51]	3000

1.3.6.4. Commercialization of SOFCs

SOFC technology has seen significant commercialization efforts in recent years. In 2006 Yakabe *et al*[52] reported on the development and testing of a 3 kW SOFC system at the Tokyo Gas Co., Ltd. (Tokyo, Japan). This system used methane as fuel, was operated at a temperature of ~780 ^oC and achieved a maximum power generation efficiency of ~45% without co-generation.

In 2012, a consortium comprising Osaka Gas Co., Ltd (Osaka, Japan), Aisin Seiki Co., Ltd (Aichi, Japan), Kyocera Corporation (Kyoto, Japan), Chofu Seisakusho Co., Ltd. (Yamaguchi, Japan) and Toyota Motor Corporation (Aichi, Japan)[46,53] completed the development and commercialization of a 0.7 kW SOFC system for residential use (Fig. 1.5a), named the 'ENE-FARM Type S.' The SOFC stack was developed and manufactured by Kyocera Corporation (Fig. 1.5b). This fuel cell system uses municipal gas as fuel, operates within the temperature range of 700-750 ^oC and achieves a power generation efficiency of 46.5%. This system does, however, employ a co-generation approach on which heat generated is used for household heating and hot water supply. This translates into an overall energy efficiency of 90%. The system costs US$33 700 which translates into ~48 000 US$/kW – a significantly higher cost than that estimated from

laboratory scale prototypes.[9] However, this residential system has been a commercial success with over 300 000 units sold by 2019.[54]

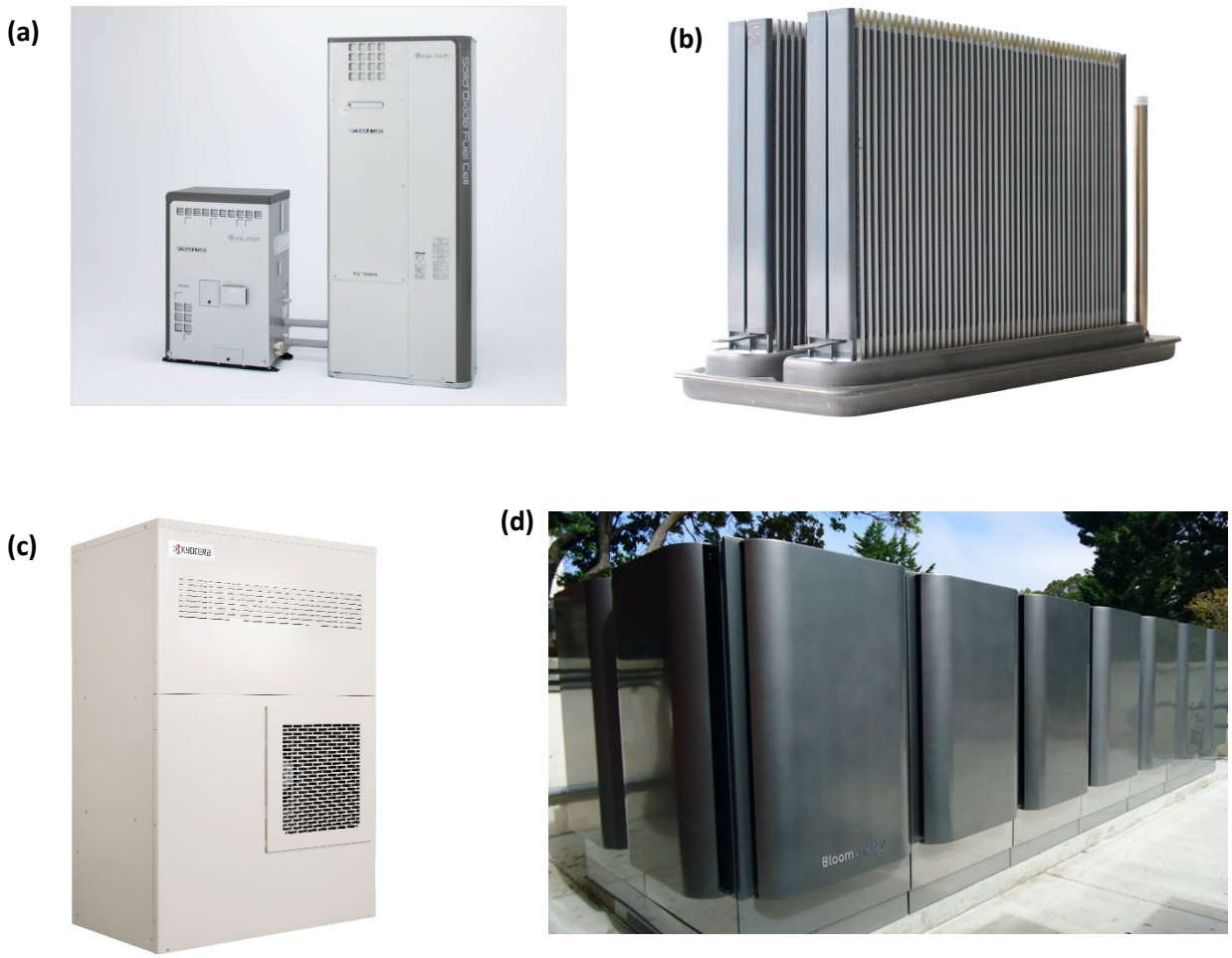

Figure 1.5. (a) 0.7 kW SOFC fuel cell stack developed by Kyocera Corporation,[60] (b) ENE-FARM Type S SOFC system,[53] (c) 3 kW SOFC system developed by Kyocera Corporation,[61] and (d) Bloom Energy Servers at Apple's Campus 2 (Apple Park) in California, USA.[62]

In 2017, Kyocera launched a 3 kW SOFC cogeneration system (Fig. 1.5c).[55] This system is suitable for institutional applications (such as retail establishments and restaurants) and is essentially four of the 0.7 kW stacks that are found in the ENE-FARM Type S incorporated into one system. The SOFC stacks have been further developed and improved since 2012. The current 3rd generation stacks boast improved power generation efficiency of 55% whilst overall energy efficiency of the system remains 90%. These

stacks are able to achieve 90 000 hours of continuous operation and are able to withstand 360 operation cycles. This equates to approximately 12 years of usage without any performance deterioration.[56] The success of Kyocera's fuel stack technology has resulted in the Japanese Ministry of Economy (METI) setting residential SOFC deployment targets of 1.4 million units by 2020 and 5.3 million units by 2030.[55] There is another company which has become somewhat synonymous with large scale, commercial SOFC systems - Bloom Energy (California, USA). Bloom Energy develops SOFC systems, aptly named 'Bloom Energy Servers,' which are large scale stationary power units that provide energy within the 100-200 kW range (Fig. 1.5d).[57] These SOFCs systems typically operate using natural or bio-gas as fuel, operate at high temperatures of ~900 ^{o}C and achieve power generation efficiencies between 53-65%.[58] Bloom Energy has supplied several thousand of these systems to companies such as Google, eBay, Apple, AT&T and Paypal[59] where they have been primarily used to power data centres.

In the automotive sector recent commercialization of SOFC technology has been shown by the automotive manufacturer Nissan.[63] Under its Intelligent Power program, Nissan has developed the world's first SOFC-powered vehicle (Fig. 1.6). The SOFC system used is called the e-Bio Fuel-Cell and forms an integral part of the car maker's commitment to the development of zero emission electric vehicle technology. Nissan plans to use bio-ethanol-fuelled SOFC technology as the source of electrical energy in its electric vehicles. This is a unique stance taken in the electrical vehicle revolution, as the vast majority of carmakers such as Tesla Motors and Toyota have opted to use externally charged lithium-based batteries to power their electric vehicles.[64] This unique approach taken by Nissan has been abundant in reward and in 2016 a working prototype was tested employing a hybrid powertrain comprising a 5 kW SOFC and a 24 kWh battery. The prototype achieved an impressive cruising range of 600 km from a mere 30 L of bio-ethanol.

Figure 1.6. The result of the Nissan Intelligent Power program - the world's first car powered by SOFC technology.[63]

1.3.6.5. SOFC device limitations

Much like any other energy generation or conversion device, SOFCs are marred by a variety of limitations.[3,19,65] Mahato *et al*[20] identified complex and challenging cell and stack fabrication, safety issues regarding the usage of flammable fuel gases and high the operating temperature as key SOFC limitations.

The operating temperature is a feature dictated by the electrolyte material in which high temperatures are required for high ionic conductivity.[20,23] The present generation of SOFCs have operating temperatures in the range of 800 - 1000 °C[3,20,21,31,32] and, although at these high temperatures the ionic conductivity of the electrolyte as well as catalytic activity of the electrodes are optimized, a variety of consequences are incurred. To reach the high operating temperature, extended start-up times are required which limits the application of SOFC devices. Most importantly, several material problems such as interfacial diffusion and reactions between electrolyte and electrode materials, thermal instability, and mechanical (or thermal) stresses, due to thermal expansion mismatch of the cell components, occur at these high temperatures.

At high temperatures, the cell components show limited stability. Secondary phase formation (through structural interconversion or chemical reaction), diffusion of materials across component interfaces as well as microstructural changes occur[20,66] – all of which degrade the cell performance. In addition, the thermally-driven expansion introduces significant mechanical stresses due to thermal expansion mismatch between adjacent cell components.[8,32,66,67] This mismatch commonly results in the delamination of adjacent layers and results in device failure (Fig. 1.7). The high operating temperature hence results in several material challenges which severely limits the lifespan of these devices. Additionally, the usage of specialized cell components which can withstand these high temperatures are required - resulting in high device cost.[8,20] These operating temperature-related effects are indeed the primary cause of the limited development and commercialization of SOFCs.

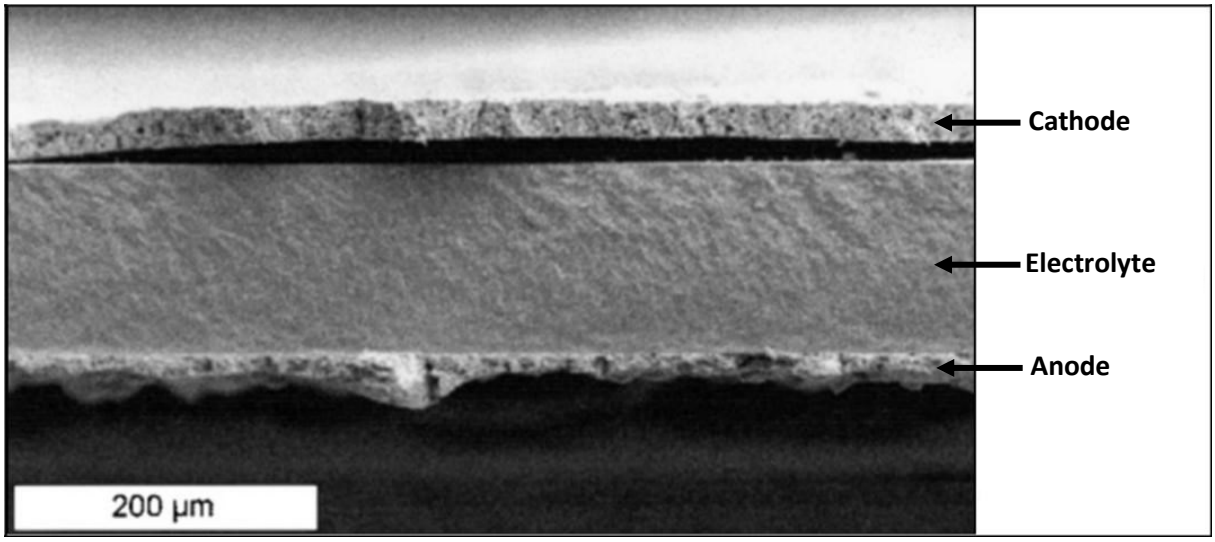

Figure 1.7. SEM image of a typical SOFC arrangement where thermal expansion mismatch and chemical instability during thermal cycling has resulted in layer delamination and ultimately cell failure. Adapted from Ref. [66].

It is clear that the majority of SOFC limitations can be overcome if the operating temperature is reduced. Significant research has focused on reducing the operating temperature of SOFCs without significantly sacrificing the benefits associated with the elevated operating temperature. This necessitates the investigation of various oxide ion conducting material systems such as to design an *improved* electrolyte.

1.4. Electrolyte materials for SOFCs

Several material systems exist that show promise as electrolyte materials for SOFC applications. Following guidelines by Basu,[68] Hussain *et al.*[69] and Ormerod,[8] an electrolyte material must satisfy the following key requirements to function successfully and efficiently:

(i) Pure oxide ion conductivity that is sufficiently high (at least 0.1 $S.cm^{-1}$) at operating temperature

(ii) High thermodynamic and chemical stability over the working temperature range

(iii) Inertness to the adjacent components during manufacturing and operation

(iv) Minimal thermal expansion mismatch with adjacent components

(v) Stable in both oxidizing (anode side) and reducing (cathode side) atmospheres

Several material systems have been studied for application as electrolyte materials in SOFCs. The most common and successful material system has been the fluorite structure type, primarily comprising of stabilized zirconia, doped ceria and stabilized δ-Bi_2O_3. The fluorite structure type has been extensively studied, over diverse compositions, for application as a SOFC electrolyte. Rhombohedral structures based on Bi_2O_3 have recently come into the spotlight as an attractive alternative to the popularized fluorite structures, especially for application in low temperature SOFCs. Several alternative structures have also been investigated as electrolytes, these include electrolytes based on BIMEVOX, pyrochlore, perovskite and related intergrowth ($LaGaO_3$, Brownmillerites, La-MOX and apatites) structures. These alterative electrolyte structures have been comprehensively reviewed[20,30,69–71] and are not reviewed here. The pertinent research done on the popular stabilized zirconia and doped ceria fluorite systems is briefly reviewed whilst electrolyte research done on Bi_2O_3-based fluorite and rhombohedral structure types is comprehensively reviewed.

1.4.1. Fluorites

Materials with the fluorite structure have the general chemical formula MO_2 where M is a metal cation in a +4 oxidation state (M^{4+}) and O is an oxygen anion in a -2 oxygen state (O^{2-}) (Fig. 1.8). The ideal fluorite structure comprises a face centred cubic (FCC) arrangement of cations with anions occupying tetrahedral sites. Zirconium oxide (ZrO_2) and cerium oxide (CeO_2) are two well-known metal oxides that crystallize in the fluorite structure. The defect fluorite structure type comprises of the same FCC arrangement of cations. However, all the crystallographically available anion sites are not occupied. This partial anion site occupancy is termed as a crystallographic *defect* which is essentially a deviation from the ideal fluorite structure. Bismuth oxide (Bi_2O_3) is a well-known example of a metal oxide which adopts the defect fluorite structure under certain conditions. Stabilized zirconia and doped ceria can also adopt the defect fluorite structure by the addition of dopant cations.

1.4.1.1. Stabilized zirconia

The first and currently the only material system to fully meet the basic electrolyte requirements of pure and high ionic conductivity and high phase stability is the stabilized zirconia electrolyte.[71] The natural polymorphism of pure ZrO_2 comprises three polymorphs.[72] A monoclinic phase is present at room temperature and transforms into a tetragonal phase at 1170 °C. The tetragonal phase converts to a cubic fluorite structure at 2370 °C. The fluorite structure is stable until its melting point of 2680 °C, and all phase transformations are reversible on cooling.

The high temperature cubic fluorite phase can be stabilized to room temperature by the addition of dopant cations such as Y^{3+} and Sc^{3+} which replace Zr^{4+} in the fluorite lattice.[20,30] The addition of acceptor dopant cations additionally introduces oxygen vacancies, which forms a defect fluorite structure and greatly enhances the oxide ion conductivity.[20,30,70] The most common electrolyte material used in SOFCs is yttria-stabilized zirconia (YSZ). Addition of approximately 8 mol% yttrium (8YSZ) has been reported to have highest oxide ion conductivity of the YSZ system. Conductivities of 0.052 $S.cm^{-1}$ at 800 ^oC and 0.178 $S.cm^{-1}$ at 1000 ^oC have been reported,[73] the latter meeting the minimum conductivity requirement of a SOFC electrolyte. The 8YSZ material is also phase stable and does not undergo any phase transformation up to 2500 ^oC which is ideal for application as a SOFC electrolyte.[20]

Another popular stabilized zirconia that has been significantly researched for application in SOFCs is scandium-stabilized zirconia (ScSZ). ScSZ materials are generally more conductive than their YSZ counterparts over similar composition and temperature ranges.[30] As an example, addition of 7.8 mol% scandium (7.8ScSZ) results in ionic conductivities of 0.120 $S.cm^{-1}$ at 800 ^oC and 0.31 $S.cm^{-1}$ at 1000 ^oC[73] which is approximately double that of 8YSZ at the same temperatures. This makes 7.8ScSZ a promising electrolyte at comparatively lower operating temperatures. However, ScSZ materials have been found to transform into a rhombohedral phase of lower conductivity at temperatures <500 ^oC[74] and exhibit increased activation energy for conduction below 500 ^oC.[30] During operation, YSZ and ScSZ experience conductivity aging which is essentially the decrease in measured ionic conductivity over extended periods of time at elevated temperatures due to local structure ordering.[75] The aging is, however, significantly greater in magnitude for ScSZ than for YSZ. The limited phase stability, conductivity aging behaviour, and the high cost of scandium,[71,76] greatly detracts from the promising conductivity of ScSZ electrolytes.

1.4.1.2. Doped ceria

Doped ceria has recently emerged as a common electrolyte material for SOFCs.[30,50,71] Ceria (CeO_2) naturally occurs as a cubic fluorite structure and this phase is stable from room temperature until its melting point of ~2400 ^oC.[20] Pure ceria does not have sufficient oxygen vacancies to enable high oxide ion conduction.[20] Hence, much like with zirconia, ceria is doped with cations, commonly Gd^{3+} and Sm^{3+}, to form a defect fluorite structure. This doping introduces oxygen vacancies and increases oxide ion conduction.[30,50,71] In general, ceria electrolytes have superior ionic conductivity to zirconia electrolytes, particularly at lower temperatures[77] and are therefore in principle ideal electrolytes for application in SOFCs.[78]

The most widely used ceria electrolyte materials are gadolinia-doped ceria (GDC) and samaria-doped ceria (SDC). GDC electrolytes show great promise for use in SOFCs due to their high ionic conductivities. Addition of 30 mol% gadolinia (30GDC) results in ionic conductivities of 0.093 $S.cm^{-1}$ at 800 ^{o}C and 0.25 $S.cm^{-1}$ at 1000 ^{o}C[73] - these conductivity values are superior to those of the industry standard 8YSZ. SDC electrolytes exhibit high ionic conductivities which are comparable to those of GDC. As an example, addition of 20 mol% samaria (20SDC) results in ionic conductivities of 0.096 $S.cm^{-1}$ at 800 ^{o}C and 0.25 $S.cm^{-1}$ at 1000 ^{o}C.[73] Although ceria electrolytes exhibit high phase stability, under reducing conditions Ce^{4+} reduces to Ce^{3+} which introduces electronic conductivity in the electrolyte.[77,79,80] Electronic conductivity is undesirable as it forms a short circuit pathway through the electrolyte which greatly reduces the efficiency of a SOFC[71] and reduces the suitability of ceria electrolytes for use in SOFCs.

1.4.2. Bismuth oxide

Several polymorphs of bismuth oxide exist; however, the high temperature cubic fluorite polymorph of bismuth oxide (δ-Bi_2O_3) has attracted the most interest as an oxide ion conductor. δ-Bi_2O_3 is widely regarded as the best oxide ion conductor with ionic conductivity of ~ 1 $S.cm^{-1}$ at ~750 ^{o}C and as such has attracted significant research towards its application as a SOFC electrolyte. More recently, a rhombohedral bismuth oxide phase has emerged as an attractive SOFC electrolyte material, particularly for application at lower temperatures. The study of these two bismuth oxide-based electrolyte phases is the focus of this thesis.

1.4.2.1. The polymorphism of Bi_2O_3

Pure Bi_2O_3 exists as six natural crystallographic polymorphs.[81–83] At low temperatures a monoclinic polymorph α-Bi_2O_3 exists (space group $P2_1/c$). On heating to ~730 °C, the monoclinic form converts into the high temperature face-centred cubic (FCC) polymorph δ-Bi_2O_3 (space group $Fm\bar{3}m$). The δ-polymorph is stable from ~730 °C until its melting point at ~825 °C. The tetragonal β-Bi_2O_3 (space group $P\bar{4}2_1c$) and body-centred cubic (BCC) γ-Bi_2O_3 (space group $I23$) polymorphs can be formed when the δ-phase is cooled below 639-650 °C.[84] The β-phase commonly converts to the α-phase upon further cooling below 300 °C whereas the γ-phase can persist to room temperature with sufficiently low cooling rates.[85] Additional metastable polymorphs orthorhombic ε-Bi_2O_3 (space group $Pbnb$) and triclinic ω-Bi_2O_3 (space group $P\bar{1}$) are formed only under specific synthetic conditions.[83] The ε-phase was formed from the hydrothermal treatment of bismuth nitrate under highly alkaline conditions at 240 °C[86] whereas the ω-phase was formed after thermal treatment of α-Bi_2O_3 deposited on a beryllium oxide (BeO) substrate at 800 °C.[87] The Bi_2O_3 lattice can also crystallize in two non-natural rhombohedral phases of space group $R\bar{3}m$ and $P6_{1(5)}/P6_{1(5)}22$[83,88,89] by doping of pure Bi_2O_3. The conductive rhombohedral phase rh-Bi_2O_3 (space group $R\bar{3}m$) is commonly formed when Bi_2O_3 is doped with larger cations such as lanthanum[88,90] and this is the rhombohedral phase of interest in this thesis. An illustration of the temperature domains identified for the six natural polymorphs of Bi_2O_3 is given in Figure 1.8[83] and a summary of the key structural data is given in Table 1.3.

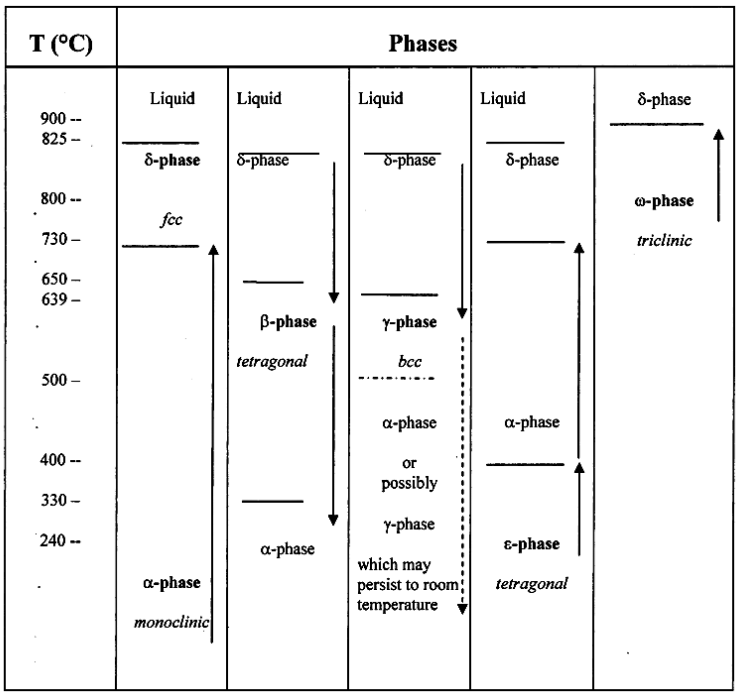

Figure 1.8. Temperature domains identified for the six natural polymorphs of bismuth oxide.[83]

Table 1.3. Key structural data of the six natural polymorphs of pure bismuth oxide and the rhombohedral phase.

Bi_2O_3 polymorph	α-mono-clinic[91]	δ-cubic[85]	β-tetra-gonal[92]	γ-cubic[93]	ε-ortho-rhombic[86]	ω-triclinic[94]	Rhombo-hedral[# 90]
Phase stability range (°C)	<730	730-825	330-650	500-639[*]	<400	<900	<800[95]
Space group (number)	$P2_1/c$ (14)	$Fm\bar{3}m$ (225)	$P\bar{4}2_1c$ (114)	$I23$ (197)	$Pbnb$ (56)	$P\bar{1}$ (2)	$R\bar{3}m$ (166)
a (Å)	5.8444(2)	5.644(2)	7.741(3)	10.2501(5)	4.9555(1)	7.2688(4)	4.0253(1)
b (Å)	8.1574(3)				5.5854(2)	8.6390(6)	
c (Å)	7.5032(3)		5.634(2)		12.7299(3)	11.9698(8)	27.6004(9)
α (°)						87.713(6)	
β (°)	112.97(1)					93.227(6)	
γ (°)						86.653(4)	

[#] $Bi_{0.775}La_{0.225}O_{1.5}$

[*] γ-cubic phase may persist to room temperature

1.4.3. The structure of δ-Bi_2O_3

The structure of δ-Bi_2O_3 has been a somewhat controversial topic with several varying structural models proposed for this phase (Fig. 1.9). Sillen[96,97] reportedly obtained δ-Bi_2O_3 by quenching Bi_2O_3 and reported the phase to crystallize in a primitive cubic structure with space group $Pn\bar{3}m$. This structure is crystallographically related to the fluorite structure, however, defects present in the oxygen sublattice are ordered in the <111> direction. Later, Gattow and Schröder[98] investigated the structure of δ-Bi_2O_3 by high temperature X-ray powder diffraction experiments. The structure of δ-Bi_2O_3 was revealed to be similar to that of the ideal fluorite (CaF_2) structure and the model proposed by Sillen wherein the oxygen sublattice is ordered was outright rejected. Instead, a structure was proposed where δ-Bi_2O_3 crystallizes in a defect fluorite structure with space group $Fm\bar{3}m$. In this structure, bismuth cations occupy the FCC positions and oxide anions partially occupy one distinct anionic site: 8c (¼, ¼, ¼). The average occupancy of the anionic sites is 75% and the vacancies are distributed randomly – this disorder of the oxygen sublattice is a distinct feature of the Gattow model. Another structural model of δ-Bi_2O_3 was proposed by Harwig[99] with a key difference in the structure of the oxygen sublattice. In this model, which was derived from neutron powder diffraction measurements, the oxygen atoms are randomly distributed from the tetrahedral 8c sites along four of the <111> directions towards the vacant octahedral site: 32f (x, x, x) where x ≈ 0.3. Hence the key structural difference between the Gattow and Harwig models is the occupancy of either the 8c or 32f sites. Neutron diffraction studies by Battle *et al.*[97,100] and later by Wachsman *et al.*[101] show

that oxygen ions partially occupy both 8c and 32f positions. Hence the structure of δ-Bi_2O_3 was reported to be a combination of both the Gattow and Harwig models. This combined model was further substantiated via neutron diffraction studies by Yashima *et al.*[102,103] which revealed δ-Bi_2O_3 to have high anionic disorder. An additional interstitial anionic site 48i (0.5, x, x) has been identified and investigated by Wachsman *et al.,*[101]Leszczynska *et al.*[104] and Abrahams *et al.*[105] via neutron diffraction studies. It is well-known that using X-ray radiation to localize partially occupied oxygen sites in close proximity to cationic sites with high electron density is challenging.[83] X-ray radiation was exclusively used in this thesis and therefore the 48i site was not used in the structural model for δ-Bi_2O_3 as its localization was not possible to a sufficient degree of accuracy. The description of the oxygen sublattice by Yashima *et al.*[103] employed a structural model with only 8c and 32f sites. This model was sufficient to describe the complex positional disorder of the oxygen sublattice. Refined atomic parameters of the δ-Bi_2O_3 structure as reported by Yashima *et al*.[103] are given in Table 1.4 and serve as the basis for the δ-Bi_2O_3 structural model used in this thesis.

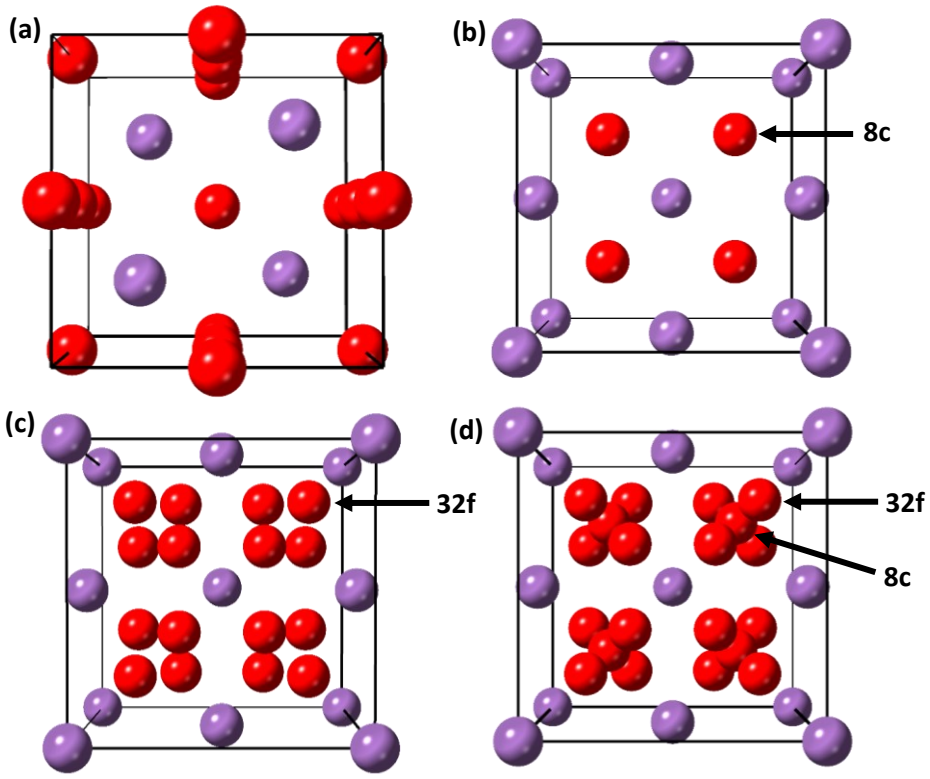

Figure 1.9. Various structural models of δ-Bi_2O_3. (a) Sillen model with ordered oxygen sublattice of *P*n$\bar{3}$m, (b) Gattow and Schröder model with oxygen atoms occupying the 8c site of *F*m$\bar{3}$m, (c) Harwig model with oxygen atoms occupying the 32f site of *F*m$\bar{3}$m and (d) Battle model with oxygen atoms occupying both the 8c and 3f sites. Purple and red spheres denote bismuth and oxygen atoms, respectively.

Table 1.4. Refined atomic parameters of δ-Bi_2O_3 measured at 778 °C[103] where g = site occupancy; U = isotropic atomic displacement parameter and x, y, z = fractional coordinates. Space group: *F*m$\bar{3}$m; *a* = 5.6549(9) Å; R_{wp} = 3.77%, R_p = 2.69%, R_e = 1.62%, Goodness of fit, R_{wp}/R_e = 2.33, R_I = 4.56%, R_f = 4.54%.

Atom	Site	g	x	y	z	U (Å^2)
Bi	4a	1	0	0	0	0.078(2)
O1	8c	0.23(22)[a]	0.25	0.25	0.25	0.08(5)
O2	32f	0.13(5)[a]	0.335(21)	0.335(21)	0.335(21)	0.121[b]

[a]The total oxygen content was fixed to be 6 in a unit cell: 8g(O1) + 32g(O2) = 6.

[b]Equivalent isotropic atomic displacement parameter calculated using the refined anisotropic atomic displacement parameters: $U_{11}(O2) = U_{22}(O2) = U_{33}(O2) = 0.12(2)$ Å^2; $U_{12}(O2) = U_{23}(O2) = U_{31}(O2) = 0.007(30)$ Å^2.

1.4.4. Ionic conduction in δ-Bi_2O_3

1.4.4.1. Diffusion pathways in δ-Bi_2O_3

The highly disordered nature of the anion sublattice in δ-Bi_2O_3 was investigated by Yashima and Ishimura[103] (Fig. 1.10) and described as being a significant contributor to the high oxide ion conduction observed. Several studies by Yashima *et al.*[102,103,106–108] and Zhong *et al.*[81] investigated the diffusion pathway of mobile anions in several oxide ion conductors. For δ-Bi_2O_3 electrolytes, diffusion pathways were initially determined to occur along both the <100> and <111> directions.[81,103] More recent investigations have found the diffusion pathway to only occur along the <100> directions (Fig. 1.11).[102,106]

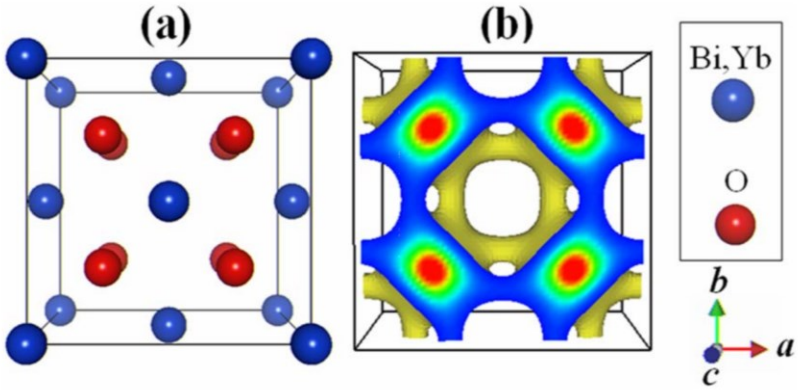

Figure 1.10. (a) Structural model and (b) the isosurface of nuclear density distribution at 0.1 fm Å^{-3} for δ-$Bi_{1.4}Yb_{0.6}O_3$. (a) An ideal fluorite type structure: average distribution of four cations and six oxide ions at the 4a and 8c sites of *F*m$\bar{3}$m, respectively. To describe the distribution around the (004) plane, only the region of 0.70 ≤ z ≤ 0.80 is drawn in (b).[102]

In work by Yashima and Ishimura,[102] the conduction pathways of δ-$Bi_{1.4}Yb_{0.6}O_3$ were investigated. The starting structure used was the ideal fluorite-type structure (Fig. 1.10). The structural disorder and diffusion pathways were visualized using the maximum-entropy method (MEM).[109,110] A high degree of disorder was present in the anion sublattice (Fig. 1.10) in comparison to that of the ideal fluorite structure. Nuclear density distribution maps at 384 and 738 °C (Fig. 1.11) further illustrate this disorder and additionally indicate an increase in disorder at higher temperatures. On heating, oxide ions shift in the <111> directions which further increases the disorder and contributes to higher conductivity at elevated temperatures. This shifting of oxide ions in <111> directions is consistent with studies by Battle *et al*.[100] on yttrium stabilized δ-$Bi_{1.46}Y_{0.54}O_3$. Additionally, oxide ion diffusion was evident along the [001] direction on the (110) plane (Fig. 1.11). This establishes that oxide ions diffuse to vacant sites in either the [100], [010] or [001] directions in three dimensional space (Fig. 1.12). Hence the resultant diffusion pathway of oxide ions in δ-Bi_2O_3 is along the <100> directions. The diffusion pathway of δ-$Bi_5PbY_2O_{11.5}$ was recently investigated by Borowska-Centkowska *et al*.[111] via molecular dynamics (MD) simulations and the oxide ion motion was similarly found to occur in the <100> directions. This oxide ion diffusion pathway is further illustrated in a supercell representation of the nuclear-density distribution of the structure (Fig. 1.12).

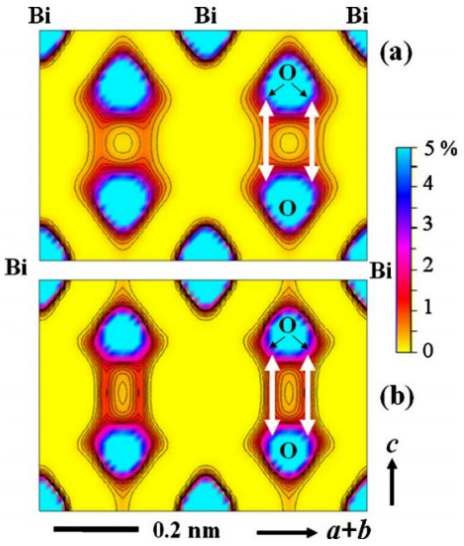

Figure 1.11. Nuclear-density distribution on the (110) plane of δ-$Bi_{1.4}Yb_{0.6}O_3$ measured at (a) 738 °C and (b) at 384 °C, with black contours in the range from 0.1 to 1.0 fm $Å^{-3}$ (0.1 fm $Å^{-3}$ step). The white arrows stand for the possible oxide-ion diffusion path along the [001] direction. The small black arrows denote the shift of oxide-ion from the regular 8c site (¼, ¼, ¼) along the <111> directions.[102]

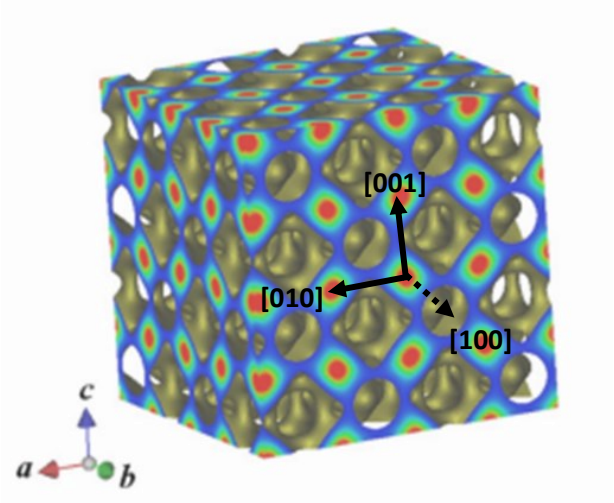

Figure 1.12. Equicontour surface of nuclear-density distribution at 0.1 fm $Å^{-3}$ with nuclear-density distribution on the {400} planes of δ-$Bi_{1.4}Yb_{0.6}O_3$ measured at 738 °C. Diffusion paths of oxide ions are seen along the <100> directions on the {400} planes. The oxide ions usually exist at the red portion around the 4c site and migrate to the nearest-neighbour 4c site through the diffusion pathway.[102]

1.4.4.2. Ionic conductivity of δ-Bi_2O_3

The conductive nature of Bi_2O_3 was initially investigated by Takahashi *et al.*[112] and the δ-polymorph was shown to have the highest conductivity of all known oxide ion conductors. The conductivity of δ-Bi_2O_3 is ~1 $S.cm^{-1}$ at ~750 °C[113–115] which is one to two orders of magnitude higher than that of stabilized zirconia and doped ceria electrolyte materials at similar temperatures (Fig. 1.13). Conductivity occurs by means of a thermally-activated hopping mechanism[23] wherein oxide ions migrate to vacant anion sites along various diffusion pathways.

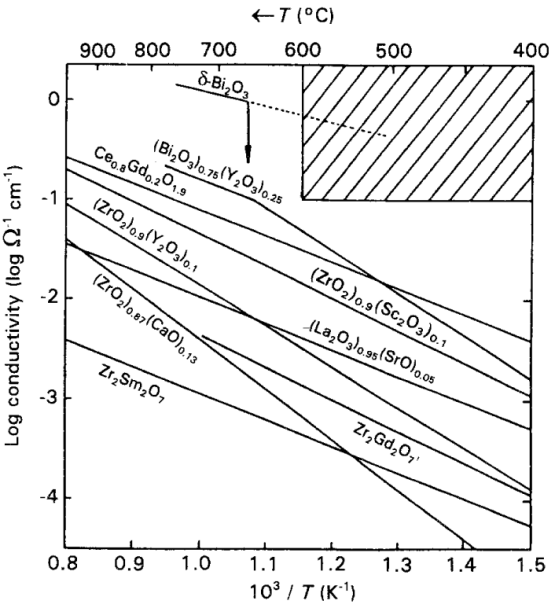

Figure 1.13. Oxide ion conductivity of selected ceramic oxides.[116,117]

The reasons for the spectacularly high conduction of δ-Bi_2O_3 has been elegantly summarized by Mairesse:[118] (i) 25% of the oxygen sites are vacant in the fluorite-type lattice, (ii) Bi^{3+} has an electronic structure characterized by the presence of a $6s^2$ lone pair – this leads to a high polarizability of the cation network[119] and (iii) Bi^{3+} has the ability to accommodate highly disordered surroundings. The use of δ-Bi_2O_3 as an electrolyte is however impractical due to the narrow phase stability range of ~730-825 °C.[99,120,121] Therefore, stabilization of this phase to lower temperatures is required for practical application as a SOFC electrolyte.

1.4.5. Stabilization of δ-Bi_2O_3

δ-Bi_2O_3 cannot be stabilized to lower temperatures in its pure form. However, addition of certain dopant atoms to Bi_2O_3 has been shown to stabilize the δ-Bi_2O_3 structure to lower temperatures, and in certain cases even to room temperature. The radius and polarizability of the dopant atom are key factors in δ-structure stabilization. Work by Jiang *et al*.[122] investigated the effect of dopant ionic radius on the crystal structure and conductivity of doped bismuth oxide - several rare earth dopants (lanthanum, neodymium, samarium, gadolinium, dysprosium, holmium, erbium, thulium and ytterbium) were investigated along with yttrium. It was found that dopants with larger ionic radii (lanthanum through gadolinium, $r \geq 1.053$ Å[123]) result in rhombohedral phase formation whereas dopants with smaller ionic radii (dysprosium through ytterbium and yttrium, $r \leq 1.027$ Å[123]) result in δ-structure stabilization, showing δ-

structure stabilization is dependent on dopant ionic radius. The correlation between ionic radius and polarizability was also investigated for several rare earth ions by Shirao *et al*.[124] It was established that the polarizability of the dopant ion was approximately proportional to the cube of the ionic radius.

The stabilization of the δ-structure via doping results in reduced conductivity. The mismatch in ionic radii between dopant and host cations results in structural distortion and reduced ion mobility. The polarizability of the cation network is reduced with the addition of dopant atoms of varying electronic structure, and this additionally contributes to the reduced conductivity.

Verkerk and Burggraaf[115] investigated the relationship between the radius of the dopant cation and the minimum amount of dopant required (X_{min} representing the mol%) to stabilize the δ-structure for several lanthanide elements and yttrium (Fig. 1.14a). The ionic conductivity of the stabilized δ-structures containing the minimum dopant content required for stabilization was additionally investigated (Fig. 1.14b). These results demonstrate that the minimum dopant content required for δ-structure stabilization is related to dopant ionic radius and that minimum dopant content is the most important factor in maximizing ionic conductivity of the stabilized δ-structure.

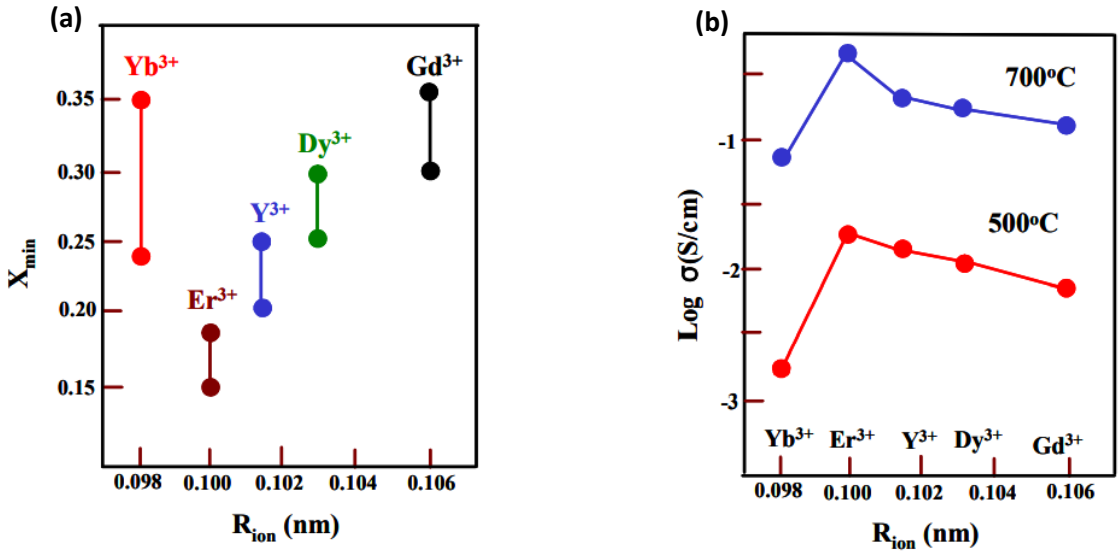

Figure 1.14. (a) X_{min} range required to stabilize the δ-structure as a function of dopant ionic radius and (b) ionic conductivity of δ-structures stabilized using lowest X_{min} for the respective dopant species.[115,125]

The stabilization of the δ-structure via doping has been extensively reviewed by Azad *et al.,*[116] Shuk *et al.*[120] and Sammes *et al.*[121] This includes the use of single dopants and in particular, the use of isovalent yttrium and rare earth dopants such as dysprosium, erbium and gadolinium for δ-structure stabilization has been widely reported.

Verkerk and Burggraaf[115] investigated the stabilization of the δ-structure by dysprosium doping and found that 28.5-50 mol% dysprosium stabilized the δ-structure to room temperature. Datta and Meehan[126] reported δ-structure stabilization with 25 mol% dysprosium dopant content which is below the range identified by Verkerk and Burggraaf. The stabilization of the δ-structure by erbium doping has been reported by Verkerk *et al.*[127,128] and Keizer *et al*.[129] and the content required was found to be in the range 17.5-45.5 mol% Er^{3+}. Additionally, doping with 20 mol% Er^{3+} was found to exhibit the highest oxide ion conductivity of any single doped δ-Bi_2O_3 system. Conductivity of ~0.023 $S.cm^{-1}$ at 500 ^oC and 0.37 $S.cm^{-1}$ at 700 ^oC has been reported for this material (Fig. 14b). Datta and Meehan[126] and Takahashi *et al.*[130] investigated the stabilization of the δ-structure by gadolinium doping. Datta and Meehan reported δ-structure stabilization with gadolinia content of 10-50 mol%. Takahashi, however, found that the δ-structure is unstable at low temperatures with gadolinia content of 5-30 mol%.[116,130]

The use of yttrium to stabilize the δ-structure has been investigated in the most detail and several investigators have attempted to establish the dopant content range required to stabilize the δ-structure.[115,126,131–133] Takahashi *et al.*[133] reported δ-structure stabilization over a range of 25-43 mol% Y^{3+} content, however, this range remains inconclusive and differs greatly from that reported by Verkerk and Burggraaf[115] (Fig. 1.14a). Conflicting dopant content ranges required for δ-structure stabilization is commonly found in the literature and is largely due to the non-attainment of equilibrium conditions in the stabilization experiments.[115,116]

The use of aliovalent dopants such as tungsten (6+), and niobium and tantalum (5+) for δ-structure stabilization has also been reported. Takahashi and Iwahara[114] reported stabilization of the δ-structure with additions of 22-27 mol% tungsten, 15-26 mol% niobium and also with 20-25 mol% tantalum. The stabilization of the δ-structure using double dopants has also been investigated. Meng *et al.*[134] investigated yttrium doped Bi_2O_3 using niobium, gadolinium, samarium and praseodymium as co-dopants. The addition of co-dopants resulted in two major benefits. Firstly, less total dopant content was required for δ-structure stabilization which was attributed to the increase in entropy of the double doped systems. Secondly, the addition of co-dopants increased the ionic conductivity of the materials, especially in the low temperature region.

The success of double doping was highlighted in studies by Jiang *et al.,*[135] Jiang *et al*.[136] and Jung *et al.*[137] where double doped bismuth oxide electrolytes were developed that display higher conductivity than 20ESB. The use of 8 mol% dysprosium and 4 mol% tungsten as double dopants (8D4WSB) resulted in ionic conductivities of 2.5×10^{-4} S.cm^{-1} at 300 °C, 0.098 S.cm^{-1} at 500 °C and 0.57 S.cm^{-1} at 700 °C.[137] Comparing this to conductivities measured for popular single doped electrolyte materials at 500 °C, the conductivity of 8D4WSB is 4 times greater than that of 20ESB, 10 times greater than that of 10GDC and 100 times greater than that of 10YSZ (Fig. 1.15).[137] As such, significant research in recent times has focused on double doped bismuth oxide systems due to significantly improved conductivity characteristics in comparison to singly doped electrolyte systems.

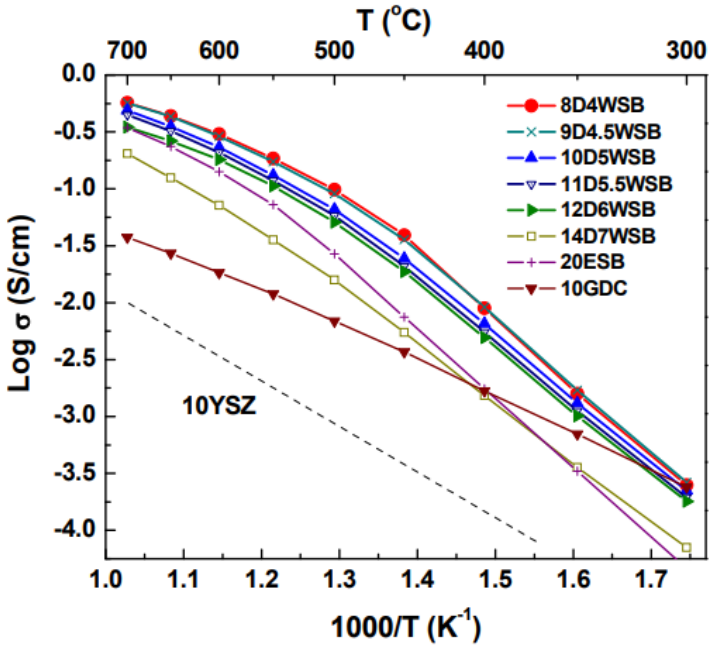

Figure 1.15. Arrhenius plot of conductivities for 8D4WSB, 9D4.5WSB, 10D5WSB, 11D5.5WSB, 12D6WSB, 14D7WSB, 20ESB and 10GDC; the dashed line represents the conductivity of 10YSZ.[137]

1.4.5.1. Phase and structural stability of stabilized δ-Bi_2O_3

Watanabe[138] investigated the phase stability of the high temperature δ-structure of bismuth oxide doped with several trivalent rare earth dopants. It was reported that the stabilized δ-structures were in fact quenched high temperature δ-structures and that these phases are metastable at temperatures below ~700 °C. Annealing these quenched phases at low temperatures resulted in the transformation of the δ-structure into the rhombohedral phase which is reported to be the true low temperature stable phase.

This phase metastability was observed in rare earth and yttrium doped bismuth oxide systems by Joshi *et al.,*[139] Takahashi *et al.*[133] and in several studies by Fung *et al.*[140–142] wherein annealing of yttrium stabilized δ-structures at temperatures below 700 °C resulted in phase transformation from the δ-structure to the rhombohedral phase.

In addition to phase stability considerations, structural stability of the δ-structure has been investigated. Over extended periods of time at elevated temperatures, the ionic conductivity of stabilized δ-structures decays. This phenomenon was reported by Jiang *et al.*[122] for trivalent rare earth and yttrium dopants and is attributed to both the transformation of the δ-structure to phases of lower conductivity and to the ordering of the anion sublattice within the δ-structure. This ordering phenomenon was extensively investigated by Boyapati *et al*.[101,143], Wachsman *et al.*[144] and Jiang *et al*.[145] and was revealed to involve the ordering of vacancies along <111> directions together with positional ordering of oxygen anions wherein migration occurs from 8c to 32f sites.

1.4.6. The structure and formation of rhombohedral bismuth oxide

The rhombohedral phase of bismuth oxide is commonly seen when the Bi_2O_3 lattice is doped with large cations.[146–148] This rhombohedral phase was initially identified in alkali earth doped bismuth oxides by Takahashi *et al.*[112] and later by Iwahara *et al.*[148] in lanthanide doped bismuth oxides. Watanabe *et al.*[132] identified this phase in the Bi_2O_3-Y_2O_3 system and described it as a conductive hexagonal phase isomorphous to rhombohedral compounds formed in alkali earth doped bismuth oxide. Additional studies have shown that doping Bi_2O_3 with lanthanides such has lanthanum, praseodymium, neodymium and terbium readily forms the rhombohedral phase.[90,147–150] This rhombohedral phase was later studied via Rietveld methods by Zhang *et al.*[151] and confirmed to crystallize in the $R\bar{3}m$ space group (Fig. 1.16). In this structure, bismuth and dopant cations jointly occupy one crystallographic site: 3a (0, 0, 0). Bismuth cations also occupy an additional site: 6c (0, 0, 0.2252) whilst oxygen anions occupy three distinct crystallographic positions: 6c (0, 0, 0.3) and 6c (0, 0, 0.091) and 6c (0, 0, 0.452). Key structural information of the rhombohedral phase formed by lanthanum doping is given in Table 1.3 and refined atomic parameters as reported by Zhang *et al*.[151] is given in Table 1.5.

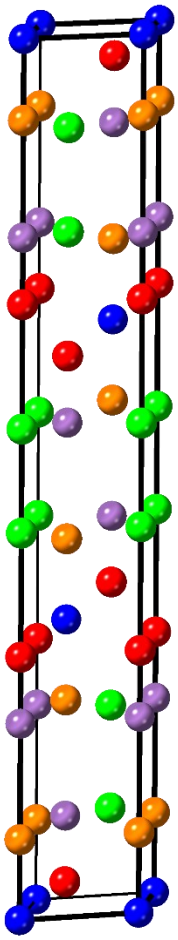

Figure 1.16. Structural model of rh-Bi_2O_3. Blue spheres denote bismuth and dopant cations in the 3a (0, 0, 0) site. Purple spheres denote bismuth cations in the 6c (0, 0, 0.2252) site. Red spheres denote oxygen atoms occupying the 6c (0, 0, 0.3) site. Orange spheres denote oxygen atoms occupying the 6c (0, 0, 0.091) site. Green spheres denote oxygen atoms occupying the 6c (0, 0, 0.452) site.

Table 1.5. Refined atomic parameters of rhombohedral $Bi_{0.8}Y_{0.2}O_{1.5}$ with space group $R\bar{3}m$.[151]

Atom	Site	Occupancy	x	y	z
Bi1	3a	0.4	0	0	0
Y	3a	0.6	0	0	0
Bi2	6c	1	0	0	0.2252
O1	6c	1	0	0	0.3
O2	6c	0.71	0	0	0.091
O3	6c	0.54	0	0	0.452

a = 3.949 Å; *c* = 27.261 Å; GOF = 2.2667.

1.4.6.1. Conductivity of rhombohedral bismuth oxide

Although significantly less conductive than the δ-phase at high temperatures, the rhombohedral phase displays good ionic conductivity in the low temperature region of ~500 °C (Table 1.6). Jolley *et al.*[146] recently investigated the rhombohedral phase of bismuth oxide as a potential electrolyte material for low temperature SOFCs. The low dopant content rhombohedral phases proved to be good ionic conductors with lanthanum and yttrium co-doped samples displaying ionic conductivity of up to 3 x 10^{-2} $S.cm^{-1}$ at 500 °C which is nearly three times higher than that of the popular GDC electrolytes at similar temperatures.[146] The conduction mechanism in rhombohedral bismuth oxide is similar to that of cubic bismuth oxide. Conductivity occurs by means of a thermally-activated hopping mechanism[23] wherein oxide ions migrate to vacant anion sites along various diffusion pathways. The nature of the diffusion pathways are yet to be investigated as was done for cubic bismuth oxides.

When cubic bismuth oxide materials are annealed at elevated temperatures for extended periods of time, a decay in ionic conductivity occurs as previously mentioned. Rhombohedral bismuth oxides were found to have significantly higher structural stability in comparison to the cubic structured oxides. This decay was found to be significantly reduced for niobium-doped rhombohedral Bi_2O_3 materials when annealed at 500 °C for long periods (Fig. 1.17).[146] This is due to the rhombohedral structure type not experiencing ordering of the anion sublattice. The minor decay in conductivity seen for rhombohedral structured oxides is due to the formation of a secondary, less conductive tetragonal phase.

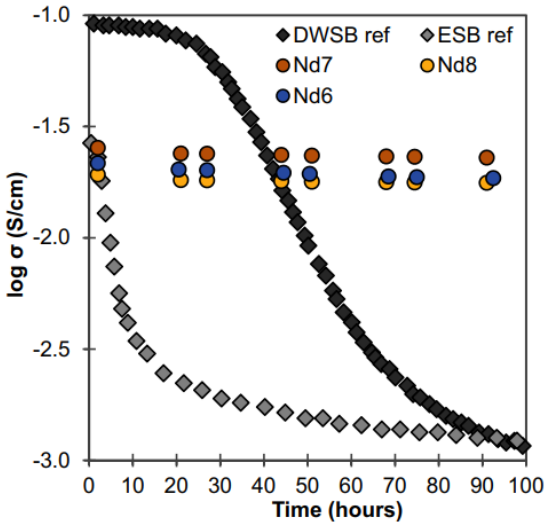

Figure 1.17. Conductivity of multiple rhombohedral niobium doped Bi_2O_3 samples as a function of aging time at 500 °C.[146] ESB and DWSB are both δ-Bi_2O_3 materials included as references.[152]

Table 1.6. Oxide ion conductivity at 500 °C of selected Bi_2O_3-based electrolytes.

Electrolyte	σ (S.cm^{-1})	Structure	Ref.
$Bi_{0.8}Sr_{0.1}O_{1.3}$	6.0 x 10^{-3}	rhombohedral	[114]
$Bi_{0.8}Ba_{0.1}O_{1.3}$	1.1 x 10^{-2}	rhombohedral	[114]
$Bi_{0.935}La_{0.051}Y_{0.014}O_{1.5}$	3.2 x 10^{-2}	rhombohedral	[146]
$Bi_{0.80}Er_{0.20}O_{1.5}$	2.1 x 10^{-2}	cubic	[120,127,129,153]
$Bi_{0.75}Y_{0.25}O_{1.5}$	1.3 x 10^{-2}	cubic	[116,120]
$Bi_{0.715}Dy_{0.285}O_{1.5}$	7.1 x 10^{-3}	cubic	[115]

1.5. Thermal expansion of δ-Bi_2O_3 and rh-Bi_2O_3

Although minimal thermal expansion mismatch with adjacent components has been identified as a crucial requirement of an electrolyte material to function successfully and efficiently in a SOFC,[68,69] the thermal expansion behaviour of bismuth oxides has been sparsely reported. Ideally, the thermal expansion of candidate bismuth oxide based electrolyte materials should match that of adjacent components currently used in SOFCs (Table 1.7). The commonly used 8YSZ electrolyte displays minor thermal expansion mismatch with materials used as adjacent cell components.

The thermal expansion behaviour of pure δ-Bi_2O_3 was initially investigated by Gattow and Schröder.[98] The coefficient of thermal expansion (CTE) was determined to be 43.6 x 10^{-6} K^{-1} over the temperature range of 675-750 °C which is significantly higher than that of 8YSZ and of adjacent cell components. Levin and Roth[93] also investigated the thermal expansion behaviour of pure δ-Bi_2O_3 and reported the CTE to be 24.0 x 10^{-6} K^{-1} over the temperature range of 500-650 °C. Although significantly lower than that reported by Gattow and Schröder, the CTE derived by Levin and Roth is still far higher than that of 8YSZ and adjacent cell components materials. Doped δ-Bi_2O_3 systems are also characterized by high degrees of thermal expansion. Wu *et al.*[154] investigated the thermal expansion behaviour of δ-20YSB and determined CTEs of 15.4 x 10^{-6} K^{-1} over 30-500 °C and 20.3 x 10^{-6} K^{-1} over 500-800 °C. These values agree more with CTEs reported by Levin and Roth for pure δ-Bi_2O_3. The expansion behaviour of δ-20YSB is also significantly higher than that observed for 8YSZ and adjacent cell component materials.

The thermal expansion behaviour of rh-Bi_2O_3 has been investigated by Drache *et al.*[150] for the rhombohedral $Bi_{0.775}La_{0.225}O_{1.5}$. No values for the CTEs were given and hence values reported here are approximations from graphical information published. Over the temperature range of ~22-700 °C, the CTE is approximately 58.3 x 10^{-6} K^{-1} along the *a*-axis and approximately 333 x 10^{-6} K^{-1} along the *c*-axis. No other studies were found that have investigated the thermal expansion behaviour of rhombohedral bismuth

oxides and these results by Drache *et al.*[150] need to be corroborated. The reported CTE values are also significantly higher than those of 8YSZ and adjacent component materials.

Table 1.7. Comparison of the CTEs determined for pure δ-Bi_2O_3, yttrium doped δ-Bi_2O_3, rhombohedral lanthanum doped Bi_2O_3 electrolyte materials to those reported for currently used SOFC components.

Component	Material	CTE (10^{-6} K^{-1})	Temperature range (°C)	Ref.
Electrolyte	pure δ-Bi_2O_3	43.6	675-750	[98]
Electrolyte	pure δ-Bi_2O_3	24.0	730-825	[93]
Electrolyte	20YSB	15.4	30-500	[154]
		20.3	500-800	
Electrolyte	rh-$Bi_{0.775}La_{0.225}O_{1.5}$	~61.8[a]	20-700	[150]
		~327.3[b]	20-700	
		~40.0[a]	800-900	
		~327.3[b]	800-900	
Electrolyte	8YSZ	10.5-10.9	30-1000	[67]
Inter-connect	Ferritic steel, X10CrAl 18	12.9-13.9	30-1000	[155]
Cathode	Perovskite, $La_{0.65}Sr_{0.3}MnO_3$	12.0-12.3	30-1000	[67]
Anode	Cermet, 40 v/o Ni + 60 v/o 8YSZ	12.5-12.6	30-1000	[155]

[a] CTE along the *a*-axis
[b] CTE along the *c*-axis

1.6. Additional stability considerations

The inertness of bismuth oxide electrolytes during cell fabrication and operation is also an area of concern. Verkerk and Burggraaf,[115] Takahashi *et al.*[156] and Yaremchenko *et al.*[157] reported the tendency of Bi_2O_3 based materials to reduce to Bi metal under reducing atmospheres at elevated temperatures (which would be present at the anode side of a SOFC). Additionally, studies by Gil *et al.*[158] and more recently by Miao *et al.*[159] and Wang *et al.*[160] showed that Bi_2O_3 has a high tendency to volatilize at elevated temperatures (~>900 °C). The reduction and volatilization of Bi_2O_3 results in the chemical degradation of the electrolyte material and hence severely limits the use of Bi_2O_3-based electrolytes in SOFCs.[115] Mahato *et al.*[20] reported the tendency towards reduction and volatilization as two of the main challenges facing Bi_2O_3 based electrolytes.

1.7. Project aim and objectives

The overall aim of this research was to explore doped bismuth oxide materials as improved SOFC electrolytes. The cubic (δ-Bi_2O_3) and rhombohedral (rh-Bi_2O_3) phases are known to be promising electrolyte materials and hence these two phases were focused on. As such, several doped bismuth oxide materials were synthesized via a citrate sol-gel synthetic route and investigated based on the criteria

established for SOFC electrolyte materials. These investigations are packaged into four objectives and are presented in individual thesis chapters.

Objective 1, investigated in chapter 3

The first study involved a detailed investigation of the structural stability, ionic conductivity and *in situ* δ-phase formation of yttrium-stabilized bismuth oxide ($Y_xBi_{2-x}O_3$). This system has been extensively studied however the amount of yttrium content required to truly stabilize the δ-phase is questionable and this was investigated. The structural stability was investigated using powder X-ray diffraction (PXRD) and Rietveld refinement methodologies as well as variable temperature Raman spectroscopy. The *in situ* formation and thermal expansion behaviour of the δ-phase is rarely reported in the literature. These features were investigated by means of synchrotron-based variable temperature PXRD and Rietveld refinement methodologies. The ionic conductivity of these phases was investigated by means of variable temperature electrochemical impedance spectroscopy which additionally indicated the presence of a phase mixture at lower temperatures. The optimum electrolyte material, based on a compromise between optimum conductivity and structural stability, within the yttrium doped bismuth oxide system is proposed.

Objective 2, investigated in chapter 4:

The second study involved an investigation of several stability criteria of yttrium-stabilized bismuth oxide ($Y_xBi_{2-x}O_3$) using both ambient and VT-PXRD. The metastability of these 'stabilized' phases under ambient conditions for extended periods of time was investigated – a phenomenon which is often overlooked and has yet to be properly investigated. Under ambient conditions, the 'stabilized' materials were found to spontaneously undergo phase transformations and selected materials were found to spontaneously react with atmospheric carbon dioxide. This carbon sequestration by bismuthate materials was reported for the first time in this work. Novel methods to enhance the ambient stability of the δ-phase were also investigated which involved pelletization and additional sintering strategies as well as annealing under inert atmospheres. An *in situ* investigation of the phase stability and thermal expansion behaviour of selected δ-phase materials is also presented wherein an abrupt increase in cubic phase lattice parameter was evident. This anomalous thermal expansion behaviour was extensively investigated in chapter 5.

Objective 3, investigated in chapter 5:

The third study involved investigating the phase stability and thermal expansion behaviour of yttrium-stabilized bismuth oxide materials via synchrotron-based *in situ* total scattering studies. Unravelling the non-linear thermal expansion (NLTE) behaviour as well as the abrupt increase in cubic phase lattice parameter is crucial for the potential application of these materials as SOFC electrolytes. The contribution from the state of disorder of the material towards the observed NLTE behaviour was investigated and particular focus placed on establishing the phase change mechanism responsible for the jump in δ-phase unit cell volume, which has not been established yet.

Objective 4, investigated in chapter 6:

The final study involved an investigation of the phase stability window and the *in* situ phase stability behaviour of the rhombohedral phase of bismuth oxide using ambient and VT-PXRD and Rietveld refinement methodologies. The formation of the rhombohedral phase is dependent on dopant ionic radius and dopant content. In this study, extensive dopant ionic radii and content ranges were investigated to further establish the rhombohedral phase stability window. The *in* situ phase stability behaviour of the rhombohedral phase has been sparsely reported and in this work synchrotron-based VT-PXRD was used to investigate this.

1.8. References

1. BP p.l.c. BP Statistical Review of World Energy. (2019). Available at: https://www.bp.com/content/dam/bp/business-sites/en/global/corporate/pdfs/energy-economics/statistical-review/bp-stats-review-2019-full-report.pdf. (Accessed: 10th March 2021)

2. BP p.l.c. BP Statistical Review of World Energy. (2020). Available at: https://www.bp.com/content/dam/bp/business-sites/en/global/corporate/pdfs/energy-economics/statistical-review/bp-stats-review-2020-full-report.pdf. (Accessed: 10th March 2021)

3. Stambouli, A. B. and Traversa, E. Solid oxide fuel cells (SOFCs): A review of an environmentally clean and efficient source of energy. *Renew. Sustain. Energy Rev*. **6**, 433–455 (2002).

4. Ruiz-Morales, J. C., Marrero-Lopez, D., Galvez-Sanchez, M., Canales-Vazquez, J., Savaniu, C. and Savvin, S. N. Engineering of materials for solid oxide fuel cells and other energy and environmental applications. *Energy Environ. Sci*. **3**, 1670–1681 (2010).

5. Shafiee, S. and Topal, E. When will fossil fuel reserves be diminished? *Energy Policy* **37**, 181–189 (2009).

6. Höök, M. and Tang, X. Depletion of fossil fuels and anthropogenic climate change-A review. *Energy Policy* **52**, 797–809 (2013).

7. Andújar, J. M. and Segura, F. Fuel cells: History and updating. A walk along two centuries. *Renew. Sustain. Energy Rev*. **13**, 2309–2322 (2009).

8. Ormerod, R. M. Solid oxide fuel cells. *Chem. Soc. Rev*. **32**, 17–28 (2003).

9. Kirubakaran, A., Jain, S. and Nema, R. K. A review on fuel cell technologies and power electronic interface. *Renew. Sustain. Energy Rev*. **13**, 2430–2440 (2009).

10. Ishikawa, T. and Yasue, H. Start-up, testing and operation of 1000 kW class MCFC power plant. *J. Power Sources* **86**, 145–150 (2000).

11. EG&G Technical Services, I. Fuel cell hand book. U.S. Department of energy - Office of Fossil Energy, National Energy Technology Laboratory 7, (2000).

12. Fitzgerald, J. and O'Bryan, N. Fuel Cells: A Better Energy Source for Earth and Space. (2005). Available at: https://www.nasa.gov/centers/glenn/technology/fuel_cells.html. (Accessed: 9th January 2021)

13. De Geeter, E. Zero emission vehicles and sustainable mobility - Zetek Power's alkaline fuel cells. SAE Tech. Pap. - Repr. From *Proc. 2001 Environ. Sustain. Conf. Exhib*. P-365 (2001). doi:10.4271/2001-01-3750

14. McAree, G. Ballard Announces Van Hool Follow-on Order For 10 Fuel Cell Modules to Power Buses in Holland. (2020). Available at: https://www.ballard.com/about-ballard/newsroom/news-releases/2020/12/17/ballard-announces-van-hool-follow-on-order-for-10-fuel-cell-modules-to-power-buses-in-holland. (Accessed: 9th January 2021)

15. Hasegawa, M. and Horiuchi, Y. Development of the FP-100i Phosphoric Acid Fuel Cell. *Fuji Electr. Rev*. **56**, 140–145 (2010).

16. Cardona, C. A., Quintero, J. A. and Paz, I. C. Production of bioethanol from sugarcane bagasse: Status and perspectives. *Bioresour. Technol*. **101**, 4754–4766 (2010).

17. Samsung SDI develops military portable DMFC. *Fuel Cells Bull*., 6–7 (2009).

18. Toshiba Launches Direct Methanol Fuel Cell in Japan as External Power Source for Mobile Electronic Devices. Toshiba Corporation (2009). Available at: https://www.toshiba.co.jp/about/press/2009_10/pr2201.htm. (Accessed: 10th January 2021)

19. Zuo, C., Liu, M. and Liu, M. Solid Oxide Fuel Cells. in *Sol-Gel Processing for Conventional and Alternative Energy* (eds. Aparicio, M., Jitianu, A. and Klein, L. C.) 7–36 (Springer-Verlag, 2012). doi:10.1007/978-1-4614-1957-0

20. Mahato, N., Banerjee, A., Gupta, A., Omar, S. and Balani, K. Progress in material selection for solid oxide fuel cell technology: A review. *Prog. Mater. Sci*. **72**, 141–337 (2015).

21. Yamamoto, O. Solid oxide fuel cells: Fundamental aspects and prospects. *Electrochim. Acta* **45**, 2423–2435 (2000).

22. Möbius, H. H. On the history of solid electrolyte fuel cells. *J. Solid State Electrochem*. **1**, 2–16 (1997).

23. Skinner, S. J. and Kilner, J. A. Oxygen ion conductors. *Mater. Today* **6**, 30–37 (2003).

24. Badwal, S. P. S. and Foger, K. Solid oxide electrolyte fuel cell review. *Ceram. Int*. **22**, 257–265 (1996).

25. Vailionis, A. X-ray Diffraction - Basic Principles of Interaction of Waves. (2013). Available at: http://www.stanford.edu/group/glam/xlab/MatSci162_172/LectureNotes/03_KinDiff, Laue, Powder.pdf. (Accessed: 8th January 2021)

26. Du, Y. and Sammes, N. M. Fabrication and properties of anode-supported tubular solid oxide fuel cells. *J. Power Sources* **136**, 66–71 (2004).

27. Singhal, S. C. Solid Oxide Fuel Cells. *Electrochem. Soc. Interface* 41–44 (2007).

28. Michihisa, K. Solid Oxide Fuel Cell (SOFC). (2008). Available at: http://www.aki.che.tohoku.ac.jp/~koyama/html/research/SOFC.html. (Accessed: 11th January 2021)

29. Minh, N. Q. Ceramic Fuel Cells. *J. Am. Ceram. Soc*. **76**, 563–588 (1993).

30. Fergus, J. W. Electrolytes for solid oxide fuel cells. *J. Power Sources* **162**, 30–40 (2006).

31. Minh, N. Q. Solid oxide fuel cell technology - Features and applications. *Solid State Ion.* **174**, 271–277 (2004).

32. Scott, J. H. The development of fuel cell technology for electric power generation: From NASA's manned space program to the 'hydrogen economy'. *Proc. IEEE* **94**, 1815–1825 (2006).

33. Abdalla, A. M., Hossain, S., Azad, A. T., Petra, M. I, Begum, F., Eriksson, S. G. and Azad, A. K. Nanomaterials for solid oxide fuel cells: A review. *Renew. Sustain. Energy Rev*. **82**, 353–368 (2018).

34. Wachsman, E. D., Marlowe, C. A. and Lee, K. T. Role of solid oxide fuel cells in a balanced energy strategy. *Energy Environ. Sci*. **5**, 5498–5509 (2012).

35. BU-105: Battery Definitions and what they mean. Battery University Group Available at: https://batteryuniversity.com/index.php/learn/article/battery_definitions. (Accessed: 18th January 2021)

36. Wachsman, E. D. and Lee, K. T. Lowering the temperature of solid oxide fuel cells. *Science* **334**, 935–939 (2011).

37. Hydrogen Program Department of Energy USA. Fuel Cells. Available at: https://www.hydrogen.energy.gov/fuel_cells.html. (Accessed: 21st January 2021)

38. Flipsen, S. F. J. Power sources compared: The ultimate truth? *J. Power Sources* **162**, 927–934 (2006).

39. How long do diesel generators last? Available at: https://www.wpowerproducts.com/news/diesel-engine-life-expectancy/. (Accessed: 11th January 2021)

40. First, R. How long do hydropower installations last? Available at: https://www.renewablesfirst.co.uk/hydropower/hydropower-learning-centre/how-long-will-hydropower-systems-last/. (Accessed: 11th January 2021)

41. How long do solar panels last? Available at: https://news.energysage.com/how-long-do-solar-panels-last/. (Accessed: 2nd January 2021)

42. Schumacher, C. and Weber, F. How to extend the lifetime of wind turbines. TÜV SÜD Industrie Service GmbH (2019). Available at: https://www.renewableenergyworld.com/2019/09/20/how-to-extend-the-lifetime-of-wind-turbines/. (Accessed: 20th January 2021)

43. BU-120: How does the Fuel Cell Work? Battery University Group (2020). Available at: https://batteryuniversity.com/learn/article/fuel_cell_technology. (Accessed: 12th January 2021)

44. Gómez, S. Y. and Hotza, D. Current developments in reversible solid oxide fuel cells. *Renew. Sustain. Energy Rev*. **61**, 155–174 (2016).

45. Guaitolini, S. V. M., Yahyaoui, I., Fardin, J. F., Encarnacao, L. F. and Tadeo, F. A review of fuel cell and energy cogeneration technologies. in *2018 9th International Renewable Energy Congress (IREC)* (2018).

46. Osaka Gas, Aisin, Kyocera, Chofu and Toyota Announce Completion of World-Class Efficiency Residential-Use Solid Oxide Fuel Cell (SOFC) Cogeneration System Co-Development and Commercialization of "ENE-FARM Type S". News Releases (2012). Available at: https://global.kyocera.com/news-archive/2012/0305_woec.html. (Accessed: 19th January 2021)

47. Wakui, T., Yokoyama, R. and Shimizu, K. Suitable operational strategy for power interchange operation using multiple residential SOFC (solid oxide fuel cell) cogeneration systems. *Energy* **35**, 740–750 (2010).

48. Naimaster, E. J. and Sleiti, A. K. Potential of SOFC CHP systems for energy-efficient commercial buildings. *Energy Build*. **61**, 153–160 (2013).

49. Liu, M., Lynch, M. E., Blinn, K., Alamgir, F. M. and Choi, Y. Rational SOFC material design: New advances and tools. *Mater. Today* **14**, 534–546 (2011).

50. Jaiswal, N., Tanwar, K., Suman, R., Kumar, D., Uppadhya, S. and Parkash, O. A brief review on ceria based solid electrolytes for solid oxide fuel cells. *J. Alloys Compd*. **781**, 984–1005 (2019).

51. Sgroi, M. F., Zedde, F., Barbera, O., Stassi, A., Sebastian, D., Lufrano, F., Baglio, V., Arico, A. S., Bonde, J. L., and Schuster, M. Cost analysis of direct methanol fuel cell stacks for mass production. *Energies* **9**, (2016).

52. Yakabe, H., Sakurai, T., Sobue, T., Yamashita, S. and Hase, K. Solid oxide fuel cells as promising candidates for distributed generators. in *IEEE International Conference on Industrial Informatics, INDIN'06* 369–374 (2006). doi:10.1109/INDIN.2006.275828

53. Japanese group unveils SOFC Ene-Farm residential cogen unit. *Fuel Cells Bull*. **4** (2012).

54. Cumulative sales of ENE-FARM have exceeded 300,000 units [in Japanese]. Available at: http://www.gas.or.jp/user/comfortable-life/enefarm-partners/common/data/20191121_web.pdf. (Accessed: 21st January 2021)

55. Kyocera develops first 3 kW SOFC unit for small business cogen. *Fuel Cells Bull*. **5** (2017).

56. Kyocera Corporation. Energy Conversion Devices - Solid Oxide Fuel Cell Stack. Available at: https://global.kyocera.com/prdct/ecd/sofc/. (Accessed: 9th January 2021)

57. Dziurdzia, B., Magonski, Z. and Jankowski, H. Commercialisation of Solid Oxide Fuel Cells - Opportunities and forecasts. *IOP Conf. Ser. Mater. Sci. Eng*. **104**, (2016).

58. Bloom Energy Server ES5-200kW. (2021). Available at: https://www.bloomenergy.com/datasheets/energy-server-es5-200kw. (Accessed: 21st January 2021)

59. Helman, C. The Forbes Investigation: How Bloom Energy Blew Through Billions Promising Cheap, Green Tech That Falls Short. Forbes Online Magazine (2020). Available at: https://www.forbes.com/sites/christopherhelman/2020/02/13/the-forbes-investigation-how-bloom-energy-blew-through-billions-promising-cheap-green-tech-that-falls-short/?sh=43b3f7763e5f. (Accessed: 21st January 2021)

60. Kyocera Corporation. KYOCERA @ CES 2020 - Advanced Devices. Available at: https://global.kyocera.com/ces/advanced-devices/. (Accessed: 20th January 2021)

61. KYOCERA Develops Industry's First 3-Kilowatt Solid-Oxide Fuel Cell for Institutional Cogeneration. Available at: https://www.businesswire.com/news/home/20170706005441/en/KYOCERA-Develops-Industrys-First-3-Kilowatt-Solid-Oxide-Fuel-Cell-for-Institutional-Cogeneration. (Accessed: 20th January 2021)

62. Campbell, M. Apple's Campus 2 to use updated Bloom Energy fuel cells first deployed at NC data center. Apple Insider Available at: https://appleinsider.com/articles/16/06/25/apples-campus-2-to-use-updated-bloom-energy-fuel-cells-first-deployed-at-nc-data-center. (Accessed: 20th January 2021)

63. Nissan unveils world's first Solid-Oxide Fuel Cell vehicle. Available at: https://usa.nissannews.com/en-US/releases/nissan-unveils-world-s-first-solid-oxide-fuel-cell-vehicle#. (Accessed: 21st January 2021)

64. Global 10 Best-Selling Plug-In Cars Are Accelerating Forward. Available at: https://www.hybridcars.com/global-10-best-selling-plug-in-cars-are-accelerating-forward/. (Accessed: 21st January 2021)

65. Fellet, M. and Rossner, W. Ceramics improve operating conditions of solid-oxide fuel cells. *MRS Bull*. **40**, 214–215 (2015).

66. Ivers-Tiffée, E., Weber, A. and Herbstritt, D. Materials and technologies for SOFC-components. *J. Eur. Ceram. Soc*. **21**, 1805–1811 (2001).

67. Tietz, F. Thermal expansion of SOFC materials. *Ionics (Kiel)*. **5**, 129–139 (1999).

68. Basu, R. N. Materials for solid oxide fuel cells. in *Recent Trends in Fuel Cell Science and Technology* (ed. Basu, S.) 286–331 (Anamaya Publishers, 2007).

69. Hussain, S. and Yangping, L. Review of solid oxide fuel cell materials: cathode, anode, and electrolyte. *Energy Transitions* **4**, 113–126 (2020).

70. Goodenough, J. B. Oxide-Ion Electrolytes. *Annu. Rev. Mater. Res*. **33**, 91–128 (2003).

71. Ralph, J. M., Schoeler, A. C. and Krumpelt, M. Materials for lower temperature solid oxide fuel cells. *J. Mater. Sci*. **36**, 1161–1172 (2001).

72. Yoshimura, M. Phase stability of zirconia. *Am. Ceram. Soc. Bull*. **67**, 1950–1955 (1988).

73. Badwal, S. P. S. and Ciacchi, F. T. Oxygen-ion conducting electrolyte materials for solid oxide fuel cells. *Ionics (Kiel)*. **6**, 1–21 (2000).

74. Weller, M., Khelfaoui, F., Kilo, M., Taylor, M. A., Argirusis, C. and Borchardt, G. Defects and phase transitions in yttria- And scandia-doped zirconia. *Solid State Ion.* **175**, 329–333 (2004).

75. Nomura, K., Mizutani, Y., Kawai, M., Nakamura, Y. and Yamamoto, O. Aging and Raman scattering study of scandia and yttria doped zirconia. *Solid State Ion.* **132**, 235–239 (2000).

76. Omar, S., Najib, W. Bin and Bonanos, N. Conductivity ageing studies on 1M10ScSZ (M^{4+} = Ce, Hf). *Solid State Ion.* **189**, 100–106 (2011).

77. Dalslet, B. T., Blennow, P., Hendriksen, P. V., Bonanos, N., Lybye, D. and Morgensen, M. Assessment of doped ceria as electrolyte. *J. Solid State Electrochem*. **10**, 547–561 (2006).

78. Artini, C. Rare-Earth-Doped Ceria Systems and Their Performance as Solid Electrolytes: A Puzzling Tangle of Structural Issues at the Average and Local Scale. *Inorg. Chem*. **57**, 13047–13062 (2018).

79. Morgensen, M., Lybye, D., Kammer, K. and Bonanos, N. Ceria Revisited: Electrolyte or Electrode Material? *ECS Proc*. **2005–07**, 1068–1074 (2005).

80. Kharton, V. V., Marques, F. M. B. and Atkinson, A. Transport properties of solid oxide electrolyte ceramics: A brief review. *Solid State Ion.* **174**, 135–149 (2004).

81. Guohua, Z., Jianglong, W. and Zhi, Z. The doping effects in δ-Bi_2O_3 oxide ionic conductor. *Phys. Status Solidi Basic Res*. **245**, 2737–2742 (2008).

82. Wang, S.-F., Hsu, Y.-F., Tsai, W.-C. and Lu, H.-C. The phase stability and electrical conductivity of Bi_2O_3 ceramics stabilized by Co-dopants. *J. Power Sources* **218**, 106–112 (2012).

83. Drache, M., Roussel, P. and Wignacourt, J. P. Structures and oxide mobility in Bi-Ln-O materials: Heritage of Bi_2O_3. *Chem. Rev*. **107**, 80–96 (2007).

84. Harwig, H. A. and Gerards, A. G. Electrical properties of the α, β, γ, and δ phases of bismuth sesquioxide. *J. Solid State Chem*. **26**, 265–274 (1978).

85. Harwig, H. A. and Gerards, A. G. The polymorphism of bismuth sesquioxide. *Thermochim. Acta* **28**, 121–131 (1979).

86. Cornei, N., Tancret, N., Abraham, F. and Mentré, O. New ε-Bi_2O_3 metastable polymorph. *Inorg. Chem*. **45**, 4886–4888 (2006).

87. Immovilli, S., Morten, B., Prudenziati, M., Gualtieri, A. and Bersani, M. Interactions between bismuth oxide and ceramic substrates for thick film technology. *J. Mater. Res*. **13**, 1865–1874 (1998).

88. Watanabe, A. Phase equilibria in the system Bi_2O_3-Y_2O_3: no possibility of δ-Bi_2O_3 stabilization. *Solid State Ion.* **86–88**, 1427–1430 (1996).

89. Liu, X., Staubitz, A. and Gesing, T. M. Thermochromic Behavior of Yttrium-Substituted Bismuth Oxides. *ACS Appl. Mater. Interfaces* **11**, 33147–33156 (2019).

90. Obbade, S., Huve, M., Suard, E., Drache, M. and Conflant, P. Powder neutron diffraction and TEM investigations of $Bi_{0.775}Ln_{0.225}O_{1.5}$ oxide conductors (Ln=La, Pr, Nd, Sm, Tb, Dy) with rhombohedral Bi-Sr-O type: Structural relationships with monoclinic ε-$Bi_{4.86}La_{1.14}O_9$ form. *J. Solid State Chem*. **168**, 91–99 (2002).

91. Ivanov, S., Tellgren, R., Rundlof, H., and Orlov, V. Structural studies of α-Bi_2O_3 by neutron powder diffraction. *Powder Diffr*. **16**, 227–230 (2012).

92. Blower, S. K. and Greaves, C. The structure of β-Bi_2O_3 from powder neutron diffraction data. *Acta Crystallogr. Sect. C Cryst. Struct. Commun*. **44**, 587–589 (1988).

93. Levin, E. M. and Roth, R. S. Polymorphism of bismuth sesquioxide. I. Pure Bi_2O_3. *J. Res. Natl. Bur. Stand. Sect. A Phys. Chem*. **68A**, 189 (1964).

94. Portefaix, N., Conflant, P., Boivin, J. C., Wignacourt, J. P. and Drache, M. New Bi-Ln-V-O Anionic Conductors with δ-Bi_2O_3 Fluorite-Type Structure (Ln=Y, Sm, Eu, Gd, Tb, Dy, Er, Yb). *J. Solid State Chem*. **134**, 219–226 (1997).

95. Drache, M., Wignacourt, J. P. and Conflant, P. Evidence for a new monoclinic Bi-La oxide solid solution: Identification and structural relationship to the rhombohedral Bi-Sr-O type. *J. Solid State Chem*. **151**, 281–285 (2000).

96. Sillen, L. G. X-Ray Studies of Bismuth Trioxide. *Ark. Kemi. Miner. Geol*. **1**, (1937).

97. Shuk, P. Oxide ion conducting solid electrolytes based on Bi_2O_3. *Solid State Ion.* **89**, 179–196 (1996).

98. Gattow, G. and Schröder, H. Über Wismutoxide. III. Die Kristallstruktur der Hochtemperaturmodifikation von Wismut(III)-oxid (δ-Bi_2O_3). *ZAAC - J. Inorg. Gen. Chem*. **318**, 176–189 (1962).

99. Harwig, H. A. On the Structure of Bismuthsesquioxide: the α, β, γ and δ-Phase. *ZAAC - J. Inorg. Gen. Chem*. **444**, 151–166 (1978).

100. Battle, P. D., Catlow, C. R. A., Drennan, J. and Murray, A. D. The structural properties of the oxygen conducting δ phase of Bi_2O_3. *J. Phys. C Solid State Phys*. **16**, 561–566 (1983).

101. Boyapati, S., Wachsman, E. D. and Chakoumakos, B. C. Neutron diffraction study of occupancy and positional order of oxygen ions in phase stabilized cubic bismuth oxides. *Solid State Ion.* **138**, 293–304 (2001).

102. Yashima, M. and Ishimura, D. Visualization of the diffusion path in the fast oxide-ion conductor $Bi_{1.4}Yb_{0.6}O_3$. *Appl. Phys. Lett*. **87**, 1–3 (2005).

103. Yashima, M. and Ishimura, D. Crystal structure and disorder of the fast oxide-ion conductor cubic Bi_2O_3. *Chem. Phys. Lett*. **378**, 395–399 (2003).

104. Leszczynska, M., Borowska-Centkowska, A., Malys, M., Dygas, J. R., Krok, F., Wrobel, W. and Abrahams, I. The double rare-earth substituted bismuth oxide system $Bi_3Y_{1-x}Yb_xO_6$. *Solid State Ion.* **269**, 37–43 (2015).

105. Abrahams, I., Liu, X., Hull, S., Norberg, S. T., Krok, F., Szmigiel-Kozanecka, A., Islam, M. S. and Stokes, S. J. A combined total scattering and simulation approach to analyzing defect structure in Bi_3YO_6, *Chem. Mater.*, **22**, 4435–4445 (2010).

106. Yashima, M. Diffusion pathway of mobile ions and crystal structure of ionic and mixed conductors-A brief review. *J. Ceram. Soc. Japan* **117**, 1055–1059 (2009).

107. Yashima, M. and Tsuji, T. Crystal structure, disorder, and diffusion path of oxygen ion conductors $Y_{1-x}Ta_xO_{1.5+x}$ (x = 0.215 and 0.30). *Chem. Mater*. **19**, 3539–3544 (2007).

108. Yashima, M., Kobayashi, S. and Yasui, T. Positional disorder and diffusion path of oxide ions in the yttria-doped ceria $Ce_{0.93}Y_{0.07}O_{1.96}$. *Faraday Discuss*. **134**, 369–376 (2007).

109. Collins, D. M. Electron density images from imperfect data by iterative entropy maximization. *Nature* **298**, 49 (1982).

110. Takata, M., Umeda, B., Nishibori, E., Sakata, M., Saitot, Y., Ohno, M. and Shinohara, H. Confirmation by X-ray diffraction of the endohedral nature of the metallofullerene $Y@C_{82}$. *Nature* **377**, 46–49 (1995).

111. Borowska-Centkowska, A., Liu, X., Krynski, M., Leszczynska, M., Wrobel, W., Malys, M., Hull, S., Norberg, S. T., Krok, F. and Abrahams, I. Defect structure in δ-$Bi_5PbY_2O_{11.5}$, *RSC Adv.*, 2019, **9**, 9640–9653

112. Takahashi, T., Iwahara, H. and Nagai, Y. High oxide ion conduction in sintered Bi_2O_3 containing SrO, CaO or La_2O_3. *J. Appl. Electrochem*. **2**, 97–104 (1972).

113. Punn, R., Feteira, A. M., Sinclair, D. C. and Greaves, C. Enhanced Oxide Ion Conductivity in Stabilized δ-Bi_2O_3. *J. Am. Chem. Soc*. **128**, 15386–15387 (2006).

114. Takahashi, T. and Iwahara, H. Oxide ion conductors based on bismuthsesquioxide. *Mater. Res. Bull*. **13**, 1447–1453 (1978).

115. Verkerk, M. J. and Burggraaf, A. J. High oxygen ion conduction in sintered oxides of the Bi_2O_3-Dy_2O_3 system. *J. Electrochem. Soc*. **128**, 75–81 (1981).

116. Azad, A. M., Larose, S. and Akbar, S. A. Bismuth oxide-based solid electrolytes for fuel cells. *J. Mater. Sci*. **29**, 4135–4151 (1994).

117. Steele, B.C.H. Oxygen Ion Conductors. in *High Conductivity Solid Ionic Conductors: Recent Trends and Applications* (ed. Takahashi, T.) 402–446 (World Scientific Publishing Co. Ltd., 1989).

118. Boivin, J. C. and Mairesse, G. Recent Material Developments in Fast Oxide Ion Conductors. *Chem. Mater*. **10**, 2870–2888 (1998).

119. Laarif, A. and Theobald, F. The lone pair concept and the conductivity of bismuth oxides Bi_2O_3. *Solid State Ion.* **21**, 183–193 (1986).

120. Shuk, P., Wiemhöfer, H. D., Guth, U., Göpel, W. and Greenblatt, M. Oxide ion conducting solid electrolytes based on Bi_2O_3. *Solid State Ion.* **89**, 179–196 (1996).

121. Sammes, N. M., Tompsett, G. A., Näfe, H. and Aldinger, F. Bismuth based oxide electrolytes—structure and ionic conductivity. *J. Eur. Ceram. Soc*. **19**, 1801–1826 (1999).

122. Jiang, N. and Wachsman, E. D. Structural Stability and Conductivity of Phase-Stabilized Cubic Bismuth Oxides. *J. Am. Ceram. Soc*. **82**, 3057–3064 (1999).

123. Shannon, R. D. Revised Effective Ionic Radii and Systematic Studies of Interatomic Distances in Halides and Chalcogenides. *Acta Crystallogr*. **32**, 751–767 (1976).

124. Shirao, K., Iida, T., Fukushima, K. and Iwadate, Y. Refractive indexes and electronic polarizabilities of molten $HoCl_3$-NaCl and $HoCl_3$-KCl mixtures. *J. Alloys Compd*. **281**, 163–168 (1998).

125. Jung, D. W. Conductivity and Stability of Bismuth Oxide-Based Electrolytes and their Applications for IT-SOFCs. (University of Florida, 2009).

126. Meehan, J. P. and Datta, R. K. The system Bi_2O_3-R_2O_3 (R=Y,Gd). *Zeitschrift fur anorganische und Allg. Chemie*. **383**, 328–337 (1971).

127. Verkerk, M. J., Keizer, K. and Burggraaf, A. J. High oxygen ion conduction in of the Bi_2O_3-Er_2O_3 system sintered oxides. *J. Appl. Electrochem*. **10**, 81–90 (1980).

128. Verkerk, M. J., Burggraaf, A. J. and Hammink, M. W. J. Oxygen Transfer on Substituted ZrO_2, Bi_2O_3, and CeO_2 Electrolytes with Platinum Electrodes I. Electrode Resistance by D-C Polarization M. *J. Electrochem. Soc*. **130**, 70–78 (1983).

129. Keizer, K., Verkerk, M. J. and Burggraaf, A. J. Preparation and properties of new oxygen ion conductors for use at low temperatures. *Ceramurg. Int*. **5**, 143–147 (1979).

130. Takahashi, T., Iwahara, H. and Arao, T. High oxide ion conduction in sintered oxides of the system Bi_2O_3-Gd_2O_3. *J. Appl. Electrochem*. **5**, 187–195 (1975).

131. Levin, E. M. and Roth, R. S. Polymorphism of bismuth sesquioxide. II. Effect of oxide additions on the polymorphism of Bi_2O_3. *J. Res. Natl. Bur. Stand. Sect. A Phys. Chem*. **68A**, 197 (1964).

132. Watanabe, A. and Kikuchi, T. Cubic-hexagonal transformation of yttria-stabilized δ-bismuth sesquioxide, $Bi_{2-2x}Y_{2x}O_3$ (x=0.215-0.235). *Solid State Ion.* **21**, 287–291 (1986).

133. Takahashi, T., Esaka, T. and Iwahara, H. High oxide ion conduction in the sintered oxides of the system Bi_2O_3-Y_2O_3. *J. Appl. Electrochem*. **5**, 197–202 (1975).

134. Meng, G., Chen, C., Han, X., Yang, P. and Peng, D. Conductivity of Bi_2O_3-based oxide ion conductors with double stabilizers. *Solid State Ion.* **28**, 297 (1988).

135. Jiang, N., Wachsman, E. D. and Jung, S. H. A higher conductivity Bi_2O_3-based electrolyte. *Solid State Ion.* **150**, 347–353 (2002).

136. Jiang, N. and Wachsman, E. D. Structural Stability and Conductivity of Phase-Stabilized Cubic Bismuth Oxides. *J. Am. Ceram. Soc*. **82**, 3057–3064 (1999).

137. Jung, D. W., Duncan, K. L. and Wachsman, E. D. Effect of total dopant concentration and dopant ratio on conductivity of $(DyO_{1.5})_x$-$(WO_3)_y$-$(BiO_{1.5})_{1-x-y}$. *Acta Mater*. **58**, 355–363 (2010).

138. Watanabe, A. Is it possible to stabilize δ-Bi_2O_3 by an oxide additive? *Solid State Ion.* **41**, 889–892 (1990).

139. Joshi, A. V., Kulkarni, S., Nachlas, J., Diamond, J., Weber, N. and Virkar, A. V. Phase stability and oxygen transport characteristics of yttria- and niobia-stabilized bismuth oxide. *J. Mater. Sci*. **25**, 1237–1245 (1990).

140. Fung, K. Z. and Virkar, A. V. Phase Stability, Phase Transformation Kinetics, and Conductivity of Y_2O_3-Bi_2O_3 Solid Electrolytes Containing Aliovalent Dopants. *J. Am. Ceram. Soc*. **74**, 1970–1980 (1991).

141. Fung, K. Z., Chen, J. and Virkar, A. V. Effect of Aliovalent Dopants on the Kinetics of Phase Transformation and Ordering in RE_2O_3-Bi_2O_3 (RE = Yb, Er, Y, or Dy) Solid Solutions. *J. Am. Ceram. Soc*. **76**, 2403–2418 (1993).

142. Fung, K. Z., Baek, H. D. and Virkar, A. V. Thermodynamic and kinetic considerations for Bi_2O_3-based electrolytes. *Solid State Ion.* **52**, 199–211 (1992).

143. Boyapati, S., Wachsman, E. D. and Jiang, N. Effect of oxygen sublattice ordering on interstitial transport mechanism and conductivity activation energies in phase-stabilized cubic bismuth oxides. *Solid State Ion.* **140**, 149–160 (2001).

144. Wachsman, E. D., Boyapati, S. and Jiang, N. Effect of dopant polarizability on oxygen sublattice order in phase-stabilized cubic bismuth oxides. *Ionics (Kiel)*. **7**, 1–6 (2001).

145. Jiang, N., Buchanan, R. M., Stevenson, D. A., Nix, W. D., Li, J. and Yang J. Anion ordering in aged stabilized bismuth oxide. *Mater. Lett*. **22**, 215–219 (1995).

146. Jolley, A. G., Jayathilake, R. and Wachsman, E. D. Optimizing rhombohedral Bi_2O_3 conductivity for low temperature SOFC electrolytes. *Ionics (Kiel)*. **25**, 3531–3536 (2019).

147. Takahashi, T., Iwahara, H. and Nagai, Y. High oxide ion conduction in sintered Bi_2O_3 containing SrO, CaO or La_2O_3. *J. Appl. Electrochem*. **2**, 97–104 (1972).

148. Iwahara, H., Esaka, T., Sato, T. and Takahashi, T. Formation of high oxide ion conductive phases in the sintered oxides of the system Bi_2O_3-Ln_2O_3 (Ln = La-Yb). *J. Solid State Chem*. **39**, 173–180 (1981).

149. Cahen, H. T., Van Den Belt, T. G. M., De Wit, J. H. W. and Broers, G. H. J. The electrical conductivity of δ-Bi_2O_3 stabilized by isovalent rare-earth oxides R_2O_3. *Solid State Ion.* **1**, 411–423 (1980).

150. Drache, M., Obbade, S., Wignacourt, J. P. and Conflant, P. Structural and Conductivity Properties of $Bi_{0.775}Ln_{0.225}O_{1.5}$ Oxide Conductors (Ln = La, Pr, Nd, Sm, Eu, Gd, Tb, Dy) with Rhombohedral Bi-Sr-O Type. *J. Solid State Chem*. **142**, 349–359 (1999).

151. Zhang, X. J., Jin, W. T., Hao, S. J., Zhao, Y. and Zhang, H. Study of the crystal structures of new buffer materials $Bi_{1-x}Y_xO_{1.5}$. *J. Supercond. Nov. Magn*. **23**, 1011–1014 (2010).

152. Jung, D. W., Duncan, K., Camaratta, M. A., Lee, K. T., Nino, J. C., and Wachsman, E. D. Effect of Annealing Temperature and Dopant Concentration on the Conductivity Behavior in $(DyO_{1.5})_x$-$(WO_3)_y$-$(BiO_{1.5})_{1-x-y}$. *J. Am. Ceram. Soc*. **93**, 1384–1391 (2010).

153. Verkerk, M. J. and Burggraaf, A. J. Oxygen Transfer on Substituted ZrO_2, Bi_2O_3, and CeO Electrolytes with Platinum Electrodes. *J. Electrochem. Soc*. **130**, 78–84 (1983).

154. Wu, Y.-C., Chang, Y.-W. and Wang, S.-F. Electrical Properties and Microstructural Analysis of Aliovalent-Ion (Y^{3+}, Nb^{5+})–Doped Bismuth-Based Solid-Oxide Electrolyte. *Ferroelectrics* **455**, 123–128 (2013).

155. Tietz, F. Innovative Materials in Advanced Energy Technologies. in *Proceedings of the 9th CIMTEC – World Ceramic Congress and Forum on New Materials* **61** (1999).

156. Takahashi, T., Esaka, T. and Iwahara, H. Conduction in Bi_2O_3-based oxide ion conductors under low oxygen pressure. I. Current blackening of the Bi_2O_3-Y_2O_3 electrolyte. *J. Appl. Electrochem*. **7**, 299–302 (1977).

157. Yaremchenko, A. A., Kharton, V. V., Naumovich, E. N. and Tonoyan, A. A. Stability of δ-Bi_2O_3-based solid electrolytes. *Mater. Res. Bull*. **35**, 515–520 (2000).

158. Gil, V., Tartaj, J., Moure, C. and Durán, P. Sintering, microstructural development, and electrical properties of gadolinia-doped ceria electrolyte with bismuth oxide as a sintering aid. *J. Eur. Ceram. Soc*. **26**, 3161–3171 (2006).

159. Miao, L., Hou, J., Dong, K. and Liu, W. A strategy for improving the sinterability and electrochemical properties of ceria-based LT-SOFCs using bismuth oxide additive. *Int. J. Hydrogen Energy* **44**, 5447–5453 (2019).

160. Wang, J., Chen, X., Xie, S., Chen, L., Wang, Y., Meng, J. and Zhou, D. Bismuth tungstate/neodymium-doped ceria composite electrolyte for intermediate-temperature solid oxide fuel cell: Sintering aid and composite effect. *J. Power Sources* **428**, 105–114 (2019).

Chapter 2. Methods of characterization

Determining the suitability of doped bismuth oxide materials as SOFC electrolytes is achieved by investigating several structure-property relationships. These relationships are investigated in this work via powder X-ray diffraction, the pair distribution function, Raman spectroscopy and electrochemical impedance spectroscopy. The use of Python programming for data visualization and curve fitting is additionally described along with the synthetic method used to synthesize all the materials reported in this thesis.

2.1. Powder X-ray diffraction (PXRD)

2.1.1. Historical background

The diffraction of X-rays by a crystalline material was first reported by Max Von Laue for which he earned the Nobel Prize in physics in 1914.[1] Around the same time, father and son duo William H. Bragg and William L. Bragg correlated the observed X-ray diffraction to the crystalline structure for which they earned the Nobel Prize in physics in 1915.[2]

2.1.2. The principle of X-ray diffraction

The phenomenon of X-ray diffraction is well documented[3] and as such only a brief summary of the pertinent concepts will be discussed here. X-ray diffraction occurs when a beam of monochromatic electromagnetic radiation is scattered by the electrons of atoms present in a crystalline material. Much like conventional optical diffraction, X-ray diffraction only occurs if the wavelength of the incident radiation is comparable to the separation of the arrangement of atoms. The diffraction results in a characteristic interference pattern and under conditions whereby constructive interference is observed the diffraction is described by Bragg's law,[3] which relates the scattering angle to the incident X-ray wavelength and the interplanar spacing:

$$n\lambda = 2d_{hkl}sin\theta \tag{2.1}$$

where n is the diffraction order, λ is the X-ray wavelength, d_{hkl} is the interplanar spacing between (hkl) planes and θ is the diffraction angle.

The magnitude of diffraction is determined by the nature and arrangement of m atoms found in the diffracting <hkl> planes and this is described by the structure factor F_{hkl}:[4–6]

$$F_{hkl} = \sum_{j=1}^{m} N_j f_j \exp[2\pi i(hx_j + ky_j + lz_j)] \tag{2.2}$$

where N_j is the fraction of every equivalent position occupied by atom *j* (i.e., the site occupancy factor (SOF)), f_j is the scattering factor of atom *j* and x_j, y_j and z_j are the fractional coordinates of atom *j*.

The scattering factor *f* describes the efficiency by which X-rays are scattered by the electrons of an atom and is a product of several terms that describe the interaction of incident X-rays with the electrons surrounding an atom. This can be described by:[7,8]

$$f = f_0 \exp\left[-\frac{B_{eq} sin^2\theta}{\lambda^2}\right] \quad (2.3)$$

where f_o is the atomic scattering factor, B_{eq} is the Debye-Waller temperature factor, λ is the X-ray wavelength and θ is the diffraction angle.

The scattering efficiency of an atom is reduced due to the kinetic nature of the atom and its electrons. Atoms in a crystalline structure are found to be vibrating about their equilibrium lattice positions and this vibration is quantified by the Debye-Waller (DW) temperature factor B_{eq}:[8]

$$B_{eq} = 8\pi^2 U_{iso}^2 \quad (2.4)$$

where U_{iso}^2 is the isotropic mean square amplitude of the atomic vibration.

The DW factor is also known as the temperature factor or thermal displacement parameter. If the vibration is anisotropic, the vibration is described by six anisotropic vibration terms B_{ij} which denote the amplitude of vibration uniquely in all directions in three dimensional space. Throughout this work, isotropic thermal displacement parameters were exclusively used.

2.1.3. Integration basics: from diffraction to usable diffractogram

Several experimental setups with unique geometrical arrangements exist for the collection of PXRD data. The most common setups are Bragg-Brentano (reflection) and Debye-Scherrer (transmission) geometry (Fig. 2.1). In this work, Bragg-Brentano geometry was employed for all lab-based PXRD experiments while Debye-Scherrer geometry was employed for all synchrotron-based experiments.

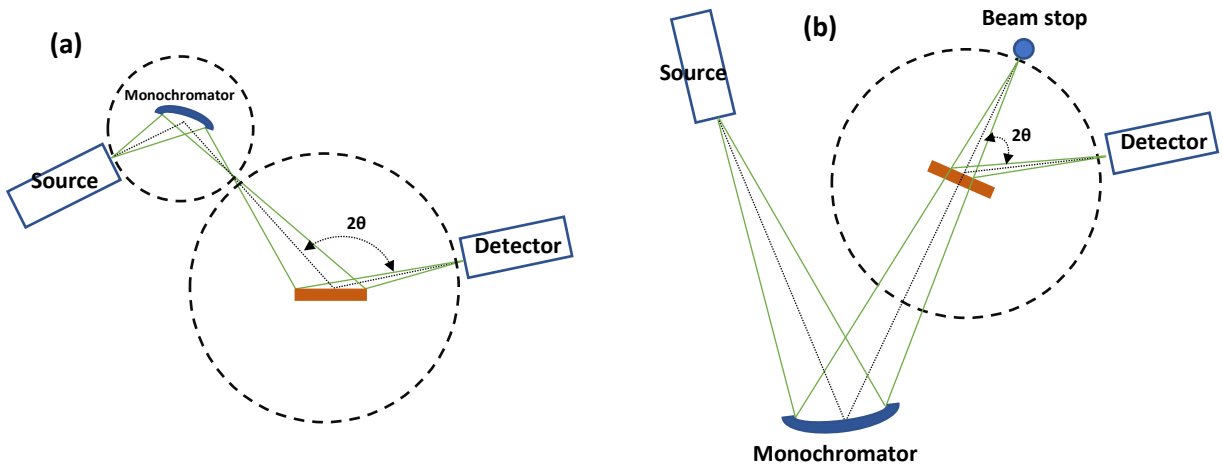

Figure 2.1. Typical (a) Bragg-Brentano and (b) Debye-Scherrer experimental setups used for the collection of PXRD data. Adapted from Refs. [9] and [10].

Irrespective of the experimental geometry employed, when a finely ground crystalline powder is exposed to an incident beam of X-ray radiation, diffraction occurs from lattice planes that satisfy Bragg's law. These <hkl> reflections result in the formation of coaxial cones called Debye-Scherrer cones[3] (Fig. 2.2).

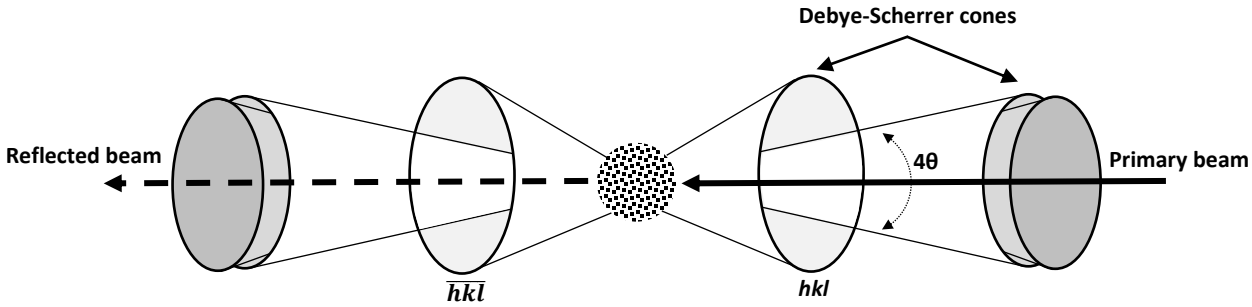

Figure 2.2. Illustration of the scattered beams that originate from a crystalline powder when exposed to a beam of X-ray radiation. Some arbitrary resulting Debye-Scherrer cones are drawn. Adapted from Ref. [3].

These Debye-Scherrer cones are integrated into 1D diffractograms which are used to investigate the crystal structure. The integration process differs based on the type of detector used. Detectors are classified as point, linear or area detectors based on whether they record the diffraction pattern in zero, one or two spatial dimensions, respectively. In this project, for the lab-based experiments a 1D linear detector was used, whereas for the synchrotron-based experiments a 2D area detector was used. In the

case of the 2D detector, the Debye-Scherrer cones appear as rings (i.e. Debye-Scherrer rings) as shown in Figure 2.3.

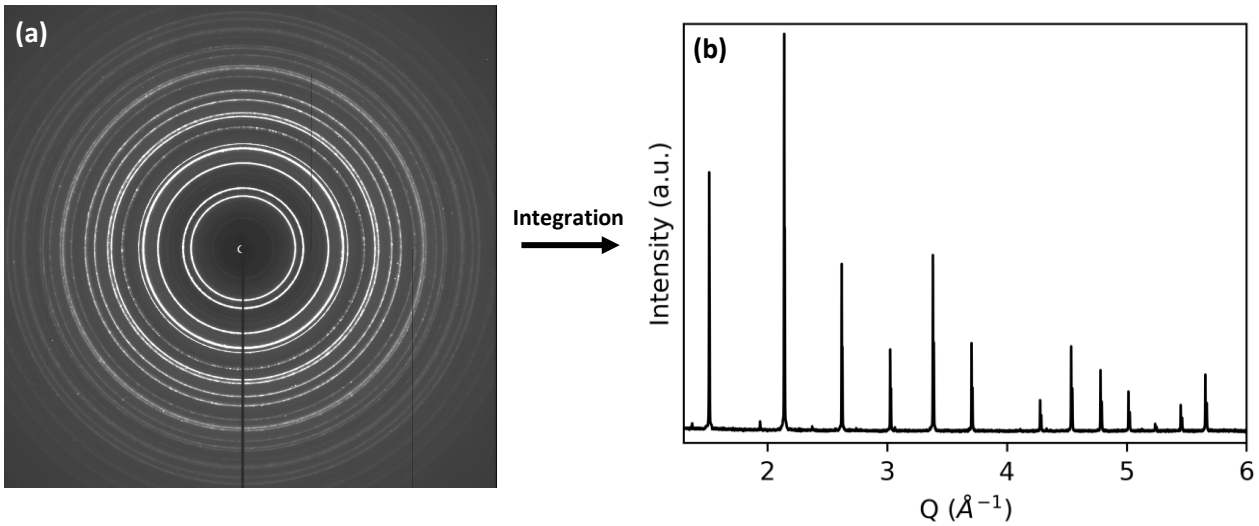

Figure 2.3. (a) Debye-Scherrer rings from a powdered crystalline sample measured on a 2D detector. (b) These rings are integrated to generate 1D diffractograms which are used for subsequent structural analysis.

The intensity around the Debye-Scherrer rings is ideally isotropic. For the more conventional lab-based measurements using a 1D detector, integration occurs over a 1D section of the rings. For a 2D detector, the entire ring or the portion of the ring that is measured is integrated and this results in greatly improved counting statistics. The integration of diffraction data collected using a 2D detector is further discussed in Section 2.2.3.1.

2.1.4. The Rietveld method

The Rietveld method is a technique that was developed in the late 1960s by Dutch crystallographer Hugo Rietveld for the analysis of powder diffractograms.[11,12] As previously mentioned, a measured powder diffractogram arises from the integration of the Debye-Scherrer rings/cones and as such consists of a sequence of peaks (each representing a Debye-Scherrer cone or ring) resting on top of a smooth background.[13] It was recognized that in a step-scanned diffractogram, there is structural information contained in each intensity at each step measured.[6] From this, the Rietveld method was formulated which essentially entails a series of least-squares refinements between a measured diffractogram and that of a calculated diffractogram. The calculated diffractogram is derived from various models that are

simultaneously refined. These include models describing instrumental factors, effects from diffraction optics, the crystal structure(s) and specimen characteristics such as lattice and thermal displacement parameters. The parameters that are simultaneously refinable in a Rietveld refinement are shown in Table 2.1.

Table 2.1. Parameters that are simultaneously refinable in a Rietveld refinement.[6]

Parameters refinable for *each* phase present
x_i; y_i; z_i; B_i; N_i*
Scale factor
Specimen-profile breath parameters
Lattice parameters
Overall temperature factor
Individual anisotropic thermal parameters
Preferred orientation
Crystallite size and microstrain
Extinction
Global refinable parameters
2θ Zero set point error
Instrumental profile
Profile asymmetry
Background
Wavelength
Specimen displacement
Specimen transparency
Absorption

*(x_i, y_i and z_i are the position coordinates, B_i is the isotropic thermal displacement parameter and N_i is the site occupancy multiplier, all for the *i*th atom in the unit cell).

The residual S_y is the variable which is minimized in the least-squared refinement:[6]

$$S_y = \sum_i w_i (y_i - y_{ci})^2 \qquad (2.5)$$

where $w_i = 1/y_i$ and y_i is the observed intensity at the *i*th step and y_{ci} is the calculated intensity at the *i*th step.

The calculated intensities y_{ci} are determined from the structure factor for the *k*th Bragg reflection, F_K, values calculated from the structural model by the summation of the calculated contributions from neighbouring Bragg reflections plus the background contribution:[6]

$$y_{ci} = s \sum_K L_K |F_K|^2 \varphi(2\theta_i - 2\theta_k) P_K A + y_{bi} \quad (2.6)$$

where *s* is the scale factor, *K* are the various Miller indices (hkl) for a Bragg reflection, L_K is the contribution from the Lorentz, polarization and multiplicity factors, φ is the reflection profile function, P_K is the preferred orientation function, *A* is the absorption factor, F_K is the structure factor for the *K*th Bragg reflection and y_{bi} is the background intensity at the *i*th step.

2.1.5. The quality of a Rietveld fit

2.1.5.1. Numerical analysis

The Rietveld method iteratively adjusts the various refinable parameters until the residual (Equation 2.5) is minimized. This entails attaining the 'best fit' between the observed and calculated diffractograms. However, the convergence of the refinement and the 'best fit' require careful monitoring to ensure that the structural model remains physically and chemically reasonable and that a global minimum is reached as opposed to a local or false minimum. Several numerical criteria[6] such as the residual profile factor R_p and the residual weighted profile factor R_{wp}, which are known as the 'R-factors', have been developed to judge the quality of the fit achieved from the refinement. From a mathematical standpoint, the most meaningful criteria is the R_{wp} factor as the numerator is the residual that is minimized (in Equation 2.5):

$$R_P = \frac{\sum |y_i - y_{ic}|}{\sum y_i} \quad (2.7)$$

$$R_{wp} = \sqrt{\frac{\sum w_i (y_i - y_{ic})^2}{\sum w_i (y_i)^2}} \quad (2.8)$$

Other R-factors include the R-structure factor R_F and the R-Bragg factor R_B which are more commonly reported for single crystal structure refinements:[6]

$$R_F = \frac{\sum \left| \sqrt{(I_K(obs))} - (I_K \sqrt{calc}) \right|}{\sum \sqrt{(I_K(obs))}} \quad (2.9)$$

$$R_B = \frac{\sum|I_K(obs) - I_K(calc)|}{\sum I_K(obs)} \quad (2.10)$$

where I_K is the intensity assigned to the *Kth* Bragg reflection at the end of the refinement cycles. Residual factors R_F and R_B are, however, non-ideal as they are based on intensities derived from the structural model and not from the actual observed Bragg intensities. This results in these residual factors being biased towards the structural model used in the refinement. Another numerically useful fit criteria is the 'goodness-of-fit' *GOF*:[6]

$$GOF = \frac{R_{wp}}{R_e} \quad (2.11)$$

where R_e is the R-expected residual factor and is the best possible R-value for the measured diffractogram:[6]

$$R_e = \sqrt{\left[\frac{(N-P)}{\sum w_i(y_i(obs))^2}\right]} \quad (2.12)$$

where *N* is the number of observations (i.e. number of data points collected) and *P* is the number of refined parameters. However, the value of R_e is significantly influenced by the quality of the data/counting statistics. Data which has been collected for a very long time will have a high number of observations and hence a very small R_e. As such, caution is required when assessing the GOF factor for adequacy of the structural model. A statistic that is also commonly reported is the weighted Durbin-Watson statistic *d* which reveals serial correlation between successive y_i values and should ideally be equal to two. This statistic is a useful indicator of the quality of fit achieved between the observed and calculated Bragg profiles:[6]

$$d = \sum_{i=2}^{N} \frac{(\Delta y_i - \Delta y_{i-1})^2}{\sum_{i=1}^{N} \Delta Y_i^2} \quad (2.13)$$

where: $\Delta Y_i = y_i(obs) - y_i(calc)$ (2.14)

2.1.5.2. Visual analysis

The various numerical criteria that exist to judge the quality of a Rietveld refinement are controversial as it is impossible to give universally acceptable ranges for these criteria. In particular, the range reported for the GOF such that the refinement has converged successfully is $0.9 \leq GOF \leq 1.3$.[6] The numerical meaningfulness of these criteria and the concept of 'How good is good enough?' has been elegantly summarized by Toby.[14] Although the numerical criteria are useful in judging the quality of a Rietveld fit, the most important criteria to judge the quality of a Rietveld fit is to graphically observe the quality of the refined fit whilst maintaining the chemical reasonableness of the refined structural model. To illustrate the shortcomings of the numerical criteria, the converged refinements of a diffractogram collected of NIST 660c (LaB_6)[15] on two different diffractometers, both under ambient conditions, are shown in Figure 2.4.

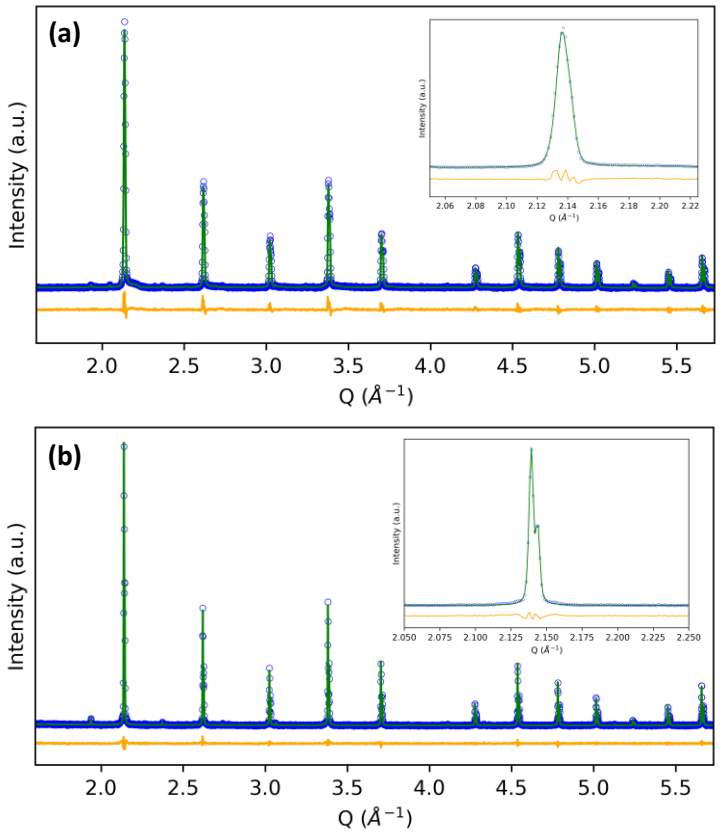

Figure 2.4. Diffractograms of the NIST 660c sample collected under ambient conditions having been analysed by means of Rietveld refinement. Data were collected on a (a) Bruker D8 Advance with Cu radiation and (b) a Bruker D2 Phaser with Co radiation. The observed pattern is shown in blue, the calculated in green and the difference in orange.

Visual analysis of the converged refined fit between the observed and calculated diffractograms collected on both instruments shows that the refinements have clearly converged successfully (i.e. excellent agreement between the observed and calculated data) whilst maintaining the chemical and physical reasonableness of the structural model. However, the derived GOF for each refinement (Table 2.2) might suggest otherwise as the GOF achieved for both refinements exceeds the upper limit proposed for this criteria.[6] Nevertheless, this numerical indicator does not show that the refinement has converged unsuccessfully. Counting statistics, although sufficient in both cases, vary between the two samples in addition to varying complex instrumental contributions to both the observed peak profile and the overall background. These contributions greatly affect the derived R-factors and the GOF values. This example emphasizes the importance of *visual analysis* in assessing the quality of a Rietveld refinement fit.

Table 2.2. Numerical parameters obtained from Rietveld refinement of data collected on NIST 660c using two different diffractometers.

Instrument	Bruker D2 Phaser	Bruker D8 Advance
R-factors	R_{wp} = 4.85	R_{wp} = 7.48
	R_p = 3.70	R_p = 5.81
	R_{ex} = 3.48	R_{ex} = 4.5
GOF	1.39	1.66

2.1.6. General Rietveld refinement considerations

2.1.6.1. Data collection and sample preparation

There exist several factors that greatly impact the quality and accuracy of a Rietveld refinement. These factors were considered and optimized when refining the diffractograms investigated in this thesis. The data collected must firstly be of a high quality. This typically involves collecting data with a high signal-to-noise ratio (i.e. low background contribution, high peak intensity and high resolution of diffraction peaks). This ensures that the structural information available to the refinement process is maximized. The instrumental contribution to the observed diffractogram, the instrument resolution function (IRF) must also be accurately determined to enable this to be accounted for in the refinement process. This function is determined, for each of the instruments used to collect diffractograms, using a suitable standard reference material (SRM) as supplied by the National Institute of Standards and Technology (NIST). Specific details of these calibrations are described in each chapter. Lastly, the quality of the sample must also be considered as this has a profound effect on the observed diffractogram. Ideally the measured

powder sample must comprise a narrow particle size distribution of randomly oriented crystallites. To achieve this, careful grinding of samples prior to measurements is required. This sample preparation strategy ensures that the observed intensities contain minimal contributions from the preferred orientation of crystallites and essentially maximizes the evenness of intensity distribution over the Debye-Scherrer cones. If this sample preparation strategy were ignored or not optimized, the diffractograms collected, in particular those collected on the 1D detectors employed in the lab-based diffractometers, would exhibit observed intensities that do not truly represent the crystal structure. This is further illustrated in Figure 2.5 using image processing software ImageJ.[16] A line profile (which represents the integration achieved using a 1D detector) is taken through two different regions of the Debye-Scherrer rings of a cubic bismuthate material (Fig. 2.5a). The integration across these two different lines results in diffractograms that have varying relative peak intensities (Figs. 2.5b and 2.5c) which stem from the inhomogeneity in intensity of the Debye-Scherrer rings. These varying intensities are not representative of the average crystal structure and will negatively affect the outcome of the Rietveld refinement. The inhomogeneity in ring intensity is further illustrated in the surface plot shown alongside (Fig. 2.5d).

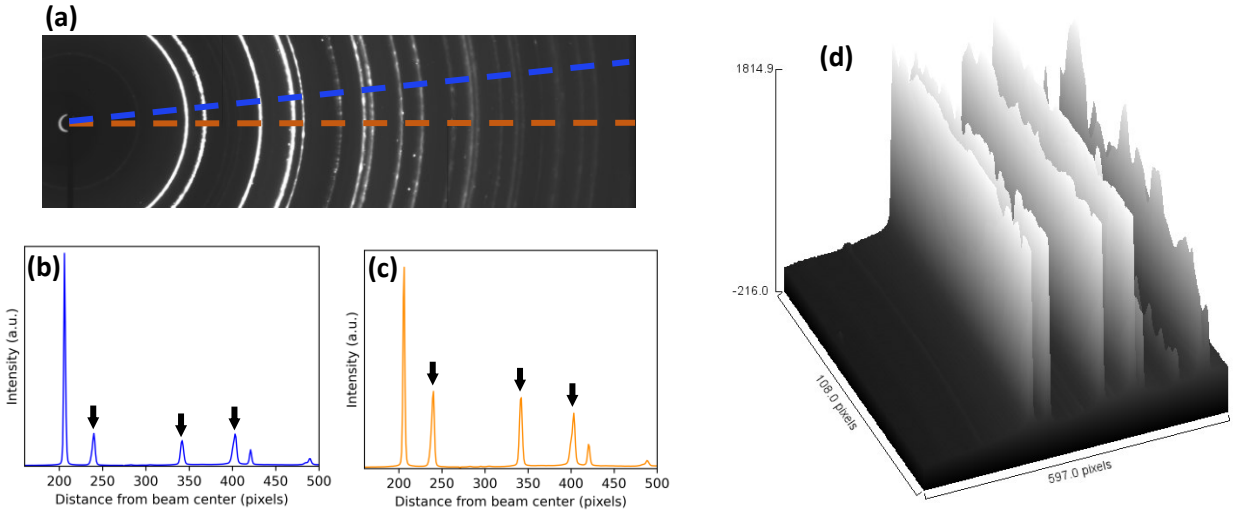

Figure 2.5. (a) Selected region of the Debye-Scherrer rings of a cubic bismuthate material with line profiles indicated that result in the diffractograms shown in (b) and (c). (d) Surface plot of a selected region of the Debye-Scherrer rings further illustrating the inhomogeneity in ring intensity.

2.1.6.2. During a Rietveld refinement

The initial values of the parameters that are refined (as was indicated in Table 2.1) must be reasonably close to the true values. Achieving this is oftentimes challenging, especially when novel structures and stoichiometries are investigated. The distinction must be made between a structure *refinement* process and a structure *solution* process. Rietveld refinement is not a structure solution process.[6] These initial values are mostly taken from the results of previous refinements of similar materials published in literature or from the results of structure solution investigations. It is common to observe that a refinement converges to a local minimum when the initial refinable parameter values (in particular structural parameters such as lattice parameter values) are simply too far off from the true values. Also, during successive refinement iterations the numerical refinement criteria must be closely monitored to ensure that the refinement has converged to a global minimum instead of a false minimum. Additionally, constant visual analysis of the refinement fit as the refinement progresses is essential to similarly ensure successful convergence.

2.1.7. Software programs for powder diffraction data analysis

The proper analysis of powder diffraction data necessitates the extensive use of various computer software.[17] A brief overview of the various software used to analyse the diffractograms reported in this thesis is reported here.

2.1.7.1. Phase identification and search-match software

The identification of the crystalline phases present in a diffractogram requires (a) a database that contains reference diffractograms and (b) a program that compares the measured and reference diffractograms and determines the quality of the match between the two diffractograms. In this thesis, phase identification was exclusively done using Bruker AXS DIFFRAC.EVA V4.2 linked to the crystallography open database (COD).[18]

2.1.7.2. Rietveld refinement software

Several different software options are available for Rietveld refinement of powder diffractograms.[17] The more popular options include GSAS and GSAS-II,[19,20] FULLPROF[21] and Topas.[22] The Rietveld refinement of all diffractograms reported in this thesis has been done using Bruker AXS TOPAS-Academic (TA) Version 6.[22,23] TA, although available only at a significant cost, offers significant advantages over the various other available software packages.[22] Most notably, TA offers rapid refinement procedure computations and it can be operated in a highly customizable and robust operational mode called *launch mode*. Refinements done via launch mode involve the production of input files in an external text editor such as jEdit,[24] which

was the editor used exclusively in this thesis. Input files essentially control and 'tell' TA what to do during the refinement process. The use of jEdit additionally enables the use of pre-defined macros which are openly contributed by experts in the Rietveld community. Overall, these features of TA ensure efficient, reproducible and scientifically legitimate Rietveld refinement analyses.

2.1.7.3. Crystal structure visualization software

The visualization of the crystal structure, both during refinement and after a refinement converges, is essential to track the progress of the refinement and to ensure the reasonableness of the final refined structure. TA has a built-in structural visualization module that displays a real time image of the structure as the refinement progresses. Additional structural visualization was done using VESTA[25] and the photo realistic rendering of the crystal structure images found in this thesis were done using CrystalMaker.[26]

2.1.8. PXRD instruments

The diffractograms presented in this thesis were collected on two lab-based diffractometers and at two synchrotron beamlines. The specific details of the PXRD measurements made are included in each chapter. A brief overview of each instrument is presented here.

2.1.8.1. Bruker D2 Phaser

Lab-based diffractograms at ambient conditions were collected using a Bruker D2 Phaser desktop diffractometer.[27] This diffractometer operates in Bragg-Brentano (reflection) geometry and was equipped with a sealed tube Co X-ray source, a Bruker Lynxeye position sensitive detector (PSD) and a secondary beam Fe filter to minimize K_β radiation. Selected instrument parameters are summarized in Table 2.3.

Table 2.3. Selected specifications of the Bruker D2 Phaser desktop diffractometer.

Parameter	Value
Goniometer radii (primary and secondary)	70.7 mm
Detector 2θ angular range	5°
Soller slit width (primary and secondary)	2.5°
X-ray tube power setting	30 kV; 10 mA
Calibrated wavelength profile	λ_1 = 1.78870 Å, λ_2 = 1.79253 Å and K_β = 1.62063 Å

2.1.8.2. Bruker D8 Advance

In situ lab-based diffractograms (measured at a range of temperatures) were collected using a Bruker D8 Advance diffractometer.[28] This diffractometer operates in Bragg-Brentano (reflection) geometry and was

equipped with a sealed tube Cu X-ray source coupled with a Göbel mirror to provide pseudo-parallel radiation, a Bruker VANTEC-1 PSD and a secondary beam Ni filter to minimize K_β radiation. *In situ* heating was achieved by using an Anton Paar XRK 900 reaction chamber[29] and samples were packed into Macor[30] ceramic sample holders for these measurements. Selected instrument parameters are summarized in Table 2.4.

Table 2.4. Selected specifications of the Bruker D8 Advance diffractometer

Parameter	Value
Goniometer radii (primary and secondary)	250 mm
Detector 2θ angular range	12°
Soller slit width (primary and secondary)	2.5°
X-ray tube power setting	40 kV; 40 mA
Calibrated wavelength profile	λ_1 = 1.54041 Å, λ_2 = 1.54418 Å and K_β = 1.47681 Å

2.1.8.3. Beamline ID22 at the ESRF

High resolution diffractograms were collected at beamline ID22 (λ = 0.3544 Å) at the European Synchrotron Radiation Facility (ESRF).[31,32] Samples were loaded into quartz capillaries and the *in situ* heating achieved using a hot-air blower. Additionally, samples were spun during measurements and samples were changed using an automated robotic sample changer.

2.1.8.4. Pair distribution function (PDF) Beamline at the NSLS-II

In situ powder diffractograms were collected at the Pair-Distribution Function (PDF) beamline (λ = 0.1671 Å) at the National Synchrotron Light Source II (NSLS-II).[33,34] Samples were loaded into quartz capillaries and *in situ* heating achieved using a hot air blower. The motorized 2D detector enables the sample-to-detector position to be changed during the experiment such as to collect 2D powder patterns that are optimized for both real and reciprocal space analysis in a rapid sequential manner. To collect high resolution powder diffractograms optimized for reciprocal space analysis, the sample-to-detector position was set to ~750 mm enabling data to be collected in the angular range of ~$0.5 < 2\theta < 15^o$, covering a region of the wave vector Q (= $4\pi/\lambda \sin\theta$) up to Q_{max} ~ 10 $Å^{-1}$. The collection of data optimized for real space analysis is discussed in Sections 2.2.5 and 2.2.8.

2.2. The atomic pair distribution function technique

The use of Bragg diffraction to analyse crystal structures provides a wealth of structural information. However, the main limitation of Bragg diffraction is that it only describes the average, long-range order

of the structure. Therefore the use of Bragg data to describe 'crystallographically challenged' materials such as disordered materials is unfeasible.[35] The pair distribution function (PDF) technique involves the simultaneous analysis of both the Bragg and diffuse scattering and is therefore often described as a 'total scattering' technique.[35–37] This enables both the local and average structure of a material to be investigated regardless of the degree of structural disorder present.[35] The PDF technique has been comprehensively described by Egami and Billinge[36] and by Billinge.[37] As such, only a brief overview of the concepts pertinent to this work are presented here.

2.2.1. Background and theory

2.2.1.1. The concept of Q-space

As detailed in Section 2.1.2, Bragg's Law describes the measurement of the scattering intensity as a function of the scattering angle, expressed as 2θ, and the wavelength of the incident radiation, λ. The diffracted intensity of an X-ray beam can also be described as a function of momentum transfer of the scattering particle Q:[37–39]

$$Q = k_{initial} - k_{final} \tag{2.15}$$

where $k_{initial}$ is the incident wavevector and k_{final} is the scattered wavevector.

Since Q describes the difference between the two wavevectors, Q is often called the *diffraction vector*, *scattering vector* or simply the *wave vector*. Q is directly related to the scattering angle according to:

$$Q = |Q| = 2ksin\theta = \frac{4\pi}{\lambda} sin\theta \tag{2.16}$$

This relationship is geometrically illustrated in Figure 2.6.

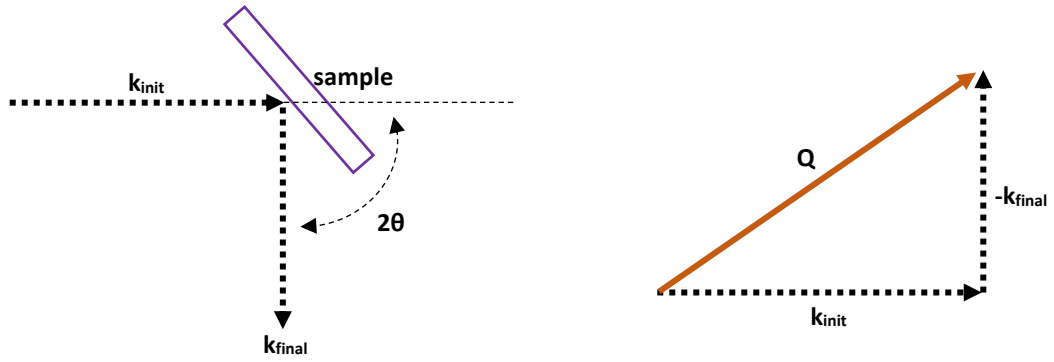

Figure 2.6. Definition of the scattering vector Q based on a simplified geometry of the powder diffraction measurement. Adapted from Ref. [39].

In describing total scattering measurements, the diffraction vector is used to describe the extent to which the diffraction measurements cover reciprocal space and hence the term 'Q-space' is oftentimes used.[37] Consider a typical diffraction measurement covering a range of $2\theta_{min} \leq 2\theta \leq 2\theta_{max}$ where $2\theta_{min}$ and $2\theta_{max}$ are the lowest and highest diffraction angles measured, respectively. In Q-space we define two terms Q_{min} and Q_{max}. Q_{min}, like $2\theta_{min}$, represents the lowest accessible diffraction angle and Q_{max}, like $2\theta_{max}$, represents the highest accessible angle.

2.2.1.2. The concept of total scattering

If a crystal is perfectly periodic, the entire spectrum of scattered X-rays will obey Bragg's Law and these scattered X-rays are collectively known as Bragg scattering. More realistically, crystals are not perfectly periodic and therefore give rise to both Bragg scattering as well as diffuse scattering. Diffuse scattering is a direct result of structural characteristics that deviate from the average structural description and therefore contribute towards the aperiodicity of the crystal structure. These characteristics commonly include vacancies, stacking faults and disorder. 'Total scattering' is a term that is frequently used to collectively describe both the Bragg and diffuse scattering by a crystal. Several correlation functions are commonly used to describe total scattering,[40] however, in this work the reduced pair distribution function *G(r)* is exclusively used. The pair distribution function (PDF) technique involves the simultaneous analysis of both the Bragg and diffuse scattering and is therefore described as a total scattering technique.

2.2.2. What is the PDF?

The PDF is simply defined as a probability distribution function in real-space. This function describes the probability of finding pairs of atoms in the material separated by a certain distance.[36,41–44] In this way, the PDF can be seen as a weighted histogram of the interatomic separations which describes the distribution of atoms in a material[45] according to the equation:[35,37]

$$G(r) = 4\pi r[\rho(r) - \rho_0] \tag{2.17}$$

where $\rho(r)$ is the atomic pair density, ρ_0 is the average atomic number density and r is the radial distance.

The PDF is analogous to the more physically intuitive radial distribution function (RDF) which describes the number of atoms present within a spherical shell of thickness dr at a distance r away from a central atom/origin:[37,46]

$$R(r) = 4\pi r^2 \rho(r) \tag{2.18}$$

where $\rho(r)$ is the atom-pair density of the material at a distance r.

The RDF peaks at radial distances that coincide with maximum atom-pair densities are illustrated in Figure 2.7.

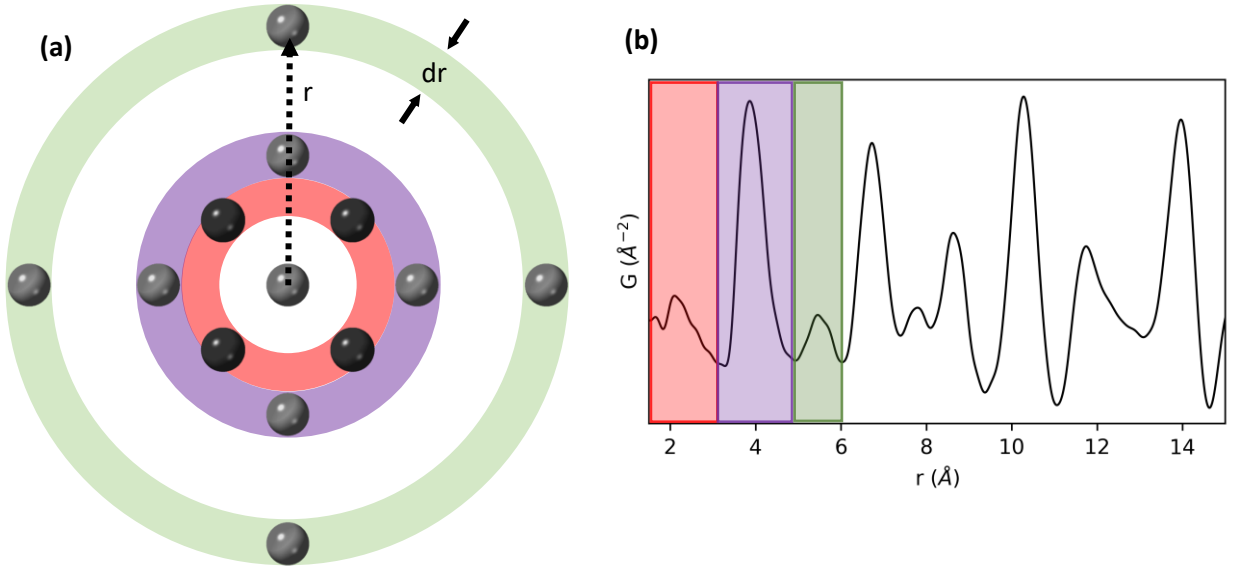

Figure 2.7. (a) RDF construction of a face centred cubic (FCC) structure showing the spherical shell construction and (b) the first three function peaks that correspond to these regions of maximum atom-pair densities. Adapted from Ref. [47].

2.2.3. Data reduction: from 2D diffraction pattern to PDF

The PDF is known to be an experimentally measurable function.[37] There exists a Fourier relationship between the reciprocal space diffraction data measurable in a diffraction experiment and the arrangement of the pairs of atoms in a material.[35] As such, the PDF can be directly accessed by Fourier transformation of the collected diffraction data. In this work, diffraction data suitable for PDF generation was collected using the rapid acquisition PDF (RA-PDF) mode.[48] The stepwise data reduction process going from 2D diffraction image to PDF is illustrated in Figure 2.8.

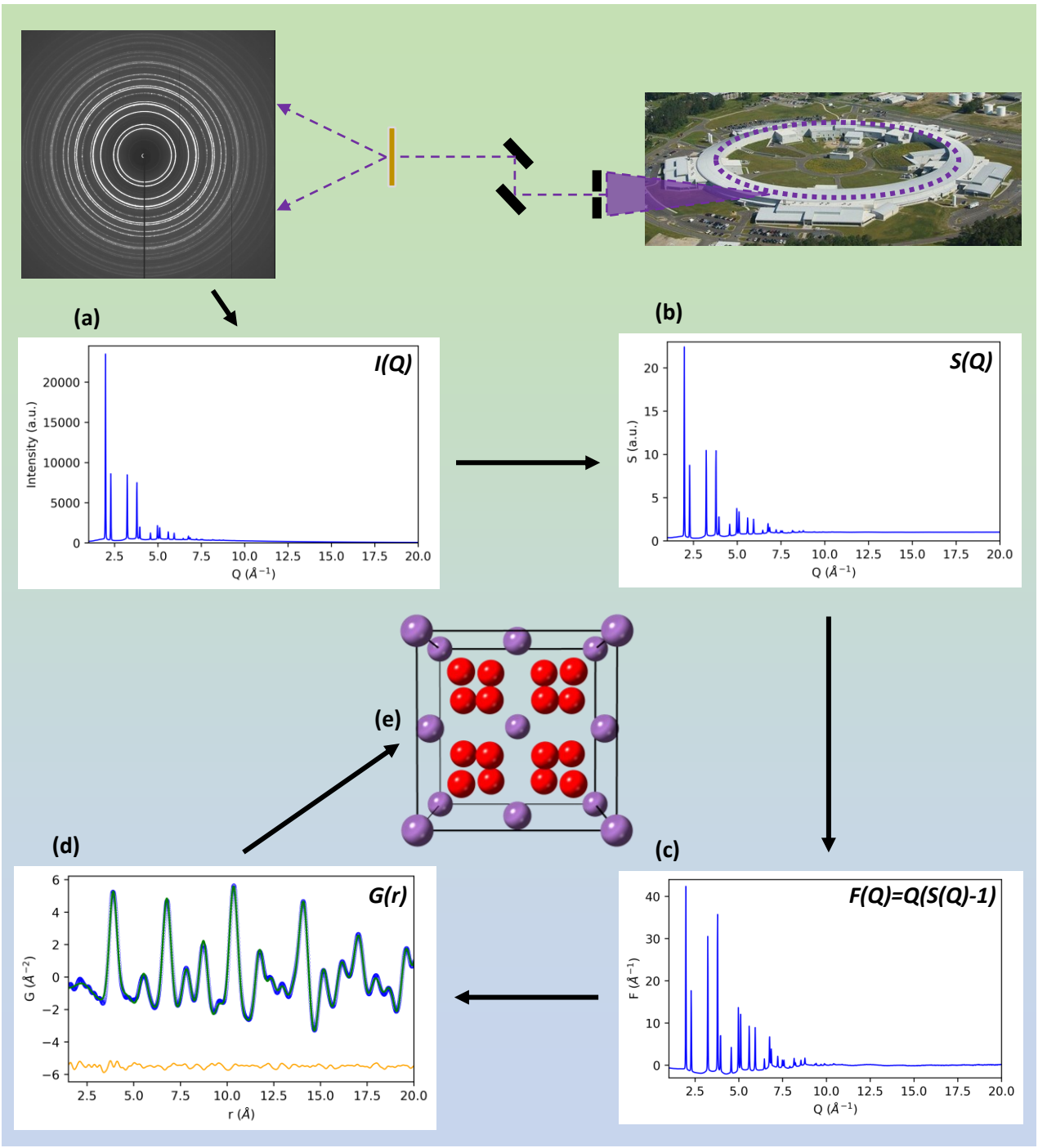

Figure 2.8. Schematic illustrating the workflow of the PDF data reduction process. Synchrotron measurements at NSLS-II (top) utilized the RA-PDF mode to capture 2D diffraction images. (a) Integration of these images and subsequent data reduction produces (b) the normalized scattering intensity *S(Q)* and (c) the reduced structure function *F(Q).* Fourier transformation of F(Q) generates (d) the reduced atomic PDF which is then (e) modelled to gain structural information. Adapted from Ref. [37].

2.2.3.1. 2D integration

The 2D diffraction images collected were integrated using Fit2D[49] to generate 1D diffractograms. In addition to being able to integrate 2D images, Fit2D also enables the calibration of certain instrumental parameters by using a standard. In this work, the sample-to-detector distance, detector tilt and the position of the beam centre were calibrated using standard reference material NIST 660C (LaB_6).[15] Prior to integration, various regions of the 2D image require masking. The area blocked by the beam stop as well as areas containing dead pixels do not contain any useful scattering information and are therefore omitted from the integration process by masking (Fig. 2.9). The integrated 1D data represented in Q-space as *I(Q)* is exported in .chi format for subsequent processing.

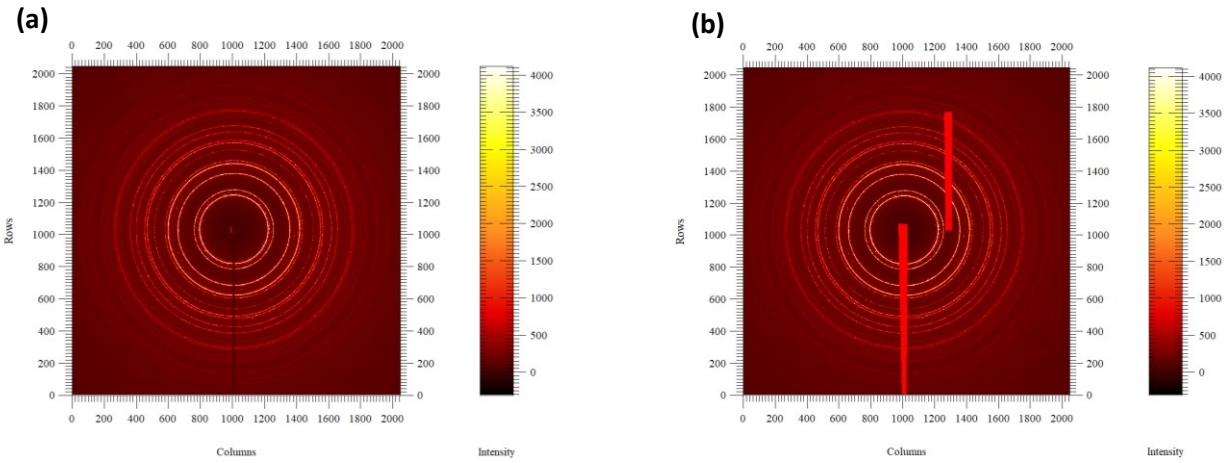

Figure 2.9. (a) 2D diffraction image of a doped bismuthate and (b) the 2D image with the mask applied (red areas) which omits the beam stop and regions containing dead pixels from the integration process.

2.2.3.2. Normalizing the 1D diffractograms

After azimuthal integration in Fit2D, the integrated *I(Q)* files are thereafter normalized using PDFgetX3.[50] The intensities measured in a total scattering experiment $I_m(Q)$ are described as:[50]

$$I_m(Q) = a(Q)I_c(Q) + b(Q) \qquad (2.19)$$

where $I_c(Q)$ is the intensity from the coherent scattering which contains all the structural information of the sample and *a(Q),* and *b(Q*) are corrections to the measured intensity that do not contain structural information.

a(Q) can represent scattering contributions in the form of sample self-absorption, sample multiple scattering and the polarization of the X-ray beam, whilst *b(Q)* can represent contributions from incoherent Compton scattering, background scattering and air scattering. Scattering that is not related to the sample is simply removed by subtracting a reference measurement which is typically an empty sample holder. This background subtraction is the first data normalization step which is followed by applying several corrections. In older PDF normalization programs, such as PDFgetX2,[51] various known corrections are thereafter applied to $I_m(Q)$ in order to determine $I_c(Q)$. These required corrections are discussed in detail elsewhere.[52] $I_c(Q)$ is subsequently transformed into the normalized scattering intensity *S(Q)* by:[50]

$$S(Q) = \frac{I_c(Q) - \langle f(Q)^2 \rangle + \langle f(Q) \rangle^2}{\langle f(Q) \rangle^2} \tag{2.20}$$

where *f(Q)* is the atomic scattering or atomic form factor, and the angle brackets indicate an average over all the atom types in the sample. A significant limitation to the real-space resolution of X-ray PDF data is *f(Q)* which falls off sharply with increasing Q and results in very limited scattering in this region in the *I(Q)* data (Fig. 2.10a). To overcome this and to enhance the diffuse scattering present over this high Q range, *F(Q)*is computed (Fig. 2.10b).

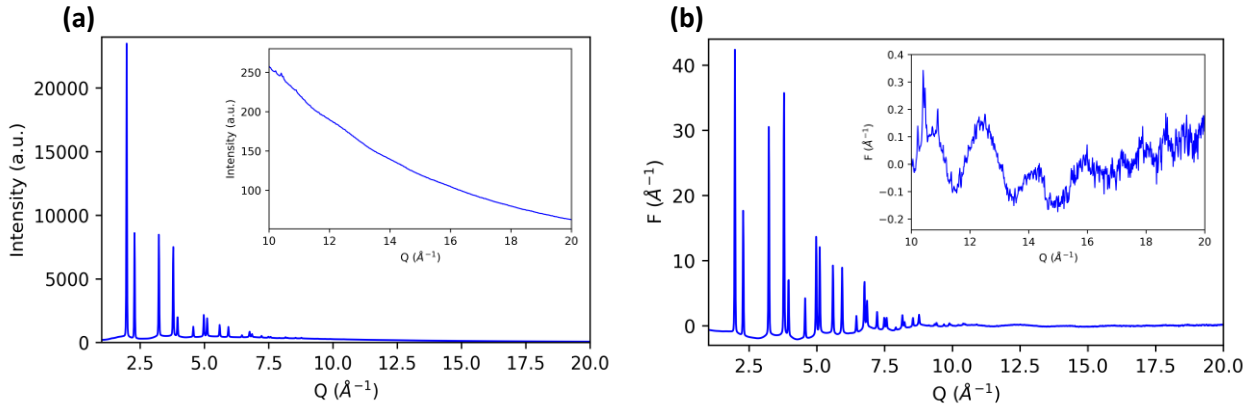

Figure 2.10. (a) *I(Q)* data of a doped bismuthate illustrating the effect of the atomic scattering factor in reducing the scattering observed at high Q. (b) *F(Q)* data illustrating significant diffuse scattering present in the high Q region.

The *S(Q)* is Fourier transformed into the PDF *G(r)* by:[50]

$$G(r) = \frac{2}{\pi}\int_{Q_{min}}^{Q_{max}} Q[S(Q) - 1]\, sin(Qr) dQ = \frac{2}{\pi}\int_{Q_{min}}^{Q_{max}} F(Q)\, sin(Qr) dQ \tag{2.21}$$

where *Q* is the magnitude of the scattering vector and *Q[S(Q)-1]* is the reduced structure function *F(Q)*.[46]

The numerous corrections required to generate PDFs are computationally intensive and require significant user input. To overcome these limitations and to enable rapid and accurate PDF generation, PDFgetX3[50] implements an *ad hoc* data reduction algorithm to determine *a(Q)* and *b(Q).* Via this data reduction algorithm, *a(Q)* and *b(Q)* are parametrized and then varied using a regression method to yield an accurate *F(Q)* function. A detailed mathematical description of this *ad hoc* reduction algorithm is described elsewhere.[50]

The generation of PDF data using the *ad hoc* data corrections implemented in PDFgetX3 requires significantly less user input and is computationally optimized. As such, PDFgetX3 allows for the batch processing of PDF data without sacrificing the accuracy of the generated PDF data in comparison to that achieved by the conventional approach of explicitly calculating the various corrections.

2.2.4. Termination errors and optimizing the PDF

The Fourier transformation described by Equation 2.21 ideally requires data within the Q-space range of Q_{min} = 0 Å^{-1} to Q_{max} = ∞ Å^{-1}. However, it is experimentally impossible for this range to be accessed and practically data is collected over a finite Q-space range from Q_{min} to Q_{max}. The Fourier transformation of *F(Q)* over this limited range of Q-space results in an oscillatory contribution to the generated PDF known as *termination ripples* or *termination errors*.[46] These ripples are generally more pronounced in the low *r* region of the PDF and are amplified for lower Q_{max} values (Fig. 2.11a).

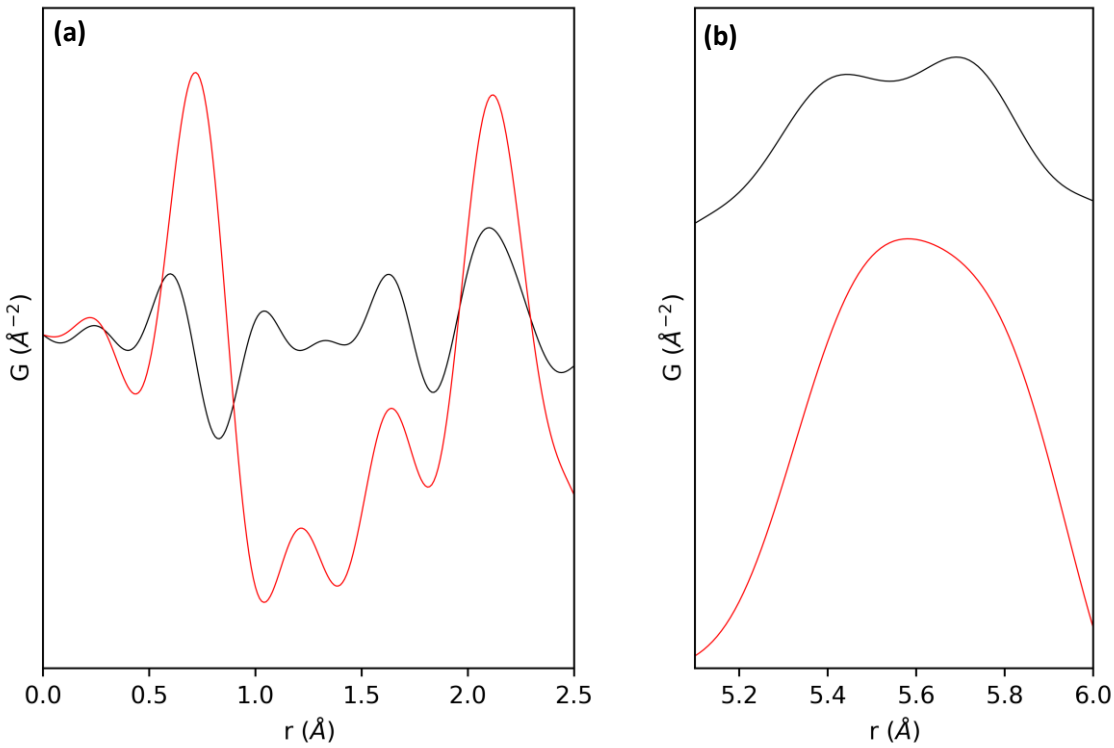

Figure 2.11. Comparison of the PDF patterns of a doped bismuthate. PDF data were generated using Q_{max} = 16 Å^{-1} (red curves) and Q_{max} = 24 Å^{-1} (red curves).

The real-space resolution of a PDF is directly related to the range of Q measured during the diffraction experiment.[46] For this, an approximation of the real-space resolution δr of a PDF has been defined as:[35]

$$\delta r \cong \frac{\pi}{Q_{max}} \tag{2.22}$$

As described in Equation 2.16, the value of Q is dependent on the wavelength of the incident X-ray radiation according to $Q = (4\pi/\lambda) \sin\theta$. From this it is clear that to maximize the resolution of a PDF, high energy (small λ) X-ray radiation is required. In this work, diffraction data suitable for PDF analysis were obtained up to a Q_{max} of ~ 26 Å^{-1}. However it was found to not be ideal to use data up to this maximum value and data were truncated at a Q_{max} = 24.0 Å^{-1}. This truncated range of Q-space was found to be the optimal range of Q to avoid termination effects and to minimize statistical noise which increases with Q. The effect of a high Q_{max} on the real-space resolution of the PDF is illustrated in Figure 2.11b. The PDF generated with a Q_{max} = 16 Å^{-1}, which is approximately the maximum range attainable on a lab diffractometer using Mo K_α radiation, is insufficient to resolve two closely overlapping PDF features present in a doped bismuthate material at elevated temperatures. This illustration emphasizes both the

requirement of a high Q_{max} for high resolution PDF data and the importance of synchrotron facilities which enable high Q_{max} to be achieved. Additionally, it is evident that obtaining high quality PDFs requires the careful balancing of the real space resolution and the increased statistical noise at higher angles.

2.2.5. Total scattering data collection: the rapid acquisition PDF (RA-PDF) technique

The experimental setup used to collect total scattering data in this work made use of the RA-PDF approach.[35,48] The RA-PDF setup uses a 2D area detector that is positioned close to the sample, to measure diffraction data. This sample-to-detector proximity enables the detector to collect data at high angles and hence enables a high Q_{max} to be obtained. These measurements were done using a Debye-Scherrer (transmission) geometry setup wherein the sample was fixed in position and placed in the beam path. The detector was generally positioned concentric with the beam as this enables the maximum extent of the Debye-Scherrer cones to be collected which maximizes counting statistics. However, positioning the detector off centre with respect to the beam centre was also done which further increases the range of Q-space that is measured. A beamstop was used to block the direct beam and as such, a portion of the scattering is blocked at low angles which defines Q_{min}. Geometrically, the range of Q-space that is measurable is defined as:

$$\tan(2\theta) = \frac{r}{d_{sd}} \tag{2.23}$$

where r is the distance between the beam centre and the edge of the detector and d_{sd} is the sample-to-detector distance. This geometrical construct is illustrated in Figure 2.12. In a RA-PDF measurement, measurement of high Q_{max} data as required for PDF measurements comes at the expense of 2θ resolution $\Delta\theta$. To measure high Q_{max} data using a 2D detector, it is necessary to condense the diffraction pattern onto the 2D detector surface which is done by minimizing d_{sd} of equation 2.23. The effect of this is a moderate Q-space resolution of ~0.05 $Å^{-1}$ which is lower than the typical ~0.02 $Å^{-1}$ Q-space resolution of a conventional PDF measurement.[48] However, the main effect of this decreased resolution is the loss of information in the high r range of the PDF. This region of the PDF is not of particular interest for the materials studied in this work and therefore represents an acceptable compromise.

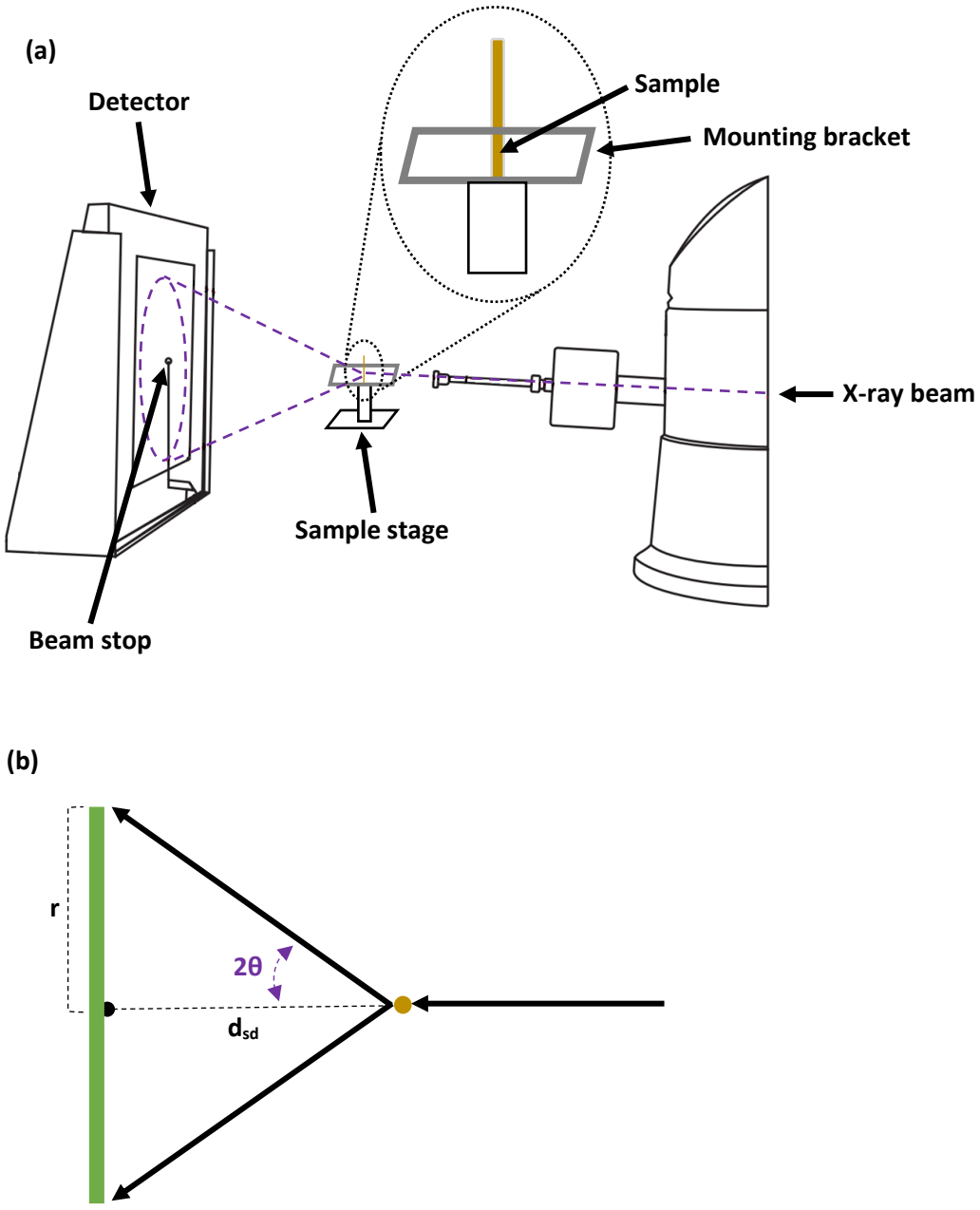

Figure 2.12. (a) Illustration of the experimental setup used for RA-PDF measurements at the PDF beamline at the National Synchrotron Light Source II (NSLS-II). (b) Illustration of the scattering geometry which is mathematically described in Equation 2.23. Adapted from Ref. [47].

2.2.6. Extracting structural information from the PDF

2.2.6.1. Model—independent analysis of the PDF

The nature of the atomic PDF as an atom-pair correlation function enables structural information to be directly extracted from the PDF without any structural modelling. There are three independent pieces of structural information contained in a PDF peak,[37,53] these features are illustrated in Figure 2.13. Firstly, the peak area/peak integrated intensity results in the coordination number of the corresponding atom-atom correlation. This is essentially equivalent to the number of atoms present in that coordination shell at a specific distance around an origin atom. Secondly, the peak position indicates a pair of atoms present with that particular separation. In this way, the peak position results in the average bond length between a pair of atoms. Lastly, the peak width is related to the thermal or static disorder. Atomic disorder will generally result in the displacement of atoms from their ideal lattice sites and give rise to a distribution of atom-atom distances. The result of this is that the PDF peaks are broadened and form Gaussian-shaped peaks. Determining these three pieces of structural information is achieved via the *direct analysis* approach which involves the fitting of *G(r)* peaks with Gaussian functions after linear subtraction of the baseline. The Gaussian fitting presented in this work was done using an in-house developed Python script. This script was benchmarked by comparing the Gaussian fit parameters determined for several *G(r)* peaks against those determined using Fityk[54] and Bruker AXS TOPAS-Academic Version 6.[22]

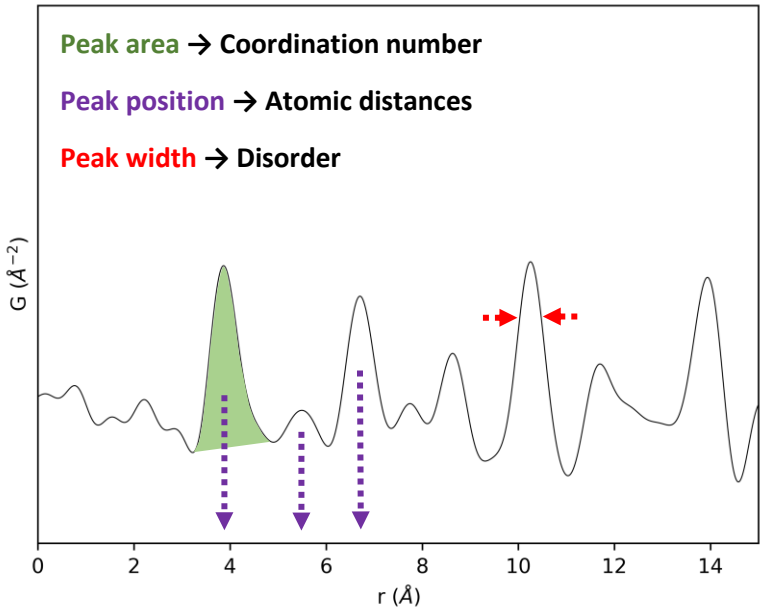

Figure 2.13. X-ray PDF of a doped bismuthate. Structural information that can be derived without structural modelling is indicated. Adapted from Ref. [55].

2.2.6.2. Modelling the PDF

Structural information can also be obtained from the PDF via modelling. The modelling is carried out in real space and essentially involves a least squares minimization process analogous to that of the conventional/full profile Rietveld method detailed in Section 2.1. PDF modelling is commonly referred to as 'PDF analysis' and the modelling of conventional reciprocal space powder diffractograms is referred to as Bragg Rietveld modelling. This formalism is adopted in this work to ensure discernment between the modelling of diffraction data in real space or in reciprocal space.

The PDF can be directly calculated from a structural model. Consider a structural model with a large number of atoms situated at positions r_v with respect to an arbitrary origin. Mathematically, this amounts to a series of delta functions $\delta(r-r_v)$ and the PDF for the structural model can be calculated using:[35]

$$G(r) + 4\pi r\rho_0 = \frac{1}{r}\sum_v \sum_u \frac{f(0)_v f(0)_u}{\langle f(0)\rangle^2}\delta(r - r_{vu}) \quad (2.24)$$

Where the *f(0)'s* are the atomic form factors evaluated at $Q = 0$ which are reasonably approximated by the number of electrons on the atom. The summations are over all atoms present in the sample and $r_{vu} = |r_v - r_u|$ is the distance separating the *v*th and *u*th atoms

As with the Bragg Rietveld approach, selected structural parameters such as lattice parameters, thermal displacement parameters and so on, are allowed to vary until the difference between the observed and calculated PDFs is minimized via the least-squares approach. For PDF analysis an R_w factor similar to that used for conventional Bragg Rietveld analysis is used to determine the quality of the achieved fit. However, the formula is slightly modified to account for the calculation in real space:[53]

$$R_w = \sqrt{\frac{\sum_{i=1}^{N}\sum \boldsymbol{w(r_i)}[\boldsymbol{G_{obs}(r_i) - G_{calc}(r_i)}]^2}{\sum_{i=1}^{N}\sum \boldsymbol{w(r_i) G_{obs}^2(r_i)}}} \quad (2.25)$$

where G_{obs} is the PDF extracted from the total scattering diffraction data, G_{calc} is the PDF calculated from the structural model and $w(r_i) = 1/\sigma(r_i)^2$ where $\sigma(r_i)$ is the standard deviation at a distance r_i.

2.2.7. Software programs for PDF data

2.2.7.1. Data reduction software

As mentioned in Section 2.2.3, data reduction beyond 2D integration was done using PDFgetX3.[50] However, this program was not used in its standalone form but via xPDFsuite (Fig. 2.14).[56] xPDFsuite is a suite of data algorithms and software tailored for the analysis of X-ray PDF data. xPDFsuite uses PDFgetX3 to reduce the integrated *I(Q)* data to produce the *S(Q)*, *F(Q)* and *G(r)* functions, however, an easy-to-use

graphical user interface (GUI) is provided which makes the data reduction process significantly easier and widely accessible. xPDFsuite also enables interactive plotting of the reduced functions which allows for the effect that pertinent variables, such as Q_{max}, have on the generated PDF data to be observed in real time. This plotting feature greatly assists with optimizing data reduction and subsequent PDF generation. The data reduction workflow is also improved by the availability of a batch processing functionality which enables several hundred data files to be reduced simultaneously. PDF data can also be modelled within xPDFsuite via PDFGui, but in this work xPDFsuite was exclusively used for data reduction.

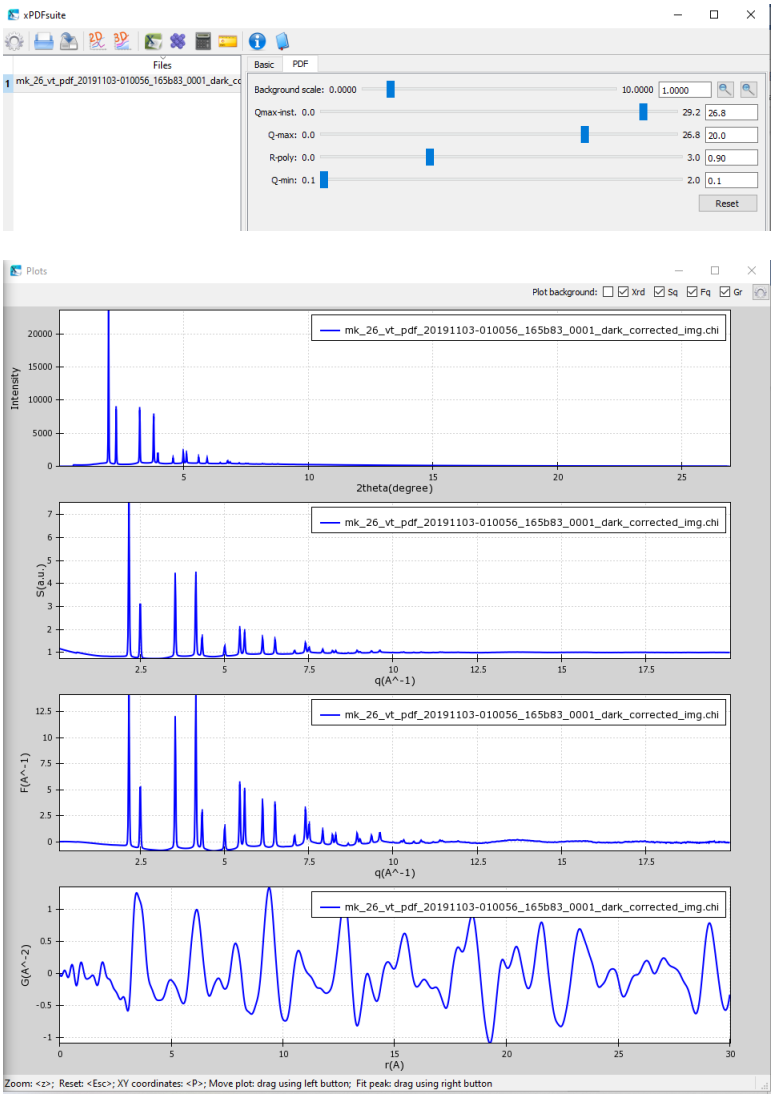

Figure 2.14. xPDFsuite screenshot of the GUI (top) and the interactive plotting (bottom). PDF data reduction parameters are varied using the GUI and the effect of this on the *I(Q)*, *S(Q)*, *F(Q)* and *G(r)* functions is observed in real time.

2.2.7.2. PDF modelling software

In comparison to the variety of software options available for Rietveld refinement of powder diffractograms, the software available for PDF data modelling is far more limited. The most commonly used software options are PDFGui[57] and Topas.[22] The modelling of PDF data reported in this thesis was done using Bruker AXS TOPAS-Academic (TA) Version 6[22,23] and refinements were done via launch mode using jEdit.[24] As mentioned in Section 2.1.7.2, TA offers significant advantages over the alternative software options. Most notable for PDF modelling are the faster refinement capabilities in addition to the ability to use pre-defined macros which are openly contributed by experts in the Rietveld community. This makes accurate PDF modelling highly accessible and fast.

2.2.8. PDF instruments

All the total scattering measurements presented in this thesis were collected at the Pair-Distribution Function (PDF) beamline (λ = 0.1671 Å) at the National Synchrotron Light Source II (NSLS-II).[33,34] For measurements collected at room temperature, samples were loaded into Kapton capillaries whereas for measurements collected *in situ*, quartz capillaries were used and *in situ* heating achieved using a hot air blower. As previously stated, data measured to higher Q_{max} increases the resolution of the generated PDFs. As such, for the total scattering measurements the detector was positioned at ~250 mm from the sample to maximize Q_{max}. Data were collected in the approximate angular range of $\sim 0 < 2\theta < 40^{o}$, covering a region of the wave vector Q ($= (4\pi/\lambda) \sin\theta$) up to Q_{max} ~26 $Å^{-1}$.

2.3. Raman spectroscopy

2.3.1. Background and theory

Raman spectroscopy is defined as a non-destructive chemical analysis technique that utilizes the interaction of light with chemical bonds to provide information related to the chemical nature and in particular, the crystal structure of a material.[58] The working principle of Raman spectroscopy, i.e. the *Raman principle*, is illustrated in Figure 2.15.

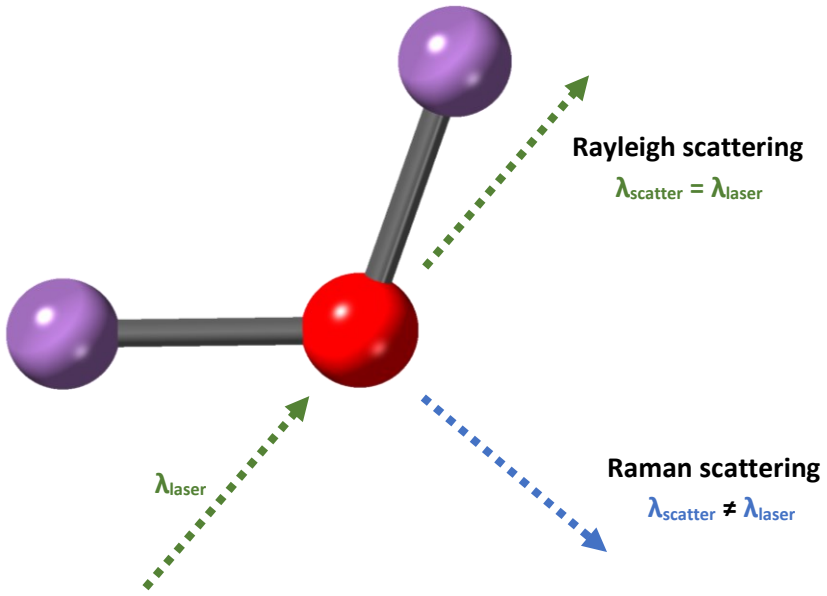

Figure 2.15. Illustration of the Raman principle. Adapted from Ref. [58].

Raman spectroscopy relies on the scattering of high intensity laser radiation by a molecule. The vast majority of the scattered light is elastically scattered. This fraction of scattered light therefore has the same energy and wavelength as that of the incident radiation and provides no useful information for chemical analysis. This type of scattering is known as Rayleigh scattering. However, for a minor fraction of the incident radiation, a vibrational perturbation occurs which involves the transfer of energy between the material and the incident photons. This inelastic scattering results in the energy of this minor fraction of scattered radiation being different to that of the incident radiation. This type of scattering is known as Raman scattering.[59] The transfer of energy can either be from the photon to the molecule, known as Stokes Raman scattering, or from the molecule to the photon which is known as anti-Stokes Raman scattering.[59] The Raman spectrum is a plot of the intensity of Raman scattered radiation as a function of

the difference in frequency in comparison to that of the incident radiation, known as the Raman shift.[59] Raman shifts correspond to the vibrational energy levels of the molecule or crystal and are affected by several structural parameters and in particular the crystallographic symmetry of the material.[58,59]

2.3.2. Use in discriminating between bismuthate polymorphs during *in situ* heating

Raman spectroscopy enables the investigation of the crystal symmetry of a material which in turn allows for crystal structure and phase identification. As a result, Raman spectra are commonly referred to as 'chemical fingerprints'[58] as the spectral features of a particular crystal system are distinct. In this thesis, Raman spectroscopy was used to for *in situ* qualitative phase analysis of yttrium doped bismuthates. This was necessary due to the immense similarity in the crystal structures of the tetragonal and cubic bismuthate polymorphs. The use of diffraction techniques were severely limited for this reason. Raman spectroscopy allows for the distinction between the two polymorphs based on the number of Raman-active modes predicted for each crystal system. This was used to monitor *in situ* phase transformation behaviour as a function of temperature, as well as the room temperature stabilization of the metastable cubic polymorph.

2.3.3. Measurement considerations

The Raman spectroscopy measurements made in this thesis do have certain limitations that are noteworthy. Firstly, Raman spectroscopy is, by definition of the Raman effect, a local structure technique. The result of this is that the Raman spectra represent the crystal structure on a local scale and do not represent the long range average crystal structure. In this way, Raman spectra provide structural information that is complimentary to the average structure information which is derived from reciprocal space PXRD measurements. Additionally, Raman spectra were only collected over small sample areas of ~1.7-3.1 μm^2. This feature is beneficial as minor impurity phase content can be identified which would otherwise go unidentified in diffraction measurements. However, sample inhomogeneity can result in differing Raman spectra if areas of varying phase composition are measured. This was largely mitigated by correct sample preparation and by ensuring that the same sample area was measured during *in situ* heating. However, during the *in situ* measurements, thermal expansion of both the sample and sample holder occurs, and this makes measuring the same portion of the sample challenging. The limited optical

microscopy capabilities of the Raman spectroscopy instrument (Fig. 2.16) makes it quite challenging to ensure that the same portion of sample is measured throughout an *in situ* measurement.

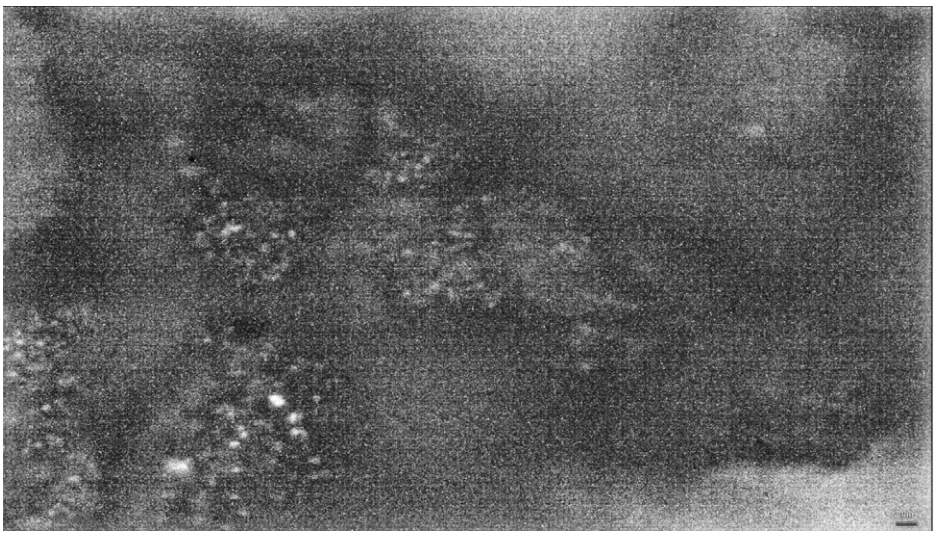

Figure 2.16. Optical microscopy image of a bismuthate sample during *in situ* variable-temperature Raman spectroscopy measurements.

Lastly, a significant decrease in Raman scattering intensity is observed at elevated temperatures. As such, the resolution of Raman spectra is progressively worsened during *in situ* heating. This limits the accuracy of the structural information available at elevated temperatures.

2.3.4. Raman spectroscopy instrumentation

For all the *in situ* variable-temperature Raman spectra presented in this thesis, a Horiba LabRam HR Raman spectrograph coupled to a Lexel Argon ion laser tuned to 514.5 nm and a Linkham TS1500 sample stage was used. Spectra were collected at 170 ^{o}C intervals with an approximate dwell time of 10 minutes in the range of 19–850 ^{o}C applying a heating rate of 10 °C min^{-1}.

2.4. Electrochemical impedance spectroscopy

Electrochemical impedance spectroscopy (EIS) is an electrochemical technique which is commonly used to characterize the electrical properties of materials and their interfaces using electronically conductive electrodes.[60–62] In this work, EIS was used to measure the oxide ion conductivity of doped bismuthate materials which is an essential property of a candidate SOFC electrolyte material.

2.4.1. Background and theory

Electrical resistance is defined as the ability of a circuit element to resist the flow of electrical current. This is defined by Ohm's Law:[63]

$$R = \frac{E}{I} \tag{2.26}$$

where *R* is the electrical resistance, *E* is the electrical potential and *I* is the current flow, all through the circuit element. Ohm's Law is widely known and is strictly only applicable to an *ideal* resistor. By definition, an ideal resistor must (1) obey Ohm's Law at all potential and current levels, (2) exhibit frequency-independent resistance and (3) display alternating current and voltage signals that are in phase with each other.[64]

Realistically, resistors do not display ideal behaviour and the use of Ohm's Law is limited in this regard. To describe this more complex, non-ideal resistance behaviour the concept of impedance was introduced. Similar to resistance, impedance is defined as the ability of a circuit to resist the flow of electrical current and is determined by measuring the current that flows through a circuit (or an electrochemical cell) when an AC potential is applied.[60,62,64,65]

When studying the impedance of an electrochemical cell, the applied potential is sinusoidal and small in magnitude such as to ensure that the cell's response is pseudo-linear.[64] This ensures that the current response to the sinusoid potential is also sinusoidal and at the same frequency, but shifted in phase (Figure 2.17). The applied potential can be expressed as:[64]

$$V_t = V_0 sin\omega t \tag{2.27}$$

where V_t is the applied potential at time *t*, V_0 is the amplitude of the signal and ω is the radial frequency. The radial frequency ω (in radians/second) is related to the frequency *f* (in hertz) by:

$$\omega = 2\pi f \tag{2.28}$$

In the pseudo-linear system, the current response to the applied potential can be expressed as:[64]

$$I_t = I_0 \sin(\omega t + \theta) \tag{2.29}$$

where I_t is the observed current at time t, I_0 is the amplitude of the signal, ω is the radial frequency and θ is the phase shift.

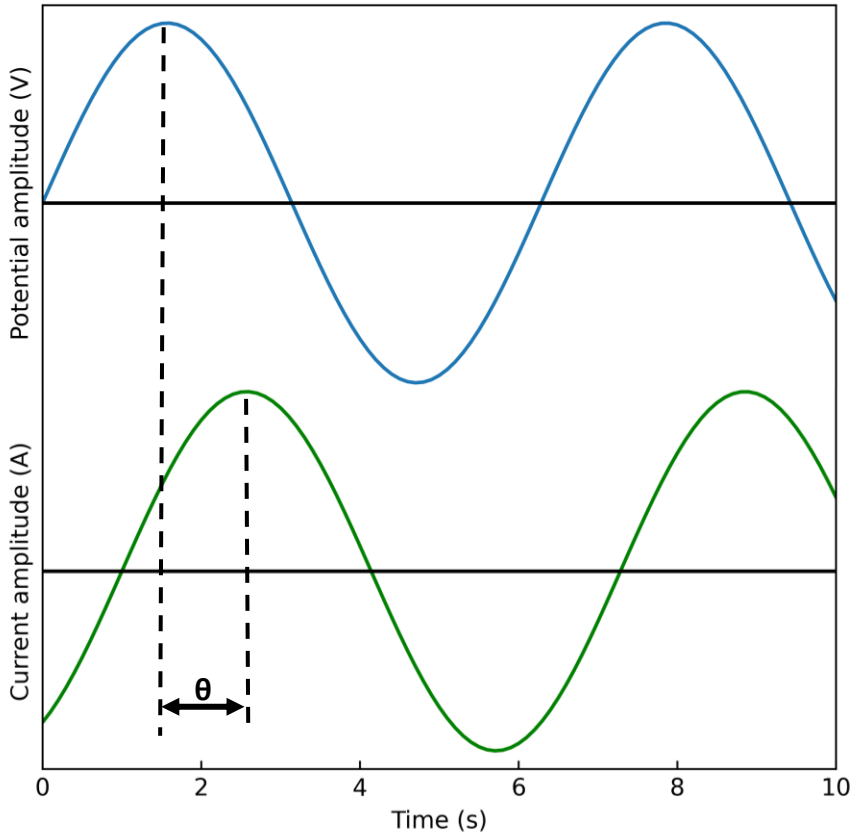

Figure 2.17. Representation of the applied sinusoidal excitation potential and the sinusoidal current response in a pseudo-linear system. Adapted from Ref. [64].

The impedance Z of an electrical component can be described using an expression analogous to Ohm's Law:[64]

$$Z_t = \frac{V_t}{I_t} \tag{2.30}$$

where Z_t is the impedance, V_t is the applied potential and I_t is the observed current, all at time t.

Combining equations 2.27 with 2.29 and 2.30 we find that:

$$Z_t = \frac{V_0 sin\omega t}{I_0 \sin(\omega t+\theta)} = Z_0 \frac{sin\omega t}{\sin(\omega t+\theta)} \quad (2.31)$$

Using Euler's relationship:

$$e^{j\theta} = cos\theta + jsin\theta \quad (2.32)$$

where $j = \sqrt{-1}$, impedance can be described as a complex function[64] where the potential function becomes:

$$V_t = V_0 e^{j\omega t} \quad (2.33)$$

and the current response becomes:

$$I_t = I_0 e^{j\omega t-\theta} \quad (2.34)$$

which enables the impedance to be described as a complex number:

$$Z(\omega) = \frac{V}{I} = Z_0 e^{j\theta} = Z_0(cos\theta + jsin\theta) \quad (2.35)$$

This expression describing the impedance *Z* is composed of both real and imaginary components:

$$Z = Z' + jZ'' \quad (2.36)$$

where *Z'* is the real component of *Z* and *Z''* is the imaginary component of *Z*.

The plot of *Z''* versus *Z'* produces a Nyquist plot and an example of this type of plot is shown in Figure 2.18.[64,66] In a Nyquist plot, each data point represents the impedance at a particular frequency value. The impedance can be represented as a vector of length $|Z|$ and the angle between this vector and the x-axis represents the phase shift, θ. The phase shift θ is described mathematically as:

$$\theta = arctan\frac{Z''}{Z'} \quad (2.37)$$

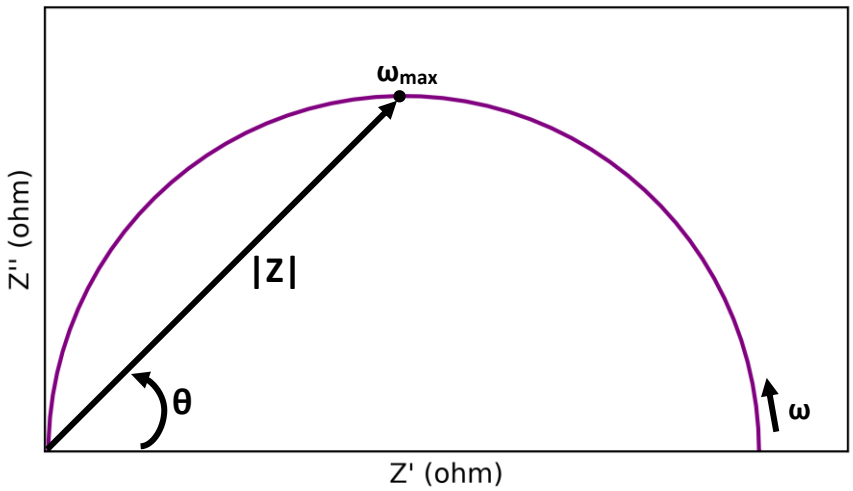

Figure 2.18. Complex plane representation of impedance showing each quantity involved.

2.4.2. Ionic conductivity measurements

2.4.2.1. Pellet preparation methodology

To measure the ionic conductivity of the doped bismuthates via EIS, the powdered samples were pelletized. For this, a portion of the annealed powders were mixed with a 2% polyvinyl alcohol solution (as a binder) and thereafter dried at 120 °C for 20 min. The resulting powder was then uniaxially pressed at 110 MPa into pellets using a 13 mm diameter die to produce pellets of ~1.2 mm thickness. The pellets were heated at 250 °C for 4 h to remove the binder and then sintered at 750 °C for 4 h to ensure maximum densification.

2.4.2.2. Data collection

Impedance of the sintered pellets was measured using a BioLogic MTZ-35 frequency response analyser interfaced to a computer running MT-Lab software version 1.21. This was coupled to a BioLogic HTF-1100 furnace and a HTSH-1100 sample holder was employed. The additional system impedances were compensated for prior to measuring the impedance of the samples. A frequency range of 0.1 Hz to 1 MHz and an excitation potential amplitude of 10 mV was employed. The measurements were taken in steps of 50 °C within the range 300–750 °C, with a 30 min dwell time per step. The sample holder contains two platinum discs, of a similar diameter to the sample pellet, between which the pellet is placed, and the spring-loaded system is tightened. No additional coatings were used on the pellet and each pellet was measured using two consecutive heating and cooling cycles.

2.4.2.3. Data analysis

The sintered pellet is polycrystalline and can be visualized, using the 'brickwork' model[61] (Fig. 2.19), as comprising of many grains that are closely packed and separated by a grain boundary.

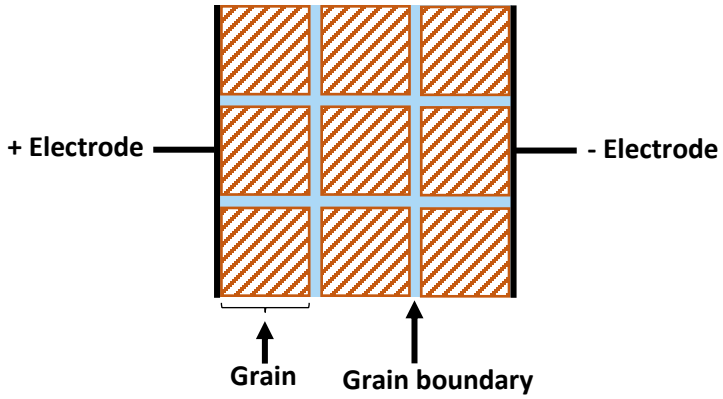

Figure 2.19. Brickwork model of the polycrystalline pellet showing the grain and grain boundary regions. Adapted from Ref. [61].

The grain and grain boundary regions of the pellet are each characterized by a resistance *R* and a capacitance *C*.[61] The current can flow between the electrodes via two diffusion pathways: by either passing through the grain bulk (the bulk pathway) or by flowing along the grain boundary (the grain boundary pathway). The Nyquist plot of the polycrystalline pellet will therefore contain two impedance responses (i.e. two semi circles, one corresponding to each *RC* element) which in the ideal case are well defined.[65] This allows for easy assignment of both the bulk and grain boundary resistances which are determined from the intercepts on the Z' axis (Fig. 2.20).

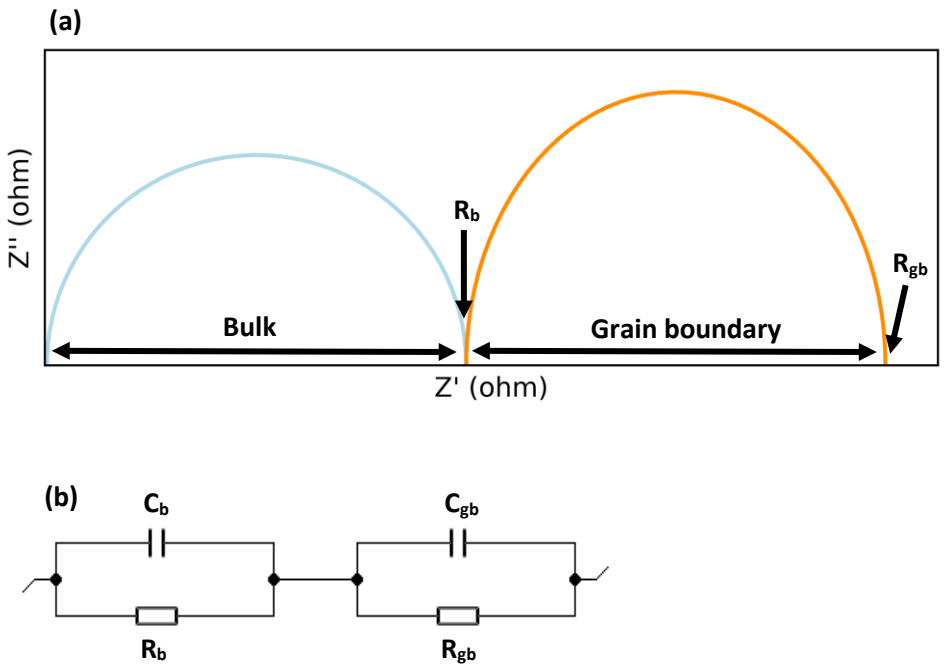

Figure 2.20. (a) Ideal Nyquist plot of a polycrystalline pellet with distinct contributions from the grain bulk and grain boundary. (b) Equivalent circuit illustrating the RC elements corresponding to the b = bulk and gb = grain boundary regions/pathways.

The assignment of the resistances to the different regions of the pellet is based on the magnitudes of the capacitances which are calculated using the relation:[61]

$$\omega_{max} RC = 1 \qquad (2.38)$$

where ω_{max} is the maximum of the impedance response (on the semi-circle) as illustrated in Figure 2.18.

Capacitances in the range of ~10^{-12} F indicate bulk resistance and ~10^{-11} - 10^{-8} F indicate grain boundary resistance.[61,62] From the Nyquist plot it is therefore possible to identify and quantify the different *RC* elements and assign them to the two regions of the polycrystalline sample. It is commonplace that the impedance responses are not sufficiently resolved to simply assign resistances based on intercepts with the Z' axis. In this work, this was evident for impedance spectra collected between 300-450 °C (Fig. 2.21a). In such cases, the contribution of each circuit element can be determined using an equivalent circuit modelling approach. In this work, EC-Lab version 11.21 was used for the equivalent circuit modelling. At elevated temperatures (500-750 °C), the impedance response in the high frequency region was insufficient to model and therefore the resistance was approximated as the real impedance at point R1

(Fig. 2.21b). Negligible grain boundary resistance is expected for doped bismuthates[67] and therefore the absence of distinct grain boundary resistance for the materials investigated in this work is unsurprising.

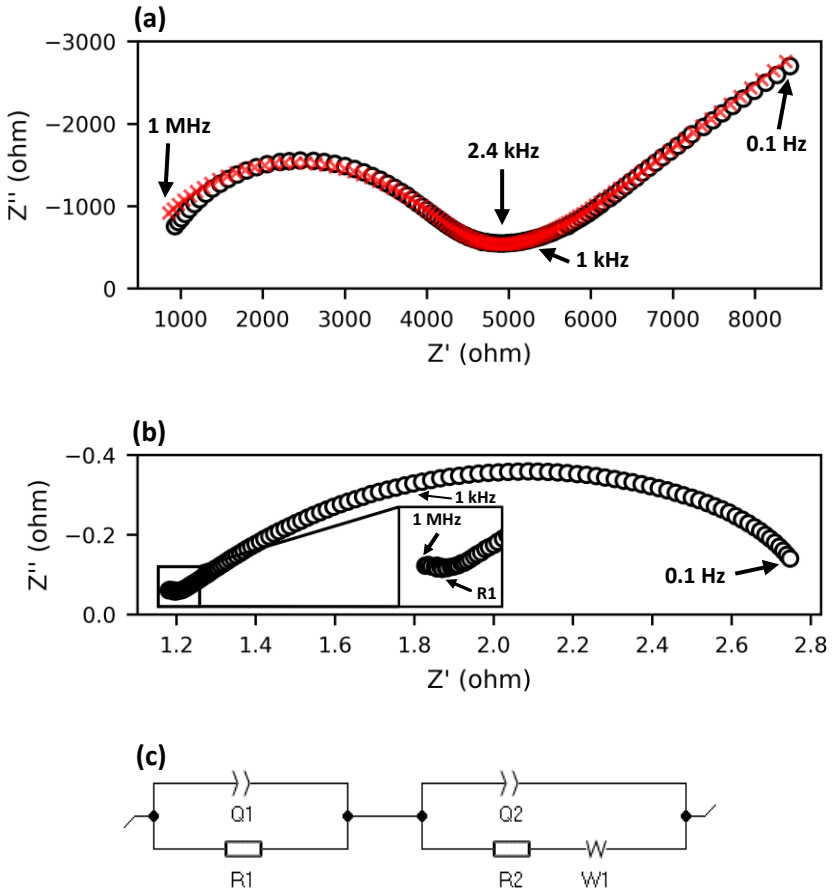

Figure 2.21. Impedance spectra of a doped bismuthate annealed at 750 °C in air at (a) 350 °C with the equivalent circuit fit shown with red markers and at (b) 750 °C indicating the point where R1 (the bulk resistance) was approximated when equivalent circuit modelling was not possible. (c) The equivalent circuit used for modelling data in the 300-450 °C range. A Warburg element was required to model the impedance caused by the diffusion of reactants at the electrode surface.

2.4.2.4. Calculating ionic conductivity and activation energy

The bulk ionic conductivity of the material was calculated from the derived bulk resistance values using:[63]

$$\sigma = \frac{1}{\rho} = \frac{l}{RA} \tag{2.39}$$

where σ is the ionic conductivity, ρ is the resistivity, l is the thickness of the pellet, A is the surface area of pellet and R is the resistance. The pellet dimensions were measured to an accuracy of 0.01 mm using a vernier calliper.

The collection of variable temperature impedance spectra enables the calculation of the activation energy of ionic conduction from the Arrhenius relationship between conductivity and temperature:[68]

$$\sigma = \sigma_0 e^{-\frac{E_a}{RT}} \tag{2.40}$$

Which can be linearized as:

$$log\sigma = log\sigma_0 - \frac{E_a}{2.303 \times RT} \tag{2.41}$$

A plot of log σ *vs*. 1/T generates an Arrhenius plot (Fig. 2.22). The slope of the Arrhenius plot can thus be used to calculate the activation energy using:

$$E_a = -2.303 \times slope \times R \tag{2.42}$$

where R = 8.314 $J.K^{-1}.mol^{-1}$. E_a is conventionally represented in terms of electron volts (eV) where 1 eV = 96485 $kJ.mol^{-1}$.

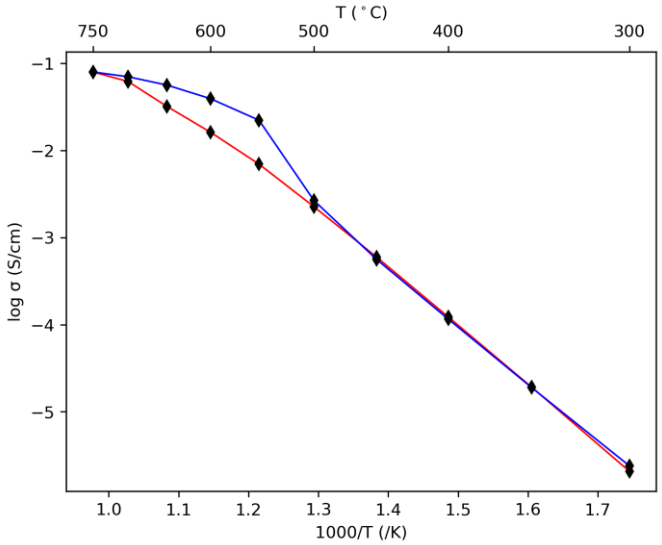

Figure 2.22. Arrhenius plot of a doped bismuthate displaying conductivity behaviour in the temperature range of 300– 750 °C showing results from both the heating (red lines) and the cooling cycles (blue lines).

2.4.3. Measurement considerations and limitations

It is a standard procedure to apply a conductive paste to the pellet surfaces prior to an EIS measurement. The conductive paste ensures intimate pellet-to-electrode contact which is required for accurate impedance measurements. In this work, the application of conductive paste was not done for two main reasons. Firstly, it was evident that the paste was readily absorbed into the pellet during sintering. This is highly undesirable as it changes the composition of the pellet and introduces material which is electronically conductive. This prevents the sensible measurement of ionic conductivity. Additionally, a reaction between the conductive paste layer and the electrodes of the cell holder was evident. This reaction adds a new interfacial material to the measurement which is undesirable as this new material will contribute towards the measured impedance spectra. Additionally, this reaction binds the pellet to the electrodes which results in significant damage to the solid platinum electrodes, preventing their longevity. The omission of a conductive paste application to the pellet surfaces undoubtably limits the quality and accuracy of the ionic conductivity measurements in this work. To mitigate this, each pellet was measured using two consecutive heating and cooling cycles. The thermal expansion contribution from the first cycle 'optimized' the pellet-to-electrode contact. Overcoming these critical measurement limitations are presently under investigation to improve future measurements.

2.5. Python programming in the era of big data

Python is a dynamic and general-purpose programming language that has in recent years found extensive use in various fields.[69] This strong uptake of Python is largely due to the language being easy to learn and to implement whilst remaining a high-level programming language. Additionally, Python is open source and comes with a large standard library that supports many common programming tasks such as the visualization of data and curve fitting.

2.5.1. Data visualization using Python

The visualization of data involves the presenting of data in a graphical format, and this has become a prevalent need in the current era of big data.[69] Data visualization is imperative as it enables the significance of large amounts of data to be presented in a more easy-to-understand format. Several Python libraries such as Pandas, Plotly and Matplotlib are available for data visualization. In this thesis the Matplotlib[70] library was exclusively used, within the IPython[71] integrated development environment (IDE), for all the data visualization requirements. All data visualization scripts were developed in-house with significant assistance and contributions from the Stack Overflow community.[72]

2.5.2. Curve fitting using Python

The fitting of bivariate data is easily achieved using the NumPy[73] library which enables numerical computing in Python. All the linear and Gaussian curve fitting presented in this thesis was achieved using in-house developed Python scripts.

2.6. Synthetic method

The synthesis of solid oxide electrolytes is most often achieved using the conventional solid state synthesis route. This route involves the mixing of precursor metal oxides in a desired stoichiometric ratio which is done either using a mortar and pestle or a ball mill. Thereafter repeated grinding and heating of the powdered material is done to ensure proper mixing of precursor oxides and to promote the solid state reaction, respectively. This synthetic technique is colloquially known as the 'shake-and-bake' technique. For all the materials reported in this thesis, an alternative soft chemical synthetic route known as the citrate sol-gel method[74] was used.

2.6.1. The citrate sol-gel method

The citrate sol-gel method employed in this work firstly involves dissolving stoichiometric amounts of metal nitrates in glacial acetic acid under conditions of moderate heating and stirring. Aqueous solutions were avoided to prevent the hydrolysis of Bi^{3+}. Once the nitrates are fully dissolved, excess citric acid is added and the resulting solution is heated at ~180 ^{o}C for ~30 minutes under moderate stirring to form a metal complex precursor paste. The precursor paste was thereafter calcined (at 450 ^{o}C for 18 h) and annealed (at 750 ^{o}C for 8 h) to produce the desired mixed metal oxide (MMO) powder. The citrate sol-gel method is illustrated in Figure 2.23.

Figure 2.23. Schematic illustrating the citrate sol-gel method utilized to synthesize the materials presented in this thesis.

2.6.2. Why the citrate sol-gel method?

In general, sol-gel synthetic techniques offer several advantages over the conventional solid state routes. These advantages include faster synthesis times and lower energy consumption, without compromising the atomic scale mixing of reactants. The citrate sol-gel method itself offers additional advantages

resulting from the homogeneity of the precursor paste. The presence of this homogeneous organic matrix during the calcination steps ensures that when nucleation occurs, the metal sites are evenly distributed and numerous. This promotes the formation of small crystallite sizes in the calcined and subsequently annealed powders. Additionally, the homogenous organic matrix ensures that the metal ions remain mixed on the atomic scale during calcination. This limits the formation of undesired side reactions which results in the formation of impurity phases and promotes particle size irregularity.[75] Lastly, the homogeneity enables lower calcination temperatures as the metal sites are intimately mixed and the mass transport between these reactive sites is significantly less hindered in comparison to the mass transport between grains obtained using conventional solid state synthetic routes.[76]

2.6.3. Critical analysis of the citrate sol-gel method

Although the citrate sol-gel method offers significant advantages over the alternative synthetic routes available, several limitations have been identified in this work. The long term phase stability of several doped bismuthates under ambient conditions is investigated in Chapter 4. It is seen that two materials of identical composition can have varying phase composition and varying phase stability characteristics over prolonged periods of time under ambient conditions. This variation in phase stability is likely due to the formation of varying trace impurity phases, during the synthetic procedure. These impurity phases crystallize over time and promote the various phase transformations observed. These trace impurities were observed via synchrotron-based diffraction experiments and an example of this is shown in Figure 2.24.

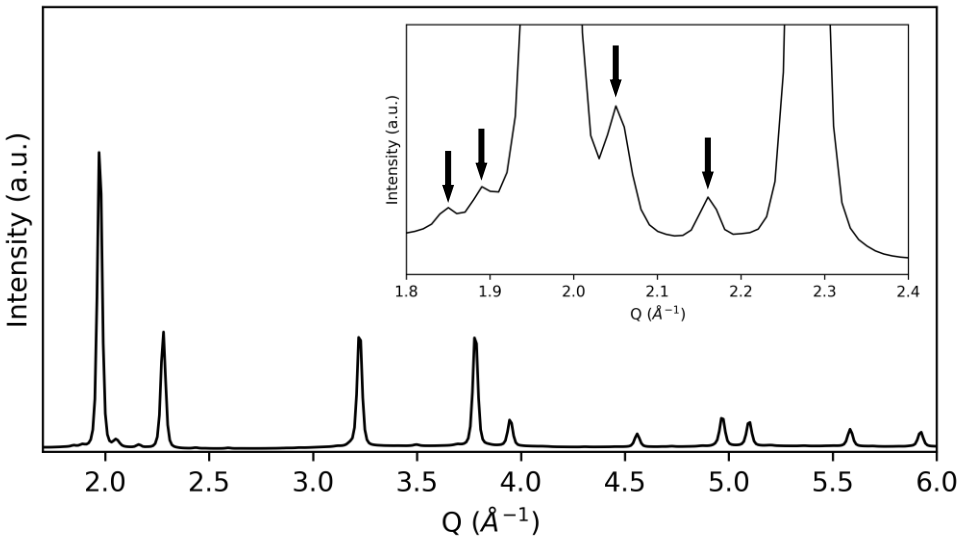

Figure 2.24. Powder diffractogram of a doped bismuthate showing the presence of trace impurity phase peaks (black arrows).

These impurity phases likely form during the formation of the metal complex precursor paste and additionally during the calcination and annealing steps of the synthetic route. Better temperature control of both the metal complex paste formation and the subsequent calcination and annealing steps are sought to prevent, or more realistically to minimize, impurity phase formation.

2.7. References

1. Nobel Prize Outreach. The Nobel Prize in Physics 1914. (2021). Available at: https://www.nobelprize.org/prizes/physics/1914/laue/lecture/. (Accessed: 17th March 2021)

2. Nobel Prize Outreach. The Nobel Prize in Physics 1915. (2021). Available at: https://www.nobelprize.org/prizes/physics/1915/summary/. (Accessed: 17th March 2021)

3. Dinnebier, R. E. and Billinge, S. J. L. Principles of powder diffraction. in *Powder Diffraction Theory and Practice* (eds. Dinnebier, R. E. and Billinge, S. J. L.) 1–19 (RSC Publishing, 2008).

4. Dreele, R. B. Von and Rodriguez-Carvajal, J. The Intensity of a Bragg Reflection. in *Powder Diffraction Theory and Practice* (eds. Dinnebier, R. E. and Billinge, S. J. L.) 58–87 (RSC Publishing, 2008).

5. Dinnebier, R. E., Evans, J. S. O. and Leineweber, A. The Rietveld method. in *Rietveld Refinement Practical Powder Diffraction Pattern Analysis Using Topas* 16–86 (De Gruyter, 2019).

6. Young, R. A. Introduction to the Rietveld method. in *The Rietveld Method* (ed. Young, R. A.) 1–39 (Oxford University Press, 1993).

7. Thompson, M. Synthesis and characterisation of δ-Bi_2O_3 related materials stabilized by substitutions of Ca, Ga, Nb and Re. (University of Birmingham, 2010).

8. Dinnebier, R. E., Leineweber, A. and Evans, J. S. O. *Rietveld Refinement Practical Powder Diffraction Pattern Analysis Using Topas*. (Walter de Gruyter GmbH, Berlin/Boston, 2019).

9. Cockcroft, J. K. and Fitch, A. N. Experimental setups. in *Powder Diffraction Theory and Practice* (eds. Dinnebier, R. E. and Billinge, S. J. L.) 20–56 (RSC Publishing, 2008).

10. Corrie, B. Synthesis and Structural Characterisation of Solid Oxide Fuel Cell Materials. (University of Birmingham, 2014).

11. Rietveld, H. M. Line profiles of neutron powder-diffraction peaks for structure refinement. *Acta Crystallogr*. **22**, 151–152 (1967).

12. Rietveld, H. M. A profile refinement method for nuclear and magnetic structures. *J. Appl. Crystallogr*. **2**, 65–71 (1969).

13. Von Dreele, R. B. Rietveld refinement. in *Powder Diffraction Theory and Practice* (eds. Dinnebier, R. E. and Billinge, S. J. L.) 266–280 (RSC Publishing, 2008).

14. Toby, B. H. R factors in Rietveld analysis: How good is good enough? *Powder Diffr*. **21**, 67–70 (2006).

15. Small, J. A. and Watters, R. L. SRM 660c - Lanthanum Hexaboride Powder - Line Position and Line Shape Standard for Powder Diffraction. National Institute of Standards and Technology 1–5 (2015). Available at: https://www-s.nist.gov/srmors/certificates/660C.pdf. (Accessed: 2nd January 2021)

16. Rashband, W. ImageJ. Research Services Branch, National Institute of Mental Health, Bethesda, Maryland, USA. (2021). Available at: https://imagej.en.softonic.com/?ex=BB-1857.3. (Accessed: 6th January 2021)

17. Cranswick, L. M. D. Computer Software for Powder Diffraction. in *Powder Diffraction Theory and Practice* (eds. Dinnebier, R. E. and Billinge, S. J. L.) 497–571 (RSC Publishing, 2008).

18. Grazulis, S., Chateigner, D., Downs, R. T., Yokochi, A. F. T., Quiros, M., Lutterotti, L. , Manakova, E., Butkus, J., Moeck, P. and Le Bail, A. Crystallography Open Database - An open-access collection of crystal structures, *J. Appl. Crystallogr.*, 2009, **42**, 726–729

19. Von Dreele, R. B. Introduction to GSAS & GSAS-II. International Union of Crystallography (2011). Available at: http://www.iucr.org/__data/iucr/powder/Erice2011/day2/d2/gsas.pdf. (Accessed: 7th January 2020)

20. Toby, B. H. and Von Dreele, R. B. GSAS-II: The genesis of a modern open-source all purpose crystallography software package. *J. Appl. Crystallogr*. **46**, 544–549 (2013).

21. Rodriguez-Carvajal, J. Recent Developments of the Program FULLPROF. *Comm. Powder Diffr. (IUCr). Newsl*. **26**, 12–19 (2001).

22. Coelho, A. A. TOPAS and TOPAS-Academic: An optimization program integrating computer algebra and crystallographic objects written in C++: *J. Appl. Crystallogr*. **51**, 210–218 (2018).

23. Coelho, A. A. TOPAS-Academic, Version 6: Technical Reference. (2016).

24. jEdit - Programmer's Text Editor. (2021). Available at: http://www.jedit.org/index.php?page=download.

25. Momma, K. and Izumi, F. VESTA. JP-Minerals (2021). Available at: https://jp-minerals.org/vesta/en/download.html.

26. CrystalMaker. CrystalMaker Software Ltd. (2021). Available at: http://www.crystalmaker.com/.

27. Bruker Corporation. D2 Phaser. (2021). Available at: https://www.bruker.com/en/products-and-solutions/diffractometers-and-scattering-systems/x-ray-diffractometers/d2-phaser.html. (Accessed: 22nd May 2021)

28. Bruker Corporation. D8 Advance. Available at: https://www.bruker.com/content/bruker/int/en/products-and-solutions/diffractometers-and-scattering-systems/x-ray-diffractometers/d8-advance-family/d8-advance.html. (Accessed: 22nd May 2021)

29. Anton Paar GmbH. Reactor Chamber: XRK 900. (2021). Available at: https://www.anton-paar.com/za-en/products/details/reactor-chamber-xrk-900/. (Accessed: 19th May 2021)

30. Corning Incorporated. MACOR® Machinable Glass Ceramic. (2021). Available at: https://www.corning.com/worldwide/en/products/advanced-optics/product-materials/specialty-glass-and-glass-ceramics/glass-ceramics/macor.html. (Accessed: 22nd May 2021)

31. Fitch, A. N. The high resolution powder diffraction beam line at ESRF. *J. Res. Natl. Inst. Stand. Technol*. **109**, 133–142 (2004).

32. Dejoie, C., Coduri, M., Petitdemange, S., Giacobbe, C., Covacci, E., Grimaldi, O., Autran, P. -O., Mogodi, M. W., Jung D. S. and Fitch, A. N. Combining a nine-crystal multi-analyser stage with a two-dimensional detector for high-resolution powder X-ray diffraction. *J. Appl. Crystallogr*. **51**, 1721–1733 (2018).

33. Shi, X., Ghose, S. and Dooryhee, E. Performance calculations of the X-ray powder diffraction beamline at NSLS-II. *J. Synchrotron Radiat*. **20**, 234–242 (2013).

34. Abeykoon, A. M. M. NSLS-II BDN Beamline 28-ID-1 (PDF) Commissioning Plan. (2018). Available at:

https://www.bnl.gov/nsls2/project/reviews/180315_IRR_PDF/files/Planning/Commissioning_Plan.pdf. (Accessed: 10th May 2021)

35. Billinge, S. J. L. and Kanatzidis, M. G. Beyond crystallography: The study of disorder, nanocrystallinity and crystallographically challenged materials with pair distribution functions. *Chem. Commun*. **4**, 749–760 (2004).

36. Billinge, S. J. L. and Egami, T. *Underneath the Bragg Peaks - Structural Analysis of Complex Materials*. (Pergamon Materials Series, 2003).

37. Billinge, S. J. L. Local Structure from Total Scattering and Atomic Pair Distribution Function (PDF) Analysis. in *Powder Diffraction Theory and Practice* (eds. Dinnebier, R. E. and Billinge, S. J. L.) 464–493 (RSC Publishing, 2008).

38. Billinge, S. J. L. and Egami, T. Structure of complex materials. in *Underneath the Bragg Peaks - Structural Analysis of Complex Materials* (ed. Cahn, R. W.) 3–22 (Pergamon Materials Series, 2003).

39. Billinge, S. J. L. and Egami, T. Crystallographic analysis of complex materials. in *Underneath the Bragg Peaks - Structural Analysis of Complex Materials* (ed. Cahn, R. W.) 25–50 (Pergamon Materials Series, 2003).

40. Keen, D. A. A comparison of various commonly used correlation functions for describing total scattering. *J. Appl. Crystallogr*. **34**, 172–177 (2001).

41. Yang, X., Masadeh, A. S., McBride, J. R., Bozin, E. S., Rosenthal, S. J. and Billinge, S. J. L. Confirmation of disordered structure of ultrasmall CdSe nanoparticles from X-ray atomic pair distribution function analysis. *Phys. Chem. Chem. Phys*. **15**, 8480–8486 (2013).

42. Bish, D. L. and Howard, S. A. Quantitative phase analysis using the Rietveld method. *J. Appl. Crystallogr*. **21**, 86–91 (1988).

43. Young, C. A. and Goodwin, A. L. Applications of pair distribution function methods to contemporary problems in materials chemistry. *J. Mater. Chem*. **21**, 6464–6476 (2011).

44. Proffen, T., Billinge, S. J. L., Egami, T. and Louca, D. Structural analysis of complex materials using the atomic pair distribution function - A practical guide. *Zeitschrift fur Krist*. **218**, 132–143 (2003).

45. Bordet, P. Local structure studies using the pair distribution function. *EPJ Web Conf*. **104**, (2015).

46. Billinge, S. J. L. and Egami, T. The method of total scattering and atomic pair distribution function analysis. in *Underneath the Bragg Peaks - Structural Analysis of Complex Materials* (ed. Cahn, R. W.) 55–98 (Pergamon Materials Series, 2003).

47. Kovyakh, A. X-ray pair distribution function analysis of transition and noble metals for industrial applications in sensing and catalysis. (University of Copenhagen, 2018).

48. Chupas, P. J. et al. Rapid-acquisition pair distribution function (RA-PDF) analysis. *J. Appl. Crystallogr*. **36**, 1342–1347 (2003).

49. Hammersley, A. P. FIT2D: A multi-purpose data reduction, analysis and visualization program. *J. Appl. Crystallogr*. **49**, 646–652 (2016).

50. Juhás, P., Davis, T., Farrow, C. L. and Billinge, S. J. L. PDFgetX3: A rapid and highly automatable program for processing powder diffraction data into total scattering pair distribution functions. *J. Appl. Crystallogr*. **46**, 560–566 (2013).

51. Qiu, X., Thompson, J. W. and Billinge, S. J. L. PDFgetX2: A GUI-driven program to obtain the pair distribution function from X-ray powder diffraction data. *J. Appl. Crystallogr*. **37**, 678 (2004).

52. Billinge, S. J. L. and Egami, T. Data collection and analysis. in *Underneath the Bragg Peaks - Structural Analysis of Complex Materials* (ed. Cahn, R. W.) 137–215 (Pergamon Materials Series, 2003).

53. Billinge, S. J. L. and Egami, T. Extracting structural information from the PDF. in *Underneath the Bragg Peaks - Structural Analysis of Complex Materials* (ed. Cahn, R. W.) (Pergamon Materials Series, 2003).

54. Wojdyr, M. Fityk: A general-purpose peak fitting program. *J. Appl. Crystallogr*. **43**, 1126–1128 (2010).

55. Chapman, K. W. Emerging operando and X-ray pair distribution function methods for energy materials development. *MRS Bull*. **41**, 231–238 (2016).

56. Yang, X., Juhas, P., Farrow, C. L. and Billinge, S. J. L. xPDFsuite: an end-to-end software solution for high throughput pair distribution function transformation, visualization and analysis. *J. Appl. Crystallogr*. (2014).

57. Farrow, C. L., Juhas, P., Liu, J. W., Bryndin, D., Bozin, E. S., Bloch, J., Proffen, Th. and Billinge, S. J. L. PDFfit2 and PDFgui: Computer programs for studying nanostructure in crystals. *J. Phys. Condens. Matter* **19**, (2007).

58. What is Raman Spectroscopy? Horiba Ltd. Available at: https://www.horiba.com/en_en/raman-imaging-and-spectroscopy/. (Accessed: 26th May 2021)

59. Baddour-Hadjean, R. and Pereira-Ramos, J. P. Raman microspectrometry applied to the study of electrode materials for lithium batteries. *AIP Conf. Proc*. **1267**, 1137–1138 (2010).

60. Macdonald, J. R. and Johnson, W. B. Fundamentals of Impedance Spectroscopy. in *Impedance Spectroscopy - Theory, Experiment, and Applications* (eds. Macdonald, J. R. and Barsoukov, E.) 1–20 (John Wiley & Sons, Inc., 2018).

61. J.T.S. Irvine, D.C. Sinclair and A.R. West. Electroceramics: Characterization by Impedance Spectroscopy. *Adv. Mater*. **2**, 132–138 (1990).

62. Sinclair, D. Characterization of Electro-materials using ac Impedance Spectroscopy. *Boletín la Soc. Española Cerámica y Vidr*. **34**, 55–65 (1995).

63. Askeland, D. R., Fulay, P. P. and Wright, W. J. Electronic materials. in *The Science and Engineering of Materials* 720–761 (Cengage Learning, 2011).

64. Gamry Instruments. Basics of Electrochemical Impedance Spectroscopy. (2021). Available at: https://www.gamry.com/application-notes/EIS/basics-of-electrochemical-impedance-spectroscopy/. (Accessed: 29th May 2021)

65. Raistrick, I. D., Franceschetti, D. R. and Macdonald, J. R. Theory. in *Impedance Spectroscopy Theory, Experiment, and Applications* (eds. Macdonald, J. R. and Barsoukov, E.) 27–129 (John Wiley & Sons, Inc., 2005).

66. PalmSens. Electrochemical Impedance Spectroscopy (EIS). (2021). Available at: https://www.palmsens.com/electrochemical-impedance-spectroscopy-eis/. (Accessed: 29th May 2021)

67. Jung, H. J. and Chung, S. Y. Absence of distinctively high grain-boundary impedance in polycrystalline cubic bismuth oxide. *J. Korean Ceram. Soc*. **54**, 413–421 (2017).

68. Askeland, D. R., Fulay, P. P. and Wright, W. J. Atom and ion movements in materials. in *The Science and Engineering of Materials* 155–190 (Cengage Learning, 2011).

69. Embarak, O. *Data Analysis and Visualization Using Python* (Apress, 2018). doi:10.1007/978-1-4842-4109-7

70. Hunter, J., Dale, D., Firing, E., Droettboom, M. and Matplotlib development team. Matplotlib. Available at: https://matplotlib.org/stable/api/legend_api.html

71. IPython. Project Jupyter (2021). Available at: https://ipython.org/.

72. Stack Overflow. Available at: https://stackoverflow.com/.

73. Oliphant, T. NumPy. (2021). Available at: https://numpy.org/.

74. Danks, A. E., Hall, S. R. and Schnepp, Z. The evolution of 'sol-gel' chemistry as a technique for materials synthesis. *Mater. Horizons* **3**, 91–112 (2016).

75. Zhang, J. J., Ning, J. W., Liu, X. J., Pan, Y. B. and Huang, L. P. Synthesis of ultrafine YAG:Tb phosphor by nitrate-citrate sol-gel combustion process. *Mater. Res. Bull*. **38**, 1249–1256 (2003).

76. Zayat, M. and Levy, D. Blue $CoAl_2O_4$ Particles Prepared by the Sol-Gel and Citrate-Gel Methods. *Chem. Mater*. **12**, 2763–2769 (2000).

Chapter 3. A detailed investigation of the structural stability, ionic conductivity and *in situ* δ-phase formation of $Y_xBi_{2-x}O_3$

M.A. Kiefer[a,c], Caren Billing[a*], Rudolph M. Erasmus[b,c], Wilson M. Mogodi,[d] David G. Billing[a,c]

[a]Molecular Science Institute, School of Chemistry, University of the Witwatersrand, Private Bag X3, Johannesburg, 2050, South Africa.

[b]Material Physics Research Institute and Microscopy and Microanalysis Unit, University of the Witwatersrand, Private Bag X3, Johannesburg, 2050, South Africa.

[c]DSI-NRF Centre of Excellence in Strong Materials, University of the Witwatersrand, Private Bag X3, Johannesburg, 2050, South Africa.

[d]Centre for Supramolecular Chemistry Research, Department of Chemistry, University of Cape Town, Rondebosch, Cape Town, South Africa.

This chapter has been submitted to the South African Journal Of Chemistry and has been formatted accordingly.

Abstract

The *in situ* δ-phase formation for a series of yttrium-doped Bi_2O_3 materials was studied by Raman spectroscopy and high resolution powder X-ray diffraction under variable temperature conditions. Contrary to previous reports, for dopant concentrations less than 25%, the cubic δ-phase was not fully stabilized at room temperature - tetragonal phase content was evident in both Raman spectra and powder diffractograms. The use of Arrhenius plots to confirm the extent of phase purity was also investigated. Both the thermal expansion and ionic conductivity of the cubic phase decreased with increasing dopant content.

Keywords**:** Bismuth oxide; PXRD; oxide ion conductor; Impedance spectroscopy; Raman spectroscopy

3.1. Introduction

The δ-phase of Bi_2O_3 shows both immense promise and a multitude of limitations as a solid oxide electrolyte. It is the highest oxide ion conducting material known, with conductivities around 1 $S.cm^{-1}$ at 750 °C.[1–3] The reasons for this spectacularly high conduction have been elegantly summarized by Boivin and Mairesse:[4] (i) 25% of the oxygen sites are vacant in the fluorite-type lattice, (ii) Bi^{3+} has an electronic structure characterized by the presence of a $6s^2$ lone pair which leads to high polarizability of the cation network and (iii) Bi^{3+} has the ability to accommodate highly disordered surroundings. It has further been shown via neutron diffraction studies that in these *F*m$\bar{3}$m-structured oxides, oxide ions are disordered across the 8c sites and the 32f sites[5,6] (as indicated in Figure 3.1). Neutron total scattering studies have indicated the occupancy of an additional 48i site which further adds to the highly disordered nature of this structure.[7] Furthermore, studies by Abrahams *et al.*[8] and Borowska-Centkowska *et al.*[9] have shown distinct relationships between the local, defect structure of Bi_2O_3 materials and physical properties such as oxide ion conductivity and thermal expansion.

Although the conductivity of the δ-phase of Bi_2O_3 is orders of magnitude higher than that commonly found for the commercial yttria stabilized zirconia (YSZ) electrolyte materials (between 0.01 – 0.1 $S.cm^{-1}$ within the temperature range of 700–1000 °C),[10–14] this phase is only stable within a narrow temperature range (730–824 °C) and is characterized by a large coefficient of thermal expansion (CTE) reported between 24.0-43.6 10^{-6} K^{-1}.[15,16] Previous studies have focused on stabilizing the δ-phase to lower temperatures by the addition of lanthanide and transition metal dopants to Bi_2O_3.[15–22] These approaches have been largely successful, with the δ-phase being stabilized to lower temperatures and in some cases, to room temperature. The presence of these dopants in the δ-phase is, however, at the expense of conductivity.[15, 18,23] Remarkably, the effect of doping on the CTE of these stabilized δ-phases is poorly reported, if at all.

This work focuses on using Y^{3+} as the dopant to stabilize the δ-phase. The range of dopant content required to stabilize the δ-phase has been investigated in several studies, however the exact range remains questionable. Previous studies by Takahashi *et al.*[24] indicated δ-phase stabilization with Y^{3+} content between 25-43 mol% whereas Kale *et al.*[19] indicated that the δ-phase was stabilized over a broad composition range of 10-40 mol% Y^{3+}. Additional studies have shown that Y^{3+} content greater than 20 mol%[6,25–29] readily stabilizes the δ-phase to room temperature. A more recent study by Liu *et al.*[30] has shown that the δ-phase is stabilized to room temperature with Y^{3+} content as low as 15 mol%. There seems to be agreement that δ-phase stabilization occurs for Y^{3+} content above 20-25 mol%, but the question remains as to whether the δ-phase is truly stabilized with Y^{3+} content below 20 mol%, and especially as low as 10-15 mol%. This issue is raised here due to peak asymmetry noted in the diffraction

pattern for the sample containing 10 mol% Y^{3+} in the work published by Takahashi *et al.*[24], although they did not comment on this. In the study by Liu *et al.*[30] peak asymmetry for the 10 mol% Y^{3+} was also noted and at this dopant level a cubic and tetragonal phase mixture is reported. This asymmetry was not noted for samples containing 15-25 mol% Y^{3+}. The pattern for the 10 mol% Y^{3+} composition was unfortunately omitted in the study by Kale *et al.*[19]

An alternative soft chemical synthetic route was employed here since it is faster and requires less energy as compared to conventional solid state methods used in the previous studies, whilst ensuring atomic scale mixing of reactants. The amount of Y^{3+} used to stabilize the δ-phase was investigated with the aim to establish the dopant range in which the δ-phase is truly stabilized on synthesis. The relationship between the dopant percentage and its effect on conductivity and δ-phase thermal expansion was studied, along with the *in situ* δ-phase formation.

3.2. Experimental

3.2.1. Synthesis and sample preparation

All samples were prepared by means of a citrate sol-gel process[31]. Stoichiometric amounts of bismuth nitrate pentahydrate ($Bi(NO_3)_3.5H_2O$, 99.99% pure, Aldrich) and yttrium nitrate hexahydrate ($Y(NO_3)_3.6H_2O$, 99.8% pure, Aldrich) were dissolved in glacial acetic acid (98% pure, MK Chemical, 99%) under moderate heating and stirring. Aqueous solutions were avoided to prevent the hydrolysis of Bi^{3+}.[31] Excess citric acid monohydrate ($C_6H_8O_7.H_2O$, ACS reagent, Aldrich) was added and the resulting mixture evaporated to form a metal complex paste. Finally, the dried precursor was calcined at 450 ^oC for 18 h to obtain the $Y_xBi_{2-x}O_3$ powders and a portion of the sample was used for the *in situ* δ-phase formation studies. The other portion was ground into a fine powder using an agate mortar and pestle and then annealed at 750 ^oC for 8 h. A range of samples were prepared with varying dopant concentration, with samples having relatively high dopant concentrations (25 and 27.5 mol% Y^{3+}) which are known to be δ-phase stabilized and those with lower dopant concentrations (10-22.5 mol% Y^{3+}) which are the samples of interest. For ease of referring to the various samples, a 10% Y_2O_3 doped Bi_2O_3 sample is called 10YSB (yttria stabilized bismuth oxide) and so on.

Pellets were prepared for impedance studies by mixing the annealed powders with a 2% polyvinyl alcohol solution (as a binder) and dried at 120 ^oC for 20 min. This was then uniaxially pressed at 110 MPa into pellets using a 13 mm diameter die to produce pellets of ~1.2 mm thickness. The pellets were heated at 250 ^oC for 4 h to remove the binder and then sintered at 750 ^oC for 4 h.

3.2.2. Raman spectroscopy

A Horiba LabRam HR Raman spectrograph coupled to a Lexel Argon ion laser tuned to 514.5 nm and a Linkham TS1500 sample stage were used to collect *in situ* variable-temperature Raman spectra. Spectra were collected at 170 °C intervals with an approximate dwell time of 10 minutes in the range of 19–850 °C applying a heating rate of 10°C min^{-1}.

3.2.3. Powder X-ray diffraction

Room temperature powder X-ray diffractograms were collected on a Bruker D2 Phaser using iron filtered CoK_{α} radiation (λ = 1.788 Å). High resolution powder diffractograms of selected calcined samples were also collected *in situ* at beamline ID22 (λ = 0.3544 Å) at the European Synchrotron Radiation Facility (ESRF). Samples were loaded into quartz capillaries and the temperature raised using a hot-air blower. Diffractograms were collected at ~50 °C intervals from room temperature to 769 °C, with the set temperatures corrected according to the facilities temperature calibration profile. Phase identification of diffractograms was done using Bruker AXS DIFFRAC.EVA V4.2 linked to the crystallography open database (COD)[32]. Rietveld refinement of the diffractograms was done using Bruker AXS TOPAS-Academic Version 6.[33] In the refinements of the lab-based diffractograms collected at room temperature, the instrument resolution function (IRF)[34] was determined using NIST 660a and was described using the fundamental parameters approach[35] using the full axial divergence model[36] to account for divergence-related asymmetry of the diffraction peaks. In the refinements of the synchrotron *in situ* diffractograms, the IRF was determined using NIST 640d and was described using the Thompson Cox Hastings (TCHZ) Pseudo-Voight function[37] with the divergence-related asymmetry effects described in an empirical way using the simple axial model.[34] In each refinement, the parameters refined were the scale factors, selected corrections, and lattice parameters. Atomic positional parameters were fixed to those published for the respective crystal structures and atomic thermal parameters were fixed to reasonable values.

3.2.4. Electrochemical impedance spectroscopy

Impedance of the sintered pellets was measured using a BioLogic MTZ-35 frequency response analyser interfaced to a computer running MT-Lab software version 1.21. This was coupled to a BioLogic HTF-1100 furnace and a HTSH-1100 sample holder was employed. The additional system impedances were compensated for prior to measuring the impedance of the samples. A frequency range of 0.1 Hz to 1 MHz and an amplitude of 10 mV was employed. The measurements were taken in steps of 50 °C within the range 300–750 °C, with a 30 min dwell time per step. The sample holder consists of two platinum discs, a similar diameter to the sample, between which the pellet is placed and the spring-loaded system is then

tightened. No additional coatings were used on the pellet. Thus, each pellet was measured using two consecutive heating and cooling cycles. The Nyquist plots were modelled via an equivalent circuit approach using EC-Lab version 11.21. From this process, ionic conductivities of the materials were calculated over the temperature range studied.

3.3. Results and discussion

3.3.1. *In situ* investigation of the δ-phase formation using Raman spectroscopy

The cubic (δ) and tetragonal (β) bismuth oxide structures (Fig. 3.1) have inherently different Bi-O bond lengths and bond strengths which leads to different sets of Raman spectral features thus allowing the discrimination between these two structures. This was clearly shown in the study by Hardcastle and Wachs.[38] The tetragonal structured material produced three prominent bands corresponding to Bi-O stretches at 462, 311 and 124 cm^{-1} indicating a distorted octahedral arrangement. The cubic structure (obtained by doping with Nb^{5+} or Ta^{5+})[38] gave two broad bands at 550 and 320 cm^{-1} which were similarly assigned to Bi-O stretches in BiO_5 polyhedra. Group theory calculations, however, predict that the defect fluorite ($Fm\bar{3}m$) structure should only have one Raman-active mode corresponding to $\Gamma = F_{2g}$ for BiO_6 octahedra.[39] Subsequent studies have clearly shown the presence of a single band at ~630 cm^{-1} for the cubic δ-phase.[29,40] This band is generally broad due to the large extent of disorder. Prominent bands below 200 cm^{-1} are assigned to external lattice vibrations and thus were not further analysed.

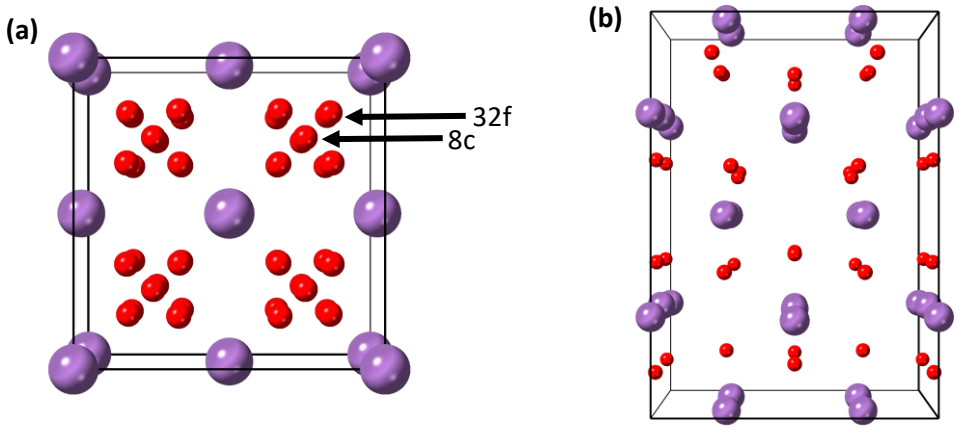

Figure 3.1. Unit cells for (a) the face-centred cubic δ-phase and (b) the tetragonal β-phase of bismuth oxide. Purple and red spheres represent the cation and anion sites, respectively. The δ-phase, a defect fluorite phase, is shown with all the possible 8c and 32f oxide positions.[7]

The room temperature Raman spectra collected of the samples that were simply calcined at 450 °C (Fig. 3.2a), indicate the presence of both the tetragonal and cubic phases. The apparent absence of the tetragonal phase for the 22.5YSB sample at room temperature is most likely due to the small sampling area and indicates sample inhomogeneity typical of phase mixtures. For spectra measured at 680 °C (Fig. 3.2b), the bands reflecting the tetragonal phase had disappeared for all doping ranges indicating a conversion to the cubic defect fluorite phase. On cooling back to ~30 °C (Fig. 3.2c) for the low dopant samples (10-15YSB), the reappearance of the most prominent peak for the tetragonal phase (at 311 cm^{-1}) indicated that the cubic phase was not fully stabilized. Figure 3.2d gives an example of an overall *in situ* heating experiment for the 17.5YSB sample demonstrating that the tetragonal phase is converted to the cubic phase somewhere between 510 and 680 °C.

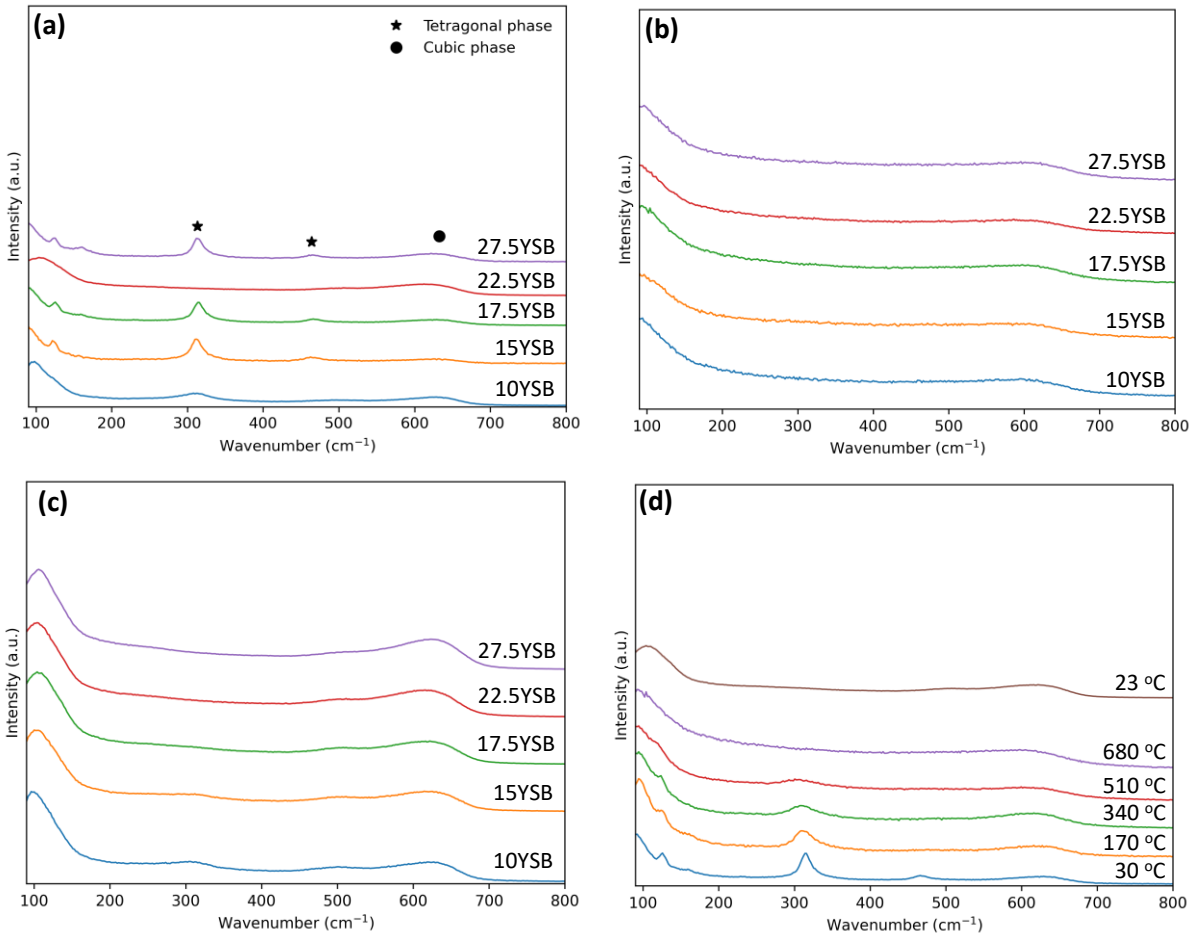

Figure 3.2. Raman spectra of the series YSB samples calcined at 450 °C collected at (a) room temperature (~23 °C) prior to undergoing any heating, (b) 680 °C during *in situ* heating and (c) upon cooling (~30 °C) after undergoing *in situ* heating measurements. A full variable temperature run is shown for 17.5YSB in (d).

An unexplained observation is the appearance of a low intensity diffuse band at ~500 cm^{-1} for all samples upon cooling (Fig. 3.2c) after the heating cycle. This is most likely due to the formation of an unidentified phase and not due to the disordering of the structure or the change in the number of oxygen vacancies.[29]

3.3.2. Ex situ and in situ investigations of the δ-phase formation using powder X-ray diffraction

As was observed from the Raman spectra (Fig. 3.2a), the diffraction patterns of all samples calcined at 450 °C exhibited a mixture of the tetragonal ($P4_2$/nmc, SG #137) and cubic ($Fm\bar{3}m$, SG #225) phases (Fig. 3.3a). From this data, which gives the average structure, the tetragonal phase is clearly present for the 22.5YSB sample. This corroborates that the apparent missing bands for the tetragonal phase for this sample (Fig. 3.2a) are due to sample inhomogeneity.

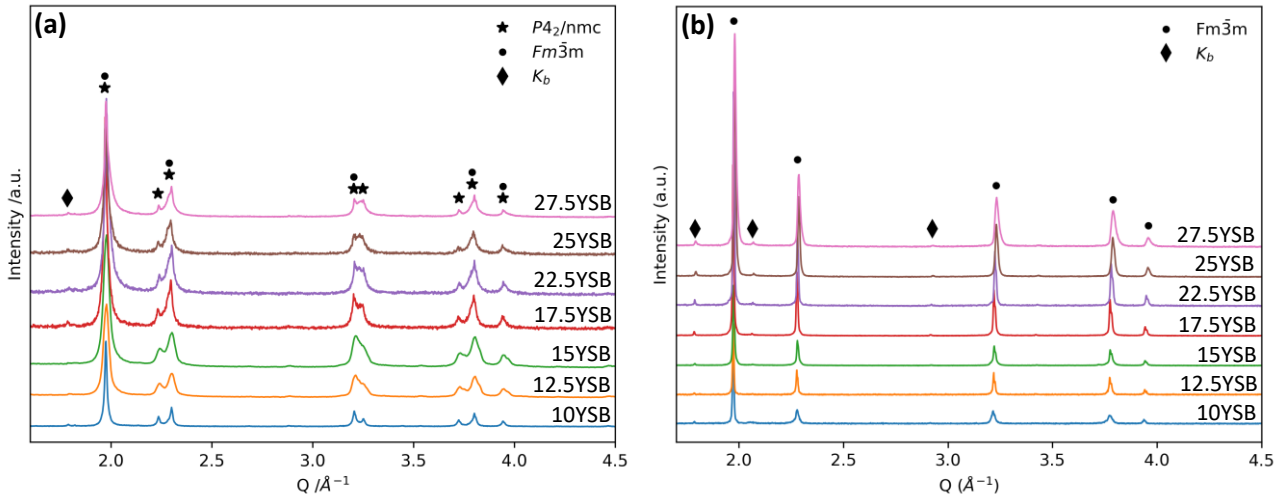

Figure 3.3. Room temperature diffractograms of the series YSB samples (a) calcined at 450 °C indicating mixtures of the tetragonal and cubic phases for all materials and (b) subsequently annealed at 750 °C showing all materials to predominantly consist of the cubic phase.

Rietveld refinements of these mixtures yielded key structural information for both phases (Table 3.1). This showed that there were no correlations between the unit cell volume and the dopant percentage when a mixture of phases was present. The significant overlap of tetragonal and cubic phase peaks, coupled with the limited resolution of the lab diffractometer, results in a degree of uncertainty in the reported lattice parameter values for the mixed phase materials. Additionally, the tetragonal phase content of the mixture significantly decreased with increasing dopant content. This indicates that higher dopant percentages favour cubic phase formation at lower temperatures.

Table 3.1. Variation of the phase composition (weight %) and cell parameters in the series of YSB materials. Values are given for both the tetragonal and cubic phases for the calcined samples, and for the dominant cubic phase for the annealed samples.

Sample	Calcined at 450 °C				Annealed at 750 °C	
	Tetragonal phase		Cubic phase		Cubic phase	
	a (Å)	c (Å)	a (Å)	Phase %	a (Å)	Phase %
10YSB	7.744(5)	11.270(6)	5.522(3)	30.7	5.536(5)	60.3
12.5YSB	7.748(7)	11.249(20)	5.503(4)	34.3	5.525(5)	69.4
15YSB	7.745(11)	11.258(26)	5.511(15)	42.9	5.522(2)	76.1
17.5YSB	7.744(9)	11.264(18)	5.508(7)	61.8	5.518(1)	92.9
22.5YSB	7.750(9)	11.269(7)	5.511(6)	75.4	5.512(1)	98.6
25YSB	7.750(12)	11.261(23)	5.503(8)	78.9	5.505(1)	100
27.5YSB	7.744(7)	11.261(15)	5.498(5)	80.8	5.500(3)	100

After further annealing these mixtures at 750 °C for 8 h, it is shown that the tetragonal phase readily converted to the cubic phase (Fig. 3.3b). However, on more critical analysis of the diffractograms, significant peak asymmetry and peak broadening was observed for the 10-22.5YSB samples, as revealed in Figure 3.4a for 10YSB. These features are indicative of tetragonal phase content,[30,41] which is in line with the results from the Raman spectra measured at ~30 °C upon cooling after the heating cycle (Fig. 3.2c). The phase content was quantified using Rietveld refinement (Table 3.1), and as expected, the tetragonal phase content shows a decrease with increasing dopant percentage. No tetragonal phase was detected above 22.5% Y^{3+} content as depicted in Figure 3.4b for 25YSB. This shows that significantly higher Y^{3+} content is required to stabilize the cubic phase than previously reported.[19,30] This again indicates that higher dopant percentages promote cubic phase purity, as was observed for the series of calcined samples (Table 3.1). Furthermore, for the largely phase pure samples the lattice parameter decreased linearly with increasing dopant percentage (Table 3.1), as predicted by Vegard's law.[42]

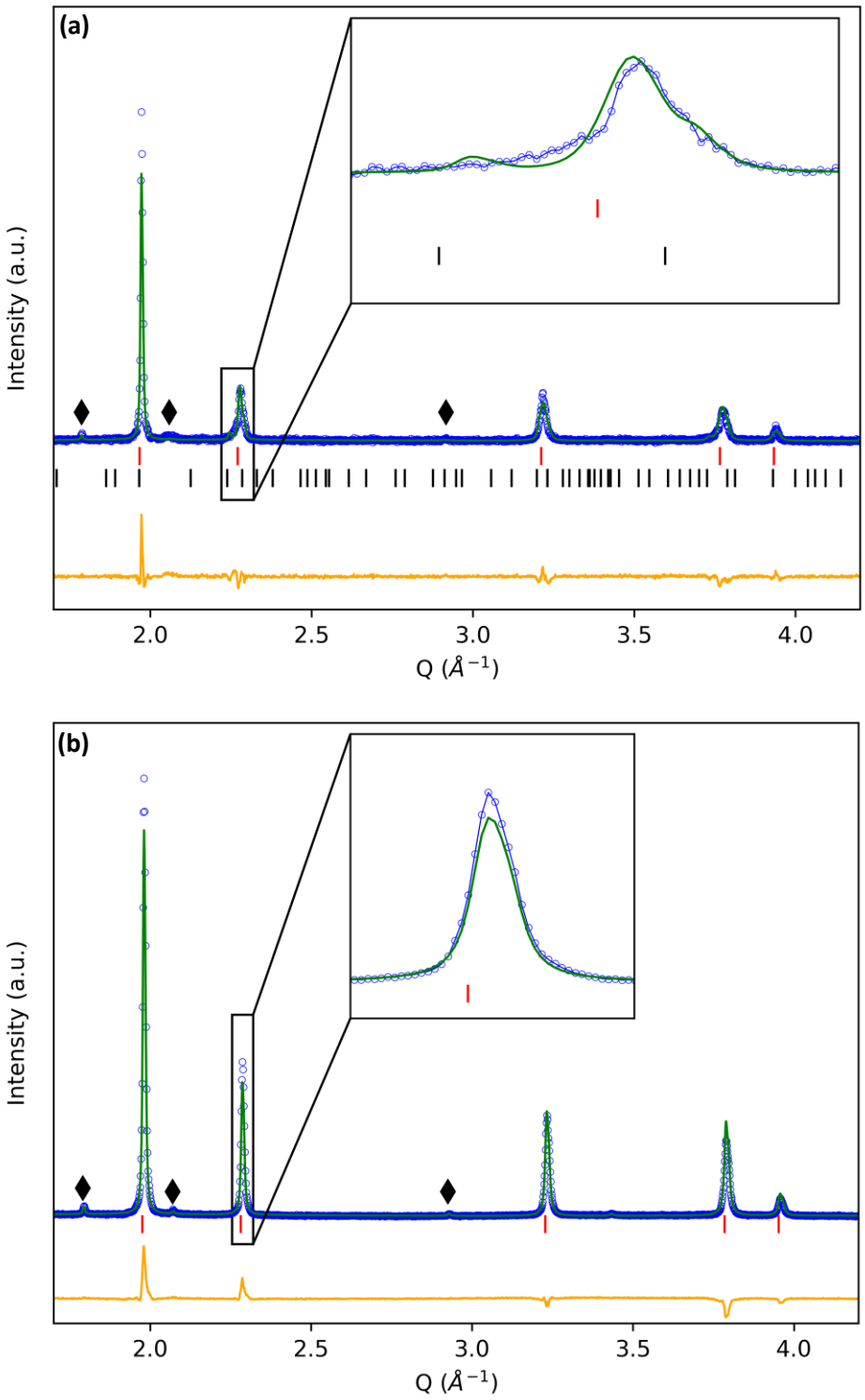

Figure 3.4. Diffractograms showing Rietveld refinement analysis for (a) 10YSB and (b) 25YSB, both annealed at 750 °C. The observed pattern is shown in blue, the calculated in green and the difference in orange. Miller indices corresponding to the cubic and tetragonal phases are shown with red and black ticks, respectively. The inset in (a) accentuates the peak asymmetry contribution from the presence of the tetragonal phase. K_β reflections are labelled with diamond markers.

Interestingly, for the 27.5YSB sample there also exists some peak asymmetry (Fig. 3.5) which is not related to the presence of the tetragonal phase. This could be indicative of either microstructural defects or an unidentified secondary phase (as was alluded to by the formation of a Raman band at ~500 cm^{-1} for all samples in Figure 3.2c). Further analysis of this anomaly is a key topic of ongoing work.

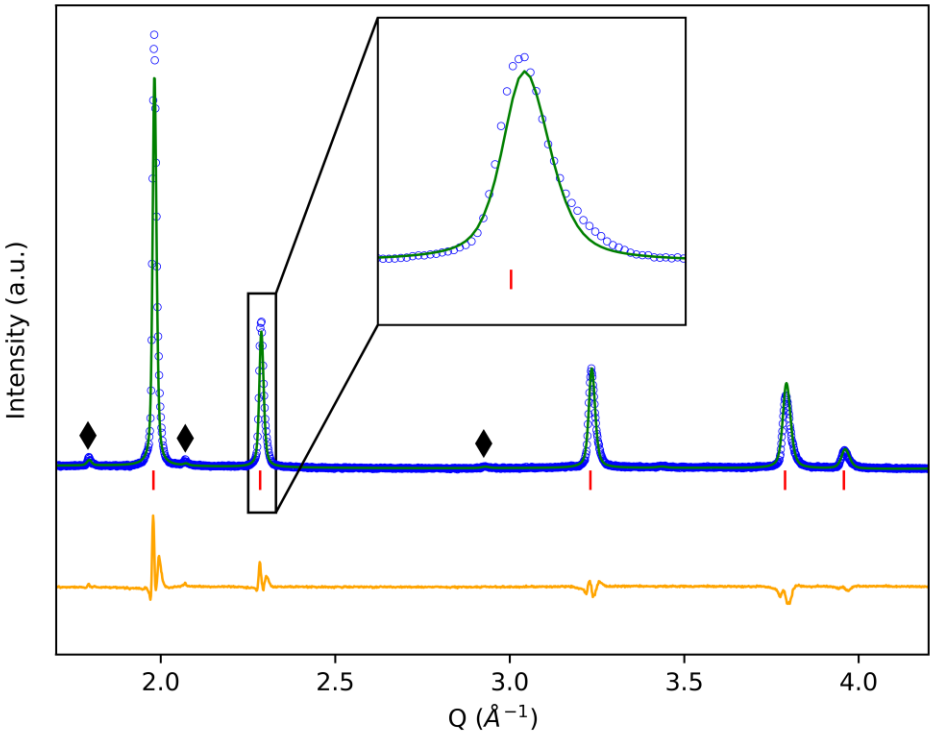

Figure 3.5. Diffractogram of the 27.5YSB sample annealed at 750 °C having been analysed by means of Rietveld refinement. The colour coding is as for Fig. 3.4 and the inset highlights the mismatch between the observed and calculated patterns due to peak asymmetry. K_β reflections are labelled with diamond markers.

Spontaneous room temperature phase transformations of these materials occur which are more pronounced for the low dopant samples and is the topic of as yet unpublished work. Therefore, samples were remade to perform impedance measurements to ensure no phase aging effects contribute to the electrochemical measurements. In this case a bismuth sub-carbonate phase (*I*mm2, SG #44) was additionally detected in the calcined materials (Fig. 3.6a). This phase arises from the initial presence of citrate which is driven off during the calcination step as CO_2. The incomplete calcination appears to form a sub-carbonate phase which is then fully converted upon annealing at 750 °C (Fig. 3.6b).

As before, the phase content was quantified for both the calcined and annealed samples using Rietveld refinement and similar trends in the lattice parameters were observed. Of interest here is the phase purity of the final annealed samples. For the 15-27.5YSB materials, the phase purity was reproducible between the first and second series of materials made. The 10YSB and 12.5YSB samples, however, showed reduced cubic phase purity (being 35.2 and 57.3%, respectively for this batch). This variation in cubic phase purity attributed to the presence of the sub-carbonate phase which is found to reduce cubic phase formation for low dopant content samples in yet unpublished work.

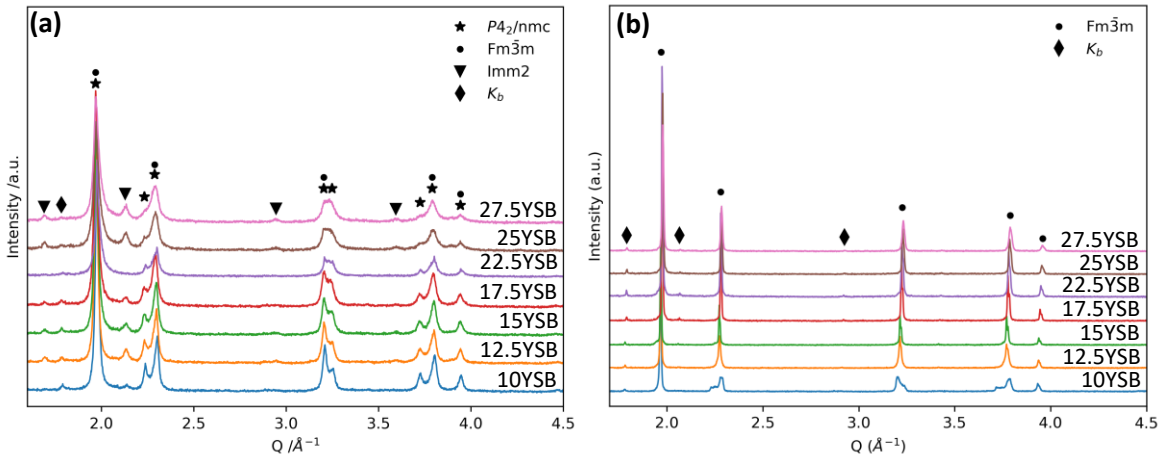

Figure 3.6. Room temperature diffractograms of a second series YSB samples (a) calcined at 450 °C and (b) subsequently annealed at 750 °C.

The average particle size for both batches of samples was ~185 nm, as derived from the PXRD Rietveld refinements. The particle size reported for powder Bi_2O_3 by Anilkumar *et al.*[43] (who also used the citrate sol-gel synthetic process) was ~100 nm from PXRD and ~50 nm from TEM. Tsuji *et al.*[44] (who used the conventional solid state synthetic method) reported a particle size of ~70 nm for yttrium doped Bi_2O_3 powder from PXRD Rietveld refinements. The solid state synthetic method requires far more grinding of samples and hence it is not surprising that the particle size is smaller in that case.

Calcined samples of selected compositions were again remade and studied *in situ* at ID-22 at the ESRF. The high resolution PXRD data of 17.5YSB (Fig. 3.7) and 15YSB (Fig. A1) clearly showed the predominantly tetragonal starting phase converting into the desired cubic phase upon heating. Throughout the heating cycle, impurity phases were present. Here too the bismuth sub-carbonate phase was initially present for 15YSB and 17.5YSB until ~390 °C. This indicates that a calcination temperature of 450 °C should be sufficient and perhaps longer calcination time should rather be implemented. Around 550-626 °C the

tetragonal phase disappears. This is in line with the observations made from the *in situ* Raman spectroscopy measurements which showed the tetragonal-cubic phase conversion taking place between 510-680 °C, but also provides a more accurate indication of the temperature range in which this conversion takes place and gives confidence that an annealing temperature of 750 °C is adequate. At higher temperatures trace quantities of unknown impurity metal oxides (likely Y_2O_3) were produced. These impurity phases largely disappeared at 769 °C and were also not prevalent in the *ex situ* samples when longer annealing times were used, however, their formation is noteworthy.

For 22.5YSB (Fig. A2), rhombohedral bismuth oxide ($R\bar{3}$m, SG #166) is initially present and no tetragonal phase content was detected. The rhombohedral phase was no longer detected by ~663 °C. The rhombohedral phase was not detected for any composition in both series of YSB materials previously synthesized. This rhombohedral phase is commonly formed when the Bi_2O_3 lattice is doped with large cations[45–47] and is not expected to be present in 22.5YSB based on the dopant radius. However, the rhombohedral phase does form when these materials are annealed for extended periods of time at temperatures below 700 °C.[48,49] This has not been reproduced in other samples of the same composition and hence it is suspected to be due to an inadvertent furnace failure with the set temperature program not necessarily being followed and annealing taking place at a lower temperature.

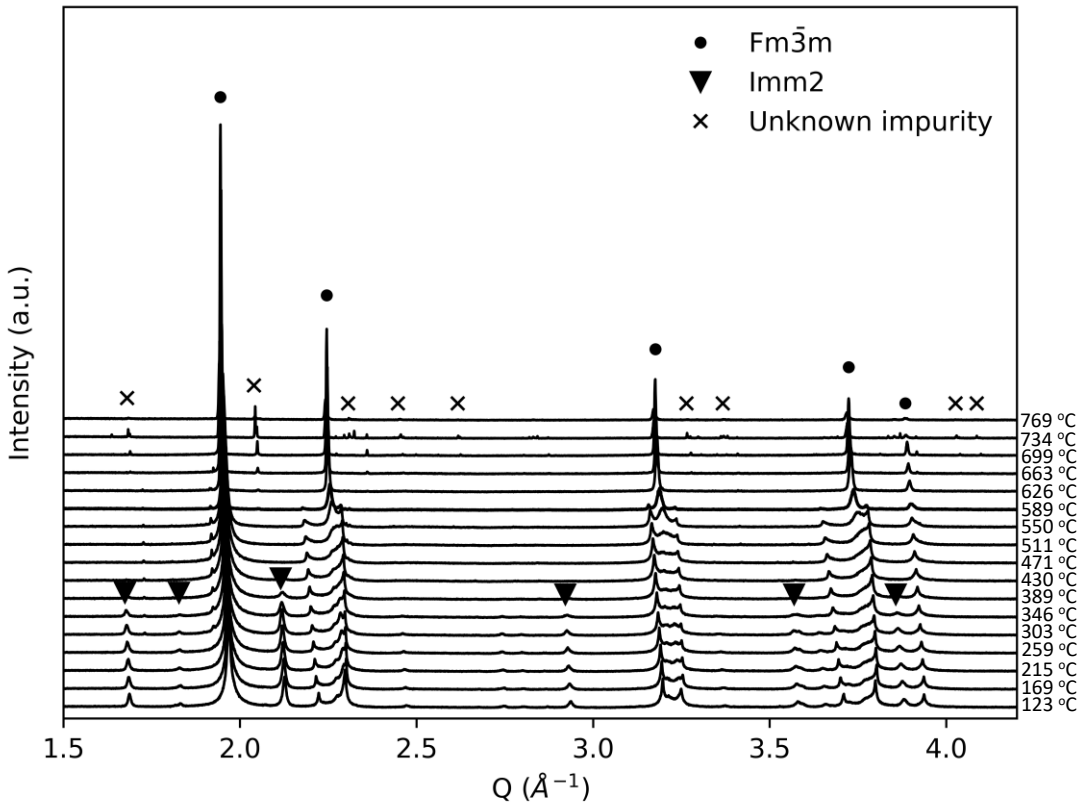

Figure 3.7. *In situ* diffractograms of the 17.5YSB sample calcined at 450 °C collected at ~40 °C intervals over the temperature range of 123-769 °C.

Between 589–769 °C a predominantly cubic phase was present and lattice parameter variations, as determined by Rietveld refinement for the three samples analysed, were employed to the establish the CTEs in this temperature range (Table 3.2). Wu *et al.*[29] found the CTE for 20YSB to vary depending on the temperature range studied. In the present work, all cubic phases studied exhibited a linear expansion in the temperature range considered. The CTEs of the YSB moieties were found to dramatically decrease with increasing Y^{3+} content. Even so, for all YSB compositions studied, the rate of thermal expansion was significantly higher than that for the commercially used YSZ electrolyte. This makes these materials unsuitable for application in a typical solid oxide fuel cell (SOFC) due to the immense thermal expansion mismatch with adjacent SOFC components as illustrated in Table 3.2.

Table 3.2. Comparison of CTEs determined for materials annealed at 750 °C studied in this work (determined between 589–769 °C) and those reported for currently used SOFC components.

Component	Material	CTE (10^{-6} K^{-1})	Ref.
Electrolyte	15YSB	152.4 ± 14.2	This work
Electrolyte	17.5YSB	78.5 ± 11.9	This work
Electrolyte	22.5YSB	27.1 ± 2.5	This work
Electrolyte	20YSB	15.4[a] and 20.3[b]	[29]
Electrolyte	8YSZ	10.5-10.9	[50]
Inter-connect	Ferritic steel, X10CrAl 18	12.9-13.9	[51]
Cathode	Perovskite, $La_{0.65}Sr_{0.3}MnO_3$	12.0-12.3	[50]
Anode	Cermet, 40 v/o Ni + 60 v/o 8YSZ	12.5-12.6	[51]

[a] CTE over the temperature range of 30-500 °C
[b] CTE over the temperature range of 500-800 °C

3.3.3. Analysis of conductivity using electrochemical impedance spectroscopy

Electrochemical impedance spectroscopy (EIS), used to determine the conductivity of these types of materials, has also proven to be extremely useful and sensitive in detecting phase changes when measurements are made as a function of temperature. Variable temperature-EIS was thus used to establish whether the extent of cubic phase purity obtained from the analysis of the XRD data was feasible.

Examples of Nyquist plots, as measured using EIS of the pelletized materials (initially annealed and then sintered at 750 °C), are displayed in Figures 3.8a - 3.8c. In the low temperature region (300-450 °C), data were modelled using an appropriate equivalent circuit as indicated in Figure 3.8d. In general, the spectra of all materials , whether it was found to be phase pure or not, displayed a single arc in the high frequency region which was fitted using a Randles circuit with R1 representing the electrolyte resistance. A constant phase element, Q1, was used to model this region indicating that the capacitances were distributed and $\alpha 1$ values ranged from ~0.7-0.8. This was required for both the mixed phase and pure cubic phased materials. R1 represents the total electrolyte resistance which incorporates the bulk and grain boundary resistance since no clear distinction could be made between these for these polycrystalline materials. Jung and Chung[52] has shown that bismuth oxide materials generally have negligible grain boundary resistance, but this cannot be confirmed here. At higher temperatures (500-750 °C) the data in the high frequency region was insufficient to model, thus the electrolyte resistance was approximated as the real impedance at point R1 indicated in Figure 3.8c. Bounded diffusion was clearly evident at the high temperatures.

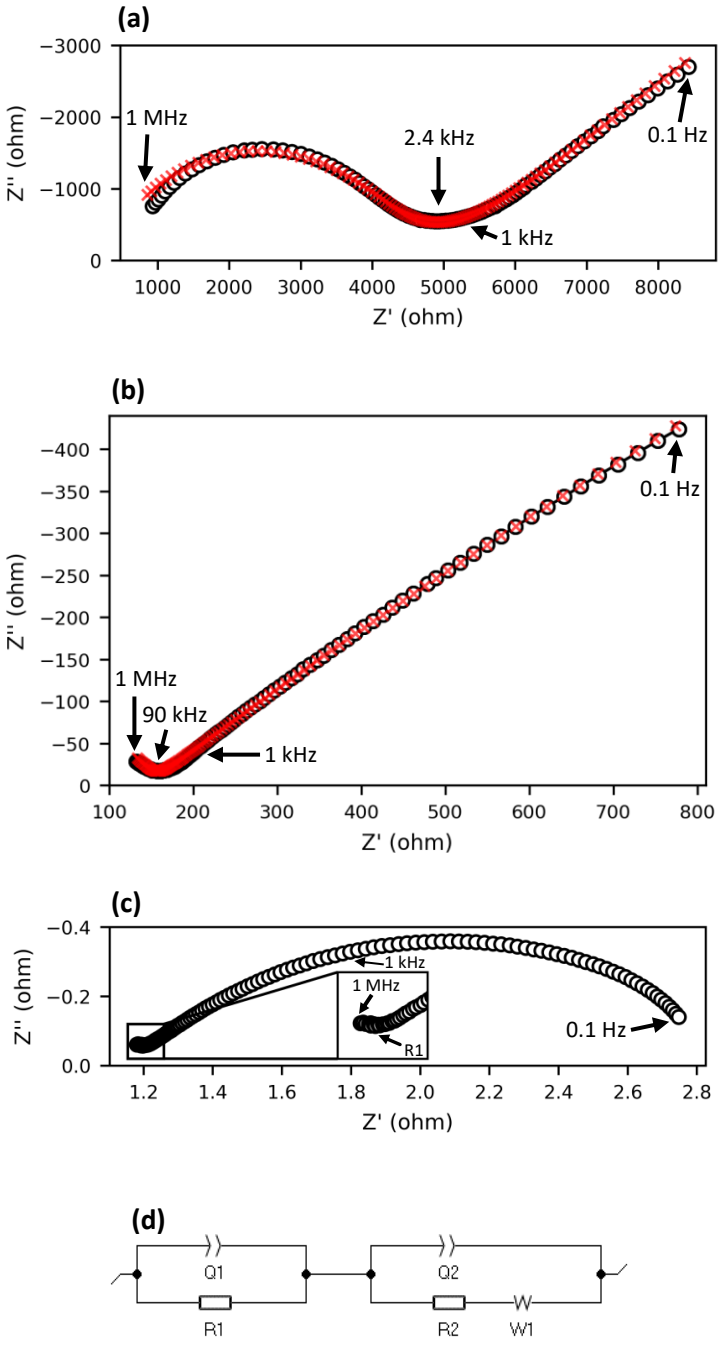

Figure 3.8. Typical impedance spectra from the second cycle of measurement for 27.5YSB annealed at 750 °C in air at (a) 350 °C and (b) 450 °C with the equivalent circuit fit shown with red markers, and at (c) 750 °C indicating the point where R1 was approximated when modelling was not possible. (d) The equivalent circuit used for modelling data in the 300-450 °C range.

As described in Section 3.2.4, the pelletized sample was sandwiched between two platinum discs, and two consecutive heating and cooling cycles were performed. The temperature dependent conductivity behaviour in the form of Arrhenius plots illustrated that the first cycle gave a large hysteresis between heating and cooling (Fig. 3.9). This was not the case for the second cycle, where the results also corresponded to those from the first cooling cycle, thus indicating that the pellet-to-electrode contact was optimized. Data from the second cycle thus served as the reported values. Even though this methodology may not produce the optimal conductivities, it is fully sufficient to investigate the extent to which phase changes occur, if at all.

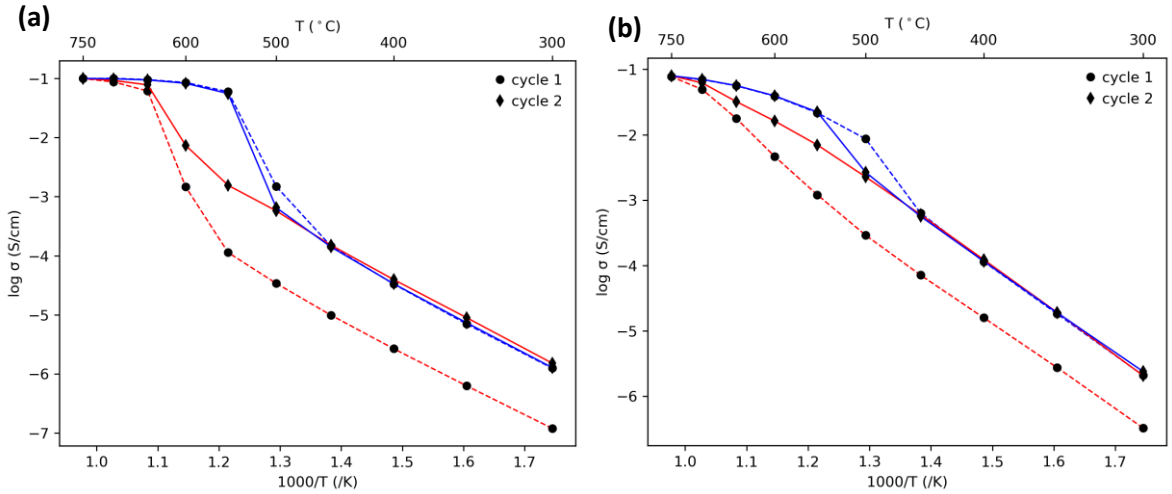

Figure 3.9. Arrhenius plots of (a) 10YSB and (b) 27.5YSB materials annealed at 750 °C in the temperature range of 300– 750 °C showing results from both the heating (red lines) and the cooling cycles (blue lines) from both measurements cycles.

As is expected from a thermally-activated conductivity mechanism that is inherent to ionic conducting ceramics, the conductivities were found to increase on heating and conversely, decrease on cooling. For the low dopant samples (10YSB, 12.5YSB and 15YSB in Figure 3.10a), it was noted that in the low temperature range, lower conductivities were observed which is clearly due to the presence of the tetragonal impurity phase still present in the annealed (at 750 °C) samples. Additionally, there is a prominent 'step function' type behaviour on both the heating and cooling cycles within the temperature range of 550–650 °C. This step is largely attributed to the conversion of the initial phase mixture into a pure cubic phase and the temperature range in which this occurs corresponds to the *in situ* phase transitions observed in both Raman spectroscopy and high resolution PXRD. The magnitude of this step is also directly related to the extent of the impurity phase present. The Arrhenius plot for 27.5YSB

(Fig. 3.10b), found to be a pure cubic phase, was linear until ~500 °C and the ensuing slight 'bend' at higher temperatures is attributed to the order-disorder transition. This order-disorder transition was noted for the low dopant samples after the phase transition step. The step in the conductivity thus confirms the presence of mixed cubic and tetragonal phases for 10-17.5YSB (Figs. 3.10a and 3.10b) as was also determined by the careful analysis of the diffraction patterns. A very small step was observed for 25YSB (Fig. 3.10b) even though it was found to be 100% pure from XRD refinements. This may reflect the presence of a less conductive phase present in the amorphous fraction of the material.

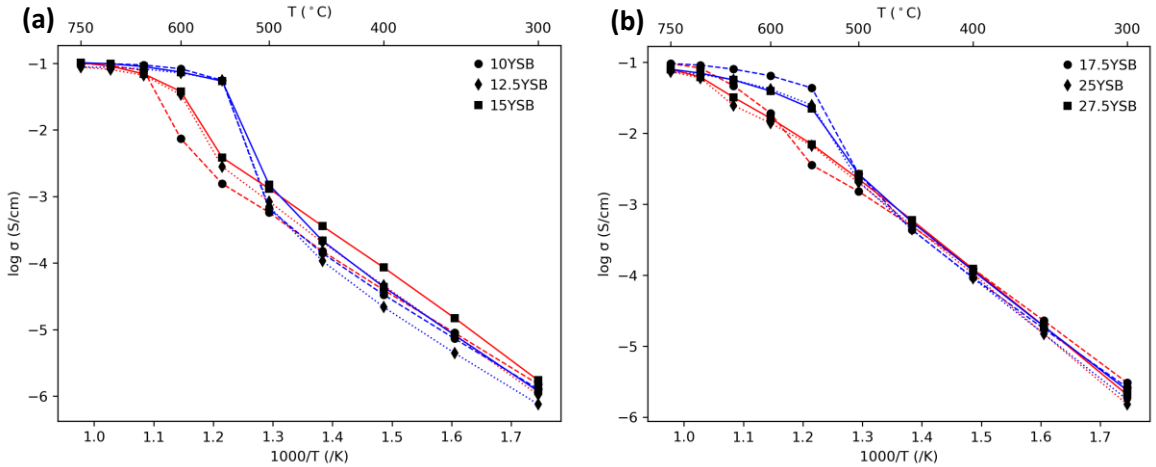

Figure 3.10. Arrhenius plots of (a) 10YSB, 12.5YSB, 15YSB and (b) 17.5YSB, 25YSB and 27.5YSB materials (annealed and sintered at 750 °C) showing results from both the heating (red lines) and the cooling cycles (blue lines).

A general trend of increasing activation energy of conduction with increasing dopant concentration was observed (Table 3.3). The 'step function' type behaviour results in a significant reduction in the activation energy at high temperature due to the formation of the highly conductive cubic phase and the occurrence of an order-disorder transition. However, the very low activation energies observed at high temperatures indicate some electronic conductivity which is unusual for cubic bismuth oxides. This phenomenon is currently under investigation. For the purer samples with higher Y^{3+} content, this feature is significantly less pronounced, if not absent, with only minor changes in activation energy during the heating and cooling cycles which are attributed to changes in the ordering of the oxygen sublattice.

Table 3.3. Activation energies of YSB materials annealed at 750 °C determined in regions over the temperature range of 300-750-300 °C.

Sample	E_a over 300-550 °C (eV)	E_a over 650-750 °C (eV)	E_a over 750-600 °C (eV)	E_a over 450-300 °C (eV)
10YSB	0.493	0.0889	0.0418	0.486
12.5YSB	0.558	0.102	0.0456	0.511
15YSB	0.545	0.139	0.0730	0.538
17.5YSB	0.504	0.259	0.0896	0.529
25YSB	0.594	0.393	0.128	0.572
27.5YSB	0.576	0.326	0.158	0.567

Ionic conductivities measured for YSB materials in previous studies are compared to those measured in this work at 600 °C and 750 °C (Table 3.4). At 750 °C both the 25YSB and 27.5YSB samples have lower conductivities in comparison to those found in previous studies. This discrepancy could be attributed to the different synthetic techniques (with either carbonate coprecipitation[26] or conventional solid state techniques[24,25] previously used) and pellet preparation methodologies used. However, more notable is the application of conductive electrodes, such as Pt, to the pellet surfaces prior to measurement.[24,25] As discussed, in the present work the pellet was sandwiched between two platinum discs of a similar diameter to the sample with no additional coating. Despite using data from the second heating and cooling cycle, this shows that these coatings clearly provide more initmate contact. A difference in measured conductivity is even dependent on the type of coating used, as demonstrated for 22.5YSB in Table 3.4, with Pt electrodes giving a higher conductivity compared to Ag electrodes.[53] It was also noted that certain conductivity values published for doped bismuth oxides at 750 and 800 °C are questionable since they exceed the benchmark of ~1 $S.cm^{-1}$ at 750 °C for pure Bi_2O_3.[54]

At 600 °C, the 25YSB and 27.5YSB samples exhibited conductivities that are also lower than the literature values on the heating cycle. However, for the cooling cycle the values obtained here are comparable to the literature values. This is due to the higher disordered state maintained on cooling to 600 °C. The state of disorder of the materials hence also affects the measured conductivity and further hinders a comparison to conductivity values found in literature. Therefore, in general, the comparison of the absolute conductivity values is challenging. The trends in the conductivities for a series of materials measured in the same manner, however, reveals very useful information.

Interestingly, markedly higher conductivities were measured at 800 °C. In the present work, measurements at this temperature were not possible due to the lower observed melting point of the materials (~780 °C). This is possibly a result of the synthetic methodology where it could be speculated

that features such as microstructure and crystallite size reduce the melting point of the material. Relating the conductivities reported in this work to that for YSZ and GDC (gadolinium-doped ceria), they were found to be comparable, and in some cases superior, to those at significantly lower temperatures (Table 3.4).

Table 3.4. Comparison of the ionic conductivity of YSB materials annealed and sintered at 750 °C studied in this work to that of singly doped electrolytes studied previously.

Composition	σ (S.cm^{-1})					Ref.
	600 °C[a]	600 °C[b]	750 °C	800 °C	1000 °C	
10YSB	0.0074	0.083	0.10	-	-	This work
12.5YSB	0.034	0.072	0.088	-	-	This work
15YSB	0.038	0.074	0.10	-	-	This work
17.5YSB	0.019	0.065	0.096	-	-	This work
25YSB	0.014	0.042	0.074	-	-	This work
27.5YSB	0.016	0.039	0.080	-	-	This work
20YSB	0.00525*	-	0.288	0.550	-	[19]
20YSB	0.0251	-	-	-	-	[55]
20YSB	-	-	-	1.97	-	[29]
22.5YSB	0.0193[#]	-	-	-	-	[53]
22.5YSB	0.0248[##]	-	-	-	-	[53]
22.5YSB	0.131	-	1.59	2.92	-	[25]
24YSB	0.08	-	-	0.56	-	[27]
25YSB	0.080	-	-	-	-	[24]
25YSB	0.077	-	0.27**	-	-	[26]
25YSB	0.0438	-	0.398	0.631	-	[25]
27.5YSB	0.0490	-	0.380	0.661	-	[25]
30YSB	0.0391	-	0.386	0.649	-	[25]
8YSZ	-	-	-	0.052	0.18	[56]
20GDC	-	-	-	0.096	0.25	[56]

[a] Conductivity measured during the heating cycle
[b] Conductivity measured during the cooling cycle
[*] Conductivity measured at 570 °C
[**] Conductivity measured at 700 °C
[#] Ag electrode painted onto pellet
[##] Pt electrode painted onto pellet

3.4. Conclusion

The variable temperature measurements using various techniques shows that the transition from a phase mixture to the δ-phase occurs around ~550–600 °C. This work also clearly shows that the δ-phase is not fully stabilised for the 10-22.5YSB materials and this establishes the dopant range in which the δ-phase is truly stabilized on synthesis. This was confirmed by results obtained from both Raman spectroscopy and PXRD. The assymetry of diffraction pattern peaks that is caused by the presence of secondary phases is

often overlooked in laboratory-based experiments.The VT-EIS measurements of these doped YSB materials (which were annealed and sintered at 750 ^{o}C) also indicated a phase change in the same temperature range, again reinforcing the presence of a phase mixture at lower temperatures.

By studying a series of YSB samples with varying dopant concentrations, it was seen that with increasing dopant concentration both the CTE and the conductivity decreased. EIS data and subsequent studies (not presented here) have also indicated that phase aging of the materials occur at room temperature, and is more pronounced for the lower dopant concentrations. This suggests that a compromise between optimum conductivity, minimal thermal expansion and phase degradation on aging would have to be considered. Based on the findings of this work, for the YSB system we predict that the optimum material for further investigation is 27.5YSB.

From the wide range of conductivies measured for the same dopant concentration, both here and reported in the literature, it can be concluded that the sample preparation and measurement strategies play a significant role in the absolute conductivity value. This is an issue that the community needs to address and provide clearer guidelines so that the results can be more directly compared.

3.5. Acknowledgments

The authors acknowledge financial support for their researh from the UKRI-GCRF START programme (Diamond Light Source, United Kingdom), National Research Foundation (NRF, South Africa) and Department of Science and Innovation (DSI, South Africa) as well as the University of the Witwatersrand. The authors are also grateful for the beamtime provided by the ESRF on ID22.

3.6. References

1. Punn, R., Feteira, A. M., Sinclair, D. C. and Greaves, C. Enhanced Oxide Ion Conductivity in Stabilized δ-Bi_2O_3. *J. Am. Chem. Soc.* **128**, 15386–15387 (2006).

2. Cahen, H. T., Van Den Belt, T. G. M., De Wit, J. H. W. and Broers, G. H. J. The electrical conductivity of δ-Bi_2O_3 stabilized by isovalent rare-earth oxides R_2O_3. *Solid State Ion.* **1**, 411–423 (1980).

3. Laarif, A. and Theobald, F. The lone pair concept and the conductivity of bismuth oxides Bi_2O_3. *Solid State Ion.* **21**, 183–193 (1986).

4. Boivin, J. C. and Mairesse, G. Recent Material Developments in Fast Oxide Ion Conductors. *Chem. Mater.* **10**, 2870–2888 (1998).

5. Battle, P. D., Catlow, C. R. A., Drennan, J. and Murray, A. D. The structural properties of the oxygen

conducting δ phase of Bi_2O_3. *J. Phys. C Solid State Phys.* **16**, 561–566 (1983).

6. Battle, P. D., Catlow, C. R. A., Heap, J. W. and Moroney, L. M. Structural and dynamical studies of δ-Bi_2O_3 oxide ion conductors. I. The structure of $(Bi_2O_3)_{1-x}(Y_2O_3)_x$ as a function of x and temperature. *J. Solid State Chem.* **63**, 8–15 (1986).

7. Liu, X., Abrahams, I., Hull, S., Norberg, S.T., Holdynski, M., and Krok, F. A neutron total scattering study of defect structure in $Bi_3Nb_{0.5}Y_{0.5}O_{6.5}$. *Solid State Ion.* **192**, 176–180 (2011).

8. Abrahams, I., Liu, X., Hull, S., Norberg, S.T., Krok, F., Szmigiel-Kozanecka, A., Islam, M.S. and Stokes, S.J. A combined total scattering and simulation approach to analyzing defect structure in Bi_3YO_6. *Chem. Mater.* **22**, 4435–4445 (2010).

9. Borowska-Centkowska, A., Liu, X., Krynski, M., Leszczynska, M., Wrobel, W., Malys, M., Hull, S., Norberg, S.T., Krok, F., and Abrahams, I. Defect structure in δ-$Bi_5PbY_2O_{11.5}$. *RSC Adv.* **9**, 9640–9653 (2019).

10. Stambouli, A. B. and Traversa, E. Solid oxide fuel cells (SOFCs): A review of an environmentally clean and efficient source of energy. *Renew. Sustain. Energy Rev.* **6**, 433–455 (2002).

11. Ruiz-Morales, J. C., Marrero-Lopez, D., Galvez-Sanchez, M., Canales-Vazquez, J., Savaniu, C. and Savvin, S.N. Engineering of materials for solid oxide fuel cells and other energy and environmental applications. *Energy Environ. Sci.* **3**, 1670–1681 (2010).

12. Zuo, C., Liu, M. and Liu, M. Solid Oxide Fuel Cells, in *Sol-Gel Processing for Conventional and Alternative Energy*, (M. Aparicio, A. Jitianu, L. C. Klein eds.), vol. 5, 1st edn., Springer, New York, USA, pp. 7-37 (2012).

13. Haile, S. M. Fuel cell materials and components. *Acta Mater.* **51**, 5981–6000 (2003).

14. Fergus, J. W. Electrolytes for solid oxide fuel cells. *J. Power Sources* **162**, 30–40 (2006).

15. Shuk, P. Oxide ion conducting solid electrolytes based on Bi_2O_3. *Solid State Ion.* **89**, 179–196 (1996).

16. Sammes, N. M., Tompsett, G. a., Näfe, H. and Aldinger, F. Bismuth based oxide electrolytes—structure and ionic conductivity. *J. Eur. Ceram. Soc.* **19**, 1801–1826 (1999).

17. Berezovsky, J., Liu, H. K. and Dou, S. X. Conductivity and microstructure of bismuth oxide-based electrolytes with enhanced stability. *Solid State Ion.* **66**, 201–206 (1993).

18. Jiang, N., Wachsman, E. D. and Jung, S. H. A higher conductivity Bi_2O_3-based electrolyte. *Solid State Ion.* **150**, 347–353 (2002).

19. Kale, K. V., Jadhav, K. M. and Bichile, G. K. Investigations on a high-conductivity solid electrolyte system, Bi_2O_3-Y_2O_3. *J. Mater. Sci. Lett.* **18**, 9–11 (1999).

20. Takahashi, T., Esaka, T. and Iwahara, H. High oxide ion conduction in the sintered oxides of the system Bi_2O_3-Gd_2O_3. *J. Appl. Electrochem.* **5**, 197–202 (1975).

21. Keizer, K., Verkerk, M. J. and Burggraaf, A. J. Preparation and properties of new oxygen ion conductors for use at low temperatures. *Ceramurg. Int.* **5**, 143–147 (1979).

22. Jung, D. W., Lee, K. T. and Wachsman, E. D. Terbium and tungsten co-doped bismuth oxide electrolytes for low temperature solid oxide fuel cells. *J. Korean Ceram. Soc.* **51**, 261–264 (2014).

23. Verkerk, M. J., Keizer, K. and Burggraaf, A. J. High oxygen ion conduction in of the Bi_2O_3-Er_2O_3 system sintered oxides. *J. Appl. Electrochem.* **10**, 81–90 (1980).

24. Takahashi, T., Iwahara, H. and Arao, T. High Oxide Ion Conduction in Sintered Oxides of the System Bi_2O_3-Y_2O_3. *J. Appl. Electrochem.* **5**, 187–195 (1975).

25. Wang, C., Xu, X. and Li, B. Ionic and electronic conduction of oxygen ion conductors in the Bi_2O_3-Y_2O_3 system. *Solid State Ion.* **13**, 135–140 (1984).

26. Lee, J. G., Kim, S. H. and Yoon, H. H. Synthesis of yttria-doped bismuth oxide powder by carbonate coprecipitation for IT-SOFC electrolyte. *J. Nanosci. Nanotechnol.* **11**, 820–823 (2011).

27. Wang, S.-F., Hsu, Y.-F., Tsai, W.-C. and Lu, H.-C. The phase stability and electrical conductivity of Bi_2O_3 ceramics stabilized by Co-dopants. *J. Power Sources* **218**, 106–112 (2012).

28. Zhang, X. J., Jin, W. T., Hao, S. J., Zhao, Y. and Zhang, H. Study of the crystal structures of new buffer materials $Bi_{1-x}Y_xO_{1.5}$. *J. Supercond. Nov. Magn.* **23**, 1011–1014 (2010).

29. Wu, Y. C., Chang, Y. W. and Wang, S. F. Electrical properties and microstructural analysis of aliovalent-ion (Y^{3+}, Nb^{5+})-doped bismuth-based solid-oxide electrolyte. *Ferroelectrics* **455**, 123–128 (2013). 30. X. Liu, A. Staubitz, T. M. Gesing, Thermochromic Behavior of Yttrium-Substituted Bismuth Oxides, *ACS Appl. Mater. Interfaces*, 2019, **11**, 33147–33156

31. Danks, A. E., Hall, S. R. and Schnepp, Z. The evolution of 'sol-gel' chemistry as a technique for materials synthesis. *Mater. Horizons* **3**, 91–112 (2016).

32. Grazulis, S., Chateigner, D., Downs, R.T, Yokochi, A.F.T., Quiros, M., Lutterotti, L., Manakova, E., Butkus, J., Moeck, P. and Le Bail, A. Crystallography Open Database - An open-access collection of crystal structures. *J. Appl. Crystallogr.* **42**, 726–729 (2009).

33. Coelho, A. A. TOPAS and TOPAS-Academic: An optimization program integrating computer algebra and crystallographic objects written in C++: An. *J. Appl. Crystallogr.* **51**, 210–218 (2018).

34. Dinnebier, R. E., Leineweber, A. and Evans, J. S. O., eds., *Rietveld Refinement Practical Powder Diffraction Pattern Analysis Using Topas*, vol. 1, 1st edn., Walter de Gruyter GmbH, Berlin/Boston, 2019, pp. 16-129

35. Cheary, R. W., Coelho, A. A. and Cline, J. P. Fundamental parameters line profile fitting in laboratory diffractometers. *J. Res. Natl. Inst. Stand. Technol.* **109**, 1–25 (2004).

36. Cheary, R. W. and Coelho, A. A. Axial Divergence in a Conventional X-ray Powder Diffractometer. I. Theoretical Foundations. *J. Appl. Crystallogr.* **31**, 851–861 (1998).

37. Thompson, P., Cox, D. E. and Hastings, J. B. Rietveld Refinement of Debye-Scherrer Synchrotron X-ray Data from Al_2O_3. *J. Appl. Crystallogr.* **20**, 79–83 (1987).

38. Hardcastle, F. D. and Wachs, I. E. The molecular structure of bismuth oxide by Raman spectroscopy. *J. Solid State Chem.* **97**, 319–331 (1992).

39. de los Reyes, M., Whittle, K.R., Zhang, Z., Ashbrook, S.E., Mitchell, M.R., Jang, L. and Lumpkin, G.R. The pyrochlore to defect fluorite phase transition in $Y_2Sn_{2-x}Zr_xO_7$. *RSC Adv.* **3**, 5090 (2013).

40. Rubbens, A., Drache, M., Roussel, P. and Wignacourt, J. P. Raman scattering characterization of bismuth based mixed oxides with Bi_2O_3 related structures. *Mater. Res. Bull.* **42**, 1683–1690 (2007).

41. Arasteh, S., Maghsoudipour, A., Alizadeh, M. and Nemati, A. Effect of Y_2O_3 and Er_2O_3 co-dopants on phase stabilization of bismuth oxide. *Ceram. Int.* **37**, 3451–3455 (2011).

42. Denton, A. R. and Ashcroft, N. W. Vegard's law. *Phys. Rev. A* **43**, K117–K118 (1991).

43. Anilkumar, M., Pasricha, R. and Ravi, V. Synthesis of bismuth oxide nanoparticles by citrate gel method. *Ceram. Int.* **31**, 889–891 (2005).

44. Tsuji, K., Herisson De Beauvoir, T., Ndayishimiye, A., Wang, K. and Randall, C. A. Cold sintering of yttria-stabilized cubic bismuth oxide: Conductivity and microstructural evolution of metastable grain boundaries with annealing. *J. Appl. Phys.* **128**, (2020).

45. Jolley, A. G., Jayathilake, R. and Wachsman, E. D. Optimizing rhombohedral Bi_2O_3 conductivity for low temperature SOFC electrolytes. *Ionics (Kiel).* **25**, 3531–3536 (2019).

46. Takahashi, T., Iwahara, H. and Nagai, Y. High oxide ion conduction in sintered Bi_2O_3 containing SrO, CaO or La_2O_3. *J. Appl. Electrochem.* **2**, 97–104 (1972).

47. Iwahara, H., Esaka, T., Sato, T. and Takahashi, T. Formation of high oxide ion conductive phases in the sintered oxides of the system Bi_2O_3-Ln_2O_3 (Ln = La-Yb). *J. Solid State Chem.* **39**, 173–180 (1981).

48. Joshi, A. V., Kulkarni, S., Nachlas, J., Diamond, J. and Weber, N. Phase stability and oxygen transport characteristics of yttria- and niobia-stabilized bismuth oxide. *J. Mater. Sci.* **25**, 1237–1245 (1990).

49. Fung, K. Z. and Virkar, A. V. Phase Stability, Phase Transformation Kinetics, and Conductivity of Y_2O_3-Bi_2O_3 Solid Electrolytes Containing Aliovalent Dopants. *J. Am. Ceram. Soc.* **74**, 1970–1980 (1991).

50. Tietz, F. Thermal expansion of SOFC materials. *Ionics (Kiel).* **5**, 129–139 (1999).

51. Tietz, F. Innovative materials in advanced energy technologies, in Proc. 9th CIMTEC - World Ceramic Congress and Forum on New Materials, (P. Vincenzini, ed.), vol. 24, Techna Publishers S.r.l., Faenza, Italy, 1999, pp. 61

52. Jung, H. J. and Chung, S. Y. Absence of distinctively high grain-boundary impedance in polycrystalline cubic bismuth oxide. *J. Korean Ceram. Soc.* **54**, 413–421 (2017).

53. Meng, G., Zhou, M. and Peng, D. A new phenomenon - the inductive impedance in Bi_2O_3 based oxygen ionic conductors. *Solid State Ion.* **18**, 756–760 (1986).

54. Harwig, H. A. and Gerards, A. G. Electrical properties of the α, β, γ, and δ phases of bismuth sesquioxide. *J. Solid State Chem.* **26**, 265–274 (1978).

55. Changzhen, W., Xiuguang, X. and Baozhen, L. Ionic and electronic conduction of oxygen ion conductors in the Bi_2O_3-Y_2O_3 system. *Solid State Ion.* **13**, 135–140 (1984).

56. Badwal, S. P. S. and Ciacchi, F. T. Oxygen-ion conducting electrolyte materials for solid oxide fuel cells. *Ionics (Kiel).* **6**, 1–21 (2000).

Chapter 4. Investigating the ambient and thermal phase stability of $Y_xBi_{2-x}O_3$ electrolytes

M.A. Kiefer[a,c], Caren Billing[a,c*], Daniel Olds[b], David G. Billing[a,c]

[a]Molecular Science Institute, School of Chemistry, University of the Witwatersrand, Private Bag X3, Johannesburg, 2050, South Africa

[b]National Synchrotron Light Source II, Brookhaven National Laboratory, PO Box 5000, Upton, NY, 11973, USA

[c]DSI-NRF Centre of Excellence in Strong Materials, University of the Witwatersrand, Private Bag X3, Johannesburg, 2050, South Africa.

This chapter has been prepared for submission and has been formatted accordingly.

Abstract

The phase stability of yttrium-stabilized Bi_2O_3 materials was investigated over prolonged periods of time under ambient conditions and following different thermal treatments. The cubic and tetragonal polymorphs that initially appeared to be stabilized were actually found to be metastable under ambient conditions and spontaneous formation of both the rhombohedral and subcarbonate phases was evident. Pelletization with additional sintering as well as annealing under an inert atmosphere were shown to enhance the long term cubic phase stability. The thermal expansion behaviour observed for high yttrium content (27.5%) material was non-linear and for lower yttrium content (15%) material an abrupt increase in the cubic phase unit cell volume was observed possibly indicating an unidentified phase change during the thermal cycle.

Keywords: Bismuth oxide; Crystal structure; Phase stability; Thermal expansion

4.1. Introduction

The phase stability of cubic δ-phase bismuthates have been the subject of substantial research towards the implementation of these materials as solid oxide fuel cell (SOFC) electrolytes. These studies effectively monitor the change in δ-phase purity of a sample under the typical operating conditions of a SOFC. These conditions typically involve extended periods of time at elevated temperatures (~500-1000 °C)[1–4]. It has been demonstrated that the δ-phase transforms into a variety of phases which are correlated to the dopant composition. Erbium-stabilized bismuthates (12.5-15 mol% Er_2O_3) show δ-phase aging into a mixture of various natural Bi_2O_3 polymorphs[5] when annealed for 250 h at 625 °C.[6] Similar phase mixtures were found for a dysprosium-stabilized bismuthate (32.5 mol% Dy_2O_3) when annealed for 300-422 h at 815-819 °C.[7] Terbium-stabilized bismuthates (25 mol% Tb_4O_7) showed δ-phase conversion into the rhombohedral phase[8,9] when annealed for 120 h at 500 °C.[2] The δ-phase yttrium-stabilized bismuthates are significantly less stable when annealed at lower temperatures – studies by Takahashi *et al.*[10] showed that annealing an yttrium-stabilized bismuthate (20 mol% Y_2O_3) sample for 24 h at 500 °C produced significant phase transformations. Yttrium-stabilized bismuthates (25 mol% Y_2O_3) also underwent a transformation from the δ-phase to the rhombohedral phase, which occurred rapidly after annealing for 100-150 h at 600 °C.[11,12] Interestingly, when simultaneously stabilized with two dopants, the phase aging outcome and onset was significantly altered[2,12–15] and could be inhibited for ~1000 h at 600 °C in the yttrium-stabilized bismuthate system (25 mol% Y_2O_3) with the addition of 2 mol% ZrO_2.[12] In the erbium-stabilized bismuthate system (20 mol% Er_2O_3), similar inhibition was achieved for ~400 h at 600 °C with the additional of 5 mol% ZrO_2.[16]

The metastability of δ-phase yttrium-stabilized bismuthates was reported by Watanabe[17] and Watanabe and Kikuchi.[18] It was postulated that stabilized δ-phases were not thermodynamically stable but rather quenched high temperature stable phases that are metastable at room temperature.[17,18] This was investigated via two approaches. Firstly, solid solutions containing 21.5-23.5 mol% Y_2O_3 were reacted at 650 °C for >100 h. For these materials a rhombohedral phase was formed. Secondly, 'stabilized' δ-phases within the same compositional range were synthesized by solid-state reaction at 850 °C for 20 h. These δ-phases were thereafter annealed at 650 °C for >160 h and found to completely transform into the rhombohedral phase. From this, the metastability of the δ-phase at room temperature was proposed. However, these studies do not conclusively indicate δ-phase metastability at room temperature. The reaction temperature of 650 °C for solid solutions is likely to be too low to form the δ-phase and the high temperature annealing of the δ-phase can promote the cubic-rhombohedral phase transformation.

A true investigation of the metastability of the δ-phase at room temperature would involve monitoring phase purity changes of stabilized δ-phase materials under ambient conditions for extended periods of time and this is done for the first time in this work. The metastability of several δ-phase and δ+β-phase mixtures are investigated under ambient conditions over extended time periods and two methods to enhance the ambient, long term stability of the δ-phase are investigated. The phase stability and thermal expansion behaviour, another critical factor which is not frequently investigated, of selected δ-phase materials are additionally investigated during thermal cycling.

4.2. Materials and Methods

4.2.1. Synthesis and sample preparation

All samples were prepared by means of a citrate sol-gel process.[19] Stoichiometric amounts of bismuth nitrate pentahydrate ($Bi(NO_3)_3.5H_2O$, 99.99% pure, Aldrich) and yttrium nitrate hexahydrate ($Y(NO_3)_3.6H_2O$, 99.8% pure, Aldrich) were dissolved in glacial acetic acid (98% pure, MK Chemical, 99%) under moderate heating and stirring. Aqueous solutions were avoided to prevent the hydrolysis of Bi^{3+}.[19] Excess citric acid monohydrate ($C_6H_8O_7.H_2O$, ACS reagent, Aldrich) was added and the resulting mixture evaporated to form a metal complex precursor paste. Finally, the dried precursor was calcined at 450 °C for 18 h to obtain the $Y_xBi_{2-x}O_3$ powders. One portion was ground into a fine powder using an agate mortar and pestle and then annealed at 750 °C for 8 h. Another portion of the annealed sample was used for the non-ambient δ-phase stability studies. A range of samples were prepared with a dopant concentration of 10 – 27.5% Y^{3+} and are labelled to reflect the doping concentration, with a 10% Y_2O_3 stabilized Bi_2O_3 sample called 10YSB (yttria stabilized bismuth oxide). Two unique batches of annealed samples of identical composition were made and are labelled as batch (a) and batch (b) to reflect this.

Pellets were prepared for stability studies by mixing the annealed powders with a 2% polyvinyl alcohol solution (as a binder) and thereafter drying at 120 °C for 20 min. The resulting powder was then uniaxially pressed at 100 kPa into pellets using a 5 mm diameter die to produce pellets of ~0.85 mm thickness. The pellets were heated at 250 °C for 4 h to remove the binder and then sintered at 750 °C for 4 h.

4.2.2. Powder X-ray diffraction

Powder diffractograms of the δ and δ+β-mixed phase materials were collected at the Pair-Distribution Function (PDF) beamline (λ = 0.1671 Å) at the National Synchrotron Light Source II (NSLS-II). Each 2D diffractogram was collected for 30 seconds and then reduced into 1D diffraction data using Fit2D.[20] Room temperature powder X-ray diffractograms of samples stored as pellets were additionally collected at room temperature on a Bruker D2 phaser using iron filtered CoK_α radiation (λ = 1.7887 Å). A Bruker D8 Advance,

using a Göbel mirror to provide pseudo-parallel CuK_α radiation (λ = 1.5404 Å) and a VÅNTEC detector equipped with an Anton Paar XRK-900 reaction chamber, was used to collect *in situ* variable-temperature powder X-ray diffraction data. Diffractograms were collected at ~30 °C intervals in the range 27-706-27 °C.

Phase identification of diffractograms was done using Bruker AXS DIFFRAC.EVA V4.2 linked to the crystallography open database (COD)[21]. Rietveld refinement of the diffractograms was done using Bruker AXS TOPAS-Academic Version 6.[22] For the refinements of all the diffractograms collected, the instrument resolution function (IRF)[23] was determined using NIST 660a (LaB_6). For the calibration of all instruments, the IRF was described using the Thompson Cox Hastings (TCHZ) Pseudo-Voight function[24] with the divergence-related asymmetry effects described in an empirical way using the simple axial model.[23] The set temperature range of 30-810-30 °C used for the lab-based diffractograms collected *in situ* was calibrated using standard reference material 640d (Si powder)[25] and applying thermal lattice expansion corrections to the temperature profile[26,27] resulting in a corrected temperature range of 27-706-27 °C. In each refinement, the parameters refined were the scale factors, selected corrections, and lattice parameters. Atomic positional parameters were fixed to those published for the respective crystal structures and atomic thermal parameters were fixed to reasonable values.

4.3. Results and discussion

4.3.1. *Ex situ* investigation of the phase stability of calcined δ+β-mixed phase materials under ambient conditions using powder X-ray diffraction

When yttrium-stabilized bismuthates with Y^{3+} content between 10-27.5% are calcined at 450 °C for 18 h, β-tetragonal ($P4_2$/nmc, SG #137) and δ-cubic ($Fm\bar{3}m$, SG #225) phase mixtures were detected using a laboratory diffractometer.[28] In this work, yttrium-stabilized bismuthates synthesized in the same manner were analysed via synchrotron-based measurements. The increased resolution and detection limits allowed the identification of two additional phases in trace quantities (for 10-25YSB) in the synthesized samples, namely, a rhombohedral ($R\bar{3}m$, SG #166) bismuth oxide phase, and an orthorhombic (*I*mm2, SG #44) bismuth subcarbonate phase (for 10-25YSB). The crystal structure of bismuth subcarbonate ($Bi_2O_2CO_3$), more commonly known as the mineral bismutite, was first reported by Grice.[29] This structure comprises alternating layers of $(Bi_2O_2)^{2+}$ and isolated $(CO_3)^{2-}$ planar groups (Fig. 4.1).[30]

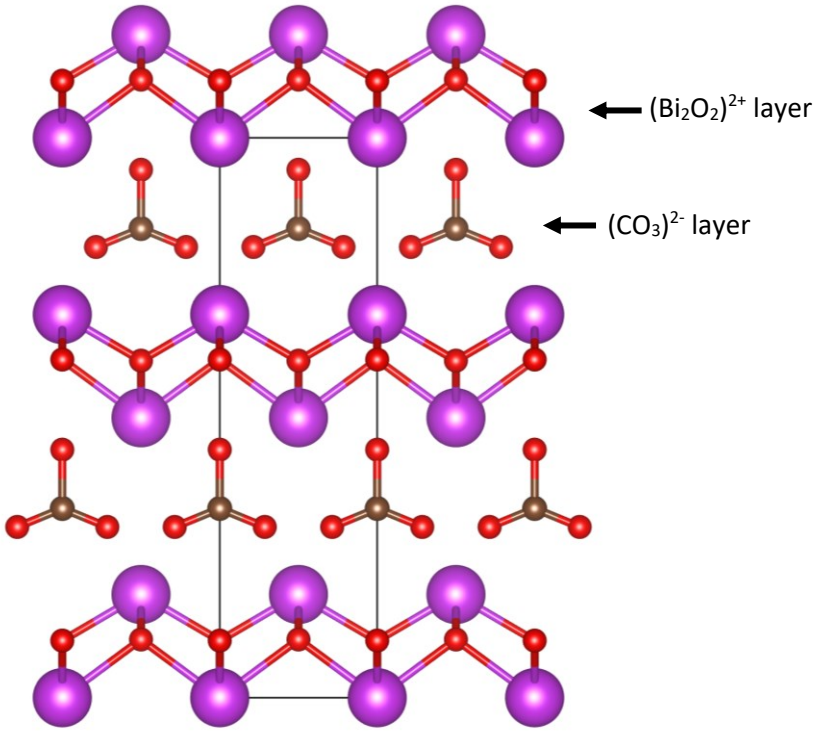

Figure 4.1. Crystal structure of bismuth subcarbonate ($Bi_2O_2CO_3$). Purple, bronze and red spheres represent bismuth, carbon and oxygen ions, respectively.[29]

When these calcined materials were stored in powder form under ambient conditions for extended periods of time, spontaneous phase transformations occurred (Fig. 4.2) which were quantified using Rietveld refinement analysis (Table 4.1). The Rietveld analysis of the calcined 10YSB material aged for a period of 35 months is given in Figure 4.3 as an example.

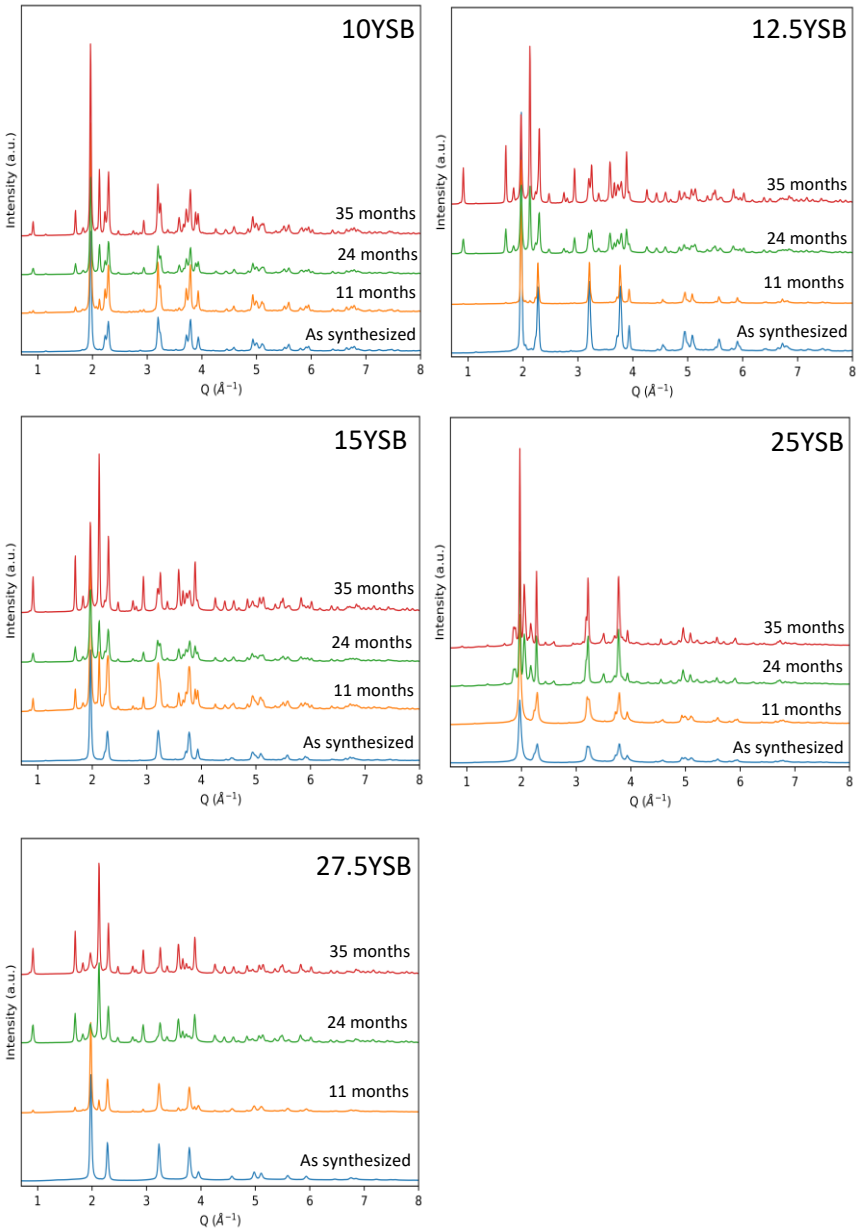

Figure 4.2. Room temperature diffractograms of the series of YSB samples calcined at 450 °C. The diffractograms collected after the initial materials were synthesized are shown in blue. The diffractograms collected after the materials were stored in powdered form under ambient conditions for 11, 24 and 35 months are shown in orange, green and red, respectively.

Table 4.1. Variation of the phase composition (weight %) in the series of YSB materials calcined at 450 °C stored under ambient conditions.

Sample	Phase composition (weight %)			
	Cubic ($Fm\bar{3}m$)	Tetragonal ($P4_2/nmc$)	Rhombohedral ($R\bar{3}m$)	Orthorhombic subcarbonate ($Imm2$)
10YSB				
As synthesized	38.0	60.3	0.9	0.8
Aged for 11 months	32.8	59.4	2.0	5.8
Aged for 24 months	27.1	46.2	1.6	25.2
Aged for 35 months	19.7	51.2	2.0	27.1
12.5YSB				
As synthesized	64.4	32.6	1.2	1.8
Aged for 11 months	64.3	30.8	1.4	3.6
Aged for 24 months	26.6	22.8	2.3	48.4
Aged for 35 months	20.1	13.3	2.2	61.4
15YSB				
As synthesized	60.5	34.1	3.4	2.0
Aged for 11 months	48.2	26.0	1.9	23.9
Aged for 24 months	37.9	25.7	2.3	34.1
Aged for 35 months	22.9	14.2	2.4	60.4
25YSB				
As synthesized	76.1	16.3	2.2	5.5
Aged for 11 months	72.8	19.7	1.8	5.7
Aged for 24 months	63.2	1.2	25.3	10.4
Aged for 35 months	63.4	3.0	23.4	10.2
27.5YSB				
As synthesized	92.4	7.6	0	0
Aged for 11 months	58.3	2.2	1.9	10.5
Aged for 24 months	18.6	5.5	5.5	70.4
Aged for 35 months	15.7	4.8	5.6	73.9

For the samples with low dopant content (10, 12.5 and 15YSB), over the period of 35 months similar phase transformations were evident (Table 4.1). Both cubic and tetragonal phase content decreased, and this was directly correlated to orthorhombic phase content increasing. The rhombohedral phase content remained largely unchanged and in minor quantities. The decrease in tetragonal phase content over the period of 35 months is, however, far less than that of the cubic phase which indicates that cubic-to-orthorhombic phase transformations are more thermodynamically favourable over this low dopant content range. It must be clarified that the spontaneous formation of the orthorhombic subcarbonate phase is a chemical transformation and occurs as a result of the reaction between the calcined YSB materials and atmospheric CO_2 according to the reaction: $Y_xBi_{2-x}O_3 + CO_2 \rightarrow Y_xBi_{2-x}O_2CO_3$. The formation of the subcarbonate phase cannot be due to the presence of this phase in its amorphous state after the calcination step as bismuth subcarbonate has been shown to decompose between 300-500 °C.[31] This is in

contrast with the phase transformations which occur between the cubic, tetragonal and rhombohedral phases. Therefore, for the samples of this low dopant content range it is clear that both the cubic and tetragonal phases are metastable, and the formation of the orthorhombic phase is favoured under ambient conditions.

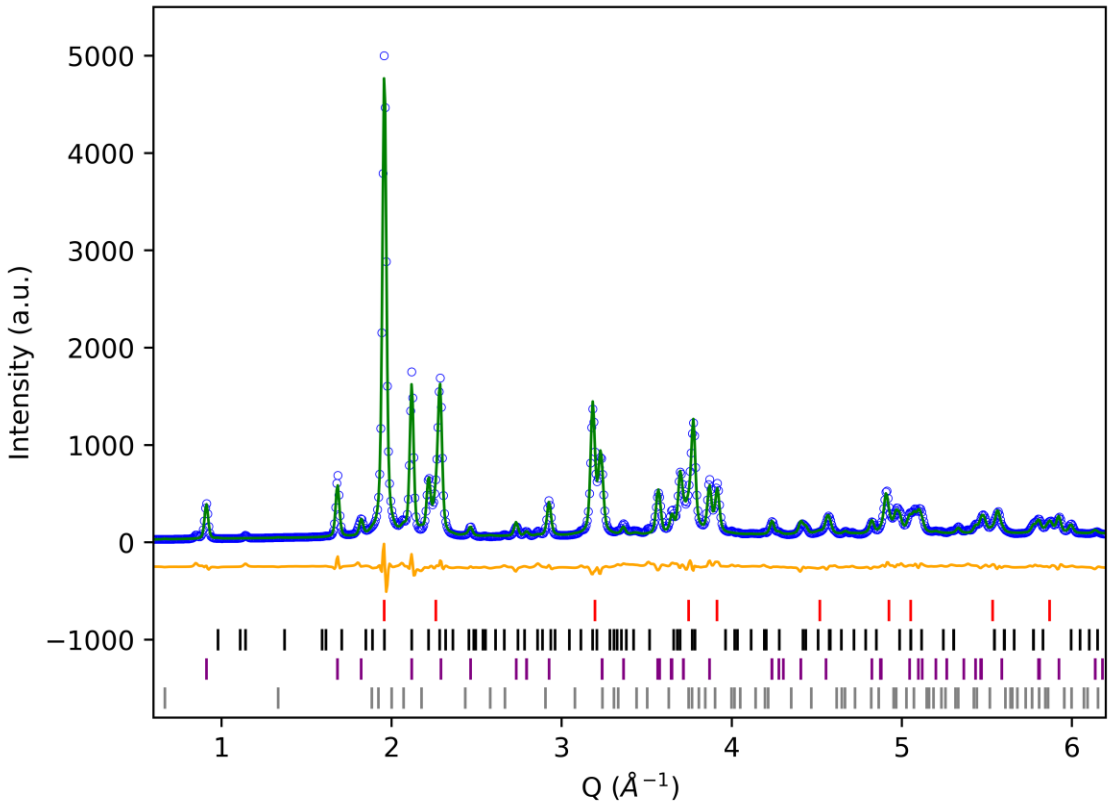

Figure 4.3. Diffractogram showing Rietveld refinement analysis for the 10YSB material calcined at 450 °C after aging under ambient conditions for a period of 35 months (R_{wp} = 7.7, R_{ex} = 7.8, GoF = 1.0). The observed pattern is shown in blue, the calculated in green and the difference in orange. Miller indices corresponding to the cubic, tetragonal, orthorhombic and rhombohedral phases are shown with red, black, purple and grey ticks, respectively.

For the higher dopant content samples (25YSB and 27.5YSB), different phase transformation behaviour is evident. For 25YSB, the cubic phase was significantly more stable than the tetragonal phase over the period of 35 months. Additionally, there was a significant increase in rhombohedral phase content but only minor orthorhombic subcarbonate phase formation. This tendency towards rhombohedral phase formation for 25YSB corroborates the findings of Watanabe[17] and Watanabe and Kikuchi[18] where for the similar dopant content range of 21.5-23.5 mol% Y_2O_3, the room temperature stable phase is reported to be the rhombohedral phase. For 27.5YSB, the cubic phase is less stable than the tetragonal phase and

there is a significant increase in orthorhombic subcarbonate phase content and only a minor increase in rhombohedral phase content. Interestingly, there is an increase in tetragonal phase content for 25YSB between the period 24 and 35 months and similarly for 27.5YSB between 11 and 24 months. This indicates that cubic-to-tetragonal phase transformations also occur for these compositions.

Collectively, the phase transformations seen for the calcined materials investigated indicate that both the cubic and tetragonal phases are not truly stabilized at room temperature. For 10-15YSB and 27.5YSB, the phase which is stable at room temperature is the orthorhombic subcarbonate phase. For 25YSB, the rhombohedral phase is likely to be the room temperature stable phase although minor orthorhombic phase formation suggests that this phase is also stable under ambient conditions at this dopant level.

4.3.2. *Ex situ* investigation of the phase stability of annealed δ- and δ+β-phase materials under ambient conditions using powder X-ray diffraction

For a portion of the sample, the calcined phase mixtures were thereafter immediately annealed at 750 °C for 8 h. Two batches of samples were made for comparison. For these annealed materials, it was shown that the tetragonal phase is readily converted into the cubic phase with phase pure samples formed when dopant content is greater than 15 mol% (Fig. 4.4). The phase composition of the annealed materials was quantified using Rietveld refinement (Tables 4.2 and 4.3 for batch **A** and **B**, respectively).

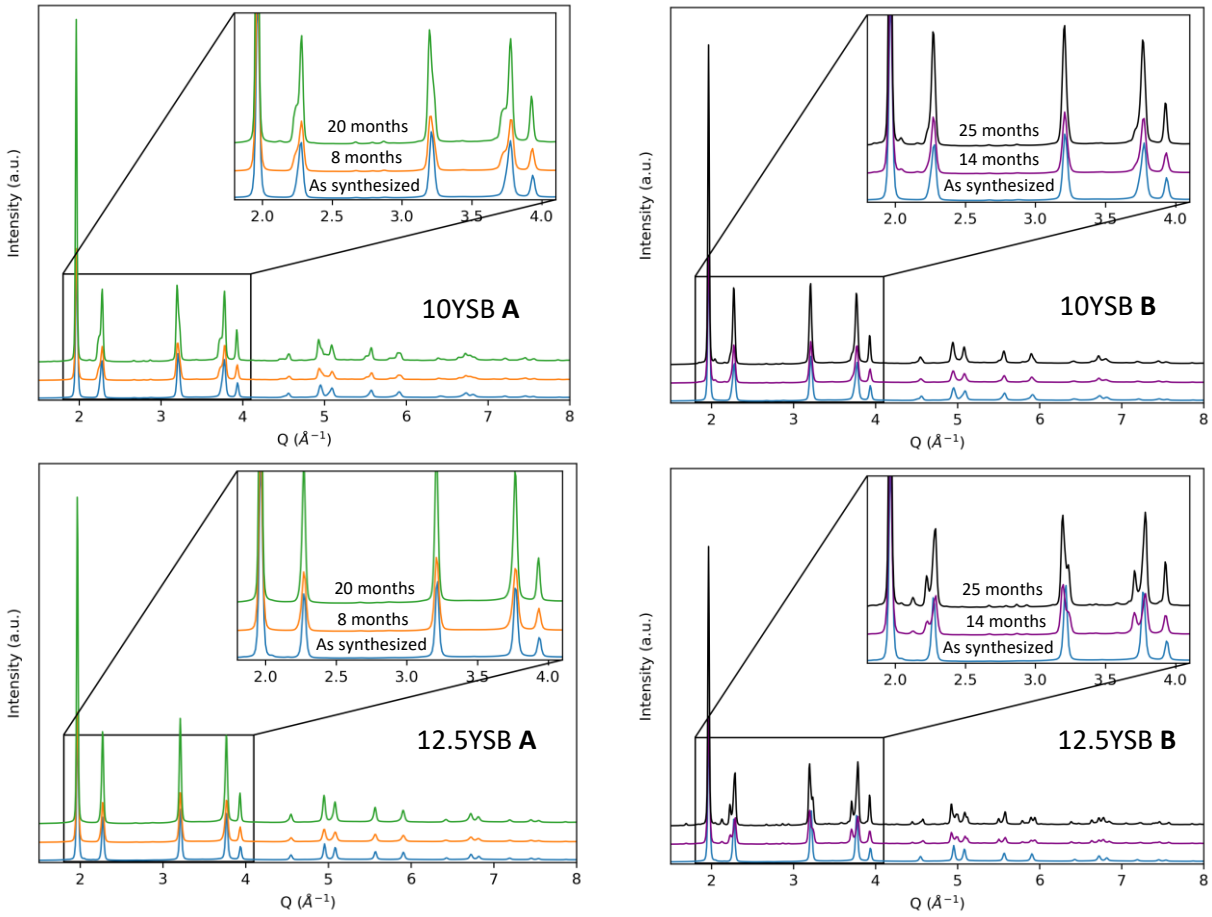

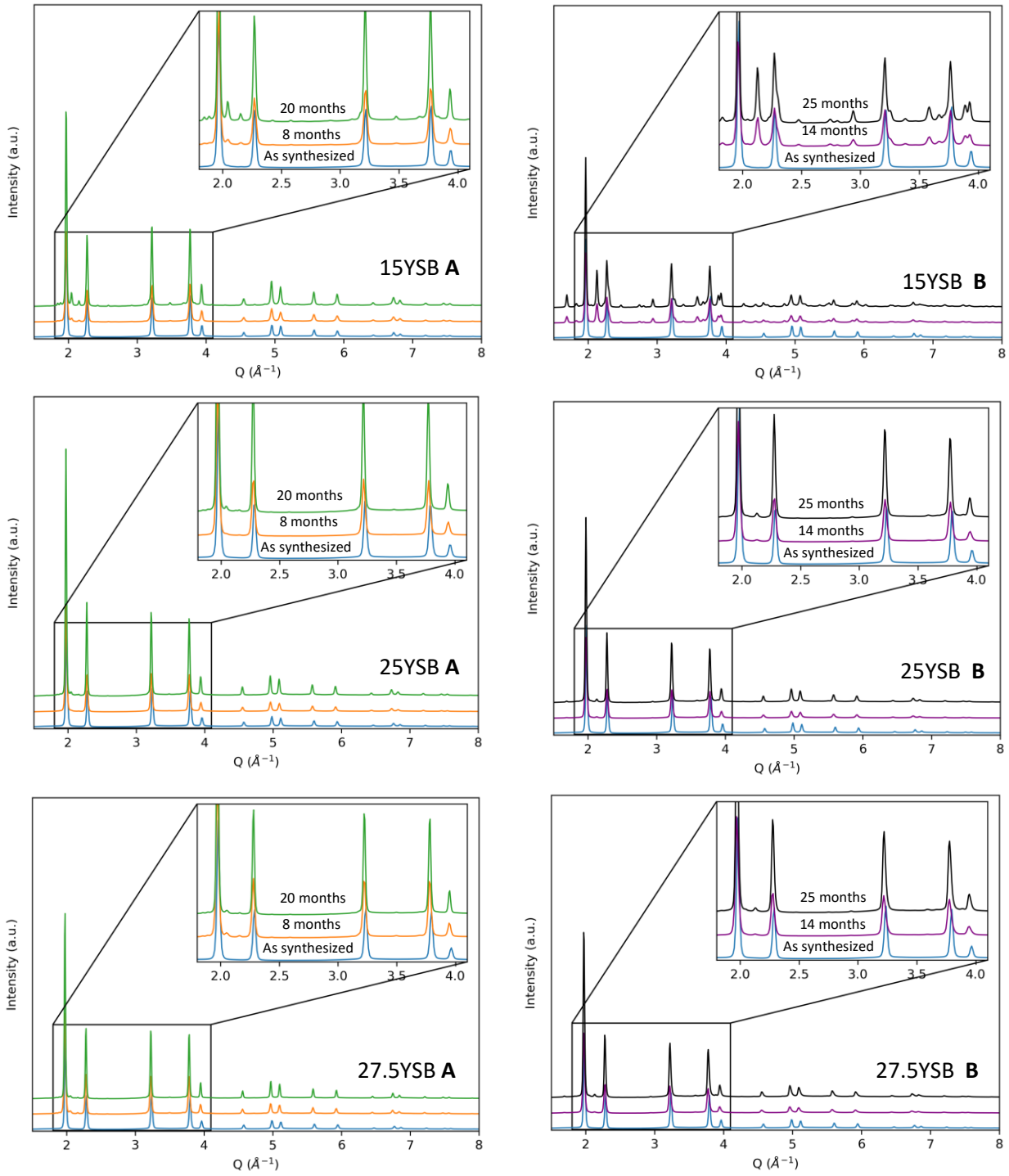

Figure 4.4. Room temperature diffractograms of the series of YSB samples calcined at 450 °C and then annealed at 750 °C. The diffractograms collected after the initial materials were annealed are shown in blue and diffractograms collected after the materials were stored in powdered form under ambient conditions are indicated. Analyses of batch **A** were done after 8 and 20 months (shown in orange and green, respectively) and batch **B** after 14 and 25 months (shown in purple and black, respectively).

Table 4.2. Variation of cubic phase purity of the series of YSB samples calcined at 450 °C and subsequently annealed at 750 °C from batch **A** measured in powder form.

Sample	Phase composition (weight %)			
	Cubic (*F*m$\bar{3}$m)	Tetragonal ($P4_2$/nmc)	Rhombohedral (*R*$\bar{3}$m)	Orthorhombic subcarbonate (*I*mm2)
10YSB				
As synthesized	46.6	53.4	0	0
Aged for 8 months	37.5	62.5	0	0
Aged for 20 months	30.0	70.0	0	0
12.5YSB				
As synthesized	68.7	31.3	0	0
Aged for 8 months	56.9	43.1	0	0
Aged for 20 months	51.1	48.9	0	0
15YSB				
As synthesized	86.0	14.0	0	0
Aged for 8 months	73.3	21.6	4.4	0.8
Aged for 20 months	66.0	27.8	5.1	1.1
25YSB				
As synthesized	100	0	0	0
Aged for 8 months	98.4	0	0.3	1.3
Aged for 20 months	96.4	0	0.6	3.0
27.5YSB				
As synthesized	100	0	0	0
Aged for 8 months	96.2	0	1.3	2.6
Aged for 20 months	94.8	0	0.9	4.3

Table 4.3. Variation of cubic phase purity of the series of YSB samples calcined at 450 °C and subsequently annealed at 750 °C from batch **B** measured in powder form.

Sample	Phase composition (weight %)			
	Cubic (*F*m$\bar{3}$m)	Tetragonal ($P4_2$/nmc)	Rhombohedral (*R*$\bar{3}$m)	Orthorhombic subcarbonate (*I*mm2)
10YSB				
As synthesized	48.9	51.1	0	0
Aged for 14 months	37.8	61.0	1.3	0
Aged for 25 months	29.2	68.1	2.7	0
12.5YSB				
As synthesized	37.2	60.7	2.0	0
Aged for 14 months	24.0	69.7	4.8	1.5
Aged for 25 months	22.0	72.9	2.8	2.3
15YSB				
As synthesized	86.1	13.9	0	0
Aged for 14 months	60.5	10.4	0.6	28.5
Aged for 25 months	53.8	16.4	0.6	29.2
25YSB				
As synthesized	100	0	0	0
Aged for 14 months	96.8	0	1.0	2.2
Aged for 25 months	96.8	0	0.3	2.9
27.5YSB				
As synthesized	100	0	0	0
Aged for 14 months	94.7	0	1.1	4.2
Aged for 25 months	90.6	0	4.8	4.7

The δ-phase bismuthates are commonly synthesized at temperatures of around 700-800 °C.[3,32–35] The *thermal prehistory* (i.e. thermal treatments already applied) of stabilized bismuthates has been shown to affect both optical[36] and magnetic[37] properties of these materials. As such, the long term phase stability under ambient conditions of the annealed materials will be compared to that of the calcined materials. The annealing of the calcined materials is done to promote cubic phase formation and stabilization and these higher temperatures are proposed to increase the long term stability of the δ-phase. The phase stability of the annealed materials were monitored for two unique batches. The purpose of this was to investigate the effect of incidental trace or amorphous impurity phase content on the long term phase transformation behaviour. After storing the annealed materials of batch **A** for 8 and 20 months and those of batch **B** for 14 and 25 months in powder form under ambient conditions, spontaneous phase changes were evident (Fig. 4.4) and are again quantified using Rietveld refinement analysis (Tables 4.2 and 4.3). The Rietveld analysis of the annealed 10YSB material from batch **A** aged for a period of 20 months is given in Figure 4.5 as an example.

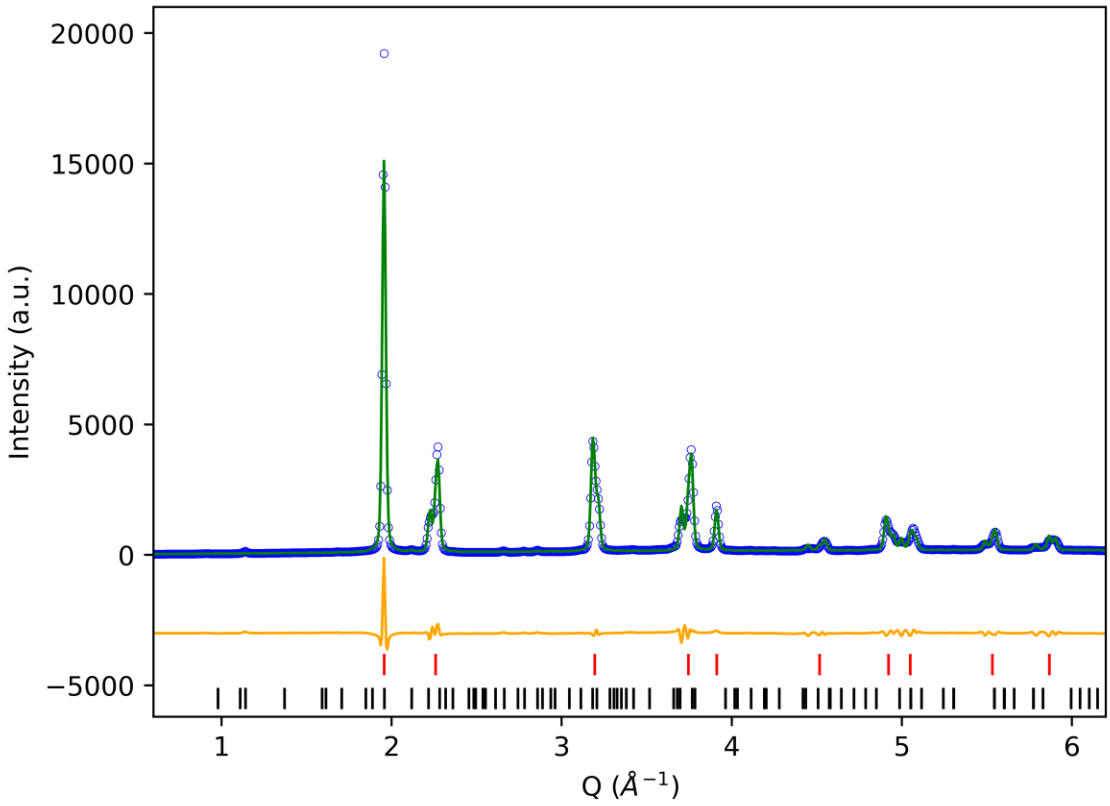

Figure 4.5. Diffractogram showing Rietveld refinement analysis for the 10YSB material from batch **A** annealed at 750 °C after aging under ambient conditions for a period of 20 months (R_{wp} = 13.9, R_{ex} = 5.1, GoF = 2.7). The observed pattern is shown in blue, the calculated in green and the difference in orange. Miller indices corresponding to the cubic and tetragonal phases are shown with red and black ticks, respectively.

For the 10YSB and 12.5YSB samples from batch **A**, the conversion of the cubic phase into the tetragonal phase was seen which clearly indicates the metastability of the cubic phase for low dopant content materials. The 10YSB and 12.5YSB samples from batch **B** showed the same cubic to tetragonal phase conversion, but together with the formation of minor rhombohedral phase content. Additionally, formation of the orthorhombic phase also occurred for 12.5YSB from batch **B** along with the reduction in rhombohedral phase content between 14 months and 25 months. For 12.5YSB the variation in phase aging behaviour between the two batches is clearly related to the distinct phase composition of the initial synthesized samples. This varying composition is most likely due to various factors in the synthetic procedure which are not fully reproducible. It is presently thought that the overall temperature control in various steps in the synthesis of these materials, in particular during the formation of the metal complex precursor paste, is responsible for the irreproducibility in phase composition. The decrease in

rhombohedral phase content for 12.5YSB from batch **B** additionally indicates that the rhombohedral phase is also metastable under ambient conditions for this composition.

The 15YSB sample from both batches displayed the greatest diversity in aging even though the phase composition of the as synthesized materials was very similar. Rhombohedral and orthorhombic phase formation was seen for the batch **A** sample along with significant cubic-to-tetragonal phase transformations. For the batch **B** sample, the cubic-to-tetragonal phase transformation was far less, and trace rhombohedral phase formation occurred along with significant orthorhombic phase formation. The latter indicates that the cubic-orthorhombic phase transformation is favourable for this particular sample. The contrasting aging behaviour seen for the two 15YSB samples is speculated to be due to the presence of varying trace impurity phases, which could be amorphous, in the as synthesized materials. These impurity phases crystallize over time and promote the various phase transformations observed.

For the 25YSB and 27.5YSB samples from both batches, the phase changes noted over the 20 month period are gradual transformations of the cubic phase to the rhombohedral and orthorhombic phases. These phase transformations are significantly less than those seen for the 10-15YSB annealed materials and for the 10-27.5YSB calcined materials. This reveals that the both the higher dopant content and the annealing step promote the long term stability of the δ-phase. The Rietveld analyses reveal that for the 27.5YSB sample from batch **A** and the 25YSB sample from batch **B**, the rhombohedral phase content initially increases and thereafter decreases while the orthorhombic phase content consistently increases. However, it must be noted that the accuracy of the phase compositions reported for these minor phases are limited due to the low concentration of these phases.

Interestingly, the rate of the cubic-to-tetragonal conversion varies between the samples of near identical composition from the two different batches. As an example, for 10YSB **A** the average rate of cubic phase purity change over the 20 month aging period is 4.3% per month whereas for the 10YSB **B** sample this rate is significantly reduced at 2.0% per month over the 25 month period. For 12.5YSB **A** the average rate of conversion is found to be 1.0% per month whereas for 12.5YSB **B** the conversion rate is found to be significantly higher at 3.6% per month. These different rates of conversion seen for samples of apparent identical composition from different synthetic batches give strong evidence of possible trace or amorphous phases present (which could develop during the metal complex precursor formation step and/or during the calcination step) due to slight irreproducibility in the synthetic method. Unravelling these synthetic details are currently sought to enable greater control over both the formation and long-term stability of the cubic phase.

The metastability of δ-phase bismuthates, as noted by Watanabe,[17] is clearly evident in both the annealed and calcined samples reported in this work. However, the spontaneous formation of the rhombohedral phase, predicted by Watanabe[17] to be the true stable phase at room temperature, is not exclusive. An orthorhombic bismuth subcarbonate readily formed under ambient conditions for several calcined and annealed samples of varying dopant content levels. The subcarbonate formation is, however, more prevalent in the calcined materials (which is considered as an intermediate step), indicating that the thermal prehistory of the materials has a significant impact on the long term phase stability. Watanabe[38] also reported that the rhombohedral phase of several stabilized bismuth oxides Bi_2O_3-MO (M = Ca, Sr or Ba), which were synthesized using the conventional solid state route, have limited stability when exposed to a humid atmosphere at room temperature. Under these conditions, the rhombohedral phase was found to decompose into monoclinic α-Bi_2O_3 and an 'unknown' phase. Similarly, spontaneous formation of the rhombohedral phase was also noted for several YSB materials in this work. Therefore, it is clear that the substituted bismuth oxide system comprises several phases which are metastable at room temperature. The observed phase is dependent on the ambient atmosphere, dopant level and thermal prehistory of the materials.

4.3.3. Investigating the effect of pelletization and additional sintering methodologies on the ambient phase stability of the δ-phase materials

In SOFC devices, the electrolyte used is in the form of a densified, sintered layer[39] which was approximated as a sintered pellet in this work. It is therefore worthwhile to investigate and compare the ambient phase stability of the YSB materials in powder and pelletized form. For this, annealed 10YSB and 27.5YSB materials were again synthesized (i.e. batch **C**) in powder form and a portion of this powder was used to make the sintered pellets. These powder and pellet samples were then stored under identical ambient conditions for 14 and 20 months, respectively. The samples were also kept in their powder or pelletized states when measured via laboratory-based PXRD.

From the diffractograms collected (Fig. 4.6) it was noted that when the material was stored as a powder, the cubic phase purity significantly decreased over the period of 14 months (Table 4.4) and the average rate of cubic-to-tetragonal phase conversion was found to be 1.8% per month. No rhombohedral or orthorhombic phase content was detected which is likely due to the limited resolution of the laboratory instrument. When pelletized, the cubic phase purity was significantly increased in comparison to the powder sample and the average rate of cubic-to-tetragonal phase conversion was found to be 0.04% per month over the 20 month period. Again, no rhombohedral or orthorhombic phase content was detected.

This indicated that the pellet preparative methodology, which includes a high pressure step and a sintering step which causes densification and average grain size growth, promotes the formation and enhances the ambient long-term stability of the cubic phase. It is noteworthy that the diffractogram collected for the pelletized materials corresponds to the pellet surface and not the bulk material. If the phase transformations observed under ambient conditions are due to the interaction of the material with the atmosphere, it is expected that the surface would degrade at a higher rate in comparison to the powdered analogues. For the 27.5YSB material, there were no phase transformations evident in either powder or pellet form over the same time period.

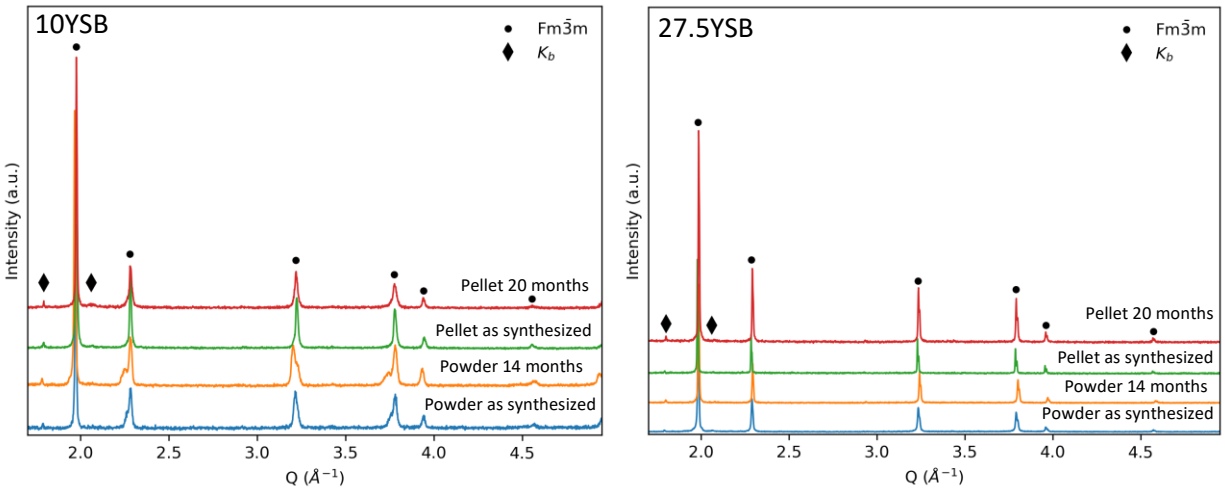

Figure 4.6. Laboratory-based room temperature diffractograms of 10YSB and 27.5YSB annealed at 750 °C showing the varying effects on phase stability under ambient conditions when materials are stored in powder and pelletized forms. The diffractograms collected after the initial annealed powder materials were synthesized are shown in blue and those after the materials were stored in powder form for 14 months are shown in orange. The diffractograms collected after the materials were pelletized and sintered are shown in green and those after the pelletized materials were stored for 20 months are shown in red.

Table 4.4. Variation of cubic phase purity of the 10YSB sample stored as an annealed powder and sintered pellet. The phase purity of the powder samples was monitored over a 14 month period whilst that of the pellet samples was monitored over a 20 month period.

10YSB batch **C**	Cubic phase %	% change/month
Powder as synthesized	49.1	1.8
Powder after 14 months	23.3	
Pellet as synthesized	98.3	0.04
Pellet after 20 months	97.6	

4.3.4. Investigating the effect of the annealing atmosphere on the ambient phase stability of the δ-phase materials

The effect of the annealing atmosphere on the long term phase stability of the δ-phase under ambient conditions was investigated for a phase pure cubic 27.5YSB material in this work. 27.5YSB material was again synthesized and annealed at 750 °C (i.e. batch **D**). Two portions of this material were then heated to ~700 °C in either an air or nitrogen atmosphere and then slow cooled to room temperature. After storing the two portions material under ambient conditions for 11 months, the sample that was heated in an air atmosphere showed significant formation of the rhombohedral phase (~6.2%), whereas the sample that was heated under a nitrogen atmosphere showed only trace rhombohedral phase formation (Fig. 4.7). These differences in phase stability are seemingly attributed to the formation of either amorphous or trace rhombohedral phase content, which are more readily formed in an oxygen-rich environment at high temperatures, as was the case during the heating under an air atmosphere. This rhombohedral phase content was then able to either crystallize under ambient conditions (if it starts off as amorphous) or promote the cubic-to-rhombohedral phase transformation over the period of 11 months. Conversely, for the same material heated under nitrogen, the absence of oxygen during heating inhibits the formation of rhombohedral phase content and hence only trace rhombohedral phase content was evident from the sluggish cubic-rhombohedral phase transformation that occurs over the 11 month aging period under ambient conditions. This change in ambient phase stability suggests that additional heating under an inert atmosphere is beneficial to the long-term phase stability of cubic YSB materials.

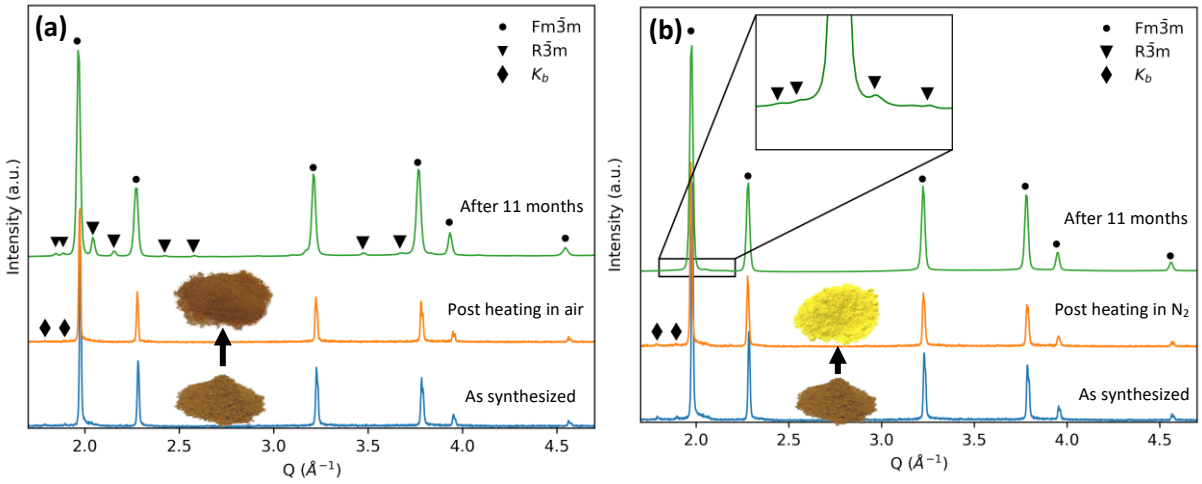

Figure 4.7. Room temperature diffractograms of 27.5YSB annealed at 750 °C showing the effect of the heating atmosphere on the ambient phase stability and thermochromic behaviour. The diffractograms collected prior to heating to ~700 °C in (a) air and (b) nitrogen are shown in blue. The diffractograms

collected after heating are shown in orange and the diffractograms collected after the materials were stored under ambient conditions for 11 months are shown in green.

Heating the 27.5YSB sample under different atmospheres was also resulted in changes to the colour of the material (see Figure 4.7). A recent study by Liu *et al.*[40] investigated the thermochromic behaviour of yttrium-substituted bismuth oxides $(Bi_{1-x}Y_x)_2O_3$ ($0.05 \leq x \leq 0.25$) which were synthesized using the conventional solid state route. These materials exhibited reversible colour changes in an air atmosphere from yellow hues at low temperatures to various brown hues at high temperatures. Similar thermochromic behaviour was encountered during the heating of the 27.5YSB material under different atmospheres (Fig. 4.7).

When the 27.5YSB material was synthesized, where it had been calcined for 18 h at 450 ^oC and annealed for 8 h at 750 ^oC in air, the sample was a dark brown colour. This is contrary to the findings of Liu *et al.*[40] who predicted high Y^{3+} content bismuthates (≥25 mol% Y^{3+}) to have a bright yellow hue at room temperature. After further heating in air, the colour was largely unchanged, and the phase purity of the material also remained unchanged (Fig. 4.7a). Conversely, after heating in a nitrogen atmosphere, the colour of the material changed to a bright yellow hue, more in line with that predicted by Liu *et al.*[40] for this sample composition at room temperature. Interestingly this colour change was not found to coincide with any change in phase composition (Fig. 4.7b). Watanabe[38] reported a colour change from yellow to brown after a Ba^{2+} stabilized bismuth oxide was annealed at 500 ^oC for ~160 h in an air atmosphere. This colour change was attributed to the decomposition of the rhombohedral stabilized bismuth oxide into the monoclinic α-Bi_2O_3 and an 'unknown' phase. If the colour change observed in this work was due to a phase change occurring, the additional phase content was beyond the resolution of the diffractometer or present in the amorphous fraction of the material. The observed colour of the materials are directly related to the electronic structure – lighter, yellow hues indicate a wide bandgap, whereas darker, brown hues indicate a narrower bandgap. Upon synthesis, having a brown-coloured 27.5YSB material at room temperature indicates that the bandgap is significantly narrower than that predicted by Liu *et al.*[40] It was also interesting to note that a non-reversible change in electronic structure occurred when heated under a nitrogen atmosphere. These differences in electronic structure could most likely be assigned to the soft chemical synthetic route employed in this work.

4.3.5. *In situ* investigation of the phase stability of the δ-phase materials using variable temperature powder X-ray diffraction

Two YSB samples, 15YSB and 27.5YSB, which were initially thought to be phase pure cubic after being annealed for 8 h at 750 °C, were further studied via laboratory-based *in situ* variable temperature diffraction measurements (Fig. 4.8) in an air atmosphere to determine the phase stability and thermal expansion properties of these materials during a thermal cycle. Upon heating the 15YSB material, the starting cubic phase expanded linearly within the range of 27-551 °C (Fig. 4.9a). Between 551-563 °C, however, the lattice expanded rapidly and minor rhombohedral phase content (~8%) became evident. Over the range of 563-706 °C, the rhombohedral phase seemed to disappear, and the rate of thermal expansion was again uniform, although significantly increased. On cooling a similar reversed trend was observed; between 706-523 °C the thermal expansion was linear, over the range of 523-477 °C the lattice contracted rapidly and between 477-27 °C the thermal expansion was again linear and significantly reduced in magnitude (Fig. 4.9a). In this case the minor rhombohedral phase content (~3%) formed from ~444 °C and remained to room temperature (Fig. 4.8). In our previous study[28] we reported the CTE of annealed (at 750 °C) 15YSB to be $152.4 \pm 14.2 \times 10^{-6}$ K^{-1} over the temperature range of 589-769 °C. In these *in situ* studies the CTE of annealed (at 750 °C) 15YSB over the similar temperature range of 563-706 °C was found to be similar in magnitude at $174.4 \pm 11.6 \times 10^{-6}$ K^{-1}. However, the CTE of this material over the lower temperature range of 27-551 °C was found in this work to be significantly reduced in magnitude at $76.3 \pm 2.3 \times 10^{-6}$ K^{-1}. This vast discrepancy in CTE exhibited over different temperature ranges indicates the presence of unidentified structural variations which result in varying thermal expansion behaviour.

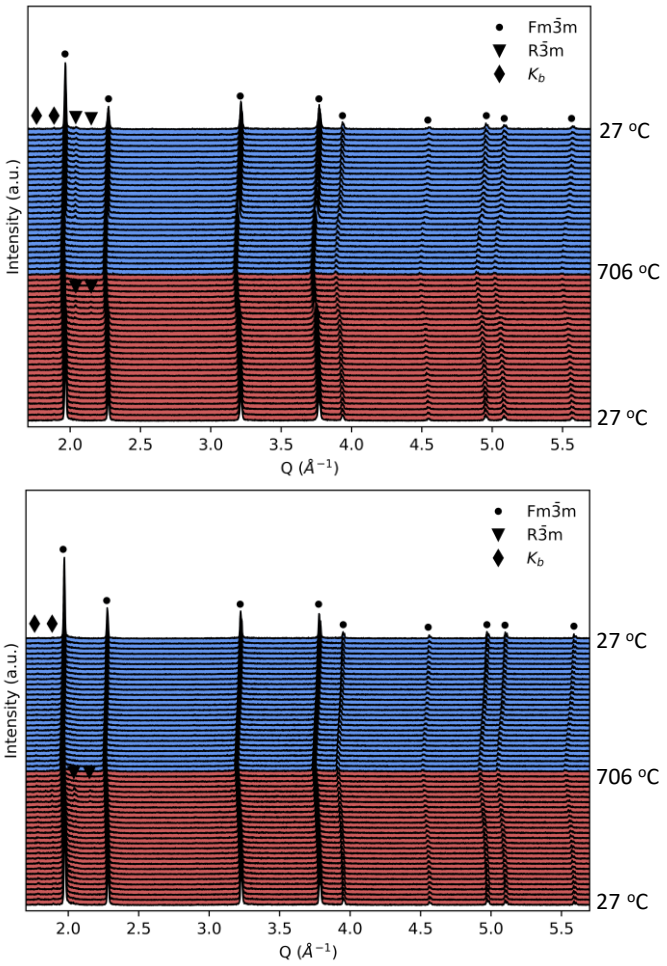

Figure 4.8. *In situ* variable temperature diffractograms collected for the annealed (at 750 °C) 15YSB (top) and 27.5YSB (bottom) materials in an air atmosphere over the temperature range of 27-706-27 °C.

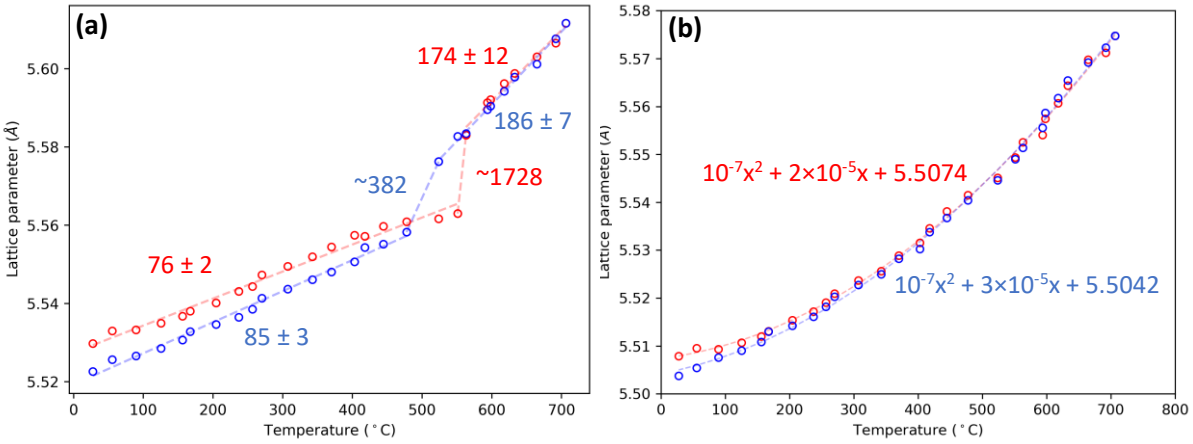

Figure 4.9. Lattice parameter variation of the cubic phase for the annealed (at 750 °C) 15YSB (a) and 27.5YSB (b) materials over the temperature range of 27-706-27 °C. (a) Approximate CTE values (in terms of 10^{-6} K^{-1}) during the heating and cooling cycles are shown in red and blue, respectively. (b) The non-linear expansion is emphasized by fitting quadratic functions to the data.

For the 27.5YSB material, trace rhombohedral phase content was formed between 594-618 °C during the heating cycle (Fig. 4.8), but no rhombohedral phase content was detected during the cooling cycle. This possibly suggests that the higher dopant percentage promotes the retention of a pure cubic sample after a thermal cycle. The rate of thermal expansion for 27.5YSB was non-linear for both the heating and cooling cycles (Fig. 4.9b) and the thermal expansion behaviour was described using second order polynomial functions. Similar non-linear thermal expansion was more recently reported by Abrahams *et al*.[41] for δ-Bi_3YO_6 and was attributed to the increase in occupancy of the anionic 48i site during the heating cycle of 25-800 °C. The site occupancy of this 48i site increased from 0.011(1) at 25 °C to 0.017(1) at 800 °C, an increase of ~55%. This increase in occupancy of the 48i site increases the local distortion of the lattice and results in larger lattice parameter values during the heating cycle. Unfortunately monitoring of actual anionic site occupancy is not possible with PXRD due to the high disparity in the scattering of X-rays by the lighter oxygen anions and the heavier bismuth and yttrium cations. It may also be that the thermal expansion behaviour of 15YSB is non-linear, but the abrupt change in lattice parameter size obscures this and is further complicated by the effects imposed by the additional rhombohedral phase. As such, elucidating the cause of this abrupt lattice parameter change is crucial to the understanding of the thermal expansion characteristics of YSB materials with low dopant content.

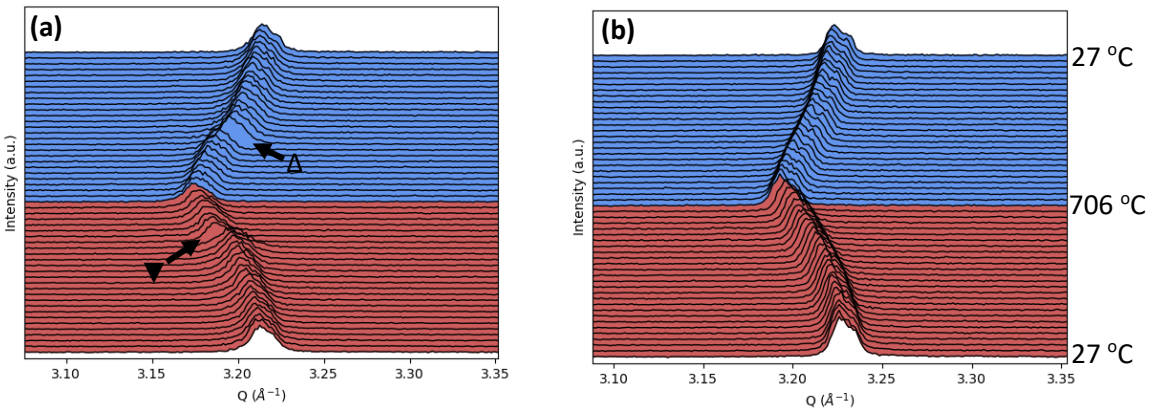

Figure 4.10. Variation in peak position of the (200) peak collected for the annealed (at 750 °C) 15YSB (a) and 27.5YSB (b) materials over the temperature range of 27-706-27 °C. There exists an abrupt change in unit cell volume during both the heating (▼ symbol, 551-563 °C) and cooling (Δ symbol, 523-477 °C) cycles for the 15YSB material. This abrupt change is absent for the 27.5YSB material.

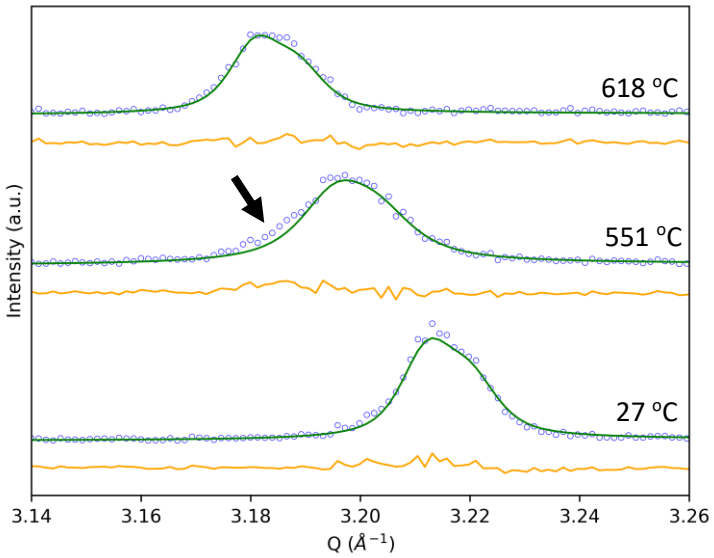

Figure 4.11. Diffractograms showing the Rietveld refinement analysis of the (200) peak for the annealed (at 750 °C) 15YSB material at 27, 551 and 618 °C with the observed pattern shown in blue, the calculated in green and the difference in orange. Refinements were done using a single cubic phase and the minor peak shoulder that forms, which is most notable where the abrupt change in unit cell volume occurs (551-563 °C), is indicated with a black arrow.

The abrupt changes in unit cell volume seen for 15YSB upon heating and cooling (emphasized in Figure 4.10) are likely due to one of two structural phenomena. The first being a phase transformation, not evident in this diffraction data. Similar abrupt thermal lattice expansion behaviour was observed in Yb-stabilized $BaCeO_3$,[42] $Bi_{14}YO_{22.5}$[43] and $Bi_{14}WO_{24}$[44] and was found to be related to phase changes. In these materials additional phases were distinctly present in the diffraction data. Our previous work[28] on low dopant YSB materials (10-22.5 mol% Y^{3+}) showed that a tetragonal secondary phase that was evident from peak asymmetries in the diffraction data collected at room temperature. For the 15YSB material studied here, these peak asymmetries were not evident at room temperature (Fig. 4.11) and incorporation of the additional tetragonal phase into the Rietveld refinement process did not improve the fit, further indicating the absence of this phase. However, during heating to 551 °C the formation of a minor peak shoulder was observed which coincided with the onset of the abrupt change in unit cell volume. This shoulder was only present in the region where the abrupt change in unit cell volume occurred (551-563 °C) and was no longer evident on further heating (Fig. 4.11). This shoulder indicates that a structural change (most likely a phase transition) occurred in the 551-563 °C temperature range, but the additional phase could not be resolved using data from the laboratory-based diffractometer. Alternatively, the volume changes could be due to the cubic phase undergoing a structural change that preserves the average crystallographic symmetry of

the material, such as an order-disorder transition of the oxygen sublattice. Such a transition would contribute to an abrupt increase in oxide ion conductivity when the material enters a more disordered state. In previous work[28] the oxide ion conductivity of a 15YSB material abruptly increased from ~550 °C during the heating cycle and abruptly decreased again from ~550 °C during the cooling cycle (Fig. 4.12). These conductivity changes occur at near identical temperature ranges in which abrupt changes in unit cell volume are evident (Figs. 4.9a and 4.10a) and hence show strong correlation. To unravel this anomalous thermal expansion behaviour, investigations of the local structure during *in situ* heating and cooling are required and these studies are the topic of ongoing work (investigated in Chapter 5 of this thesis).

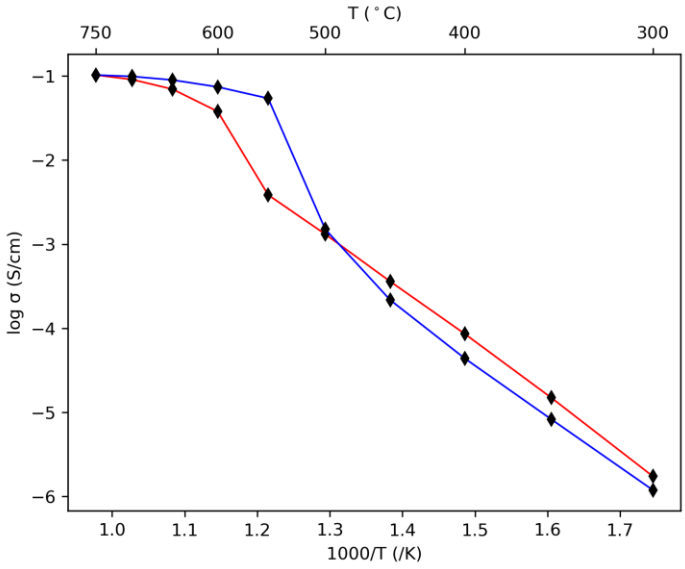

Figure 4.12. Arrhenius plot of annealed (at 750 °C) 15YSB material in the temperature range of 300-750 °C showing results from both the heating (red lines) and the cooling cycles (blue lines) corresponding to the second thermal cycle.[28] Abrupt changes in conductivity are observed at 550 °C during both the heating and cooling cycles.

4.4. Conclusion

The stability studies under ambient conditions have revealed a remarkable phenomenon in which various yttrium substituted bismuthate ceramics undergo spontaneous phase transformations under ambient conditions. This was more prominent for materials only calcined at 450 °C, but also observed for those that were further annealed at 750 °C. The phase transformations indicate that both the cubic and tetragonal polymorphs are metastable at room temperature and the thermal prehistory was found to affect the phase stability characteristics. The spontaneous formation of both the rhombohedral and

orthorhombic subcarbonate phases was observed in this work. The formation of the latter phase presumably occurs from the reaction between the stabilized bismuth oxides and atmospheric CO_2. This spontaneous carbon capture by stabilized bismuth oxides is reported here for the first time. Interestingly, varying phase fractions were formed for compositionally identical samples that were annealed at 750 ^oC for different synthetic batches, and the rate of the phase transformations also differed significantly between these samples. These observations indicate synthetic method irreproducibility. When pelletized, the cubic phase purity of an annealed 10YSB material was found to increase, likely due to the additional sintering process, and the overall aging reduced in comparison to the same sample stored in powder form. Additional heating of powdered samples in a nitrogen atmosphere was also found to significantly increase ambient phase stability of the cubic phase over extended periods of time.

During a thermal cycle, the annealed 15YSB sample underwent abrupt volume changes and an impurity phase was formed during both heating and cooling cycles. The abrupt volume changes are thought to be due to either an order-disorder transition or more likely due to an unidentified phase transformation. For the 27.5YSB sample, the volume change, although non-linear, was significantly more gradual and although a rhombohedral impurity phase was formed during the heating cycle, for this higher dopant composition, no impurity phases were formed on cooling.

Further work in investigating the formation of phases during the ambient phase aging process for both the calcined and annealed samples would provide improved insight on the mechanism responsible for these spontaneous transformations. Crucially, additional total scattering-based techniques are required to investigate amorphous phase content. Implementing multiple thermal cycles on the materials would enable the rhombohedral phase formation to be further studied and would enable a more comprehensive understanding of the phase stability of these materials during and after several thermal cycles. High resolution PXRD measurements would allow for the presence of a secondary phase to be investigated and total scattering studies are sought to unravel the structural changes that contribute to the anomalous thermal expansion behaviour.

4.5. References

1. Azad, A. M., Larose, S. and Akbar, S. A. Bismuth oxide-based solid electrolytes for fuel cells. *J. Mater. Sci.* **29**, 4135–4151 (1994).

2. Jung, D. W., Lee, K. T. and Wachsman, E. D. Terbium and tungsten co-doped bismuth oxide electrolytes for low temperature solid oxide fuel cells. *J. Korean Ceram. Soc*. **51**, 261–264 (2014).

3. Stambouli, A. B. and Traversa, E. Solid oxide fuel cells (SOFCs): A review of an environmentally clean and efficient source of energy. *Renew. Sustain. Energy Rev*. **6**, 433–455 (2002).

4. Fergus, J. W. Electrolytes for solid oxide fuel cells. *J. Power Sources* **162**, 30–40 (2006).

5. Harwig, H. A. and Gerards, A. G. The polymorphism of bismuth sesquioxide. *Thermochim. Acta* **28**, 121–131 (1979).

6. Verkerk, M. J., Keizer, K. and Burggraaf, A. J. High oxygen ion conduction in sintered oxides of the Bi_2O_3-Er_2O_3 system. *J. Appl. Electrochem*. **10**, 81–90 (1980).

7. Watanabe, A. Polymorphic transformation of δ-Bi_2O_3 stabilized with Ln_2O_3 (Ln=Sm, Eu, Gd, Tb, and Dy) into a new phase with a C-type rare-earth oxide-related structure. *Solid State Ion.* **79**, 84–88 (1995).

8. Jolley, A. G., Jayathilake, R. and Wachsman, E. D. Optimizing rhombohedral Bi_2O_3 conductivity for low temperature SOFC electrolytes. *Ionics (Kiel)*. **25**, 3531–3536 (2019).

9. Takahashi, T., Iwahara, H. and Nagai, Y. High oxide ion conduction in sintered Bi_2O_3 containing SrO, CaO or La_2O_3. *J. Appl. Electrochem*. **2**, 97–104 (1972).

10. Takahashi, T., Iwahara, H. and Arao, T. High Oxide Ion Conduction in Sintered Oxides of the System Bi_2O_3-Y_2O_3. *J. Appl. Electrochem*. **5**, 187–195 (1975).

11. Fung, K. Z., Virkar, A. V. and Drobeck, D. L. Massive Transformation in the Y_2O_3-Bi_2O_3 System. *J. Am. Ceram. Soc*. **77**, 1638–1648 (1994).

12. Fung, K. Z. and Virkar, A. V. Phase Stability, Phase Transformation Kinetics, and Conductivity of Y_2O_3-Bi_2O_3 Solid Electrolytes Containing Aliovalent Dopants. *J. Am. Ceram. Soc*. **74**, 1970–1980 (1991).

13. Arasteh, S., Maghsoudipour, A., Alizadeh, M. and Nemati, A. Effect of Y_2O_3 and Er_2O_3 co-dopants on phase stabilization of bismuth oxide. *Ceram. Int*. **37**, 3451–3455 (2011).

14. Chou, T., Liu, L. Der and Wei, W. C. J. Phase stability and electric conductivity of Er_2O_3-Nb_2O_5 co-doped Bi_2O_3 electrolyte. *J. Eur. Ceram. Soc*. **31**, 3087–3094 (2011).

15. Huang, K., Feng, M. and Goodenough, J. B. Bi_2O_3-Y_2O_3-CeO_2 solid solution oxide-ion electrolyte. *Solid State Ion.* **89**, 17–24 (1996).

16. Fung, K. Z., Baek, H. D. and Virkar, A. V. Thermodynamic and kinetic considerations for Bi_2O_3-based electrolytes. *Solid State Ion.* **52**, 199–211 (1992).

17. Watanabe, A. Is it possible to stabilize δ-Bi_2O_3 by an oxide additive? *Solid State Ion.* **41**, 889–892 (1990).

18. Watanabe, A. and Kikuchi, T. Cubic-hexagonal transformation of yttria-stabilized δ-bismuth sesquioxide, $Bi_{2-2x}Y_{2x}O_3$ (x=0.215-0.235). *Solid State Ion.* **21**, 287–291 (1986).

19. Danks, A. E., Hall, S. R. and Schnepp, Z. The evolution of 'sol-gel' chemistry as a technique for materials synthesis. *Mater. Horizons* **3**, 91–112 (2016).

20. Hammersley, A. P. FIT2D: A multi-purpose data reduction, analysis and visualization program. *J. Appl. Crystallogr.* **49**, 646–652 (2016).

21. Gražulis, S., Chateigner, D., Downs, R. T., Yokochi, A. F. T., Quiros, M., Lutterotti, L., Manakova, E., Butkus, J., Moeck, P. and Le Bail, A. Crystallography Open Database - An open-access collection of crystal structures. *J. Appl. Crystallogr*. **42**, 726–729 (2009).

22. Coelho, A. A. TOPAS and TOPAS-Academic: An optimization program integrating computer algebra and crystallographic objects written in C++. *J. Appl. Crystallogr.* **51**, 210–218 (2018).

23. Dinnebier, R. E., Leineweber, A. and Evans, J. S. O. Rietveld Refinement Practical Powder Diffraction Pattern Analysis Using Topas. (Walter de Gruyter GmbH, Berlin/Boston, 2019).

24. Thompson, P., Cox, D. E. and Hastings, J. B. Rietveld Refinement of Debye-Scherrer Synchrotron X-ray Data from Al_2O_3. *J. Appl. Crystallogr.* **20**, 79–83 (1987).

25. Kaiser, D. L. and Watters, R. L. National Institute of Standards and Technology, Certificate Standard reference material 640d - Silicon Powder - Line Position and Line Shape Standard for Powder Diffraction. (2010).

26. Lyon, K. G., Salinger, G. L., Swenson, C. A. and White, G. K. Linear thermal expansion measurements on silicon from 6 to 340 K. *J. Appl. Phys*. **48**, 865–868 (1977).

27. Okada, Y. and Tokumaru, Y. Precise determination of lattice parameter and thermal expansion coefficient of silicon between 300 and 1500 K. *J. Appl. Phys*. **56**, 314–320 (1984).

28. Kiefer, M. A., Billing, C., Erasmus, R. M., Mogodi, W. M. & Billing, D. G. A detailed investigation of the structural stability, ionic conductivity and in situ δ-phase formation of $Y_xBi_{2-x}O_\delta$. *Unpubl. Manuscr.* (2021).

29. Grice, J. D. A solution to the crystal structures of bismutite and beyerite. *Can. Mineral.* **40**, 693–698 (2002).

30. Huang, H., Tian, N., Jin, S., Zhang, Y. and Wang, S. Syntheses, characterization and nonlinear optical properties of a bismuth subcarbonate $Bi_2O_2CO_3$. *Solid State Sci*. **30**, 1–5 (2014).

31. Sheng, S., Jin, S. and Cui, K. Thermal decomposition of nanostructured bismuth subcarbonate. *Materials (Basel).* **13**, 1–10 (2020).

32. Sammes, N. M., Tompsett, G. A., Näfe, H. and Aldinger, F. Bismuth based oxide electrolytes—structure and ionic conductivity. *J. Eur. Ceram. Soc*. **19**, 1801–1826 (1999).

33. Takahashi, T. and Iwahara, H. Oxide ion conductors based on bismuthsesquioxide. *Mater. Res. Bull*. **13**, 1447–1453 (1978).

34. Wachsman, E. D. Development of a Lower Temperature SOFC. *ECS Transactions*, **25**, 783–788 (2009).

35. Shuk, P., Wiemhöfer, H. D., Guth, U., Göpel, W. and Greenblatt, M. Oxide ion conducting solid electrolytes based on Bi_2O_3. *Solid State Ion.* **89**, 179–196 (1996).

36. Girsova, M. A., Firstov, S. V. and Antropova, T. V. Structural and optical properties of the bismuth-containing quartz-like glasses. *J. Phys. Conf. Ser*. **541**, (2014).

37. Kravchenko, E. A. Magnetism of bismuth(III) oxide-based compounds. *Solid State Phenom*. **233–234**, 113–116 (2015).

38. Watanabe, A. Phase stability of $Bi_{0.765}Sr_{0.235}O_{1.383}$- type bismuth mixed oxides with hexagonal symmetry. *Solid State Ion.* **35**, 281–283 (1989).

39. Kawamoto, H. Research and Development Trends in Solid Oxide Fuel Cell Materials. *Sci. Technol. Trends* **26**, 52–70 (2008).

40. Liu, X., Staubitz, A. and Gesing, T. M. Thermochromic Behavior of Yttrium-Substituted Bismuth Oxides. *ACS Appl. Mater. Interfaces* **11**, 33147–33156 (2019).

41. Abrahams, I., Liu, X., Hull, S., Norberg, S. T., Krok, F., Szmigiel-Kozanecka, A., Islam, M. S. and Stokes, S. J. A combined total scattering and simulation approach to analyzing defect structure in Bi_3YO_6. *Chem. Mater*. **22**, 4435–4445 (2010).

42. Yamaguchi, S. and Yamada, N. Thermal lattice expansion behavior of Yb-doped $BaCeO_3$. *Solid State Ion.* **162–163**, 23–29 (2003).

43. Struzik, M., Malys, M., Krynski, M., Wojcik, M., Dygas, J. R., Wrobel, W., Krok, F. and Abrahams, I. Structural and electrical behavior in $Bi_{14}YO_{22.5}$. *RSC Adv*. **5**, 83471–83479 (2015).

44. Borowska-Centkowska, A., Krok, F., Abrahams, I., Wrobel, W., Dygas, J. R. and Hull, S. Thermal variation of structure and electrical conductivity in $Bi_{14}WO_{24}$. *Solid State Ion.* **202**, 14–21 (2011).

Chapter 5. Investigating the thermal expansion behaviour of $Al_zY_xBi_{2-x-z}O_3$ electrolytes using *in situ* total scattering studies.

M.A. Kiefer[a,c], Caren Billing[a,c], Daniel Olds[b], David G. Billing[a,c]

[a]Molecular Science Institute, School of Chemistry, University of the Witwatersrand, Private Bag X3, Johannesburg, 2050, South Africa

[b]National Synchrotron Light Source II, Brookhaven National Laboratory, PO Box 5000, Upton, NY, 11973, USA

[c]DSI-NRF Centre of Excellence in Strong Materials, University of the Witwatersrand, Private Bag X3, Johannesburg, 2050, South Africa.

This chapter has been prepared for submission and has been formatted accordingly.

Abstract

The thermal expansion behaviour of yttrium-stabilized Bi_2O_3 materials was investigated using *in situ* total scattering. The non-linear thermal expansion behaviour observed for 27.5% yttrium content was linked to changes in disorder of the cationic sublattice. For 10% yttrium and for 10% yttrium, 1% aluminium content, the abrupt increase in cubic phase unit cell volume was found to be due to the tetragonal-cubic phase transformation and a mechanism for this phenomenon was proposed. Impedance measurements also indicated that changes in the state of disorder of the materials occur during heating.

Keywords: Bismuth oxide; Thermal expansion; Phase stability; Total scattering

5.1. Introduction

The thermal expansion behaviour of the materials used in solid oxide fuel cells (SOFCs) is critical for successful device function. The materials should ideally show low positive thermal expansion and the thermal expansion of adjacent materials should be near identical to prevent delamination leading to premature device failure.[1] Previous studies have investigated yttrium-stabilized δ-bismuthates as SOFC electrolytes.[2–6] These materials were found to be very promising from a conductivity standpoint with ionic conductivities measured to be greater than those of the commercialized yttrium-stabilized zirconia (YSZ) and gadolinia-doped ceria (GDC) electrolytes at comparatively lower temperatures. The thermal expansion behaviour of selected yttrium-stabilized bismuthates was previously investigated over 27-706-27 °C.[7] For $Bi_{0.85}Y_{0.15}O_{1.5}$ (15YSB), which was found to be a phase pure cubic material at room temperature from variable temperature powder X-ray diffraction (VT-PXRD) measurements, the thermal expansion behaviour initially showed positive linear thermal expansion from room temperature up to ~550 °C. Thereafter an abrupt increase in cubic unit cell parameter was observed and this was followed by a second region of linear thermal expansion from ~560 °C to 706 °C. The co-efficient of thermal expansion (CTE) in the high temperature region was larger in comparison to that observed in the low temperature region. For a higher yttrium content sample $Bi_{0.725}Y_{0.275}O_{1.5}$ (27.5YSB), which was also found to be phase pure cubic at room temperature, non-linear thermal expansion (NLTE) behaviour was observed over the entire temperature range investigated and no abrupt changes in the cubic unit cell parameter were observed for this composition.

Total scattering studies by Abrahams *et al.*[8] also indicated NLTE behaviour of Bi_3YO_6 and reported this to be correlated to changes in oxide ion distribution during heating, in particular, an increase in the 48i site occupancy. Similar total scattering studies by Leszczynska *et al.*[9] of Bi_3YbO_6 showed NLTE behaviour over the 350-600 °C range and was also attributed to the increase in site occupancy of the 48i site. Powder X-ray diffraction (PXRD) and neutron studies by Leszczynska *et al.*[10] of $Bi_3Y_{1-x}Yb_xO_6$ (x = 0.25, 0.50 and 0.75) described thermal expansion behaviour which was divided into two approximately linear regions with the transition temperature at around 400-500 °C, again attributed to changes in the oxide ion distribution. Borowska-Centkowska *et al.*[11] recently used total scattering studies to investigate the defect structure in δ-$Bi_5PbY_2O_{11.5}$ and also found thermal expansion behaviour comprising two regions of linear thermal expansion above 150 °C. The transition temperature between the two regions was at around 450 °C and this was shown to be correlated to both changes in oxygen stoichiometry and to changes in oxide ion distributions. Using laboratory-based variable temperature PXRD (VT-PXRD) measurements, Holdynski *et al.*[12] also reported two linear regions of thermal expansion for the $Bi_4Nb_{1-x}Y_xO_{8.5-x}$ system ($0.0 \leq x \leq 1.0$) –

one below ~400 °C and one above ~500 °C. This thermal expansion behaviour was attributed to changes in the oxide ion distribution and local vacancy ordering.

Laboratory-based VT-PXRD measurements by Struzik *et al*[13] investigated the thermal expansion behaviour of $Bi_{14}YO_{22.5}$ and showed that a large jump in unit cell volume during heating between 600-650 °C was associated with the tetragonal-cubic phase transition. Similarly, on cooling a similar jump was observed for the reverse phase transition, but over a lower temperature range (from ~550 °C). Borowska-Centkowska *et al.*[14] observed similar volume changes for $Bi_{14}WO_{24}$ using VT-PXRD. The jump in unit cell volume between 750-800 °C during heating was attributed to the same phase transition where additional volume is required to accommodate the disorder of the δ-phase.

The investigation of the NLTE behaviour and the jump in δ-phase unit cell volume of stabilized bismuthates during a thermal cycle is crucial for the potential application of these materials as SOFC electrolytes. In this work, synchrotron-based total scattering measurements are used to probe the thermal expansion behaviour of a cubic stabilized bismuthate as well as tetragonal and cubic phase mixtures. The contribution from the state of disorder of the material towards the observed NLTE behaviour is investigated and particular focus is placed on establishing the phase change mechanism responsible for the rapid increase in δ-phase unit cell volume, which has not been established yet.

5.2. Materials and Methods

5.2.1. Sample preparation

All samples were prepared by means of a citrate sol-gel process. Stoichiometric amounts of bismuth nitrate pentahydrate ($Bi(NO_3)_3.5H_2O$, 99.99% pure, Aldrich) and yttrium nitrate hexahydrate ($Y(NO_3)_3.6H_2O$, 99.8% pure, Aldrich) and additionally for the double doped sample, aluminium nitrate nonahydrate ($Al(NO_3)_3.9H_2O$, 99.99% pure, Aldrich), were dissolved in glacial acetic acid (98% pure, MK Chemical, 99%) under moderate heating and stirring. Aqueous solutions were avoided to prevent the hydrolysis of Bi^{3+}. Excess citric acid monohydrate ($C_6H_8O_7.H_2O$, ACS reagent, Aldrich) was added and the resulting mixture evaporated to form a metal complex paste. Finally, the dried precursor was calcined at 450 °C for 18 h, then ground into a fine powder using an agate mortar and pestle and then annealed at 750 °C for 8 h to obtain the $Al_zY_xBi_{2-x-z}O_3$ powders used for the *in situ* total scattering studies. Three samples were prepared with a varying dopant concentration and are labelled to reflect this. The 10% Y_2O_3 doped Bi_2O_3 sample is called 10YSB (yttria stabilized bismuth oxide) and similarly 27.5YSB and 10Y1AlSB are labelled.

Pellets were prepared for impedance studies by mixing the annealed powders with a 2% polyvinyl alcohol solution (as a binder) and dried at 120 ^{o}C for 20 min. This was then uniaxially pressed at 110 MPa into pellets using a 13 mm diameter die to produce pellets of ~1.2 mm thickness. The pellets were heated at 250 ^{o}C for 4 h to remove the binder and then sintered at 750 ^{o}C for 4 h.

5.2.2. High-energy powder X-ray diffraction experiments

5.2.2.1. Data collection

In situ variable temperature powder diffractograms of 10YSB, 10Y1AlSB and 27.5YSB were collected at the Pair-Distribution Function (PDF) beamline (λ = 0.1671 Å) at the National Synchrotron Light Source II (NSLS-II). The nature of the synchrotron-based instrument[15] allows for the data collected to be of a superior resolution to that measured using lab-based instruments. Each 2D diffractogram was collected for 30 seconds and then reduced into 1D diffraction data using Fit2D.[16] Samples were loaded into quartz capillaries and heated using a hot air blower at a ramp rate of 10 ^{o}C per minute with a dwell time of 30 seconds prior to each measurement. The set temperature range of 60-810-60 ^{o}C was calibrated using standard reference material 640d (silicon powder)[17] and applying thermal lattice expansion corrections to the temperature profile[18,19] resulted in a corrected temperature range of 32-636-32 ^{o}C. 2D powder patterns optimized for both real and reciprocal space were collected simultaneously as near and far field measurements, respectively. Data optimized for reciprocal space analyses were collected in the angular range of ~$0.5 < 2\theta < 15^{o}$, covering a region of the wave vector $Q = ((4\pi/\lambda) \sin \theta)$ up to Q_{max} ~ 10 Å^{-1}. Data optimized for real space analyses were collected in the angular range of ~$0.5 < 2\theta < 41^{o}$, covering a region of the wave vector $Q = ((4\pi/\lambda) \sin \theta)$ up to Q_{max} ~ 26 Å^{-1}. All 2D diffraction data were integrated using FIT2D[16] to generate intensity *vs.* 2θ data which was used for the subsequent analyses.

5.2.2.2. Data analysis of the average crystallographic structure

The average crystallographic structure was determined from the analysis of diffractograms optimized for reciprocal space analysis. The diffractograms were indexed using Bruker AXS DIFFRAC.EVA V4.2 and Rietveld refinement of the diffractograms was done using Bruker AXS TOPAS-Academic Version 6.[20] Instrumental parameters *dQ*, *lor* and *alpha*[21] were extracted from Bragg data of standard reference material 660c (LaB_6)[22] and used to describe the instrument resolution function of both the average Bragg and PDF refinements. *dQ* is a parameter that defines the Gaussian full width at half maximum (FWHM) instrumental width of the Bragg data in *Q*. Owing to the poor approximation of Bragg peak shapes as pure Gaussians, the parameter *lor* models a Lorentzian contribution to the Bragg peak shape and since the

Bragg FWHM increases as a function of *Q*, *r*-dependent broadening is present. This *r*-dependent broadening is modelled with a convolution *alpha*.

5.2.2.3. Data analysis of the local crystallographic structure

The local structure was investigated through the analysis of diffractograms optimized for real space analysis, adopting the *G(r)* formalism as detailed in the sections below.

5.2.2.3.1. The atomic PDF method

The atomic PDF is commonly obtained from total scattering data of powder samples. The function, *G(r)*, describes the probability of finding an atom at a certain distance *r* from another atom[23–27] and essentially describes the distribution of atoms in a sample[28] according to the equation:

$$G(r) = 4\pi r[\rho(r) - \rho_0] \quad (5.1)$$

where $\rho(r)$ is the atomic pair density, ρ_0 is the average number density and *r* is the radial distance.

The PDF is experimentally obtained from the sine Fourier transform of the normalized scattering intensity *S(Q)*[23,24] according to the equation:

$$G(r) = \frac{2}{\pi}\int_{Q_{min}}^{Q_{max}} Q[S(Q) - 1]\, sin(Qr) dQ \quad (5.2)$$

where *Q* is the magnitude of the scattering vector. For elastic scattering, $Q = (4\pi/\lambda) \sin\theta$ with 2θ the scattering angle and λ the wavelength of the radiation used.

5.2.2.3.2. Total scattering data processing and analysis

The integrated data was processed using PDFGetX3[29] to generate *S(Q)* and the PDF, *G(r)*. The PDF data presented here were truncated at a Q_{max} = 24.0 Å^{-1} which was found to be the optimal range of *Q* to maximize real space resolution whilst avoiding termination effects and minimizing statistical noise, which increase with *Q*. Analysis of the PDFs were done via the 'Real Space Rietveld' method[23], using Bruker AXS TOPAS-Academic Version 6.[20,30,31] To avoid ambiguity, Rietveld refinement in reciprocal space will be termed 'Bragg Rietveld' whereas the Rietveld-like data analysis of PDF data will be termed 'PDF analysis.'

5.2.2.3.3. Criteria of fit for the Rietveld analyses

For a typical Bragg Rietveld analysis, the degree of accuracy of the refinement is defined by the agreement factor:[32]

$$\boldsymbol{R_w} = \sqrt{\frac{\sum \boldsymbol{w_m}\left(\boldsymbol{y_{o,m}} - \boldsymbol{y_{c,m}}\right)^2}{\sum \boldsymbol{w_m} \boldsymbol{y_{o,m}^2}}} \tag{5.3}$$

where $y_{o,m}$ and $y_{c,m}$ are the observed and calculated data at data point m, respectively, and w_m is the weighting given to data point m where $w_m = 1/\sigma(y_{o,m})^2$ and $\sigma(y_{o,m})$ is the standard error in $y_{o,m}$.

For a PDF analysis, a similar R_w factor is applied, however, the formula is slightly modified to account for the calculation in real space:[33]

$$R_w = \sqrt{\frac{\sum_{i=1}^{N} \sum \boldsymbol{w}(\boldsymbol{r_i})[\boldsymbol{G_{obs}}(\boldsymbol{r_i}) - \boldsymbol{G_{calc}}(\boldsymbol{r_i})]^2}{\sum_{i=1}^{N} \sum \boldsymbol{w}(\boldsymbol{r_i}) \boldsymbol{G_{obs}^2}(\boldsymbol{r_i})}} \tag{5.4}$$

where G_{obs} is the PDF extracted from the total scattering diffraction data, G_{calc} is the PDF calculated from the structural model and $w(r_i) = 1/\sigma(r_i)^2$ where $\sigma(r_i)$ is the standard deviation at a distance r_i.

5.2.3. Electrochemical impedance spectroscopy

Impedance of the sintered pellets was measured using a BioLogic MTZ-35 frequency response analyser interfaced to a computer running MT-Lab software version 1.21. This was coupled to a BioLogic HTF-1100 furnace and a HTSH-1100 sample holder were employed. The additional system impedances were compensated for prior to measuring the impedance of the samples. A frequency range of 0.1 Hz to 1 MHz and an amplitude of 10 mV was employed. The measurements were taken in steps of 50 °C within the range 300–750 °C, with a 30 min dwell time per step. The sample holder consists of two platinum discs, of a similar diameter to the sample, between which the pellet is placed and the spring-loaded system in then tightened. No additional coatings were used on the pellet. Each pellet was measured using two consecutive heating and cooling cycles. The Nyquist plots were modelled via an equivalent circuit approach using EC-Lab version 11.21. From this process, ionic conductivities of the materials were calculated over the temperature range studied.

5.3. Results and discussion

5.3.1. Analysis of the average structure evolution of 27.5YSB during *in situ* heating using Bragg scattering

The NLTE behaviour of stabilized bismuthates has been largely attributed to changes in oxide ion distribution.[8–12] NLTE behaviour was previously observed for 27.5YSB over the temperature range of

27-706-27 °C[7] and speculated to be caused by changes in oxide ion distribution. Another possible cause for the observed NLTE behaviour are changes in the overall state of disorder of the material. The thermal expansion of 27.5YSB was again investigated in this work using higher resolution VT-PXRD measurements to investigate the contribution of metal ion lattice disorder on the observed NLTE behaviour.

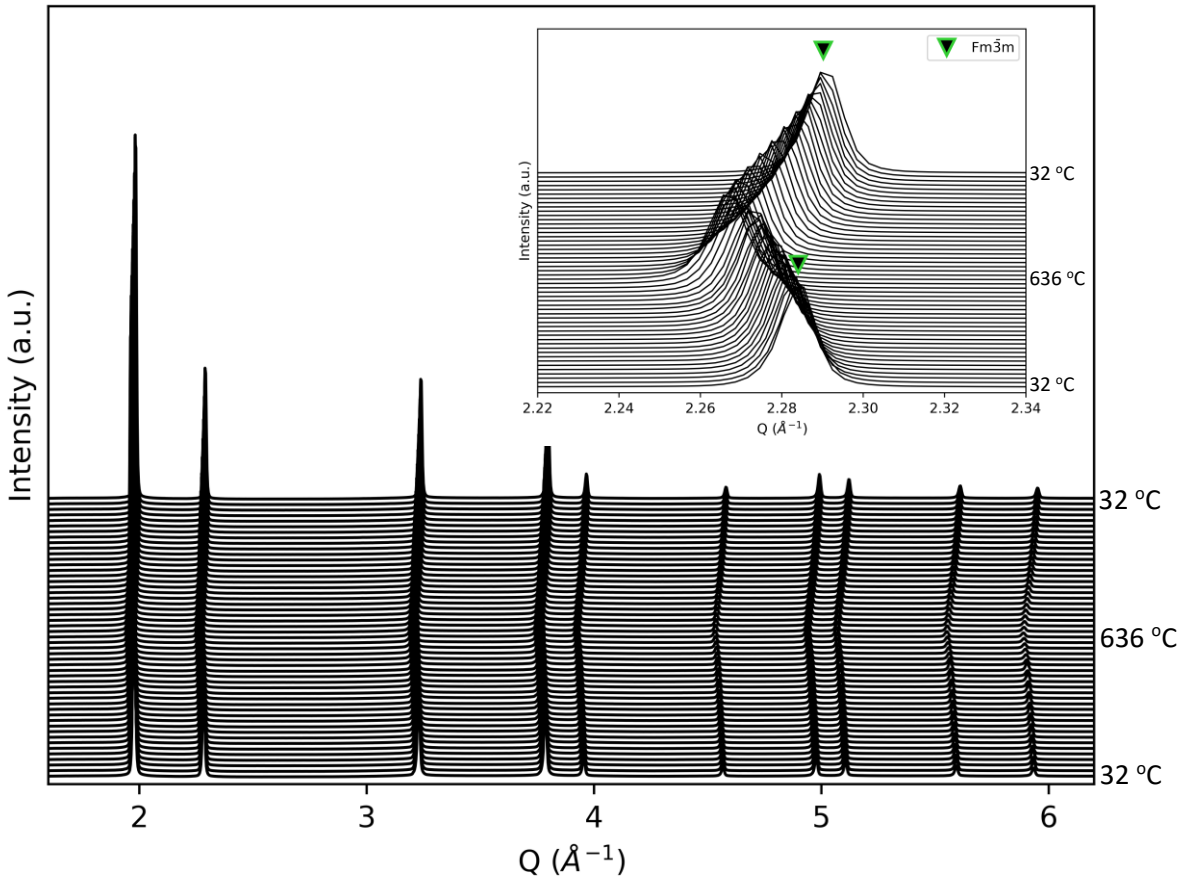

Figure 5.1. *In situ* VT-diffractograms collected for the 27.5YSB material over the temperature range of 32-636-32 °C. No impurity phases or abrupt unit cell volume changes were present during either the heating or cooling cycles.

The diffractograms collected for the 27.5YSB material display no peak asymmetries nor any phase change behaviour, indicating that it is a phase pure cubic material over both the heating and cooling cycles (Fig. 5.1). This material displayed NLTE behaviour (Table 5.1 and Fig. 5.2) over the temperature range investigated, as was exhibited in our previous work.[7] The increased resolution and heating control enabled by the synchrotron-based experiment in this work allows for the thermal expansion behaviour to be probed in significantly increased detail.

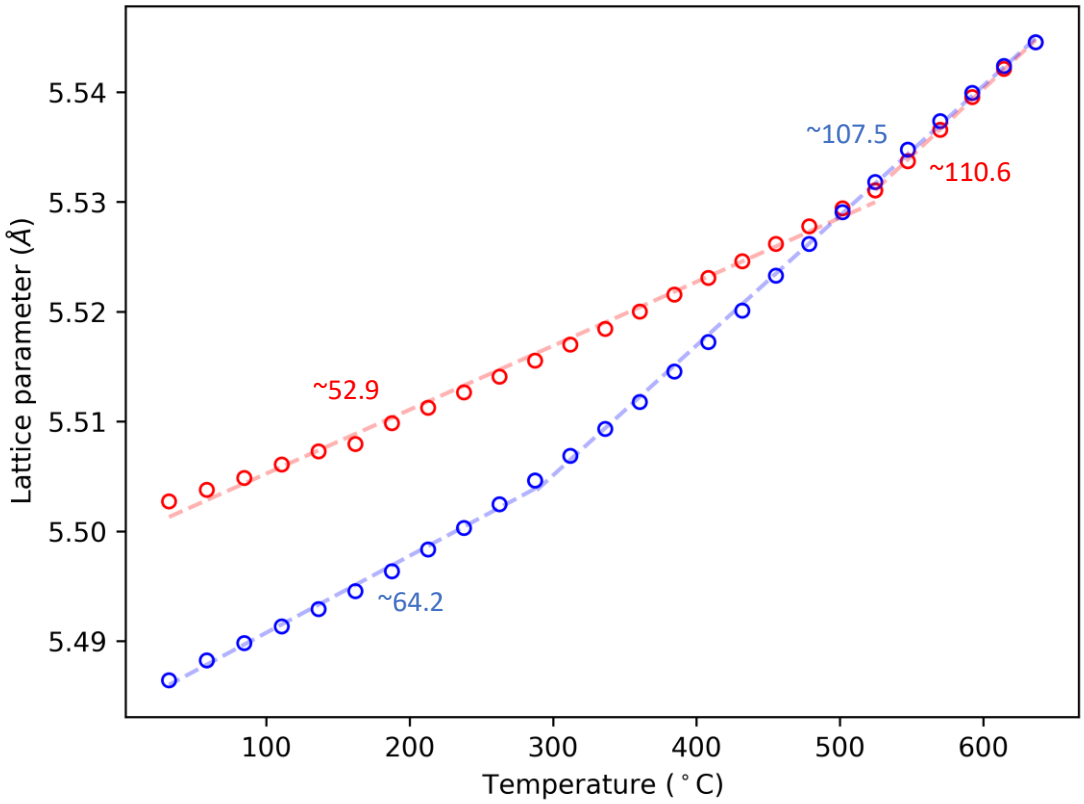

Figure 5.2. Cubic phase lattice parameter variation of the 27.5YSB material over the temperature range of 32-636-32 °C. The heating cycle is shown with red lines and the cooling cycle with blue lines. Approximate linear CTEs (x 10^{-6} K^{-1}) from Table 5.1 are indicated.

This increased resolution enables the non-linearity in thermal expansion to be resolved into two approximately linear regions: a linear low-temperature region and a linear high-temperature region are present during both the heating and cooling cycles (Fig. 5.2 and Table 5.1). The presence of similar linear low- and high-temperature regions of thermal expansion has been reported by Holdynski *et al.*[12] in the $Bi_4Nb_{1-x}Y_xO_{8.5-x}$ system ($0.0 \leq x \leq 1.0$) and the change in CTE magnitude was attributed to changes in oxide ion distribution and local vacancy ordering.[10–12] An alternative explanation for the changes observed in the CTEs is a change in the overall state of disorder of the material, as is proposed in this work. During heating an order-disorder transition could occur and as such the material in its disordered state is postulated to have a higher CTE, and hence it is expected that a disorder-order transition would occur during cooling.

Table 5.1. Cubic phase CTE variation of the 27.5YSB material over the temperature range 32-636-32 °C

Temp range (°C)	CTE (10^{-6} K^{-1})
32-525	52.9 ± 1.3
525-636	110.6 ± 1.7
636-287	107.5 ± 1.0
287-32	64.2 ± 1.5

Interestingly, the 27.5YSB material exhibited a substantial decrease in the unit cell parameter (~0.0163 Å) after the overall thermal cycle. Previous work by Struzik *et al*.[13] reported a decrease in unit cell volume of $Bi_{14}YO_{22.5}$ after a thermal cycle and attributed this change to differing degrees of disorder after the thermal cycle. It was suggested that the slow cooling of the sample during the VT-PXRD measurement induced structural relaxation (i.e. a decrease in disorder) which would result in a decreased unit cell volume after the thermal cycle. The decreased unit cell volume observed for 27.5YSB in this work was likely due to similar structural relaxation.

5.3.2. Analysis of the local structure evolution of 27.5YSB during *in situ* heating using PDF analysis

From the *in situ* Bragg data for 27.5YSB it was ascertained that the average structure of the material was cubic throughout the thermal cycle, but a change in the CTE magnitude was observed during both the heating and cooling cycles. This change was possibly due to changes in the order of the material. *In situ* real space data was used to further investigate this order-disorder transition. The PDF of a material generates peaks at values of *r* that correspond to interatomic distances between pairs of atoms in the material. From these peaks, various information pertaining to the local structure can be derived. The peak position describes the bond length distribution whereas the peak area and peak width are related to the coordination number and disorder, respectively.[26] Figure 5.3 shows the *G(r)* curves for the 27.5YSB material in the $1.5 \leq r \leq 30$ Å range collected *in situ* over the temperature range of 32-636-32 °C.

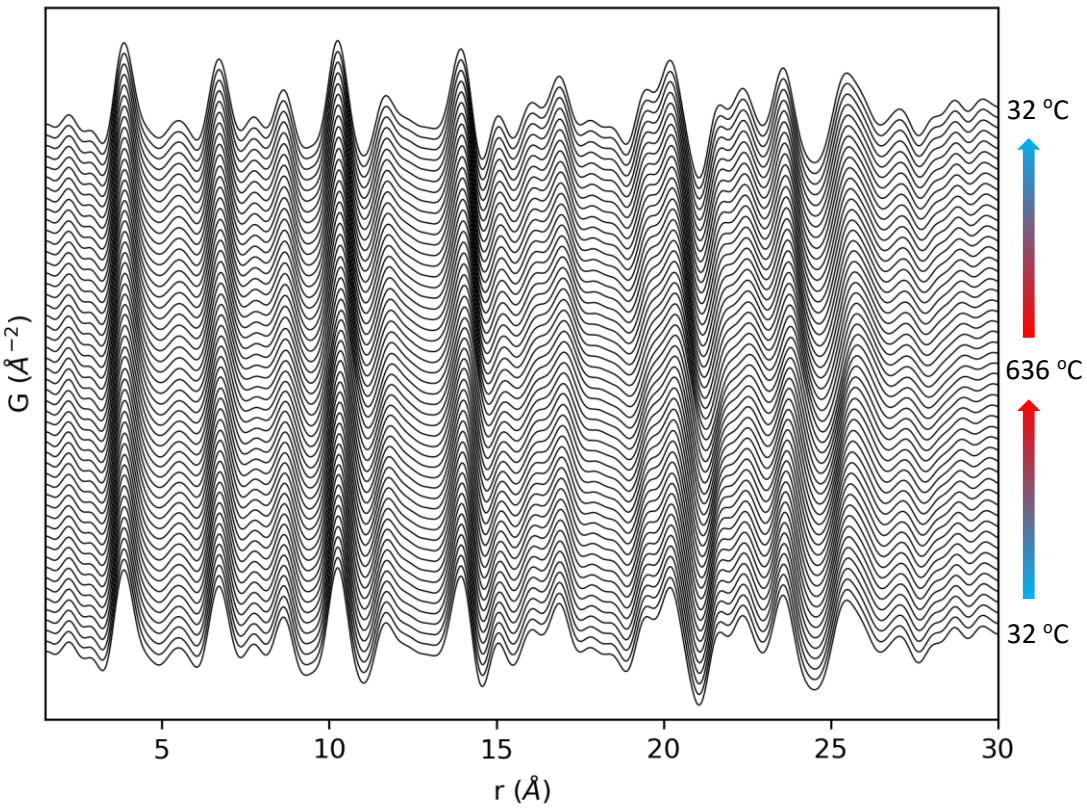

Figure 5.3. *In situ* PDFs collected for the 27.5YSB material over the temperature range of 32-636-32 °C.

Since the 27.5YSB material was phase pure throughout the thermal cycle it enabled focusing on short interatomic distances (i.e. distances within a single unit cell) and the assignment of several *G(r)* peaks to pairs of atoms present in the average *F*m$\bar{3}$m crystal structure (Fig. 5.4a).

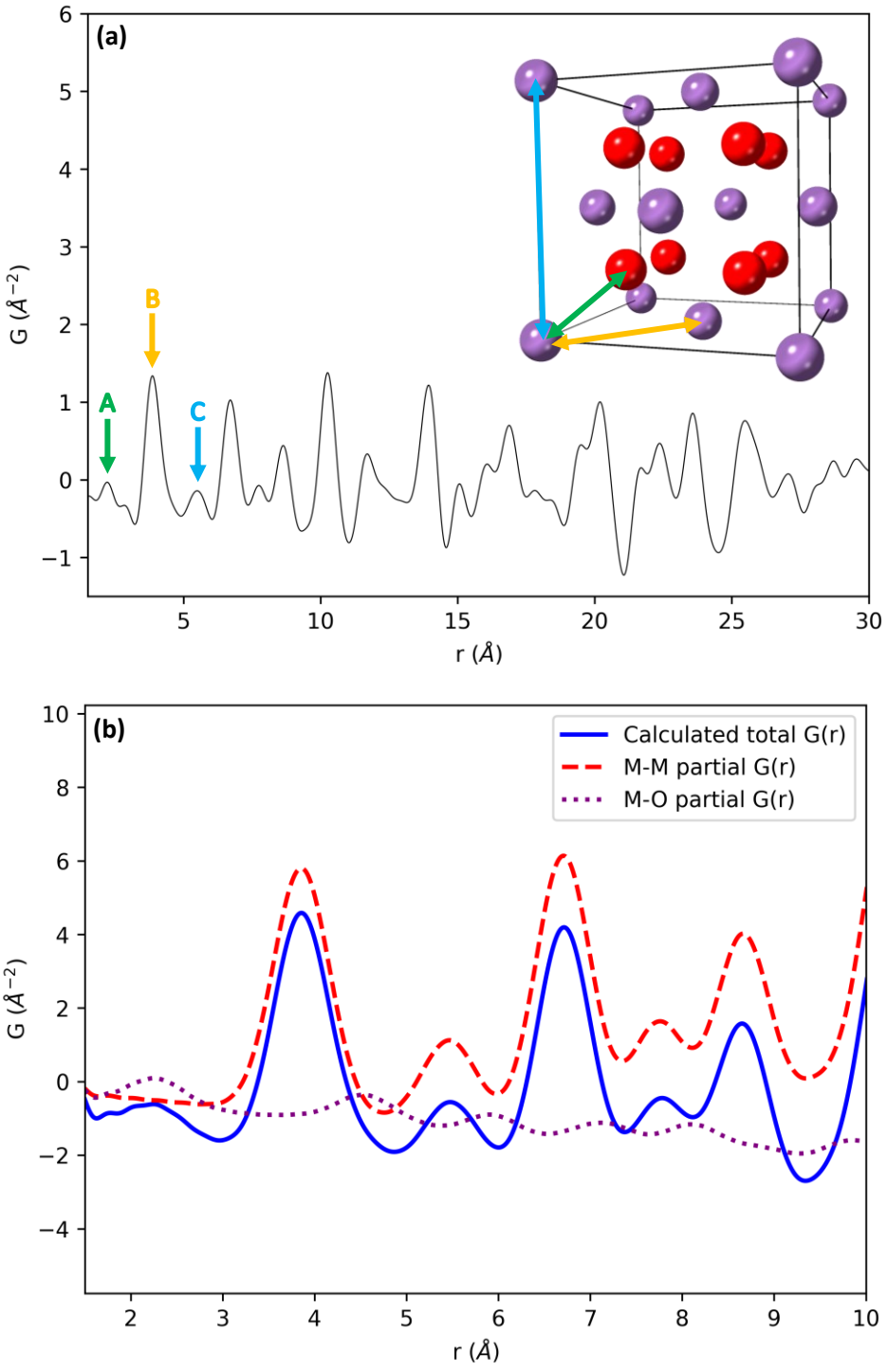

Figure 5.4. (a) *In situ* PDF collected for 27.5YSB at 32 °C. Interatomic distances responsible for the first three peaks are indicated in the unit cell of *F*m$\bar{3}$m with only the 8c oxygen sites included for clarity. Purple and red spheres represent metal and oxygen ions, respectively. (b) Total and partial PDFs of the 27.5YSB material calculated for the average fluorite structure derived from the Bragg Rietveld analysis at 32 °C.

Peak A is the M-O nearest neighbour (NN) distance in the structure. This peak is noisy due to the prominent termination ripple contributions at low-*r,* and it is of low intensity and broad as it describes the bond length distribution of M-O NN distances to three crystallographically unique oxygen sites: M-O_{8c}, M-O_{32f} and M-O_{48i}. These broad M-O bond length distributions present in the fluorite structure limit the resolution of this peak in comparison to peaks resulting from M-M pairs (Fig. 5.4b). Additional resolution limitation of M-O bonds is due to the immense disparity in scattering strength of X-ray radiation between the M and O atoms. Hence this PDF feature is not discussed further. Peak B is the M-M NN distance which corresponds to the distance between M atoms on the corners and M atoms on the face of the unit cell. This feature is referred to as the M_1-M_1 interaction. Peak C coincides with the *F*m$\bar{3}$m cell parameter and as such is assigned to the distance between M atoms long the corners of the unit cell. This feature is referred to as the M_2-M_2 interaction. Peaks B and C are investigated as they each correspond to unique M-M atomic pairs present within the cubic phase unit cell and no significant *G(r)* peak overlap is expected (Fig. 5.4b). Hence monitoring these peaks during *in* situ heating will provide an indication of the M-M bond length changes and state of disorder of the material, albeit only the state of disorder of the cation sublattice.

PDF analyses were initially used to investigate the nature and correlation length of disorder present in the 27.5YSB material. This analysis was performed using low-*r vs*. high-*r* refinements wherein the average *F*m$\bar{3}$m structure was refined against the *G(r)* data over varying length scales. In this work, the low-*r* region data ($1.5 \leq r \leq 10$ Å) and the high-*r* region data ($10 \leq r \leq 30$ Å) were fitted independently to investigate if the average structure model correctly describes the local structure, and if so, over what length scales. The same approach was applied to all the PDFs collected *in situ* to investigate the local structure evolution during the thermal cycle. The best fits achieved at selected temperature steps during the heating cycle over the low-*r* and high-*r* ranges are shown in Figure 5.5.

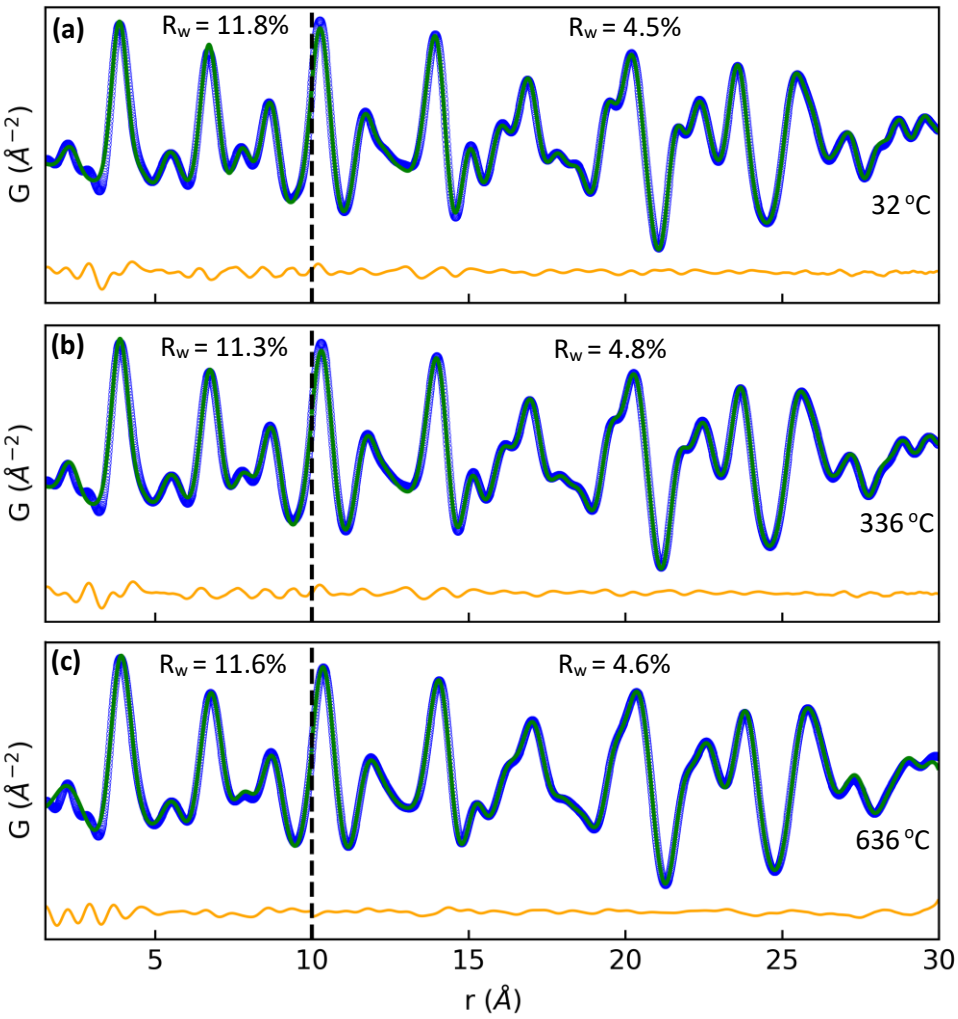

Figure 5.5. Selected PDF low-*r* and high-*r* refinements using PDF analysis and the average cubic *F*m$\bar{3}$m structure over both *r* ranges for 27.5YSB. Refinements shown are for data collected at (a) 32 °C, (b) 336 °C and (c) 636 °C. Observed (blue markers), calculated (green curve) and difference (orange curve) profiles are shown along with agreement factors.

The PDF analyses for 27.5YSB showed that the average structural model had varying success in fitting the experimental *G(r)* data over different length scales and correctly interpreted the experimental *G(r)* data over the entire 1.5 ≤ *r* ≤ 30 Å range during the thermal cycle. The fit quality over the 1.5 ≤ *r* ≤ 10 Å range was reduced in comparison to that over the 10 ≤ *r* ≤ 30 Å range. The average structural model did, however, reasonably interpret the position, intensity and shape of the experimental *G(r)* peaks in the low *r* range and this decrease in fit quality was attributed to local disorder over the 1.5 ≤ *r* ≤ 10 Å range. This disorder could be viewed as defect clusters in which the interatomic bond lengths had multiple distributions which deviated from the average structural model. The extent of disorder present in this

material seemed to be limited to $r \leq$ ~10 Å and exhibited a similar trend over the thermal cycle. In this work, this low *r* range is described as the most distorted shell, varying significantly from the average structure. The *G(r)* peaks B and C in the low *r* range were investigated using the so-called direct analysis approach. This involves the fitting of *G(r)* peaks with Gaussian functions after linear subtraction of the baseline (Figs. 5.6a, 5.6b, 5.7a and 5.7b). The Gaussian fitting was done using an in-house developed Python script which was benchmarked by comparing the Gaussian fit parameters determined for several *G(r)* peaks against those determined using Fityk[34] and Bruker AXS TOPAS-Academic Version 6.[20] Direct analysis enables the position and width of the peaks to be determined throughout the thermal cycle which provides useful insight on the local structure and disorder variation as a function of temperature.

The position of both peaks B (Fig. 5.6c) and C (Fig. 5.7c), representing the M-M pairs within the unit cell, shift to higher *r* values with increasing temperature as expected for positive thermal expansion and this was also observed in the Bragg Rietveld analyses. This indicates that thermal expansion occurs on a local level as well. The width of peaks B and C, related to the disorder for the corresponding atomic pairs, was also monitored as a function of temperature (Figs. 5.6d and 5.7d, respectively) and appears to increase linearly with increasing temperature. This is expected for this system as higher temperatures would increase disorder due to the increased thermal motion of atoms. However, there was no abrupt increase in peak width which is expected for the abrupt order-disorder transition. The increase in the width of peak B (Fig. 5.6d) with increasing temperature is more correlated than that observed for peak C (Fig. 5.7d). This possibly indicates the presence of multiple bond length distributions present that contribute to peak C and hence the fitting achieved with a single Gaussian function is not optimal. For peak B, a single Gaussian function successfully represented the peak profile and hence indicated one bond length distribution corresponding to this *G(r)* peak. This emphasizes the need to monitor more than a single *G(r)* peak when applying a direct analysis. Interestingly, the width of peak B observed during the cooling cycle was larger than that observed during the heating cycle. This trend is similar to that observed for the change in unit cell volume from the Bragg Rietveld analyses (Fig. 5.2) and indicates that a more ordered state was achieved on cooling.

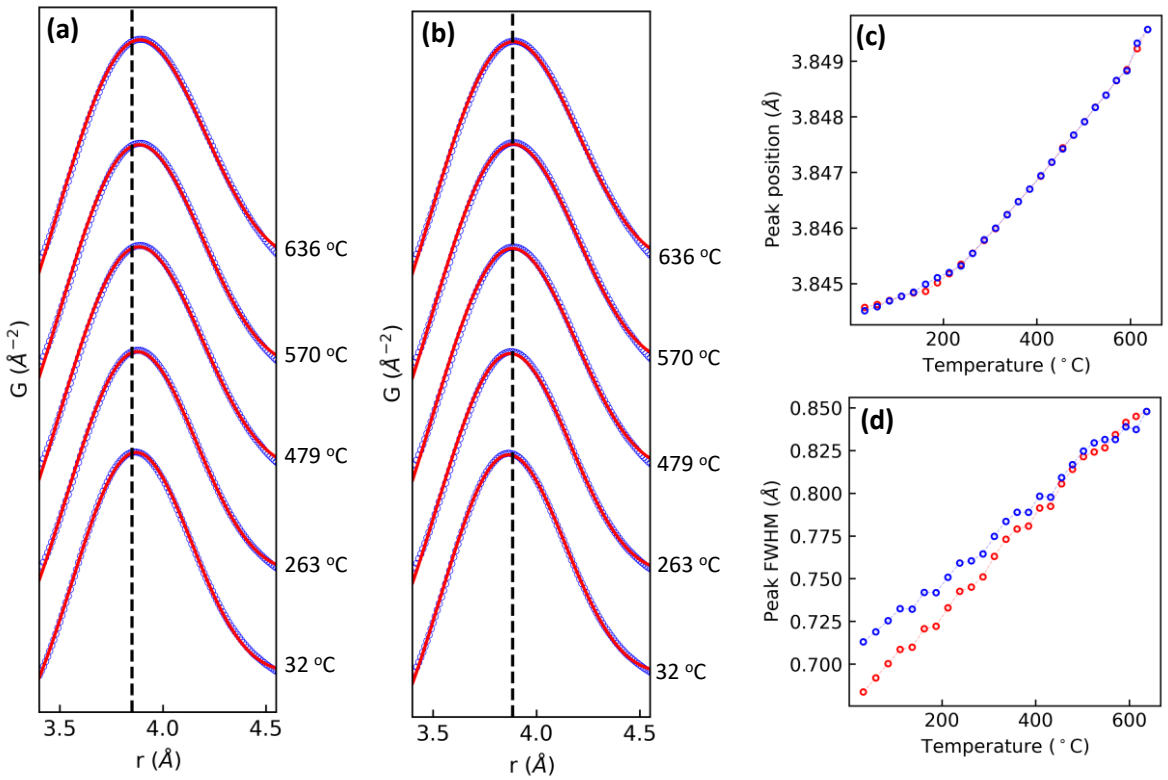

Figure 5.6. Gaussian fits (red lines) of PDF peak B (blue markers) for 27.5YSB at selected temperatures during the (a) heating and (b) cooling cycles. The black dotted line in (a) indicates the first peak position (at 32 °C) for comparison and similarly the black dotted line in (b) indicates the peak position at 636 °C. Variation of the (c) peak position and (d) peak width during both the heating (red markers) and cooling (blue markers) cycles are shown. Standard errors associated with peak position and FWHM are ~0.0001 Å and ~0.003 Å, respectively.

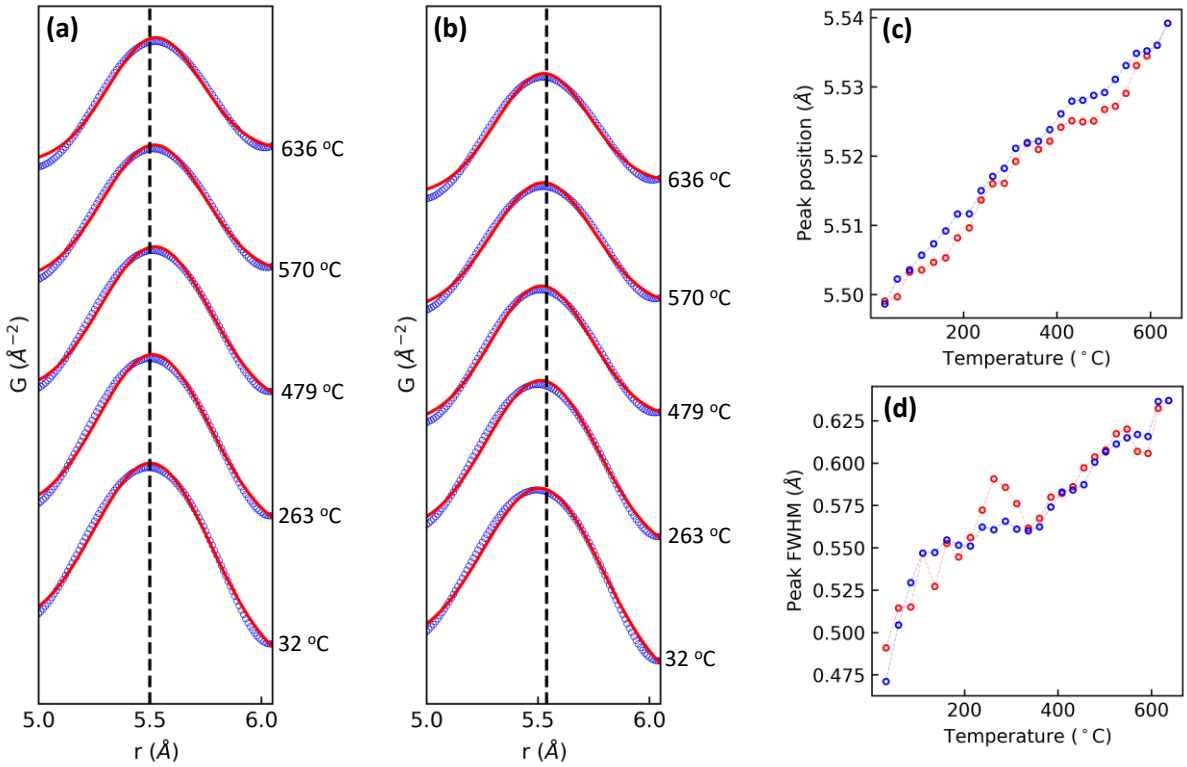

Figure 5.7. Gaussian fits (red lines) of PDF peak C (blue markers) for 27.5YSB at selected temperatures during the (a) heating and (b) cooling cycles. The black dotted line in (a) indicates the first peak position (at 32 °C) for comparison and similarly the black dotted line in (b) indicates the peak position at 636 °C. Variation of the (c) peak position and (d) peak width during both the heating (red markers) and cooling (blue markers) cycles are shown. Standard errors associated with peak position and FWHM are ~0.003 Å and ~0.009 Å, respectively.

Ideally the structural disorder of the material during the thermal cycle should be determined by monitoring the variation of the thermal displacement parameters of both the metal cations and oxygen anions. Unfortunately the use of X-ray scattering experiments to probe the nature and structure of the oxygen sublattice is not possible, as discussed. Therefore, only the thermal displacement parameters of the metal cations were monitored via both the Bragg Rietveld and PDF analyses (Fig. 5.8). Systematic increases in the cationic thermal displacement parameter are expected due to increased thermal motion during heating. This is visualized in the same way as a linear CTE wherein heating of the material results in a linear increase in unit cell parameter. A deviation from a regular increase in thermal motion serves as an indicator of an abrupt change in the state of disorder of the material which represents the order-disorder transition. For both the Rietveld and PDF analyses, to avoid over-parameterization and consequent parameter correlations, only the cell parameter and one thermal displacement parameter for

all cationic sites were allowed to vary. Both analyses show an increase in the cationic thermal displacement parameters with heating as expected, however, the magnitude of the thermal displacement parameters derived is questionable. In general, δ-bismuthates are known to be highly disordered, and this disorder is accentuated by elevated temperatures, however, for metal oxides the realistic range for this parameter is reported to be between ~0.013-0.038 Å^2.[35] It must also be noted that in the PDF analysis approach taken in this work (i.e. small-box modelling in Topas) the only parameter that is varied to account for peak broadening is U_{iso} and this results in the unrealistic inflation of this value during the refinements. Since the U_{iso} values derived here for the YSB materials surpass the reported realistic range, the emphasis is rather placed on the trends observed in the changes in U_{iso} with increasing temperature. Changes in U_{iso} during heating derived from the Bragg Rietveld analysis (Fig. 5.8a) are approximately linear until ~500 °C, thereafter a sharp increase in U_{iso} is observed which indicates an abrupt increase in disorder. From the PDF analysis (Fig. 5.8b) the increase in U_{iso} is approximately linear until ~384 °C, followed by a similar sharp increase in U_{iso}. This transition is visualized as an abrupt transition to a state of increased disorder – significantly more disorder than that which is gained via thermal motion during heating or that which is inherently present in this disordered material system.

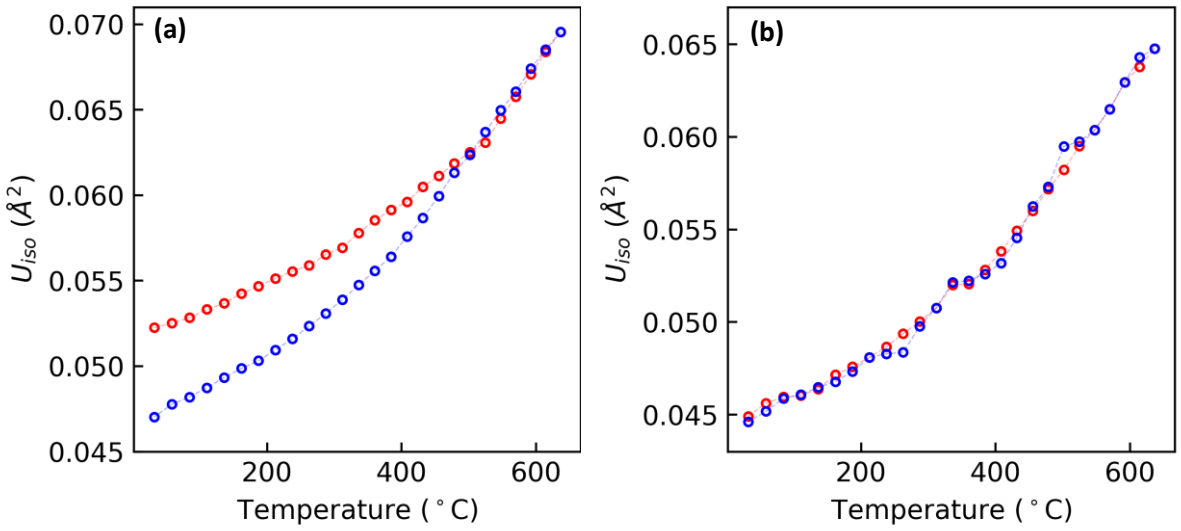

Figure 5.8. Variation of the cationic thermal displacement parameter (U_{iso}) of annealed δ-27.5YSB derived from the (a) *in situ* Bragg Rietveld and (b) *in situ* PDF analyses. Standard errors associated with U_{iso} derived from Bragg Rietveld and PDF analyses are ~0.0005 Å^2 and ~0.0003 Å^2, respectively.

The discrepancy in transition temperature between the average and local structural analyses is noteworthy. The lower transition temperature observed for the local structure indicates that the order-disorder transition is initially confined to the local structure. This is consistent with the results from the low-*r vs*. high-*r* PDF analyses (Fig. 5.5) which indicated that high disorder is initially present in the defect cluster. This is expected to lower the activation energy of the order-disorder transition on the local scale as a whole and this is what was observed. The average, long range structure experiences the similar transition at a higher temperature which indicates that the activation energy for this transition is higher over extended length scales. Interestingly, the average long range structure exhibits structural relaxation (i.e. less disorder) after the thermal cycle (Fig. 5.8a) whereas the average local structure remains unchanged (Fig. 5.8b). These abrupt increases in disorder coincide with the abrupt changes in the CTE derived from both the Bragg and PDF analyses (Fig. 5.9), where the latter was determined over the $1.5 \leq r \leq 30$ Å range. This indicates that these changes in disorder contribute to the observed increase in the CTE magnitude. A more disordered material is therefore proposed to have an increased rate of thermal expansion and the order-disorder transition can be monitored by investigating changes to the rate of thermal expansion of the material. Interestingly, the lattice parameter variation derived from both analyses follow the same trend (Fig. 5.9). This indicates that the thermal expansion behaviour of the average long-range and average local structure is similar.

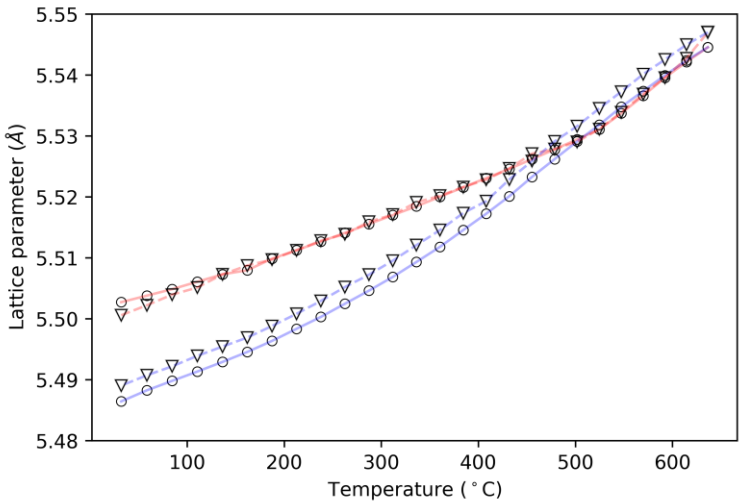

Figure 5.9. Cubic phase lattice parameter variation of the 27.5YSB material over the temperature range of 32-636-32 °C derived from *in situ* Bragg Rietveld (circle markers, same as Fig. 5.2) and PDF (triangle markers) analyses. The heating cycle is shown with red lines and the cooling cycle with blue lines. Standard errors associated with lattice parameters derived from Bragg Rietveld and PDF analyses are ~0.0007 Å and ~0.0001 Å, respectively.

5.3.3. Analysis of the average structure evolution of 10YSB and 10Y1AlSB during *in situ* heating using Bragg scattering

The *in situ* thermal stability of 15YSB has been previously investigated using lab-based PXRD over the temperature range of 27-706-27 °C.[7] During initial heating (in the temperature range of ~27-551 °C) the thermal expansion was linear. However, upon further heating a very abrupt increase in the lattice parameter was noted over 551-563 °C and was then followed by a second region of linear thermal expansion of increased magnitude (in the temperature range of 563-706 °C). On cooling, similar behaviour was seen with an abrupt change in lattice parameter occurring over a lower temperature range of 523-477 °C and the rate of thermal expansion returning to a magnitude similar to that which was initially observed. The abrupt changes in lattice parameter for 15YSB are possibly due to a phase transformation[13,14] although no additional phases were detected which could be attributed to the limited resolution of the lab diffractometer used. In this work, the *in situ* variable temperature phase stability of 10YSB and 10Y1AlSB, both comprised of cubic ($F\bar{3}m$, SG #225) and tetragonal ($P4_2/nmc$, SG #137) phase mixtures, are investigated using synchrotron-based PXRD over the temperature range of 32-636-32 °C. Previous work by Struzik *et al.*[13] and Borowska-Centkowska *et al.*[14] showed that the tetragonal-cubic phase transformation of doped bismuthates occurs above 500°C and this was also observed in our previous work on YSB materials.[6] Therefore, the *in situ* variable temperature investigation employed serves to elucidate the effect of this phase transformation on the changes observed in the cubic phase lattice parameter.

For sample 10YSB, a starting cubic and tetragonal phase mixture was identified by the prominent peak asymmetry which is primarily caused by the tetragonal phase content.[6] This asymmetry is present during heating over the temperature range of 32-547 °C and again during cooling over the range of 432-32 °C, indicating the presence of a phase pure cubic material over the temperature range of 570-636-455 °C (Fig. 5.10).

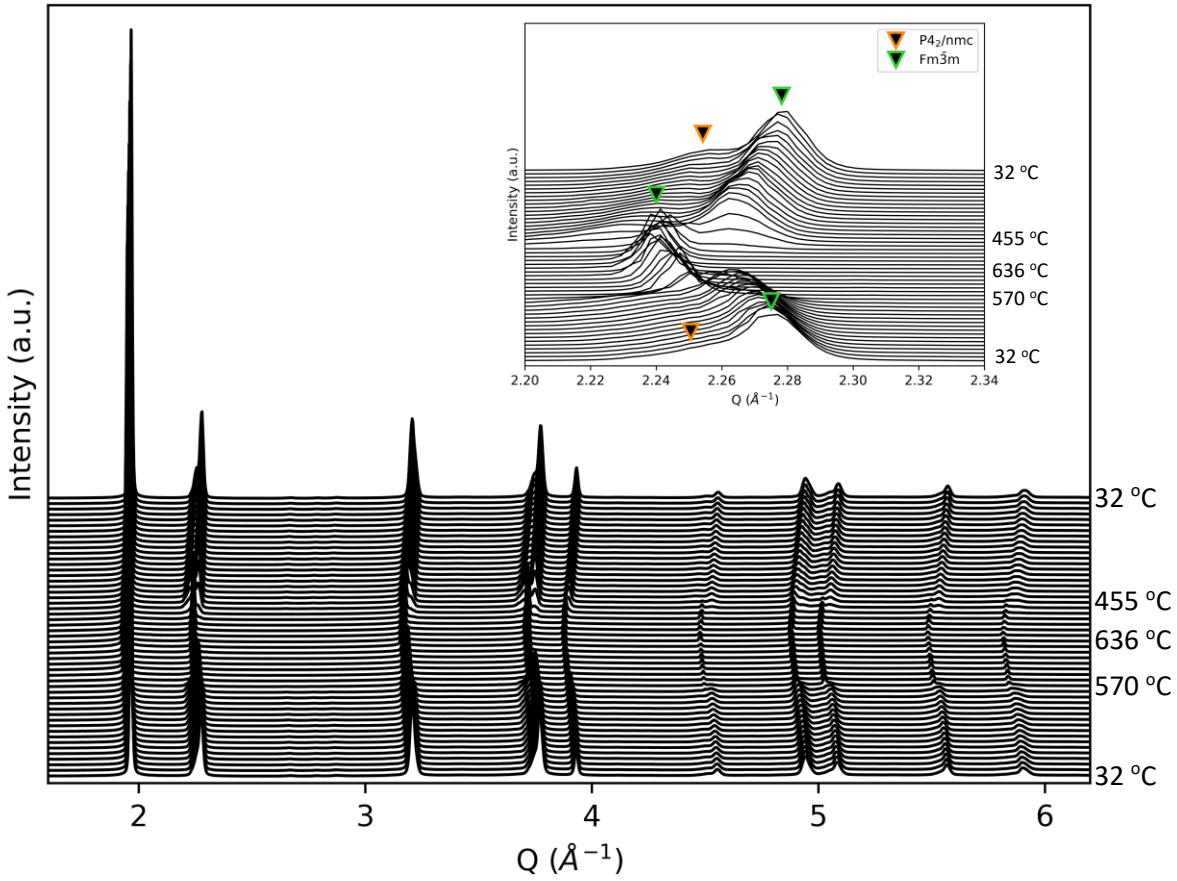

Figure 5.10. *In situ* diffractograms collected for the 10YSB material over the temperature range of 32-636-32 °C. Tetragonal phase content (evident as peak asymmetries in the inset) is present during the heating cycle (orange ▼, 32-547 °C) and reappears during the cooling cycle (orange ▼, 432-32 °C). An abrupt change in unit cell volume of the cubic phase is also evident during both the heating (green ▼, 479-525 °C) and cooling cycles (green ▼, 455-360 °C).

The fit from a Rietveld analysis of the 10YSB material at ~32°C during the heating cycle is given in Figure 5.11 as an example and the phase content for the phase mixture during both the heating and cooling cycles was determined by multiphase Rietveld refinement. Due to the prominent overlap of diffraction peaks for the cubic and tetragonal phases, fitting of peak asymmetries is problematic (as shown in the inset of Figure 5.11). This leads to some uncertainty in the refined parameters as illustrated by the

fluctuation in the refined cubic phase content during the thermal cycle (Fig. 5.12a). Although this fluctuation could in principle reflect a dynamic phase equilibrium between the tetragonal and cubic phases, it is not expected for this material system and rather emphasizes the limitation of the Rietveld analyses to resolve phase fractions of a multiphase system where significant peak overlap exists.

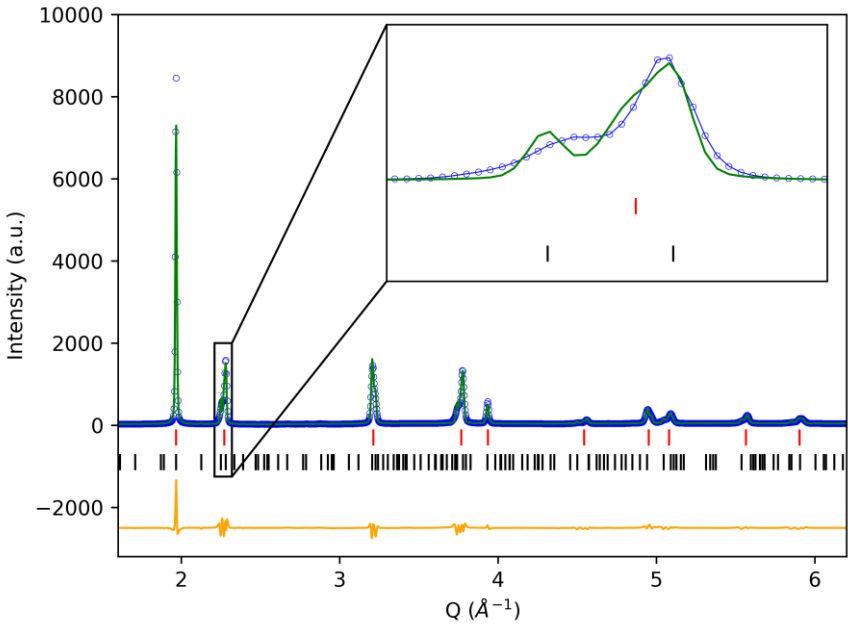

Figure 5.11. *In situ* diffractogram of the 10YSB material collected at ~32 °C analysed by means of Rietveld refinement. The observed pattern is shown in blue, the calculated in green and the difference in orange. Miller indices corresponding to the cubic and tetragonal phases are shown with red and black ticks, respectively. The inset in (a) accentuates the peak asymmetry contribution from the presence of the tetragonal phase.

The thermal expansion behaviour of the cubic phase fraction of 10YSB was investigated by monitoring the variation in lattice parameter over the thermal cycle (Fig. 5.12b and Table 5.2). The rate of thermal expansion observed for 10YSB over 525-636 °C during the heating cycle (120.8 x 10^{-6} K^{-1}) is lower compared to that for δ-15YSB[6] over 589-769 °C (152.4 x 10^{-6} K^{-1}) which is unexpected since higher Y^{3+} content was found to decrease the CTE. An abrupt unit cell volume change was observed for the cubic phase during heating over the range 479-525 °C (Fig. 5.12b) and an increased CTE over the remaining heating cycle range of 525-636 °C is evident. This increased magnitude of thermal expansion is maintained during the initial section of the cooling cycle over the range of 636-455 °C. With further cooling a similar abrupt change in unit cell volume occurs, however, over a slightly lower and wider temperature range of

455-384 °C and between 384-32 °C the thermal expansion behaviour returns to the magnitude that was measured over the initial heating temperature range.

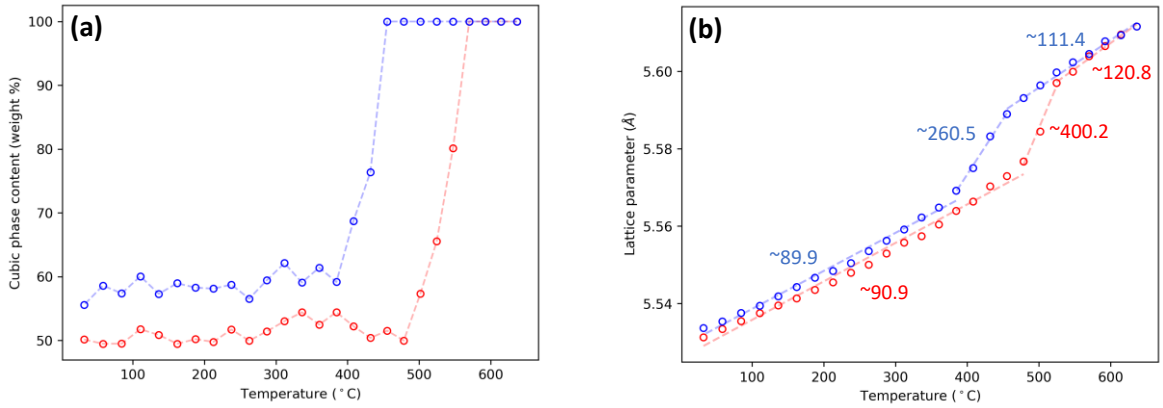

Figure 5.12. (a) Cubic phase purity and (b) cubic phase lattice parameter variation of the 10YSB material over the temperature range of 32-636-32 °C. The heating cycles are shown with red markers and the cooling cycle with blue markers. Approximate linear CTEs (x 10^{-6} K^{-1}) from Table 5.2 are indicated in (b).

Table 5.2. Cubic phase CTE variation of the 10YSB material over the temperature range 32-636-32 °C.

Temp range (°C)	CTE (10^{-6} K^{-1})
32-479	90.9 ± 2.5
479-525	~400.2
525-636	120.8 ± 5.1
636-455	111.4 ± 4.4
455-384	~260.5
384-32	89.9 ± 2.5

The abrupt changes in cubic phase lattice parameter during both the heating and cooling cycles coincide with the temperature range at which abrupt changes in phase purity are observed (Fig. 5.12). As such, it was predicted that higher tetragonal phase content would amplify the abrupt lattice parameter changes. The *in situ* variable temperature phase stability of the 10Y1AlSB material was similarly investigated (Fig. 5.13). Jolley *et al.*[36] recently demonstrated that the phase observed in the doped bismuth oxide system is dependent on both the average dopant ionic radius and the total dopant concentration. As such the incorporation of Al^{3+} in the 10YAlSB material reduces the average dopant ionic radius by ~4.3% (Al^{3+} = 0.535 Å, Y^{3+} = 1.019 Å[37]) in comparison to that of 10YSB and this promotes tetragonal phase formation. The tetragonal phase content of 10Y1AlSB prior to the *in situ* measurement is ~70% (Fig. 5.14a) which is significantly greater than the ~50% tetragonal phase content observed for 10YSB (Fig. 5.12a). The

cubic phase content of 10Y1AlSB was also found to fluctuate during the thermal cycle and an apparent slight decrease in cubic phase content was seen with increasing temperature (Fig. 5.14a) – these features are attributed to the same reasons described for 10YSB.

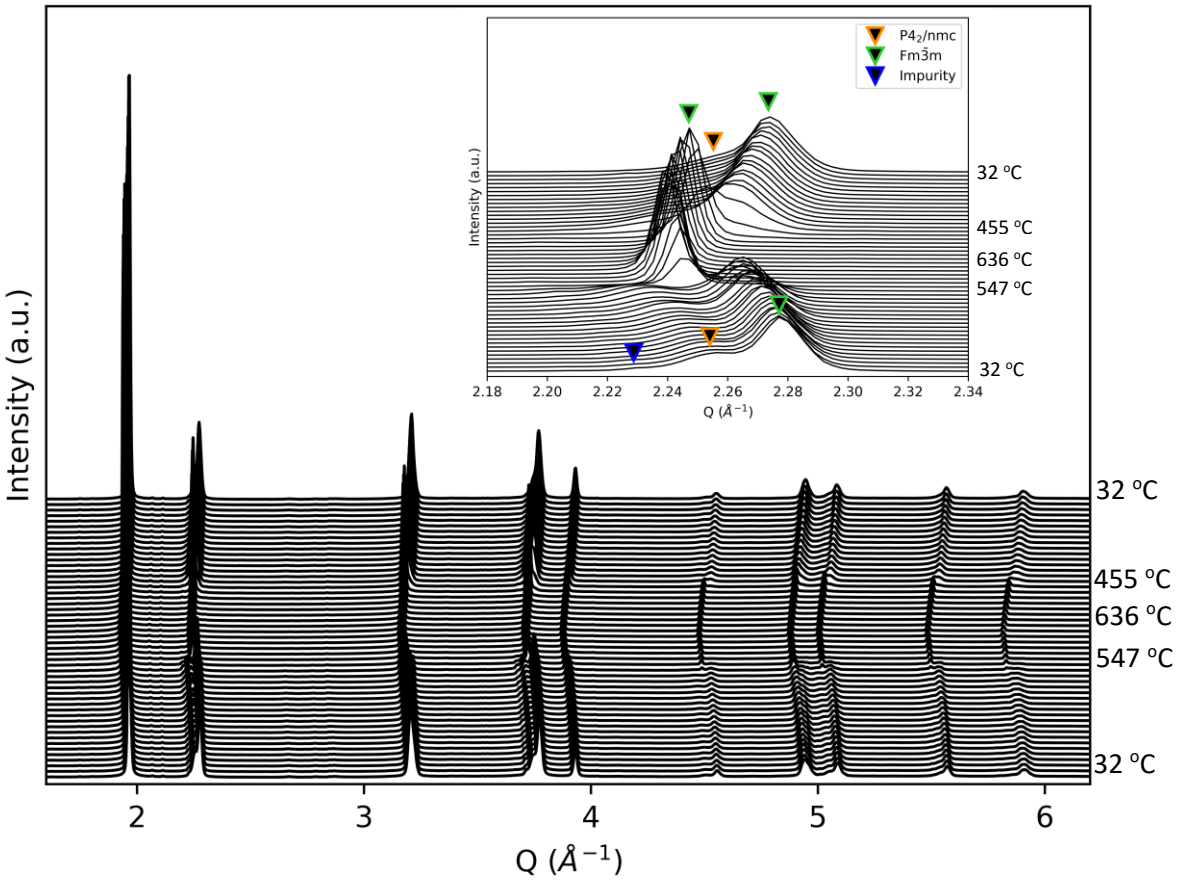

Figure 5.13. *In situ* diffractograms collected for the 10Y1AlSB material over the temperature range of 32-636-32 °C. The tetragonal phase (evident as peak asymmetries in the inset) was present during the heating cycle (orange ▼ symbol, 32-525 °C) and during the cooling cycle (orange ▼ symbol, 432-32 °C) whilst an additional, unidentified impurity phase is also present during the heating cycle (blue ▼ symbol, 32-111 °C). An abrupt change in unit cell volume of the major cubic phase is also evident in both the heating (green ▼ symbol, 479-502 °C) and cooling cycles (green ▼ symbol, 432-384 °C).

Since the tetragonal phase content is significantly higher for 10Y1AlSB, the peak asymmetry is more resolved. There is also an additional peak asymmetry feature (a small peak shoulder) that indicates the presence of an unidentified impurity phase between 32-111 °C. On heating the overall material becomes phase pure (Fig. 5.14a) over a narrower temperature range than for 10YSB. The cubic phase expands uniformly between 32-479 °C (Fig. 5.14b and Table 5.3), then between 479-502 °C the cubic phase also

experiences an abrupt, dramatic unit cell expansion, however, for 10Y1AlSB this occurs at a significantly higher rate and is more pronounced as expected due to the higher tetragonal phase content. Thereafter, the cubic phase also has an increased rate of thermal expansion which is maintained on cooling until the second abrupt unit cell volume change occurs between 432-384 °C. This change is also more rapid than that observed for 10YSB. The final cooling segment (384-32 °C) shows a similar rate of thermal expansion to the initial heating segment, much like that shown for the 10YSB sample and the unknown impurity is no longer present. Importantly, these changes in the CTE magnitude observed for both 10YSB and 10Y1AlSB during the thermal cycle indicate changes in the state of disorder of the material as was described for 27.5YSB. The increase in the rates observed for the abrupt changes in lattice parameter of 10Y1AlSB (Fig. 5.14b) in comparison to that of 10YSB (Fig. 5.12b) clearly indicates that the tetragonal-cubic phase transition contributes to this abrupt cubic lattice parameter expansion.

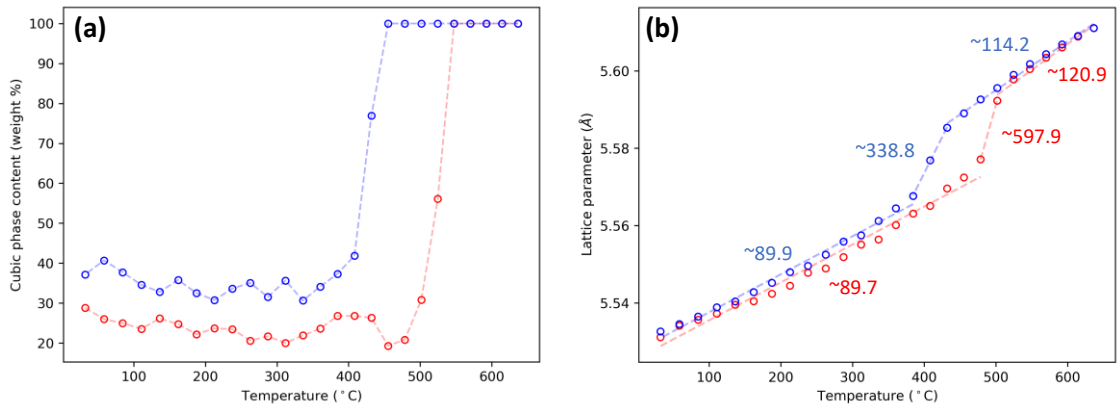

Figure 5.14. (a) Cubic phase purity and (b) cubic phase lattice parameter variation of the 10Y1AlSB material over the temperature range of 32-636-32 °C. The heating cycles are shown with red markers and the cooling cycle with blue markers. Approximate linear CTEs (x 10^{-6} K^{-1}) from Table 5.3 are indicated in (b).

Table 5.3. Cubic phase CTE variation of the 10Y1AlSB material over the temperature range 32-636-32 °C

Temp range (°C)	CTE (10^{-6} K^{-1})
32-479	89.7 ± 3.1
479-502	~597.9
502-636	120.9 ± 7.1
636-432	114.2 ± 3.4
432-384	~338.8
384-32	89.9 ± 2.5

Interestingly, the rate of thermal expansion for both 10YSB and 10Y1AlSB materials measured after the respective changes in the initial rates of thermal expansion (i.e. in the high temperature regions) are similar to that of the 27.5YSB material in the high temperature region. For both the 10YSB and 10Y1AlSB materials, the unit cell volume at 32 ^{o}C is nearly unchanged after the thermal cycle indicating that negligible structural relaxation is exhibited after the thermal cycle. The abrupt changes in thermal expansion of 10YSB and 10Y1AlSB clearly coincide with the observed changes in cubic phase purity of the respective materials. As such a phase change mechanism is proposed to account for this thermal expansion behaviour (Fig. 5.15). It is postulated that the tetragonal and cubic phase fractions initially present undergo somewhat independent phase transformations during heating. The initially present cubic phase (δ_1) is structurally maintained during heating and expands linearly during heating (δ_1^*). The initially present tetragonal phase (β) transforms into a second cubic phase (δ_2^*), of the same crystal system as δ_1^*, during heating. The lattice parameter of δ_2^* is, however, greater than that of δ_1^*. The presence of two crystallographically similar phases would not be evident in the PXRD data, and the lattice parameter derived from Rietveld analysis using a single cubic phase would represent the average lattice parameter of the two similar cubic phases. This average lattice parameter is greater than that of the originally present cubic phase owing to the contribution of the large lattice parameter of δ_2^*. Hence during *in situ* heating where the tetragonal-cubic phase transition occurs, an abrupt increase in cubic phase lattice parameter is observed.

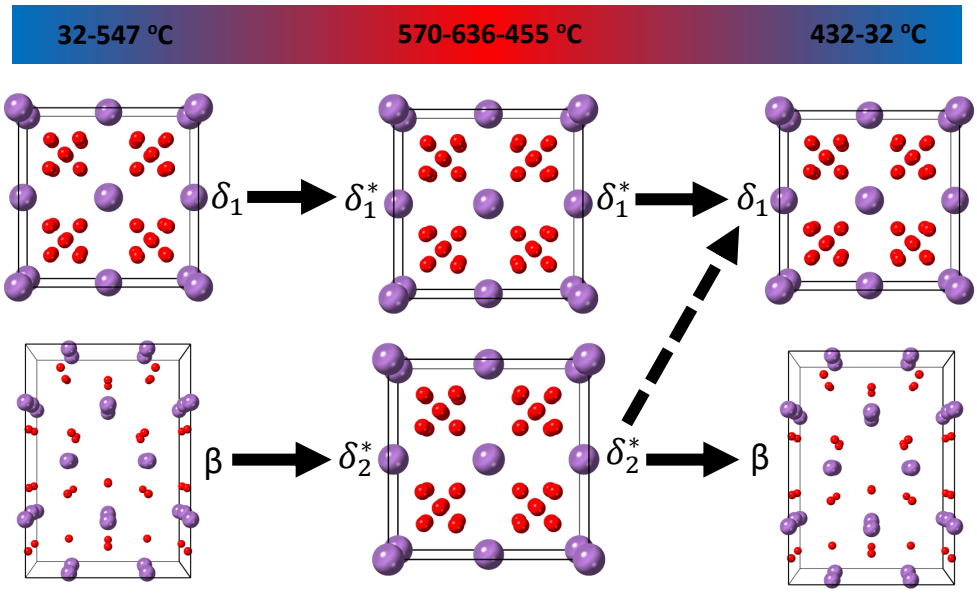

Figure 5.15. Proposed phase change mechanism for the cubic and tetragonal phase mixture of 10YSB and 10Y1AlSB over the studied temperature range. Initially present cubic δ_1 and tetragonal β phases undergo independent phase transformations into high temperature δ-phases δ_1^* and δ_2^*, respectfully. Only the 8c and 32f oxygen sites are included in the cubic phases for clarity. Details pertinent to the proposed mechanism are discussed in the text.

During cooling, the δ_1^* phase is again maintained and exhibits linear thermal expansion. The δ_2^* phase, however, largely transforms back to the same β tetragonal phase but with a small amount also forming the δ_1 phase. The latter accounts for the increased cubic phase content observed after the *in situ* measurement for both 10YSB and 10Y1AlSB. A portion of the δ_2^* phase could also remain during cooling which would account for the slightly larger average lattice parameter observed at room temperature. Although the proposed phase change mechanism accounts for the abrupt changes in cubic phase lattice parameter, the changes observed in CTE magnitude over the low and high temperature linear regions are not ascribed to these *in situ* phase transformations. The structural models obtained from the Bragg Rietveld analyses are biased towards the average long-range structure since only Bragg scattering is used.[38] The PDF analyses use total scattering (i.e. Bragg and diffuse scattering) and hence emphasize the local structure and are sensitive to the chemical short range order.[27] Therefore, these two Rietveld analyses are complementary and when used in conjunction give a more complete representation of the overall structure of the materials. In particular, the *in situ* heating PDF analysis enables the structural evolution or changes on a local scale to be investigated and this allows for the proposed phase change mechanism to be further probed.

5.3.4. Analysis of the local structure evolution of 10YSB and 10Y1AlSB during *in situ* heating using PDF analysis

The *in situ* PDF analysis of the 27.5YSB material showed that the change in magnitude of the CTE can be linked to the increasing disorder of the material and the occurrence of the order-disorder transition. The PDF analysis of 10YSB and 10Y1AlSB is not as straightforward since during heating the phase mixtures convert to phase pure cubic materials. This conversion coincided with a jump in the lattice parameter of the cubic phase fraction leading to the proposed phase change mechanism (Fig. 5.15). In addition, the CTE of the pure cubic phase in the high temperature region exhibited an increase in magnitude and was similar to that observed in the phase pure cubic 27.5YSB material over a similar temperature range. Figure 5.16 shows the *G(r)* curves for the 10YSB material in the 1.5 ≤ *r* ≤ 30 Å range collected *in situ* over the temperature range of 32-636-32 °C. From visual analysis it is evident that the profile of the *G(r)* peaks change over the entire *r* range during the thermal cycle, however, over the high temperature region where the material was found to be phase pure cubic from the Bragg data (♦ symbol in Figure 5.16) there are vast changes seen in the profile of the *G(r)* peaks. These changes were further investigated here to support the proposed phase change mechanism as well as the occurrence of the order-disorder transition.

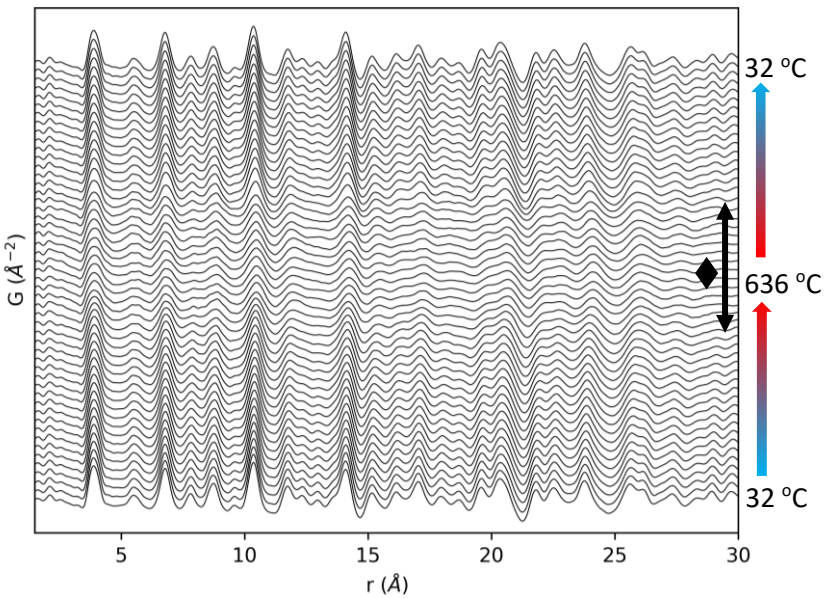

Figure 5.16. *In situ* PDFs collected for the 10YSB material over the temperature range of 32-636-32 °C. The region in which the material was found to be phase pure cubic from the Bragg data is indicated (♦ symbol, 570-636-455 °C).

The tetragonal and cubic polymorphs have been shown to have a high degree of structural similarity.[39,40] This was observed in the Bragg data, which provides information pertaining to the average long range structure, wherein significant overlapping of diffraction peaks from these two polymorphs was evident. The tetragonal phase content results in the formation of asymmetric diffraction peaks that differ from the shape expected based on the instrument resolution function (IRF). As such, the two polymorphs were able to be discerned with reasonable accuracy. In the corresponding PDF data, which provides information of the local, short range structure, it is more challenging to discern between the two polymorphs owing to the high degree of local structure similarity. Calculated PDFs for the cubic and tetragonal phases are compared to that of the observed PDF for 10YSB at 32 °C in Figure 5.17. It is apparent that the local structure of both phases are similar to that for the mixed phase material which emphasizes the challenges in resolving the contribution of each phase to the observed local structure.

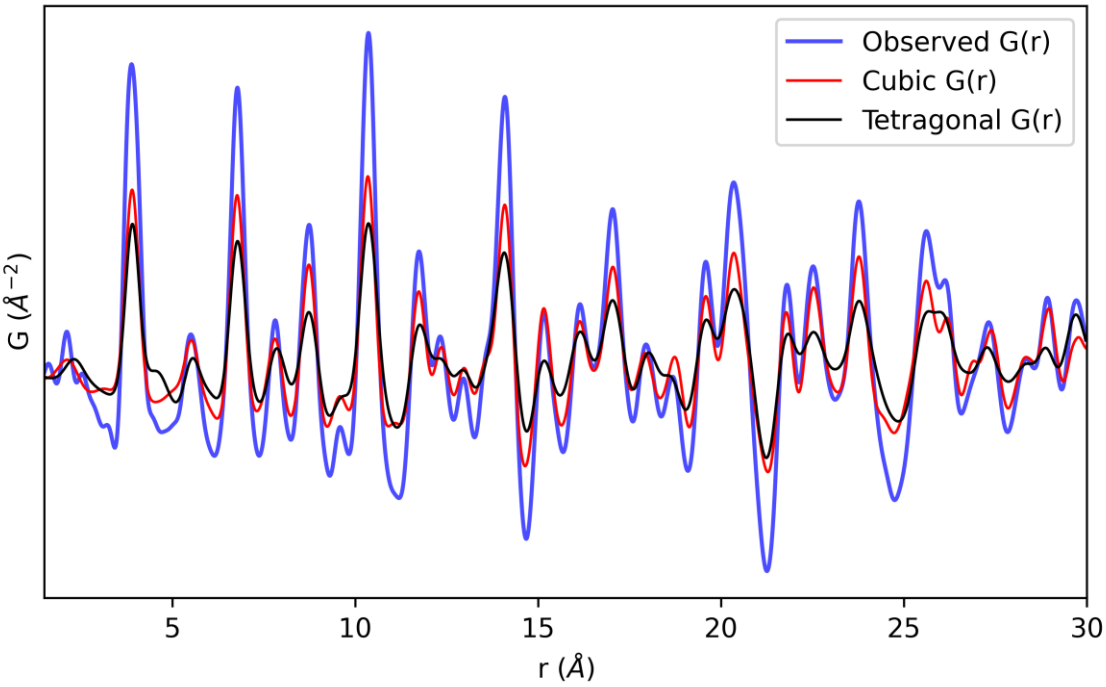

Figure 5.17. Observed PDF of annealed 10YSB collected at 32 °C (blue) in comparison with calculated PDFs of cubic (red) and tetragonal (black) 10YSB structures derived from the Bragg Rietveld analyses.

This local structure similarity between the two phases was further investigated using the low-*r vs*. high-*r* refinement approach. The observed *G(r)* data for 10YSB at 32 °C is used to illustrate the structural similarity on the local scale (Fig. 5.18) between the average cubic and tetragonal structures when

individually refined against the *G(r)* data over varying length scales as described for 27.5YSB. Additionally, both structures are then simultaneously refined against the *G(r)* data.

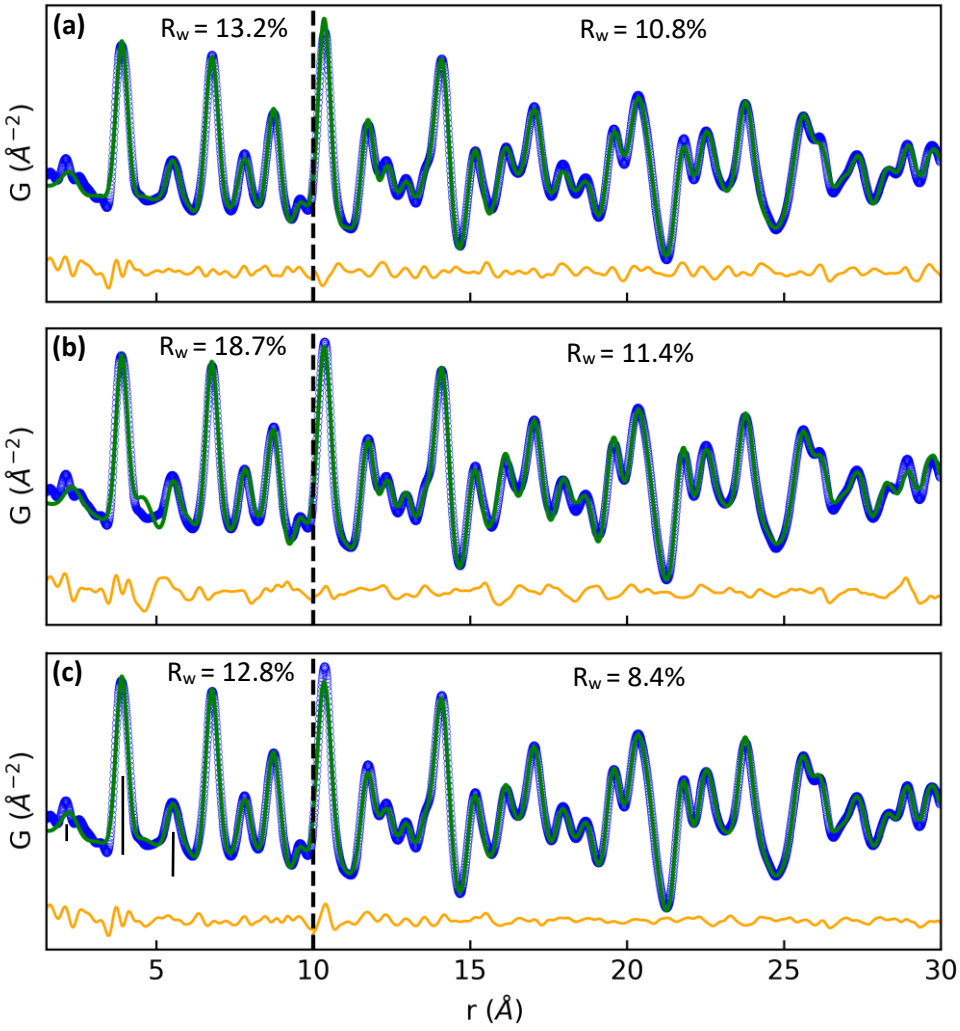

Figure 5.18. Selected PDF refinements over the low-*r* and high-*r* ranges for 10YSB. Refinements shown are for data collected at 32 °C fitted using (a) a single cubic phase, (b) a single tetragonal phase or (c) both cubic and tetragonal phases simultaneously. Observed (blue markers), calculated (green curve) and difference (orange curve) profiles are shown along with agreement factors.

From the refinements for 10YSB (Fig. 5.18), several interesting features are evident. Over the 1.5 ≤ *r* ≤ 10 Å range, the cubic phase reasonably interprets the experimental *G(r)* data (Fig. 5.18a), whereas the same fitting achieved using the tetragonal phase (Fig. 5.18b) resulted in a worsened fit. The fit incorporating both the cubic and tetragonal phases (Fig. 5.18c) – the *biphasic* model – unsurprisingly resulted in a similar

quality of fit to that achieved using the cubic phase in this low-*r* range. This indicates that the local structure of the mixed phase material over the $1.5 \leq r \leq 10$ Å range is significantly more cubic in structure. Over the $10 \leq r \leq 30$ Å range, the quality of the fits attained by cubic phase (Fig. 5.18a) and the tetragonal phase (Fig. 5.18b) were comparable. The biphasic model, however, resulted in an improved fit quality over the high-*r* range, which was evident from both the agreement factors and the interpretation of *G(r)* features. This indicates that the local structure over the high-*r* range contains both cubic and tetragonal phase features.

The extreme *G(r)* peak overlap seen for the cubic and tetragonal phases limits the use of the *in situ* PDF analyses to monitor changes to the phase purity of the material during heating. As such, the phase purity range established from the Bragg Rietveld analyses was used to determine the temperature range in which the *biphasic* structural model was used for the PDF analysis refinements.

Looking at the cationic thermal displacement parameter for 10YSB (Fig. 5.19) derived from both the PDF and Bragg Rietveld analyses, abrupt changes during both the heating and cooling cycles were observed. For the Bragg Rietveld analyses (Fig. 5.19a) a jump in U_{iso} occurred from ~502 ^{o}C during heating and from ~432 ^{o}C during cooling. For the PDF analyses over the $10 \leq r \leq 30$ Å range (Fig. 5.19b), similar jumps in U_{iso} were observed from ~520 ^{o}C and ~470 ^{o}C during heating and cooling, respectively. These jumps in U_{iso} derived from both sets of Rietveld analyses coincide with the abrupt changes in the cubic phase lattice parameter and cubic phase CTE (Fig. 5.12 and Table 5.2).

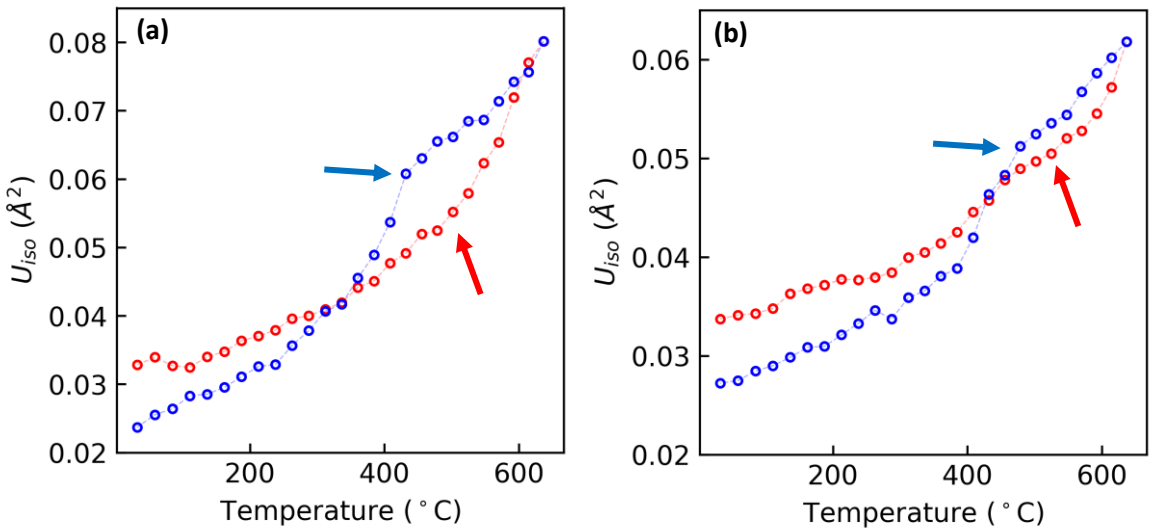

Figure 5.19. Variation of the cationic thermal displacement parameters of annealed 10YSB derived from *in situ* (a) Bragg Rietveld and (b) PDF analyses. Heating cycle shown with red markers and the cooling cycle shown with blue markers. The onset of abrupt changes in U_{iso} during heating (red arrows) and cooling (blue arrows) are indicated. Standard errors associated with U_{iso} derived from Bragg and PDF analyses are ~0.001 Å^2 and ~0.002 Å^2, respectively.

The proposed phase change mechanism (Fig. 5.15) of 10YSB predicts the presence of two crystallographically similar cubic phases at elevated temperatures. These two phases are only distinguished by their distinct lattice parameter values which are too similar to be distinguished in the Bragg Rietveld analyses. However, evidence for the presence of these two phases can be sought from the direct analysis of the *in situ* PDF data. The difference in lattice parameter is expected to result in differing M_1-M_1 and M_2-M_2 bond lengths which would result in the broadening or splitting of peaks B and C owing to the peaks now corresponding to two (or multiple) bond length distributions. As such, for 10YSB the evolution of *G(r)* peaks B and C were monitored during the heating and cooling cycles (Fig. 5.20).

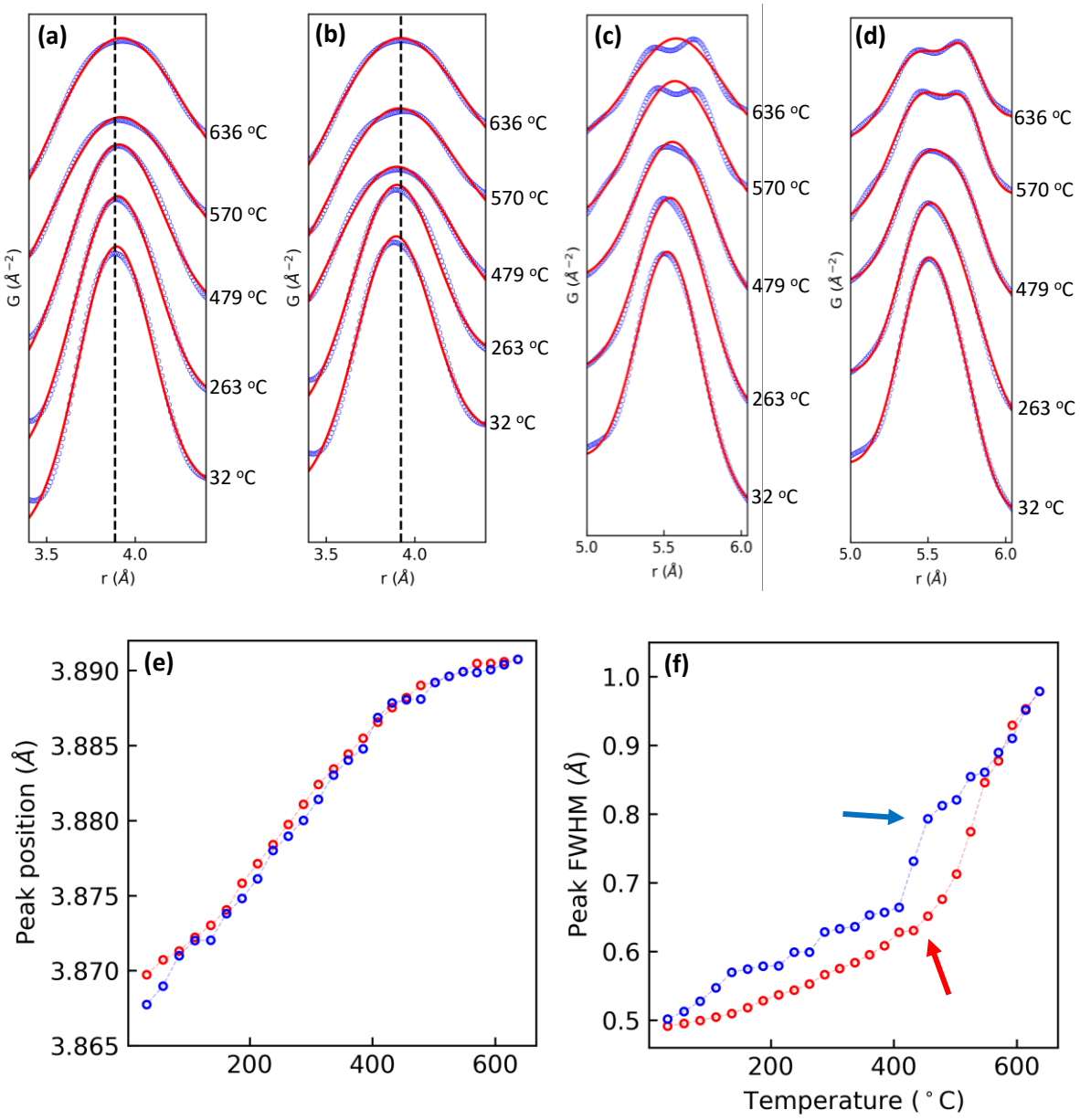

Figure 5.20. Gaussian fits (red lines) to peak B of 10YSB at selected temperatures during the (a) heating and (b) cooling cycles. The black dotted line in (a) indicates the first peak position (at 32 °C) for comparison and similarly the black dotted line in (b) indicates the peak position at 636 °C. Peak C is fitted with (c) a single Gaussian (red line) and (d) two Gaussians at selected temperatures in the heating cycle. The variation in (e) position and (f) width of peak B *vs*. temperature derived from the single Gaussian fitting are plotted. The onset of abrupt changes in peak FWHM during heating (red arrow) and cooling (blue arrow) are indicated. Standard errors associated with peak position and FWHM are ~0.0002 Å and ~0.03 Å, respectively.

The evolution of peak B during *in situ* heating was investigated by *direct analysis* and from this, several structural inferences were made. The fitting of a Gaussian function to the peak (Fig. 5.20a and 5.20b) results in a good representation of the peak throughout the thermal cycle. As such, the peak position (Fig. 5.20e) and peak width (Fig. 5.20f) can be accurately derived from the Gaussian fitting. The peak position is found to shift to higher *r* values during heating as expected based on the positive thermal expansion of the material. The non-linearity seen in the increase in peak position is likely due to the tetragonal-cubic phase transition that occurs which would affect the derived peak position due to the overlap of tetragonal and cubic *G(r)* peaks at this *r* range. The increase in peak width seen during heating is initially approximately linear as expected from the increased thermal motion of atoms during heating. The abrupt increase in peak width seen from ~450 ^{o}C indicates a corresponding increase in the disorder present in the material and/or the presence of two similar bond length distributions. This further indicates the occurrence of the order-disorder transition and possibly the presence of a second M_1-M_1 bond length distribution. The latter supports the proposed phase change mechanism. A similar investigation of the evolution of peak C during *in situ* heating is shown in Figure 5.20. Fitting the peak using a single Gaussian function (Fig. 5.20c) clearly decreases in quality during heating. At elevated temperatures, the fitting of peak C is achieved using two Gaussian functions (Fig. 5.20d) and this indicates that two unique bond length distributions are increasingly present during heating and fully discernible over the temperature range in which two unique cubic phases are predicted to coexist based on the proposed phase change mechanism (Fig. 5.15).

The *in situ* PDF analysis of 10Y1AlSB is largely similar to that of 10YSB. Both materials were determined to be tetragonal and cubic phase mixtures, with the 10Y1AlSB material having higher tetragonal phase content in comparison. Hence during *in situ* heating, 10Y1AlSB is also predicted to follow the proposed phase change mechanism (Fig. 5.15). In this way, the investigation of 10Y1AlSB substantiates the findings of the analogous investigation of 10YSB.

Figure 5.21 shows the *G(r)* curves for the annealed 10Y1AlSB material in the 1.5 ≤ *r* ≤ 30 Å range collected *in situ* over the temperature range of 32-636-32 °C. Similar to that observed for the 10YSB material, for the 10Y1AlSB material over the high temperature region in which the average structure is phase pure cubic (♦ in Figure 5.21) there are marked changes seen to the profile of the *G(r)* peaks. These changes were investigated and found to substantiate the proposed phase change mechanism as well as the occurrence of the order-disorder transition.

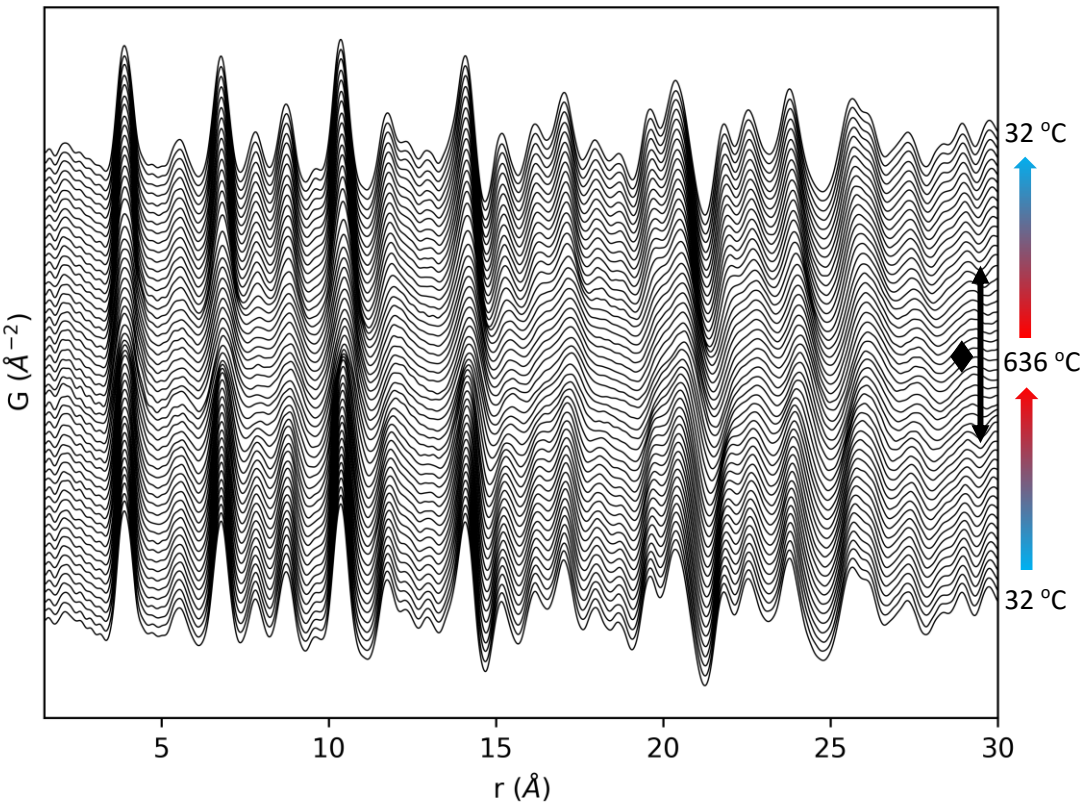

Figure 5.21. *In situ* PDFs collected for an annealed (at 750 °C) 10Y1AlSB material over the temperature range of 32-636-32 °C. The region in which the material was found to be phase pure cubic from the Bragg data is indicated (♦, 547-636-455 °C).

The local structure similarity of the cubic and tetragonal phases are investigated using the low-*r vs*. high-*r* refinement approach as was done for 10YSB and 27.5YSB. The observed *G(r)* data for 10Y1AlSB at 32 °C is again used and the average cubic and tetragonal structures are individually refined against the *G(r)* data over varying length scales, as well as both structures are simultaneously refined against the *G(r)* data.

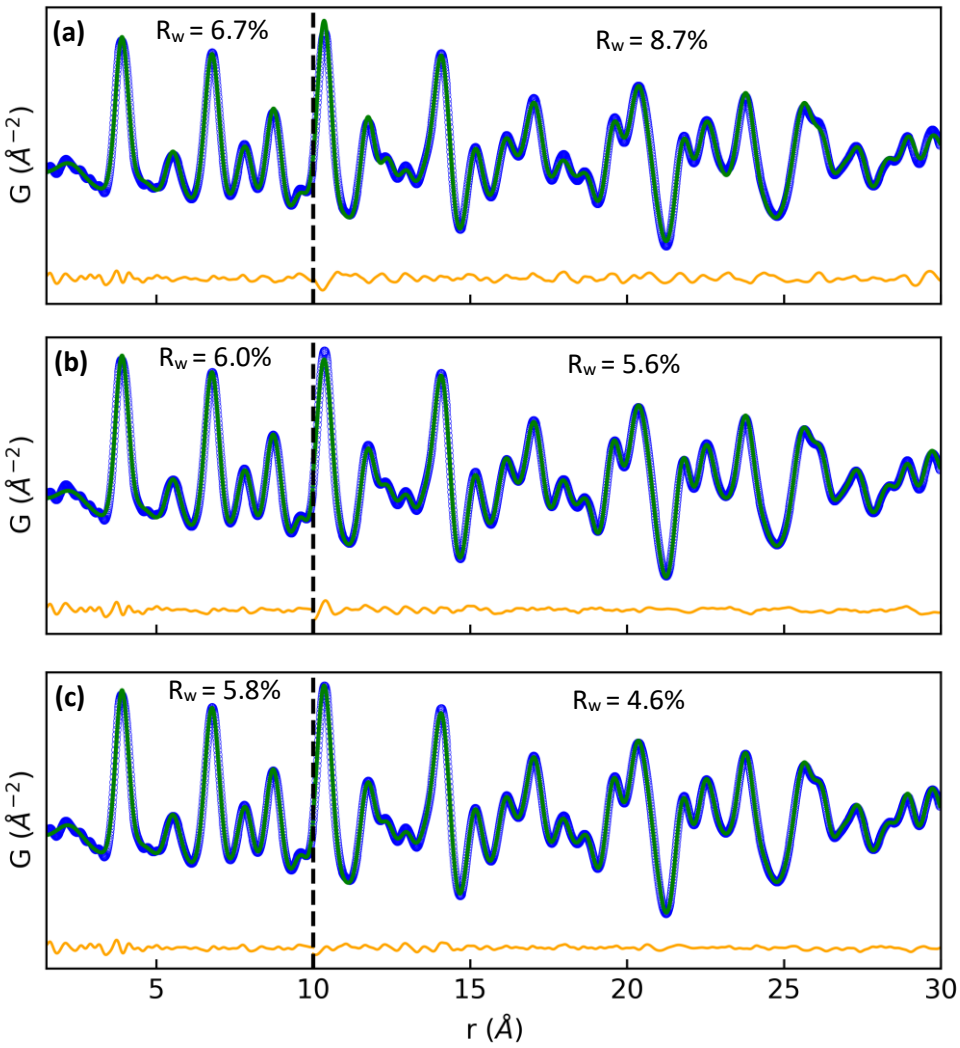

Figure 5.22. Selected PDF refinements over the low-*r* and high-*r* ranges for 10Y1AlSB. Refinements shown are for data collected *in situ* at 32 °C and fitting is achieved by either a (a) single cubic phase, (b) single tetragonal phase or (c) both cubic and tetragonal phases simultaneously. Observed (blue markers), calculated (green curve) and difference (orange curve) profiles are shown along with agreement factors.

The low-*r* *vs*. high-*r* refinements of 10Y1AlSB (Fig. 5.22) show contrasting results to that obtained for 10YSB (Fig. 5.18). Over the 1.5 ≤ *r* ≤ 10 Å range, both the cubic and tetragonal phases successfully interpret the experimental *G(r)* data (Figs. 5.22a and 5.22b) and little improvement to the fit is achieved by using the *biphasic* model (Fig. 5.22c). Over the 10 ≤ *r* ≤ 30 Å range, the tetragonal phase interprets the experimental *G(r)* data well and the quality of fit achieved is markedly higher than that achieved using the cubic phase. This indicates that over the higher *r* range the local structure more closely resembles that of the tetragonal phase. This was not observed for the 10YSB material. The quality of fit achieved using the *biphasic* model results in an improved fit quality over the entire 1.5 ≤ *r* ≤ 30 Å range and as before, the *biphasic* model is required to accurately model the *G(r)* data. As before, the phase purity range established from the Bragg Rietveld analyses was used to determine the temperature range in which the *biphasic* structural model was used for the PDF analysis refinements over the 10 ≤ *r* ≤ 30 Å range. From these refinements, the variation in cationic U_{iso} were monitored during the thermal cycle (Fig. 5.23).

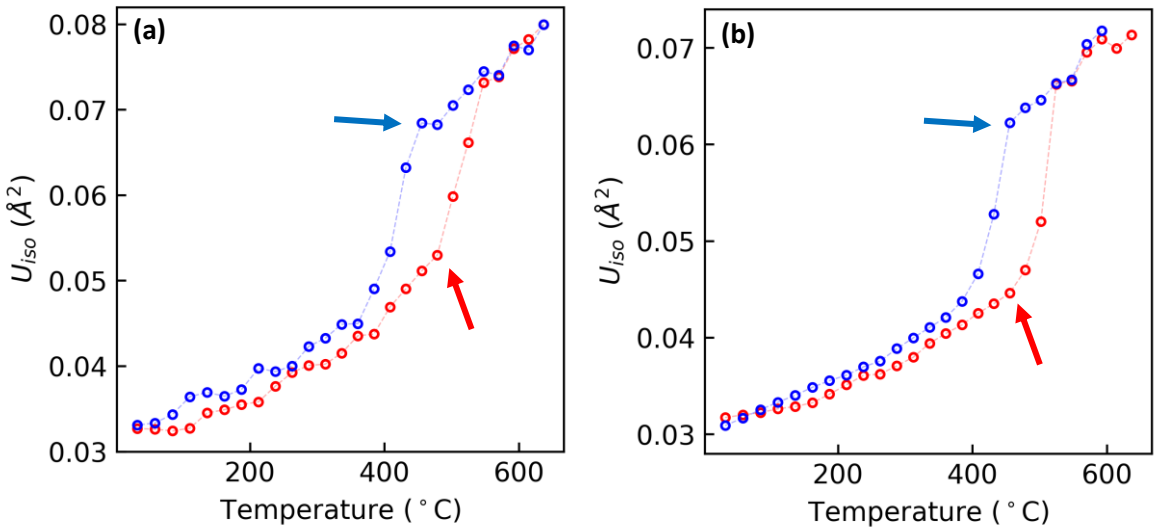

Figure 5.23. Variation of the cationic thermal displacement parameters of annealed 10Y1AlSB derived from (a) *in situ* Bragg Rietveld and (b) PDF analyses. The onset of abrupt changes in U_{iso} during heating (red arrows) and cooling (blue arrows) are indicated. Standard errors associated with U_{iso} derived from Bragg and PDF analyses are ~0.005 Å^2 and ~0.003 Å^2, respectively.

The observed changes in the cationic thermal displacement parameter for 10Y1AlSB derived from both the Bragg Rietveld and PDF analyses show abrupt changes during both the heating and cooling cycles. These changes are more pronounced than that observed for 10YSB (Fig. 5.19). These abrupt changes in U_{iso} occur at nearly identical temperatures for both types of analyses, indicating that the order-disorder

transition occurs over the similar temperature ranges over both local and long range length scales. These changes in U_{iso} also correlate with the abrupt changes in the cubic phase lattice parameter and cubic phase CTE changes (Fig. 5.14 and Table 5.3), as was observed for 10YSB.

The proposed phase change mechanism (Fig. 5.15) was also investigated for 10Y1AlSB via *direct analysis* by monitoring the evolution of *G(r)* peaks B and C (Fig. 5.24) during *in situ* heating. The fitting of a Gaussian function to peak B (Fig. 5.24a and 5.24b) results in a good representation of the peak throughout the heating cycle and the peak position (Fig. 5.24e) and peak width (Fig. 5.24f) can be accurately derived from the Gaussian fitting. The peak position shifts reflects the same behaviour as that seen for 10YSB. The increase in peak width upon heating is initially linear due to increased thermal motion of atoms. The abrupt increase in peak width is seen at ~479 ^{o}C and demonstrates an abrupt increase in the disorder or the presence of two similar bond length distributions as before.

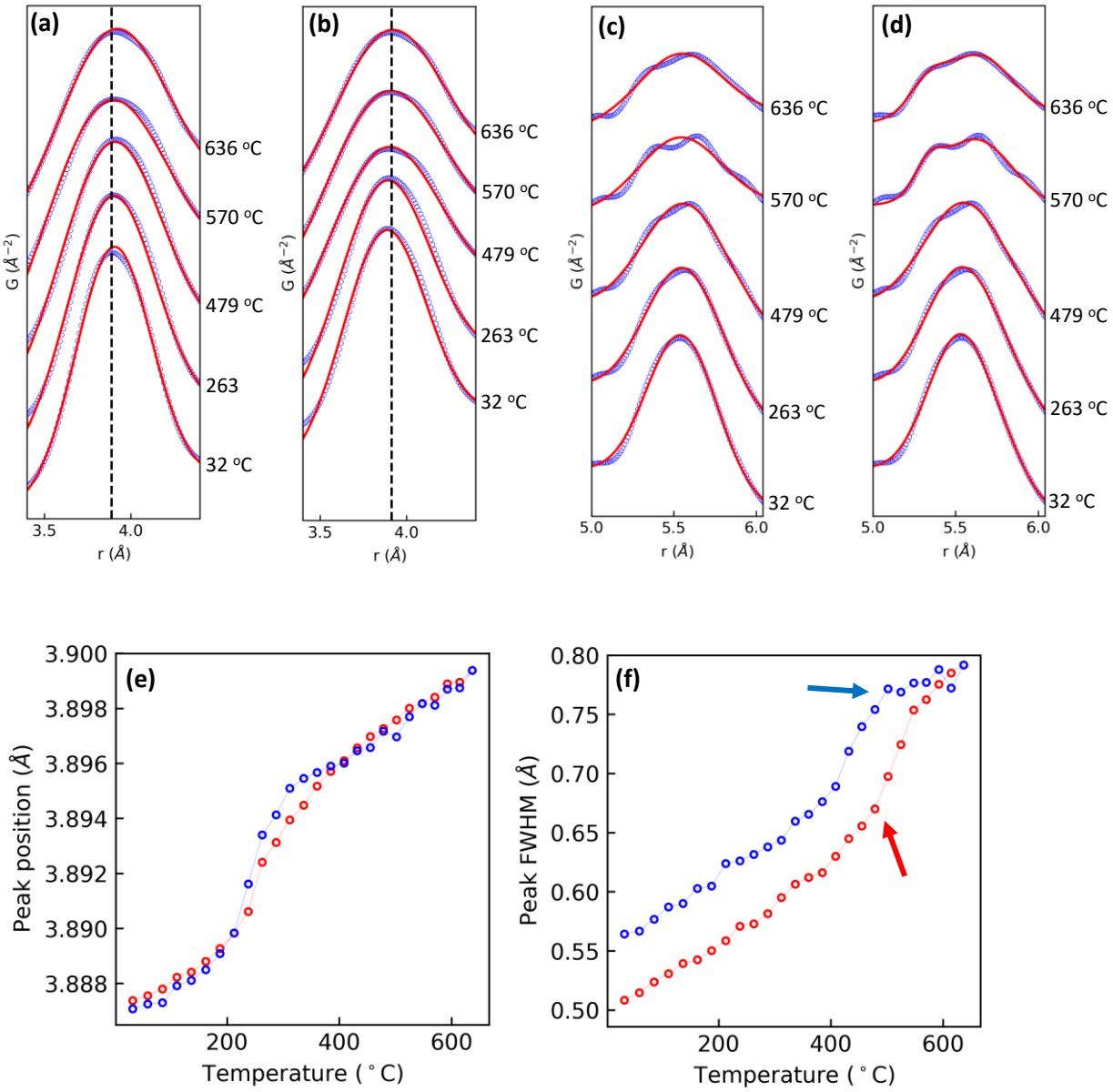

Figure 5.24. Gaussian fits (red lines) to peak B of 10Y1AlSB at selected temperatures during the (a) heating and (b) cooling cycles. The black dotted line in (a) indicates the first peak position (at 32 °C) for comparison and similarly the black dotted line in (b) indicates the peak position at 636 °C. (c) Fits of a single Gaussian (red line) and (d) two Gaussians to peak C of 10Y1AlSB at selected temperatures during the heating cycle. (e) Position and (f) width of peak B *vs*. temperature derived from the Gaussian fitting. The onset of abrupt changes in peak FWHM during heating (red arrow) and cooling (blue arrow) are indicated. Standard errors associated with peak position and FWHM are ~0.0001 Å and ~0.009 Å, respectively.

Similar investigation of the evolution of peak C during *in situ* heating in Figure 5.24 again shows fitting can be achieved using a single Gaussian function (Fig. 5.24c) in the lower temperature range, but at elevated temperatures two Gaussian functions (Fig. 5.24d) have to be used which indicates that two unique bond length distributions are increasingly present during heating and fully discernible over the temperature range in which two unique cubic phases are predicted to coexist. This further substantiates the proposed phase change mechanism (Fig. 5.15).

5.3.5. The effect of local structure changes on ionic conductivity

The ionic conductivity of 10YSB and 27.5YSB was investigated and found correlate with the phase change behaviour of the materials (Fig. 5.25). It was not possible to measure the ionic conductivity of 10Y1AlSB due to instrument unavailability. For 10YSB (Fig. 5.25a) abrupt changes in conductivity were observed during both the heating and cooling cycles. During the heating cycle, these changes occurred over 550-650 ^{o}C whereas during cooling, similar changes were observed over 550-500 ^{o}C. These temperature ranges show strong correlation to the tetragonal-cubic phase transformation (Fig. 5.12 and Table 5.2) and changes in the state of disorder of the material (Figs. 5.19 and 5.20). The abrupt increase in conductivity is primarily due to the formation of a more conductive phase pure cubic material along with the contribution from the order-disorder transition. The order-disorder transition that commonly is associated with changes in ionic conductivity pertain to a transition of the anionic sublattice[41] which differs from the cationic sublattice transition which was investigated in this work.

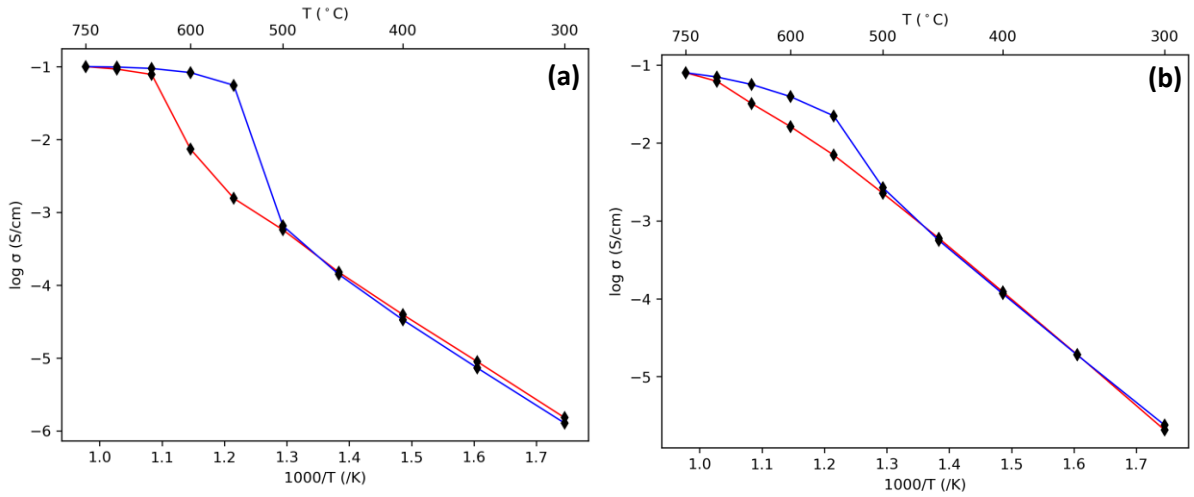

Figure 5.25. (a) Arrhenius plot of 10YSB and (b) 27.5YSB in the temperature range of 300-750 ^{o}C showing results from both the heating (red lines) and the cooling cycles (blue lines).

Conversely, for 27.5YSB the conductivity behaviour (Fig. 5.25b) was more consistent with the thermally-activated hopping mechanism of ionic conduction[42] and also reflects the *in situ* phase studies which showed no abrupt unit cell volume changes to the average structure (Figs. 5.1 and 5.2). However, the changes observed in the CTE of the material (Fig. 5.2 and Table 5.1), particularly during heating, coincides with the non-linear conductivity change at ~550 ^{o}C which represents a change in the activation energy of oxide ion conduction. The correlations between the ionic conductivity behaviour and the *in situ* structural investigations strongly indicates that the state of cationic disorder additionally affects the ionic conductivity behaviour.

5.4. Conclusion

The thermal expansion behaviour of three stabilized bismuthates was investigated in this work using *in situ* total scattering measurements. Bragg scattering measurements were used to probe the NLTE behaviour of a phase pure cubic 27.5YSB material. The thermal expansion behaviour was resolved into two regions of approximate linear thermal expansion, for both the heating and cooling cycles, with the larger CTE occurring in the higher temperature range. It was postulated that the change in the CTE is due to the order-disorder transition of the cationic sublattice. This was supported by monitoring changes in thermal displacement parameters of the cations during the thermal cycle using *direct analysis* of PDF features.

From *in situ* Bragg scattering measurements of 10YSB and 10Y1ALSB, which were both found to be cubic and tetragonal phase mixtures, a change in the CTE of the cubic phase was observed over the thermal cycle. An abrupt increase in the cubic phase lattice parameter was evident which coincided with the tetragonal-cubic phase transformation. To account for the abrupt lattice parameter increase, a phase change mechanism was proposed and substantiated by local structure analysis and by monitoring the changes in disorder of the material. *Direct analysis* of PDF features and monitoring changes in thermal displacement parameters of the cations showed that changes in disorder coincide with the observed tetragonal-cubic phase transformation and changes in the CTE. *Direct analysis* additionally showed the presence of a second cubic phase over the temperature range in which a phase pure cubic material was observed from Bragg scattering measurements. These results substantiate the proposed phase change mechanism and additionally indicate the contribution from the state of disorder of the material to the CTE. Lastly, ionic conductivity measurements of 10YSB show abrupt increases in ionic conductivity which coincide with both the tetragonal-cubic phase transformation and changes in the state of disorder. Similar measurements of the 27.5YSB material show changes in conductivity which coincide with changes in the

CTE of the material. This indicates that changes in the disorder of the cationic sublattice, which are clearly evident in the EIS data, contribute towards the changes observed in the CTE.

5.5. References

1. Ivers-Tiffée, E., Weber, A. and Herbstritt, D. Materials and technologies for SOFC-components. *J. Eur. Ceram. Soc*. **21**, 1805–1811 (2001).

2. Sammes, N. M., Tompsett, G. A., Näfe, H. and Aldinger, F. Bismuth based oxide electrolytes—structure and ionic conductivity. *J. Eur. Ceram. Soc*. **19**, 1801–1826 (1999).

3. Jiang, N. and Wachsman, E. D. Structural Stability and Conductivity of Phase-Stabilized Cubic Bismuth Oxides. *J. Am. Ceram. Soc*. **82**, 3057–3064 (1999).

4. Takahashi, T., Esaka, T. and Iwahara, H. High oxide ion conduction in the sintered oxides of the system Bi_2O_3-Y_2O_3. *J. Appl. Electrochem*. **5**, 197–202 (1975).

5. Kale, K. V., Jadhav, K. M. and Bichile, G. K. Investigations on a high-conductivity solid electrolyte system, Bi_2O_3-Y_2O_3. *J. Mater. Sci. Lett*. **18**, 9–11 (1999).

6. Kiefer, M. A., Billing, C., Erasmus, R. M., Mogodi, W. M. and Billing, D. G. A detailed investigation of the structural stability, ionic conductivity and in situ δ-phase formation of $Y_xBi_{2-x}O_6$. *Unpubl. Manuscr*. (2021).

7. Kiefer, M. A., Billing, C., Olds, D. and Billing, D. G. Investigating the ambient and in situ thermal phase stability of $Y_xBi_{2-x}O_3$ electrolytes. *Unpubl. Manuscr*. (2021).

8. Abrahams, I., Liu, X., Hull, S., Norberg, S. T., Krok, F., Szmigiel-Kozanecka, A., Islam, M. S. and Stokes, S. J. A combined total scattering and simulation approach to analyzing defect structure in Bi_3YO_6. *Chem. Mater*. **22**, 4435–4445 (2010).

9. Leszczynska, M., Liu, X., Wrobel, W., Malys, M., Norberg, S. T., Hull, S., Krok, F., and Abrahams I. Total scattering analysis of cation coordination and vacancy pair distribution in Yb substituted δ-Bi_2O_3. *J. Phys. Condens. Matter* **25**, (2013).

10. Leszczynska, M., Borowska-Centkowska, A., Malys, M., Dygas, J. R., Krok, F., Wrobel, W., and Abrahams I. The double rare-earth substituted bismuth oxide system $Bi_3Y_{1-x}Yb_xO_6$. *Solid State Ion.* **269**, 37–43 (2015).

11. Borowska-Centkowska, A., Liu, X., Krynski, M., Leszczynska, M., Wrobel, W., Malys, M., Hull, S., Norberg, S. T., Krok, F., and Abrahams, I. Defect structure in δ-$Bi_5PbY_2O_{11.5}$. *RSC Adv*. **9**, 9640–9653 (2019).

12. Holdynski, M., Sintyureva, M., Liu, X., Leszczynska, M., Krok, F., Hull, S. and Abrahams, I. Structure and conductivity in the $Bi_4Nb_{1-x}Y_xO_{8.5-x}$ oxide-ion conducting system. *Solid State Ion.* **328**, 8–16 (2018).

13. Struzik, M., Malys, M., Krynski, M., Wojcik, M., Dygas, J. R., Wrobel, W., Krok, F. and Abrahams, I. Structural and electrical behavior in $Bi_{14}YO_{22.5}$. *RSC Adv*. **5**, 83471–83479 (2015).

14. Borowska-Centkowska, A., Krok, F., Abrahams, I., Wrobel, W., Dygas, J. R. and Hull, S. Thermal variation of structure and electrical conductivity in $Bi_{14}WO_{24}$. *Solid State Ion.* **202**, 14–21 (2011).

15. Shi, X., Ghose, S. and Dooryhee, E. Performance calculations of the X-ray powder diffraction beamline at NSLS-II. *J. Synchrotron Radiat*. **20**, 234–242 (2013).

16. Hammersley, A. P. FIT2D: A multi-purpose data reduction, analysis and visualization program. *J. Appl. Crystallogr.* **49**, 646–652 (2016).

17. Kaiser, D. L. and Watters, R. L. SRM 640d - Silicon Powder - Line Position and Line Shape Standard for Powder Diffraction. 1–5 (2010).

18. Lyon, K. G., Salinger, G. L., Swenson, C. A. and White, G. K. Linear thermal expansion measurements on silicon from 6 to 340 K. *J. Appl. Phys*. **48**, 865–868 (1977).

19. Okada, Y. and Tokumaru, Y. Precise determination of lattice parameter and thermal expansion coefficient of silicon between 300 and 1500 K. *J. Appl. Phys.* **56**, 314–320 (1984).

20. Coelho, A. A. TOPAS and TOPAS-Academic: An optimization program integrating computer algebra and crystallographic objects written in C++. *J. Appl. Crystallogr*. **51**, 210–218 (2018).

21. Chater, P. A. Topas PDF Macros. Available at: https://github.com/pachater/topas/blob/master/pdf.inc.

22. Small, J. A. and Watters, R. L. SRM 660c - Line Position and Line Shape Standard for Powder Diffraction (Lanthanum Hexaboride Powder). 1–5 (2015). doi:10.1002/9783527809080.cataz11352

23. Billinge, S. J. L. and Egami, T. Underneath the Bragg Peaks - Structural Analysis of Complex Materials. (Pergamon Materials Series, 2003).

24. Yang, X., Masadeh, A. S., McBride, J. R., Božin, E. S., Rosenthal, S. J. and Billinge, S. J. L. Confirmation of disordered structure of ultrasmall CdSe nanoparticles from X-ray atomic pair distribution function analysis. *Phys. Chem. Chem. Phys.* **15**, 8480–8486 (2013).

25. Bish, D. L. and Howard, S. A. Quantitative phase analysis using the Rietveld method. *J. Appl. Crystallogr*. **21**, 86–91 (1988).

26. Young, C. A. and Goodwin, A. L. Applications of pair distribution function methods to contemporary problems in materials chemistry. *J. Mater. Chem*. **21**, 6464–6476 (2011).

27. Proffen, T., Billinge, S. J. L., Egami, T. and Louca, D. Structural analysis of complex materials using the atomic pair distribution function - A practical guide. *Zeitschrift fur Krist*. **218**, 132–143 (2003).

28. Bordet, P. Local structure studies using the pair distribution function. *EPJ Web Conf*. **104**, (2015).

29. Juhás, P., Davis, T., Farrow, C. L. and Billinge, S. J. L. PDFgetX3: A rapid and highly automatable program for processing powder diffraction data into total scattering pair distribution functions. *J. Appl. Crystallogr*. **46**, 560–566 (2013).

30. Coelho, A. A., Chater, P. A. and Kern, A. Fast synthesis and refinement of the atomic pair distribution function. *J. Appl. Crystallogr*. **48**, 869–875 (2015).

31. Chater, P. Pair Distribution Function Refinements using TOPAS v6. 1–33 (2017).

32. Coelho, A. A. TOPAS-Academic, Version 6: Technical Reference. (2016).

33. Billinge, S. J. L. and Egami, T. Extracting structural information from the PDF. in *Underneath the Bragg Peaks - Structural Analysis of Complex Materials* (Pergamon Materials Series, 2003).

34. Wojdyr, M. Fityk: A general-purpose peak fitting program. *J. Appl. Crystallogr.* **43**, 1126–1128 (2010).

35. Dinnebier, R. E., Leineweber, A. and Evans, J. S. O. *Rietveld Refinement Practical Powder Diffraction Pattern Analysis Using Topas*. (Walter de Gruyter GmbH, Berlin/Boston, 2019).

36. Jolley, A. G., Jayathilake, R. and Wachsman, E. D. Optimizing rhombohedral Bi_2O_3 conductivity for low temperature SOFC electrolytes. *Ionics (Kiel)*. **25**, 3531–3536 (2019).

37. Shannon, R. D. Revised Effective Ionic Radii and Systematic Studies of Interatomic Distances in Halides and Chalcogenides. *Acta Crystallogr*. **32**, 751–767 (1976).

38. Playford, H. Y., Owen, L. R., Levin, I. and Tucker, M. G. New Insights into Complex Materials Using Reverse Monte Carlo Modeling. *Annu. Rev. Mater. Res*. **44**, 429–449 (2014).

39. Hull, S., Norberg, S. T., Tucker, M. G., Eriksson, S. G., Mohn, C. E. and Stølen, S. Neutron total scattering study of the δ and β phases of Bi_2O_3. *J. Chem. Soc. Dalt. Trans.* 8737–8745 (2009).

40. Drache, M., Roussel, P. and Wignacourt, J. P. Structures and oxide mobility in Bi-Ln-O materials: Heritage of Bi_2O_3. *Chem. Rev*. **107**, 80–96 (2007).

41. Yashima, M. and Ishimura, D. Crystal structure and disorder of the fast oxide-ion conductor cubic Bi_2O_3. *Chem. Phys. Lett*. **378**, 395–399 (2003).

42. Skinner, S. J. and Kilner, J. A. Oxygen ion conductors. *Mater. Today* **6**, 30–37 (2003).

Chapter 6. Exploring the stability zone and *in situ* phase behaviour of rhombohedral Bi_2O_3

Mathias Ameer Kiefer[a,b], Caren Billing[a,b], Daniel Olds[c] and David Gordon Billing[a,b]

[a]Molecular Science Institute, University of the Witwatersrand, Private Bag X3, Johannesburg, Gauteng, 2050, South Africa

[b]DSI-NRF Center of Excellence in Strong Materials, University of the Witwatersrand, Private Bag X3, Johannesburg, Gauteng, 2050, South Africa

[c]National Synchrotron Light Source II, Brookhaven National Laboratory, PO Box 5000, Upton, New York, 11973, USA

This chapter has been prepared for submission to Acta Crystallographica Section B and has been formatted accordingly.

Abstract

Rhombohedral bismuth oxide has recently emerged as a promising SOFC electrolyte material. The compositional range of stability of this phase has been sparsely reported and was extensively explored in this work using yttrium, lanthanum and aluminium doping regimes. The phase behaviour of rhombohedral-rich materials was also investigated *in situ* over 360-656 ^{o}C and found to exhibit complex characteristics. Abrupt changes in thermal expansion of both the cubic and rhombohedral phases are consistent with the phase transformations observed. Separation of the (009) and (104) peaks of the rhombohedral phase during the thermal cycle was identified as an excellent visual marker of the rhombohedral to cubic phase transformation.

Keywords: Bismuth oxide; Crystal structure; Phase stability; Thermal expansion

6.1. Introduction

Bismuth oxide-based materials are known to crystallize in several phases, as depicted in Figure 6.1, with both composition and thermal history playing a role in determining which is dominant under specific conditions.[1–5] The high oxide ionic conductivity of the δ-cubic polymorph has caused this phase to be extensively studied, in particular for application as a solid oxide fuel cell (SOFC) electrolyte.[1–3] The use of yttrium doping to stabilize the δ-cubic phase of Bi_2O_3 has been successful, with minimal loss of ionic conductivity.[6–13] Bi_2O_3 can also crystallize in a rhombohedral phase that also exhibits ionic conductivity and this phase is commonly formed when the Bi_2O_3 lattice is doped with large cations.[14–16] The existence of the rhombohedral phase was initially identified in the Bi_2O_3-Y_2O_3 system by Watanabe *et al.*[17] as an ionically conductive hexagonal phase isomorphous to rhombohedral compounds formed in alkali earth doped bismuth oxides. This rhombohedral phase was later studied via Rietveld methods by Zhang *et al.*[12] and confirmed to crystallize in the $R\bar{3}m$ space group. Additional studies have shown that doping Bi_2O_3 with lanthanum readily forms the rhombohedral phase.[15,16,18–20]

The use of aluminium as a dopant with Bi_2O_3 has not been explored extensively. Studies of the Bi_2O_3-Al_2O_3 system have shown the presence of both a perovskite $BiAlO_3$ phase[21] and an orthorhombic $Bi_2Al_4O_9$ phase.[22] The latter phase, being structurally similar to an Aurivillius type structure, has been shown to exhibit mixed (i.e. ionic and electronic) conductivity. The structure and ionic conductivity of bismuth aluminates was investigated by Bloom *et al.*[23] where neither the cubic nor rhombohedral phase was formed, but instead a $Bi_2Al_4O_9$-perovskite type structure formed that exhibited high ionic conductivity.

Yttrium and lanthanum co-doping has been investigated by Jolley *et al.*[14] with the aim of optimizing rhombohedral phase conductivity and establishing the rhombohedral phase stability window with cation substitution levels of less than 10%. It was shown that the average dopant ionic radius and total dopant percentage determines the rhombohedral phase stability window and by careful dopant regimes, the rhombohedral ($R\bar{3}m$, SG #166), cubic ($Fm\bar{3}m$, SG #225), tetragonal ($P4_2/nmc$, SG #137), or monoclinic ($P2_1/c$, SG #14) phases (Fig. 6.1) can be formed either individually or as phase mixtures.

Rhombohedral bismuth oxide has been shown to have high ionic conductivity, at lower temperatures in comparison to the conducting δ-phase. Pioneering work by Takahashi *et al.*[15] investigated the ionic conductivity of several rhombohedral bismuth oxides doped with strontium, calcium or lanthanum. Notably, the conductivity of $(Bi_2O_3)_{0.8}(SrO)_{0.2}$ was found to be 0.22 $S.cm^{-1}$ at 700 °C. Additional work by Iwahara *et al.*[16] identified rhombohedral $(Bi_2O_3)_{0.9}(Nd_2O_3)_{0.9}$ and $(Bi_2O_3)_{0.7}(Sm_2O_3)_{0.3}$ as excellent ionic conductors with conductivities approaching 1 $S.cm^{-1}$ at 700 °C. More recently, Drache *et al.*[20] found

rhombohedral $Bi_{0.775}La_{0.225}O_{1.5}$ to have ionic conductivity of 0.001 $S.cm^{-1}$ at 400 °C and Jolley *et al.*[14] found rhombohedral $Bi_{0.935}La_{0.051}Y_{0.014}O_{1.5}$ to have ionic conductivity of 0.03 $S.cm^{-1}$ at 500 °C. These conductivity properties have made the rhombohedral phase increasingly attractive as a SOFC electrolyte material.

In this work, the rhombohedral phase stability compositional ranges established by Jolley *et al.,*[14] Mercurio *et al.,*[24] Iwahara *et al.*[16] and Takahashi *et al.*[15] were further investigated by lanthanum, aluminium and yttrium co-doping. Specifically, the average dopant ionic radii and total dopant percentage are investigated over wider ranges to explore the rhombohedral phase stability range for this material system in greater detail. This serves to bridge the gap between the ranges established by Jolley *et al.,*[14] Mercurio *et al.,*[24] Iwahara *et al.*[16] and Takahashi *et al.*[15] Additionally, the thermal stability and phase behaviour of the rhombohedral phase, which has not been precisely reported, was also investigated.

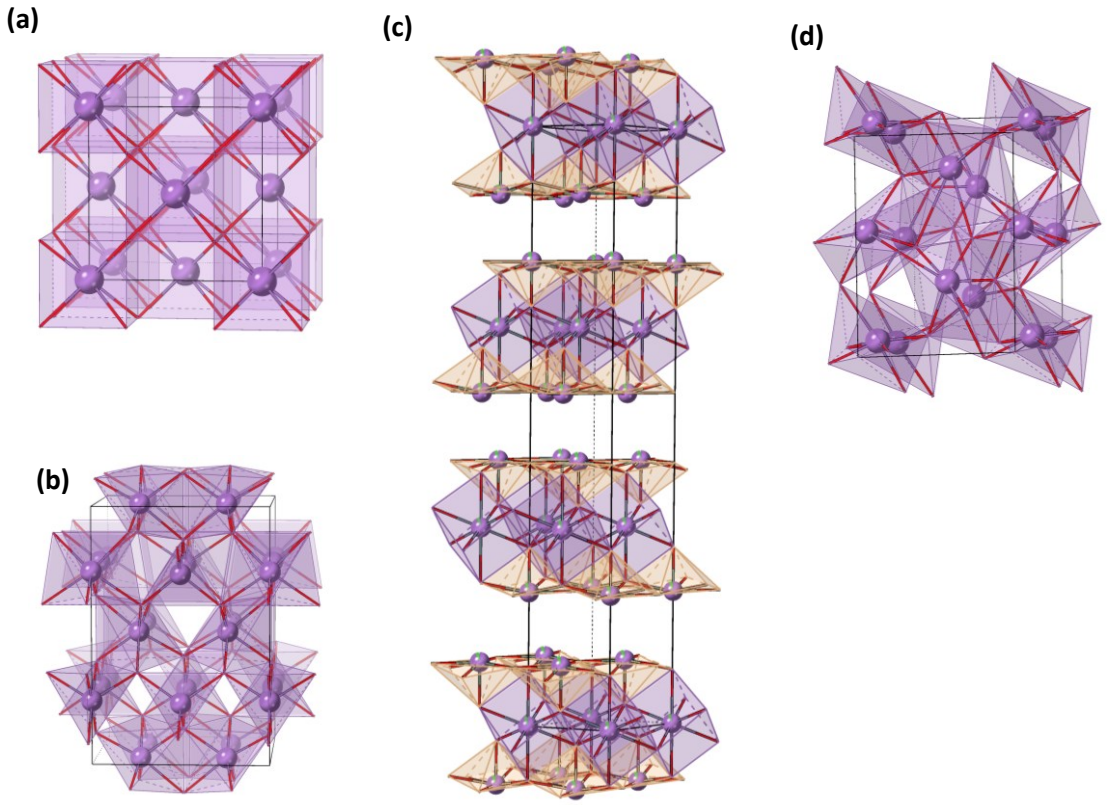

Figure 6.1. Unit cells for the (a) face-centred cubic δ-phase, (b) tetragonal β-phase, (c) rhombohedral phase and (d) monoclinic α-phase of bismuth oxide where purple spheres represent the cation sites. Rhombohedral bismuth oxide exhibits a layered packing arrangement consisting of two unique bismuth polyhedra.

6.2. Materials and methods

6.2.1. Synthesis and sample preparation

All samples were prepared by means of a citrate sol-gel process.[25] Stoichiometric amounts of bismuth nitrate pentahydrate ($Bi(NO_3)_3.5H_2O$, 99.99% pure Aldrich), yttrium nitrate hexahydrate ($Y(NO_3)_3.6H_2O$, 99.8% pure, Aldrich) and lanthanum nitrate hexahydrate ($La(NO_3)_3.6H_2O$, 99.99% pure, Aldrich) or aluminium nitrate nonahydrate ($Al(NO_3)_3.9H_2O$, 99.99% pure, Aldrich) were dissolved in glacial acetic acid (98% pure, MK Chemical, 99%) under moderate heating and stirring. Aqueous solutions were avoided to prevent the hydrolysis of Bi^{3+}. Excess citric acid monohydrate ($C_6H_8O_7.H_2O$, ACS reagent, Aldrich) was added and the resulting mixture evaporated to form a metal complex paste. Finally, the dried precursor was calcined at 450 ^oC for 18 h, then ground into a fine powder using an agate mortar and pestle and then annealed at 750 ^oC for 8 h to obtain the mixed metal oxide powders. Samples were prepared with varying dopant concentration and are labelled to reflect this. As an example, the 6% Y_2O_3, 9% La_2O_3 doped Bi_2O_3 sample is called 6Y9LSB and the 17% Y_2O_3, 3% Al_2O_3 sample is called 17Y3ASB.

6.2.2. Powder X-ray diffraction

Room temperature powder X-ray diffractograms were collected on a Bruker D2 Phaser using iron filtered CoK_α radiation (λ = 1.788 Å). *In situ* powder diffractograms of selected samples were collected at the Pair-Distribution Function (PDF) beamline (λ = 0.1671 Å) at the National Synchrotron Light Source II (NSLS-II). The nature of the synchrotron-based instrument[26] allows for the data collected to be of a superior resolution to that measured using lab-based instruments with significantly improved signal-to-noise ratio and collection limits. Each 2D diffractogram was collected for 30 seconds and then reduced into 1D diffraction data using Fit2D.[27] Samples were loaded into quartz capillaries and heated using a hot air blower at a ramp rate of 10 ^oC per minute with a dwell time of 30 seconds prior to each measurement. The set temperature range of 450-850-450 ^oC was calibrated using standard reference material 640d (Si powder)[28] and applying thermal lattice expansion corrections to the temperature profile[29,30] resulted in a corrected temperature range of 360-656-360 ^oC. Diffractograms were qualitatively assessed using Bruker AXS DIFFRAC.EVA V4.2 and Rietveld refinement of the diffractograms was done using Bruker AXS TOPAS-Academic Version 6.[31] In the refinements of the lab-based diffractograms collected at room temperature, the instrument resolution function (IRF)[32] was determined using NIST 660a (LaB_6) and was described using the fundamental parameters approach[33] using the full axial divergence model[34] to account for divergence-related asymmetry of the diffraction peaks. In the refinements of the synchrotron *in situ* diffractograms, the IRF was determined using NIST 640d and was described using the Thompson Cox Hastings (TCHZ)

Pseudo-Voight function[35] with the divergence-related asymmetry effects described in an empirical way using the simple axial model.[32] In each refinement, the parameters refined included the scale factors, selected corrections, and lattice parameters. Atomic positional parameters were fixed to those published for the respective crystal structures and atomic thermal parameters were fixed to reasonable values.

6.3. Results and discussion

6.3.1. Investigation of the rhombohedral phase boundary using powder X-ray diffraction

The phase stability window of the rhombohedral phase has been previously investigated and is described as the range of dopant content and dopant ionic radius wherein pure rhombohedral phase forms. The work by Jolley *et al.*[14] was the first study in which the dopant content and ionic radius was nuanced to accurately establish this phase stability window. Jolley *et al.*[14] investigated sample compositions, doped using La, Y, Er, Nd, Sm, Gd, Ca and Sr, with a total dopant content between 6-10% resulting in a variation of the average dopant ionic radius over 1.06-1.15 Å. The average dopant ionic radius is the weighted average of the two dopants' ionic radii. Similarly, Mercurio *et al.*[24] roughly investigated the rhombohedral phase stability window over a significantly higher dopant content range. Several members of the Bi_2O_3-Ln_2O_3-TeO_2 (Ln = La, Sm or Gd) system were found to form the rhombohedral phase over a total dopant content range of 25-50% which reflects a variation in the average dopant ionic radius range of 1.012-1.097 Å. Work by Takahashi *et al.*[15] investigated the rhombohedral phase formation in the Bi_2O_3-SrO system and found that the rhombohedral phase forms for 20-40% SrO content (ionic radius of Sr^{2+} = 1.260 Å). Additionally, Iwahara *et al.*[16] investigated the Bi_2O_3-Ln_2O_3 (Ln = La, Nd or Sm) system and found that the rhombohedral phase forms for 12-28% La_2O_3, 10-30% Nd_2O_3 and 30% Sm_2O_3 which reflects a variation in the average dopant ionic radius range of 1.079-1.160 Å. In this work, the phase stability window established for rhombohedral Bi_2O_3 was significantly expanded utilizing a double doping scheme to investigate the phase stability over a wide range of dopant content (7.5-25% total dopant) and average dopant ionic radius (0.907-1.154 Å) (Figs. 6.2 and 6.3).

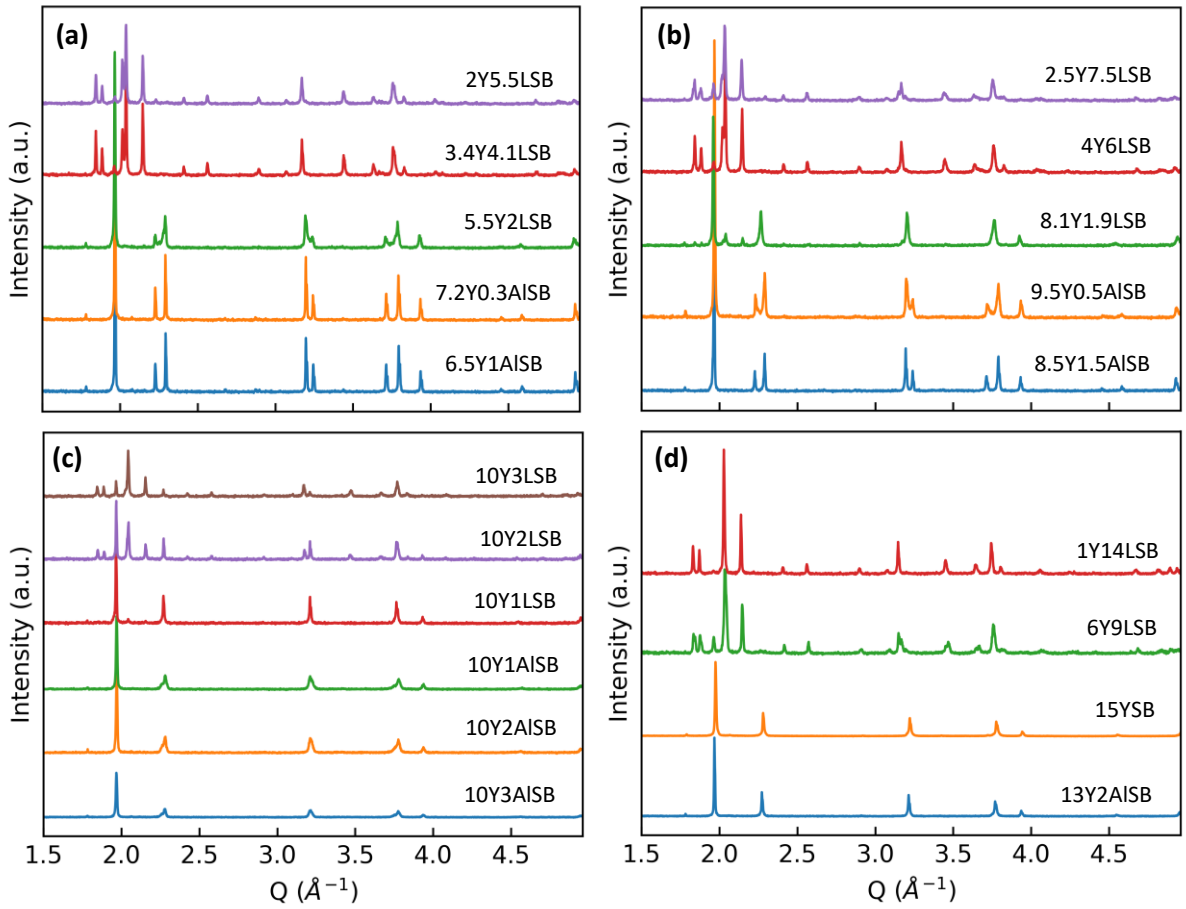

Figure 6.2. Room temperature diffractograms of doped bismuthates annealed at 750 °C with (a) 7.5%, (b) 10%, (c) 11-13% and (d) 15% total dopant content.

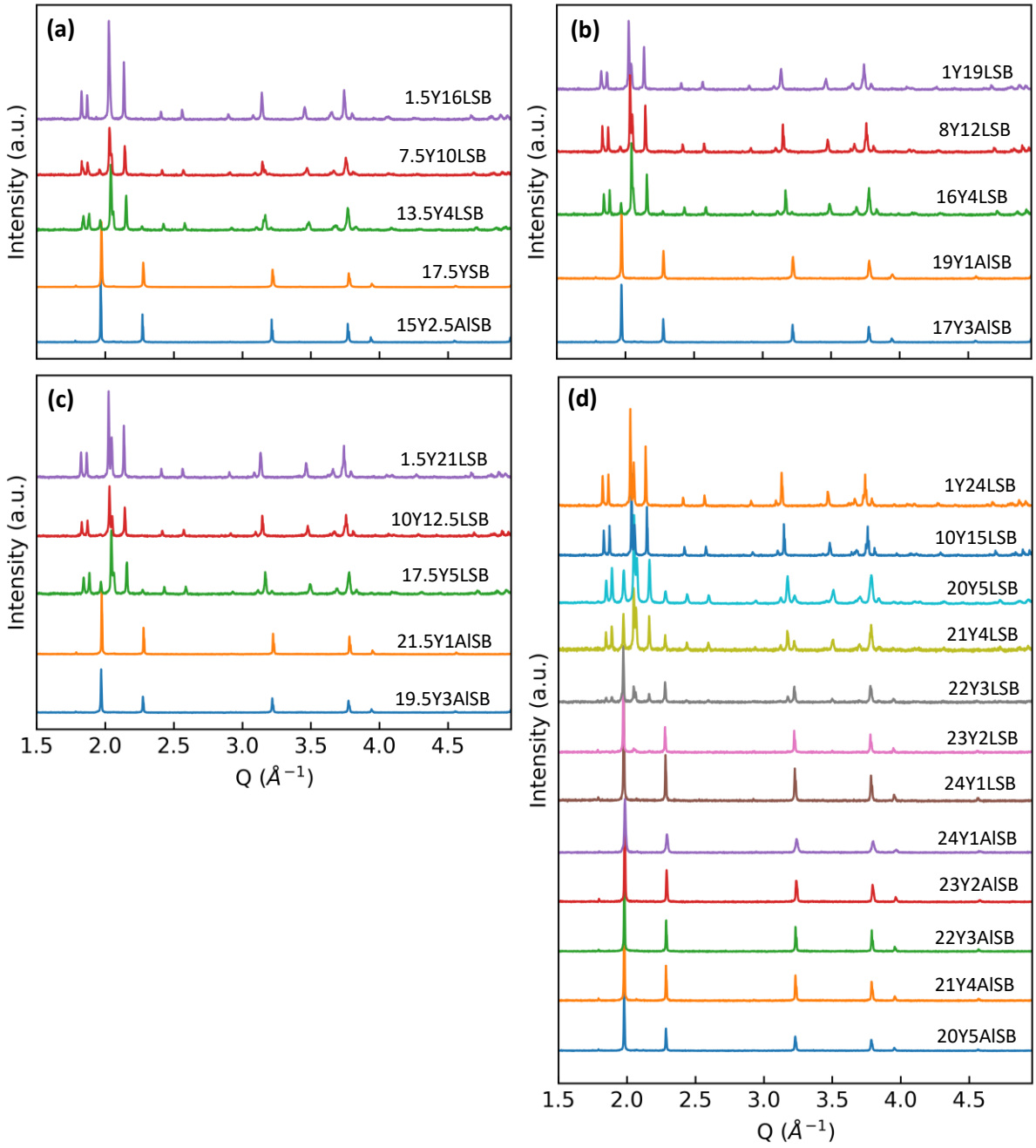

Figure 6.3. Room temperature diffractograms of doped bismuthates annealed at 750 °C with (a) 17.5%, (b) 20%, (c) 22.5% and (d) 25% total dopant content.

Lanthanum and yttrium as well as aluminium and yttrium were selected as co-dopant combinations based on their ionic radii. La and Bi have similar ionic radii (La^{3+} = 1.16 Å, Bi^{3+} = 1.17 Å)[36] while Y and Al have smaller ionic radii (Y^{3+} = 1.019 Å, Al^{3+} = 0.535 Å).[36] The high disparity in ionic radii enables the ratios of Y to La and Y to Al to be varied such as to explore a wide range of relative dopant ionic radii (Table 6.1).

Table 6.1. Bi_2O_3 compositions, relative ionic radius and quantitative phase content based on Rietveld refinement.

Name	Composition	Dopant ionic radius (Å)	Phase content (weight %)		
			Cubic	Tetragonal	Rhombohedral
7.5% dopant concentration					
6.5Y1ASB	$Bi_{0.925}Y_{0.065}Al_{0.01}O_{1.5}$	0.954	0	100	0
7.2Y0.3ASB	$Bi_{0.925}Y_{0.072}Al_{0.003}O_{1.5}$	1.000	0	100	0
5.5Y2LSB	$Bi_{0.925}Y_{0.055}La_{0.02}O_{1.5}$	1.057	30.6	69.4	0
3.4Y4.1LSB	$Bi_{0.925}Y_{0.034}La_{0.041}O_{1.5}$	1.096	3.0	2.2	94.8
2Y5.5LSB	$Bi_{0.925}Y_{0.02}La_{0.055}O_{1.5}$	1.122	1.6	4.4	94.1
10% dopant concentration					
8.5Y1.5ASB	$Bi_{0.9}Y_{0.085}Al_{0.015}O_{1.5}$	0.946	26.7	73.3	0
9.5Y0.5ASB	$Bi_{0.9}Y_{0.095}Al_{0.005}O_{1.5}$	0.995	18.8	81.2	0
8.1Y1.9LSB	$Bi_{0.9}Y_{0.081}La_{0.019}O_{1.5}$	1.046	14.7	85.3	0
4Y6LSB	$Bi_{0.9}Y_{0.04}La_{0.06}O_{1.5}$	1.104	3.7	2.5	93.8
2.5Y7.5LSB	$Bi_{0.9}Y_{0.025}La_{0.075}O_{1.5}$	1.125	3.3	8.9	87.8
11-13% dopant concentration					
10Y3ASB	$Bi_{0.87}Y_{0.1}Al_{0.03}O_{1.5}$	0.907	28.7	71.3	0
10Y2ASB	$Bi_{0.88}Y_{0.1}Al_{0.02}O_{1.5}$	0.938	35.4	64.6	0
10Y1ASB	$Bi_{0.89}Y_{0.1}Al_{0.01}O_{1.5}$	0.975	50.9	49.1	0
10Y1LSB	$Bi_{0.89}Y_{0.1}La_{0.01}O_{1.5}$	1.032	81.8	10.8	7.4
10Y2LSB	$Bi_{0.88}Y_{0.1}La_{0.02}O_{1.5}$	1.043	42.6	0	57.4
10Y3LSB	$Bi_{0.87}Y_{0.1}La_{0.03}O_{1.5}$	1.052	16.3	0	83.7
15% dopant concentration					
13Y2ASB	$Bi_{0.85}Y_{0.13}Al_{0.02}O_{1.5}$	0.955	73.2	26.8	0
15YSB	$Bi_{0.85}Y_{0.15}O_{1.5}$	1.019	69.6	31.4	0
6Y9LSB	$Bi_{0.85}Y_{0.06}La_{0.09}O_{1.5}$	1.104	6.4	2.8	90.8
1Y14LSB	$Bi_{0.85}Y_{0.01}La_{0.14}O_{1.5}$	1.151	0	2.4	97.6
17.5% dopant concentration					
15Y2.5ASB	$Bi_{0.825}Y_{0.15}Al_{0.025}O_{1.5}$	0.950	84.4	15.6	0
17.5YSB	$Bi_{0.825}Y_{0.175}O_{1.5}$	1.019	86.7	13.3	0
13.5Y4LSB	$Bi_{0.825}Y_{0.135}La_{0.04}O_{1.5}$	1.051	7.7	1.0	91.3
7.5Y10LSB	$Bi_{0.825}Y_{0.075}La_{0.1}O_{1.5}$	1.100	3.9	3.2	92.9
1.5Y16LSB	$Bi_{0.825}Y_{0.015}La_{0.16}O_{1.5}$	1.148	0	0	100
20% dopant concentration					
17Y3ASB	$Bi_{0.8}Y_{0.17}Al_{0.03}O_{1.5}$	0.946	94.6	5.4	0
19Y1ASB	$Bi_{0.8}Y_{0.19}Al_{0.01}O_{1.5}$	0.995	97.3	2.7	0
16Y4LSB	$Bi_{0.8}Y_{0.16}La_{0.04}O_{1.5}$	1.047	8.2	2.0	89.8
8Y12LSB	$Bi_{0.8}Y_{0.08}La_{0.12}O_{1.5}$	1.104	0	4.5	95.5
1Y19LSB	$Bi_{0.8}Y_{0.01}La_{0.19}O_{1.5}$	1.153	0	0	100
22.5% dopant concentration					
19.5Y3ASB	$Bi_{0.775}Y_{0.195}Al_{0.03}O_{1.5}$	0.954	90.4	9.6	0
21.5Y1ASB	$Bi_{0.775}Y_{0.215}Al_{0.01}O_{1.5}$	0.997	92.1	7.9	0
17.5Y5LSB	$Bi_{0.775}Y_{0.175}La_{0.05}O_{1.5}$	1.050	9.7	0	90.3
10Y12.5LSB	$Bi_{0.775}Y_{0.1}La_{0.125}O_{1.5}$	1.097	3.5	0	96.5
1.5Y21LSB	$Bi_{0.775}Y_{0.015}La_{0.21}O_{1.5}$	1.151	0	0	100
25% dopant concentration					
20Y5ASB	$Bi_{0.75}Y_{0.2}Al_{0.05}O_{1.5}$	0.922	100	0	0
21Y4ASB	$Bi_{0.75}Y_{0.21}Al_{0.04}O_{1.5}$	0.942	100	0	0
22Y3ASB	$Bi_{0.75}Y_{0.22}Al_{0.03}O_{1.5}$	0.961	100	0	0
23Y2ASB	$Bi_{0.75}Y_{0.23}Al_{0.02}O_{1.5}$	0.980	100	0	0
24Y1ASB	$Bi_{0.75}Y_{0.24}Al_{0.01}O_{1.5}$	1.000	100	0	0
24Y1LSB	$Bi_{0.75}Y_{0.24}La_{0.01}O_{1.5}$	1.025	100	0	0
23Y2LSB	$Bi_{0.75}Y_{0.23}La_{0.02}O_{1.5}$	1.030	89.5	0	10.5
22Y3LSB	$Bi_{0.75}Y_{0.22}La_{0.03}O_{1.5}$	1.036	63.0	0	37.0
21Y4LSB	$Bi_{0.75}Y_{0.21}La_{0.04}O_{1.5}$	1.042	21.2	0	78.8
20Y5LSB	$Bi_{0.75}Y_{0.2}La_{0.05}O_{1.5}$	1.047	18.0	0	82.0
10Y15LSB	$Bi_{0.75}Y_{0.1}La_{0.15}O_{1.5}$	1.104	0	0	100
1Y24LSB	$Bi_{0.75}Y_{0.01}La_{0.24}O_{1.5}$	1.154	0	0	100

When the total dopant content was 7.5% and the relative dopant ionic radius was varied by altering the ratio of Y to La and Y to Al (Fig. 6.2a). Jolley *et al.*[14] predicted pure rhombohedral Bi_2O_3 to be present over an average dopant ionic radius range of ~1.10-1.14 Å at a total dopant content of 7.5%. In this work, pure rhombohedral Bi_2O_3 was not formed over the 0.954-1.122 Å average dopant ionic radius range investigated at the same total dopant level of 7.5%. Over the average dopant ionic radius range of 0.954-1.000 Å pure tetragonal Bi_2O_3 was present and the Rietveld analysis of the 7.2Y0.3ASB sample is given in Figure 6.4 as an example. At an average dopant ionic radius of 1.057 Å, a cubic and tetragonal phase mixture was present. Over the range of 1.096-1.122 Å, rhombohedral-rich phase mixtures comprising both cubic and tetragonal phases in minor quantities were evident and the Rietveld analysis of the 2Y5.5LSB sample is given in Figure 6.5 as an example.

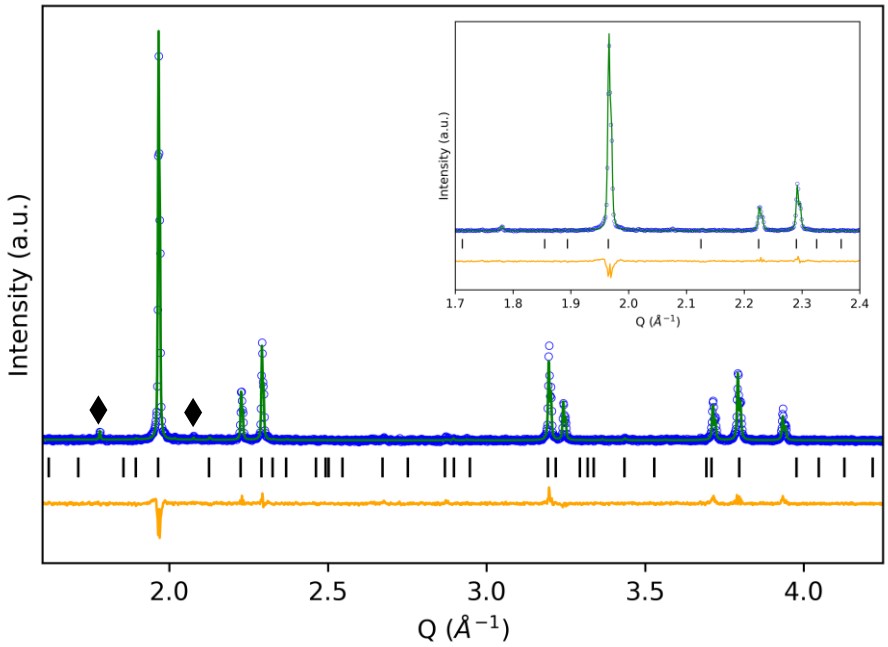

Figure 6.4. Diffractogram showing Rietveld refinement analysis for the 7.2Y0.3ASB material. The observed pattern is shown in blue, the calculated in green and the difference in orange. Miller indices corresponding to the tetragonal phase is shown with black ticks. K_β reflections are labelled with diamond markers.

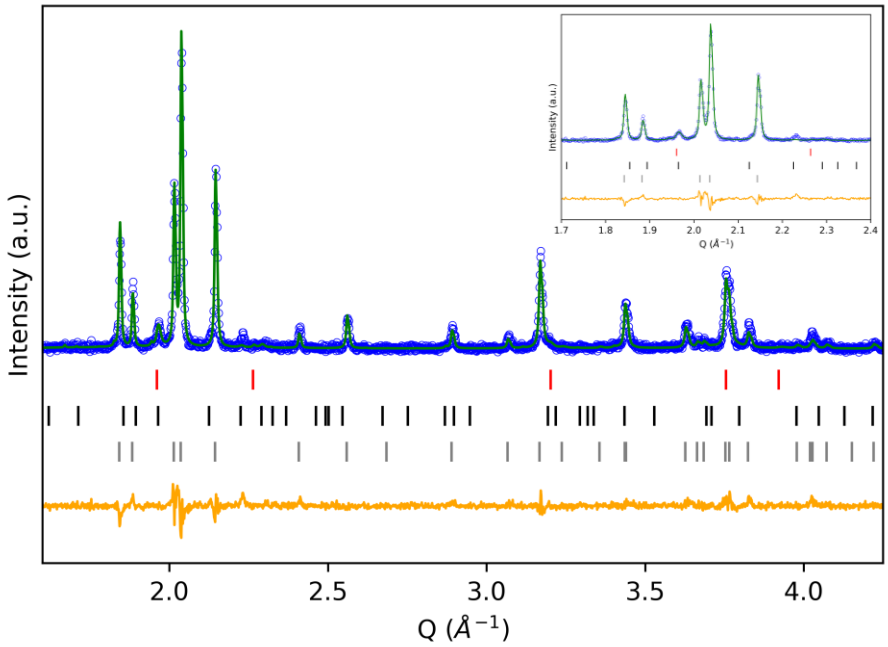

Figure 6.5. Diffractogram showing Rietveld refinement analysis for the 2Y5.5LSB. The observed pattern is shown in blue, the calculated in green and the difference in orange. Miller indices corresponding to the cubic, tetragonal and rhombohedral phases are shown with red, black and grey ticks, respectively.

The rhombohedral phase stability window was similarly investigated at a significantly higher dopant content of 25%. Over an average dopant ionic radius range of 0.922-1.025 Å, pure cubic Bi_2O_3 was present, and the Rietveld analysis of the 20Y5ASB sample is given in Figure 6.6 as an example. Between 1.030-1.047 Å, cubic and rhombohedral Bi_2O_3 phase mixtures were present and rhombohedral phase content was found to increase with increasing average dopant ionic radius at this dopant content level. The Rietveld analysis of the 22Y3LSB sample is given in Figure 6.7 as an example. Between 1.104-1.154 Å, pure rhombohedral Bi_2O_3 was present and the Rietveld analysis of the 1Y24LSB sample is given in Figure 6.8 as an example. The rhombohedral phase presence over this range coincides with the rhombohedral phase stability window established by Iwahara *et al.*[16]

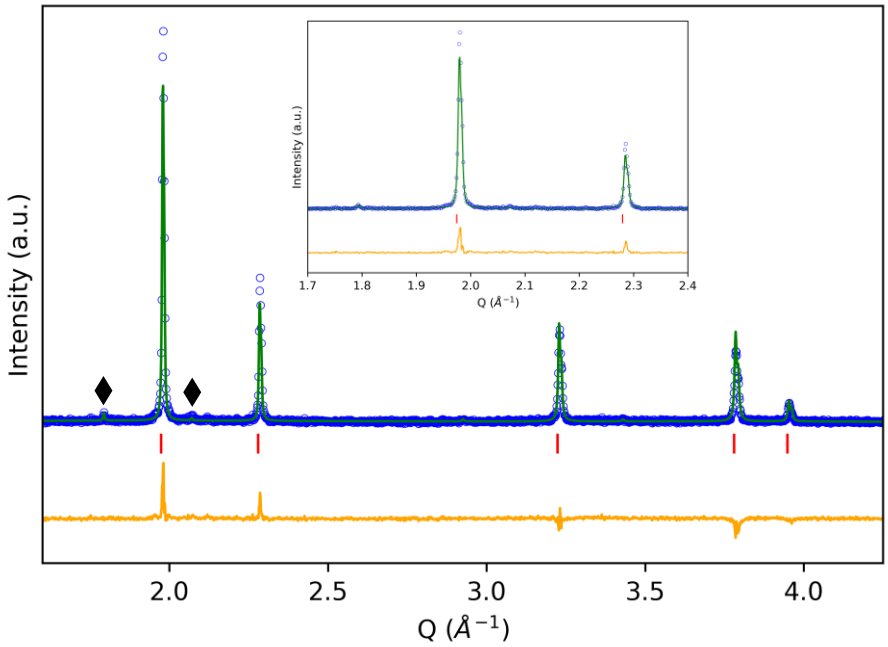

Figure 6.6. Diffractogram showing Rietveld refinement analysis for the 20Y5ASB. The observed pattern is shown in blue, the calculated in green and the difference in orange. Miller indices corresponding to the cubic phase are shown with red ticks. K_β reflections are labelled with diamond markers.

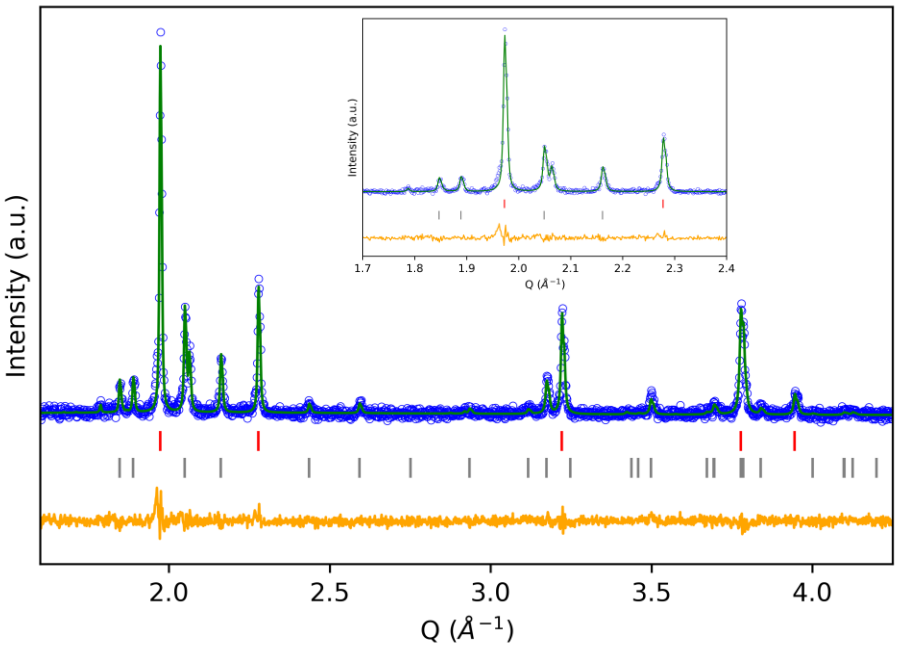

Figure 6.7. Diffractogram showing Rietveld refinement analysis for the 22Y3LSB material. The observed pattern is shown in blue, the calculated in green and the difference in orange. Miller indices corresponding to the cubic and rhombohedral phases are shown with red and grey ticks, respectively.

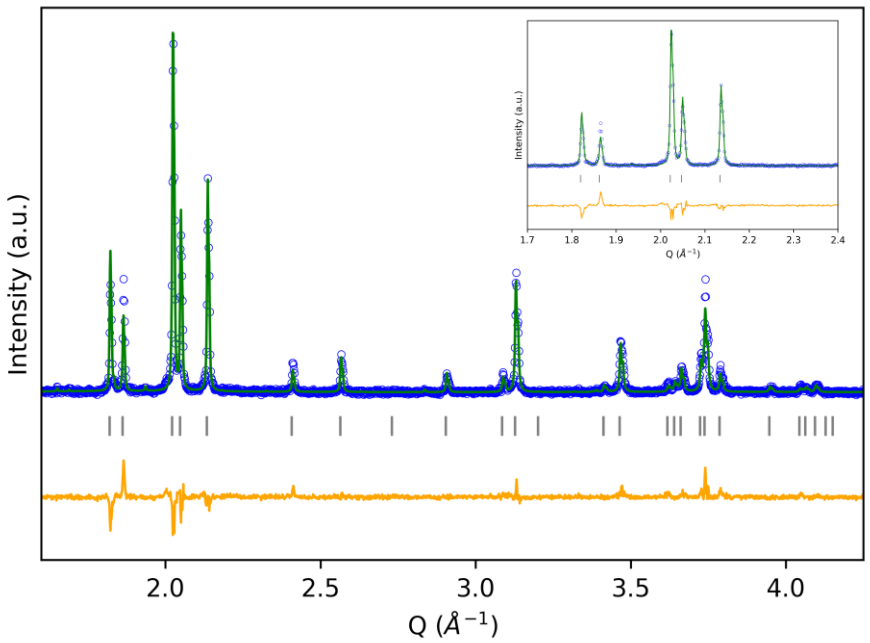

Figure 6.8. Diffractogram showing Rietveld refinement analysis for the 1Y24LSB material. The observed pattern is shown in blue, the calculated in green and the difference in orange. Miller indices corresponding to the rhombohedral phase are shown with grey ticks.

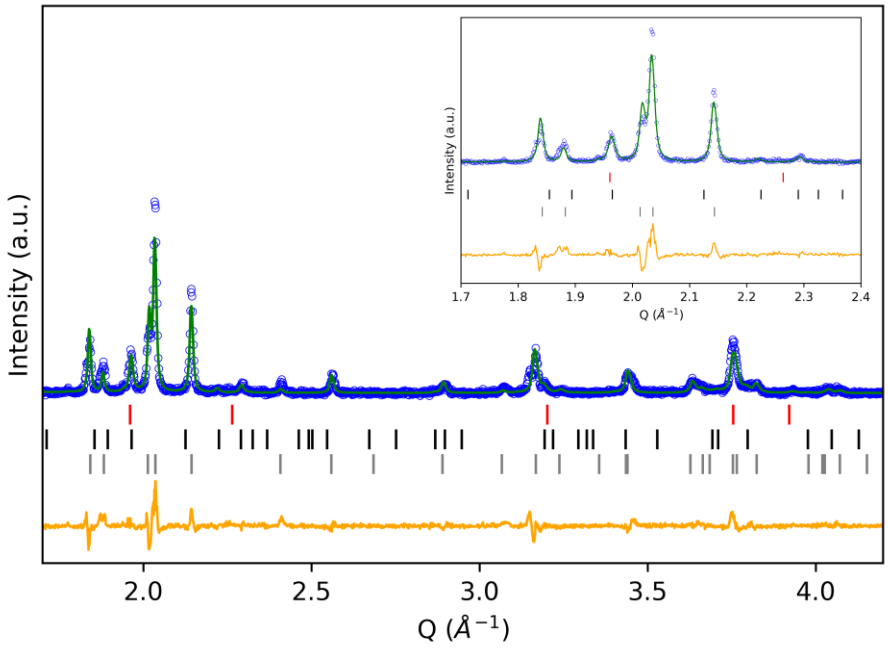

Figure 6.9. Diffractogram showing Rietveld refinement analysis for the 2.5Y7.5LSB material annealed at 750 °C. The observed pattern is shown in blue, the calculated in green and the difference in orange. Miller indices corresponding to the cubic, tetragonal and rhombohedral phases are shown with red, black and grey ticks, respectively.

The compositional range over which the rhombohedral phase exists was further investigated between 10-25% total dopant content over an average dopant ionic radius range of 0.909-1.153 Å. Over this wide range, phase mixtures were almost entirely present. The pure rhombohedral phase was present at an average dopant ionic radii of approximately 1.15 Å over a total dopant content range of 17.5-22.5%. Notably, at 10% total dopant content Jolley *et al.*[14] predicted the pure rhombohedral phase to be present over an average dopant ionic radius range of ~1.065-1.14 Å. In this work phase mixtures were evident over the same range. The Rietveld analysis of the 2.5Y7.5LSB sample is given in Figure 6.9 as an example. Overall, the rhombohedral phase stability window has been expanded which coincides with that which was established by Iwahara *et al.*[16] as shown in Figure 6.10.

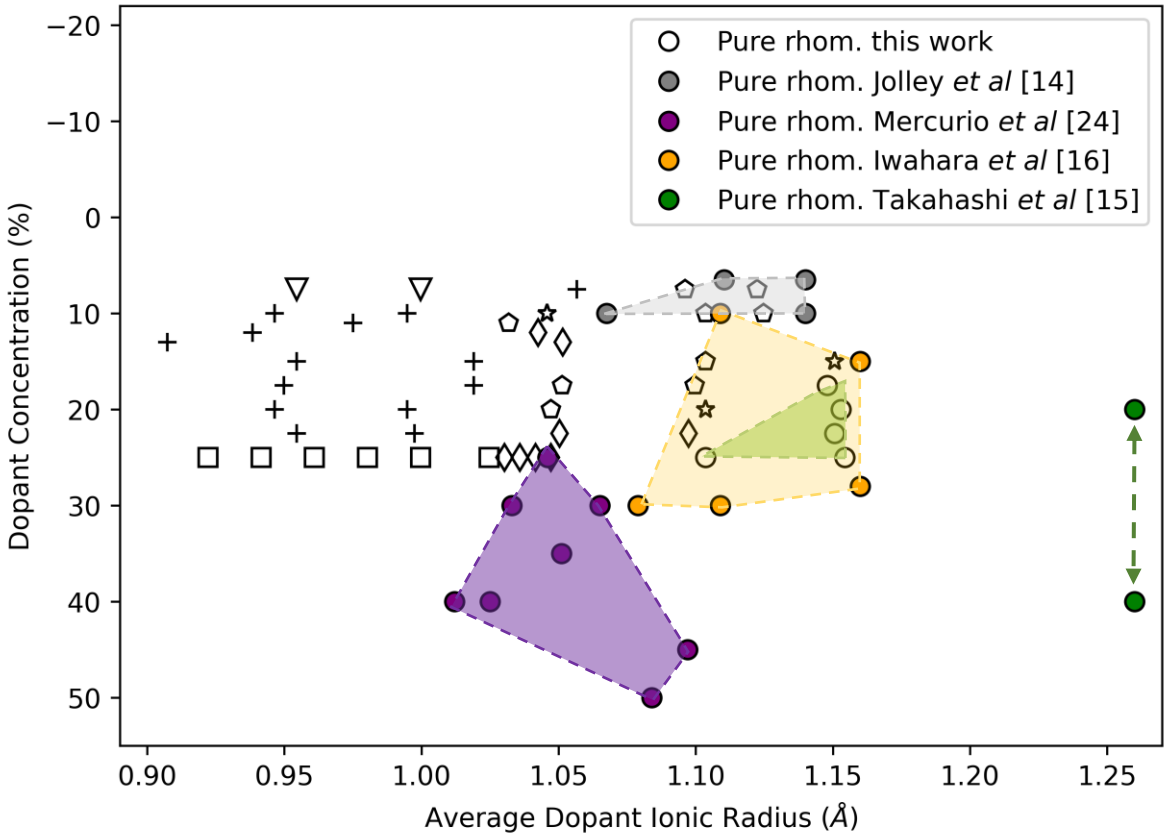

Figure 6.10. Approximate phase stability window of rhombohedral Bi_2O_3 determined in this work (green area) given as a function of total dopant content and average dopant ionic radius. Circles indicate compositions that are entirely rhombohedral and comprise data from this work and from literature as colour coded according to the legend. Additionally from this work, (△) indicate Bi_2O_3 compositions that are entirely tetragonal while (□) indicate pure cubic compositions. (+) indicate tetragonal/cubic phase mixtures, (☆) indicate tetragonal/rhombohedral phase mixtures, (◊) indicate cubic/rhombohedral phase mixtures and (⬠) indicate cubic/tetragonal/rhombohedral phase mixtures.

The investigation of the rhombohedral phase stability window in this work significantly expands on the previous investigations by a wider dopant radius region, in particular over the low average radius region, having been investigated. However, the phase stability window established in this work only coincides with that established by Iwahara *et al.*[16] The phase stability window established by Takahashi *et al.*[15] cannot be compared as the ranges of average dopant ionic radius and dopant concentration do not coincide with that which was investigated in this work. The phase stability window established by Mercurio *et al.*[24] occurs over a significantly higher total dopant content range in comparison to that investigated in this work. However, Mercurio *et al.*[24] reported pure rhombohedral Bi_2O_3 at a dopant content level of 25% and average dopant ionic radius of ~1.05 Å. This point on the phase stability window is not in agreement with the findings in this work where phase mixtures were evident at the same dopant level and average dopant ionic radius. As previously mentioned, the phase stability window of rhombohedral Bi_2O_3 established by Jolley *et al.*[14] also does not coincide with the phase stability findings in this work over similar ranges of total dopant content and average dopant ionic radii. These discrepancies in the rhombohedral phase stability window are likely due to the varying synthetic methodologies applied, in addition to the different dopants used. In this work, a soft chemical citrate gel technique is used to synthesize material precursors which are calcined at 450 ^oC and then annealed at 750 ^oC in air to yield the final material. Jolley *et al.*[14] employed a standard solid state synthesis route with both annealing and subsequent sintering done at 800 ^oC in air. Takahashi *et al.*[15] also employed a standard solid state synthesis technique, however, annealing was done at 700~800 ^oC and subsequent sintering between 800-1000 ^oC in air (compositionally-dependent sintering temperature). Iwahara *et al.*[16] also employed a standard solid state synthesis technique, however, annealing was done at 800-1100 ^oC and subsequent sintering between 850-1150 ^oC in air (compositionally-dependent sintering temperature). Mercurio *et al.*[24] also employed a standard solid state synthesis technique, however, key differences are noted with the other studies mentioned above. The metal oxides were initially annealed for 24 hours under a pure nitrogen atmosphere at 800-900 ^oC. Thereafter, powders were annealed for 24 hours at 800 ^oC and then either air quenched or allowed to slowly cool to room temperature. These variations in the synthetic route are likely responsible, at least in part, for the observed differences in the phase stability window of rhombohedral Bi_2O_3 (Fig. 6.10).

6.3.2. *In situ* investigation of the phase stability of 2Y5.5LSB and 2.5Y7.5LSB using variable temperature powder X-ray diffraction

Rhombohedral Bi_2O_3 has been shown to have excellent ionic conductivity[14,16,24,37,38] at comparatively lower temperatures than that of the cubic phase, which makes these materials attractive as electrolytes for application in low temperature SOFCs. However for such application these materials must exhibit high structural stability during thermal cycling as well as a low rate of thermal expansion. These stability criteria are investigated in this work over the temperature range of 32-656-32 °C for 2Y5.5LSB and 2.5Y7.5LSB. These materials are initially predominantly rhombohedral (94% and 88%, respectively) and contain the lowest total dopant content which is advantageous for maximizing ionic conductivity.[14] Both of these materials have been shown to contain minor cubic and tetragonal phase content and although this mixed phase characteristic is not ideal, it serves to elucidate the various phase transitions that occur during thermal cycling which has not been investigated before.

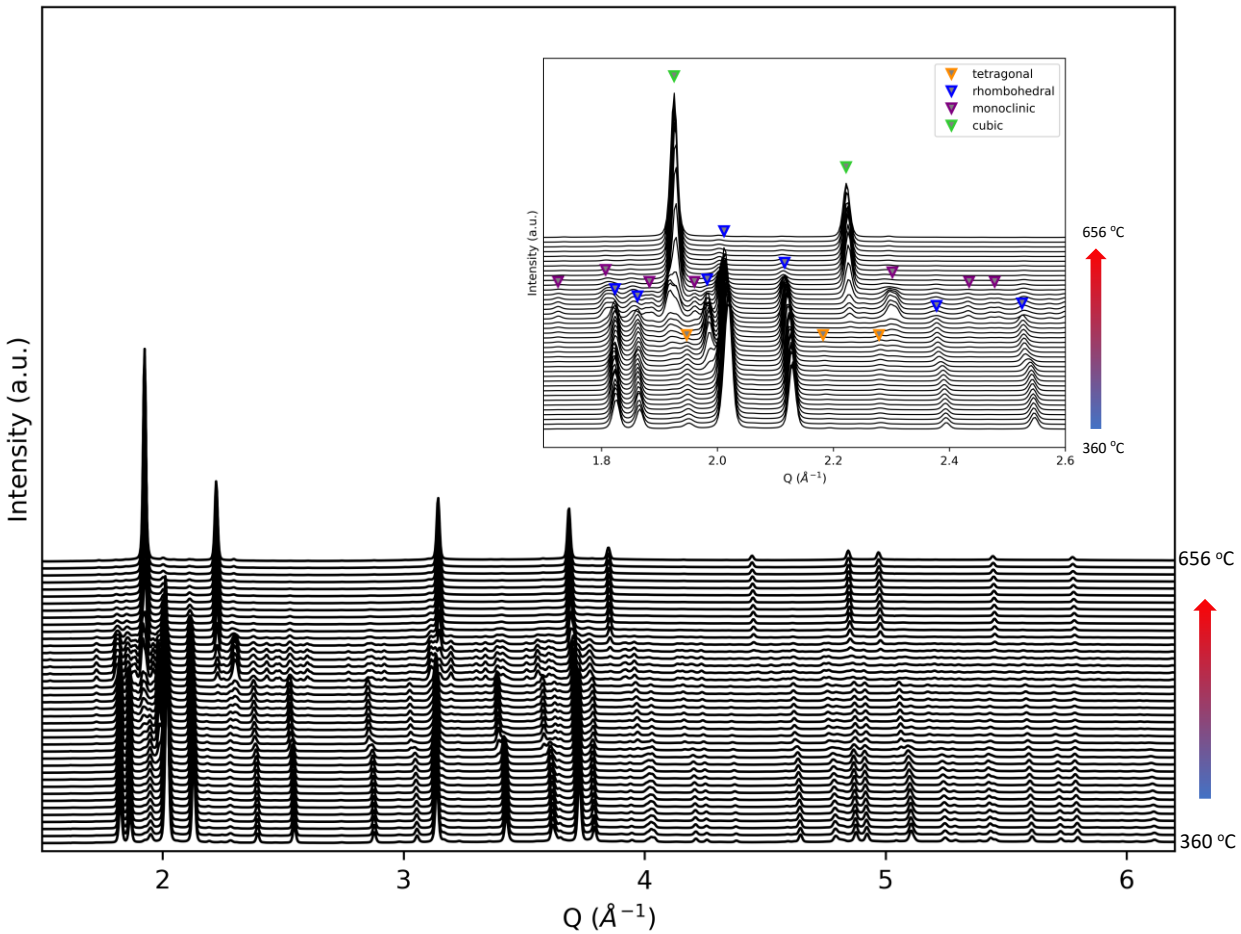

Figure 6.11. *In situ* diffractograms of the 2Y5.5LSB sample annealed at 750 °C collected at ~7 °C intervals over the temperature range of 360-656 °C.

For 2Y5.5LSB, several phase transitions are evident during the thermal cycle. During heating between 32-656 °C (Figs. 6.11 and 6.12a), the rhombohedral/tetragonal/cubic phase mixture was maintained until ~440 °C. Thereafter, a monoclinic phase additionally formed, and the rhombohedral phase content began to decrease. On further heating to ~525 °C, the monoclinic phase exhibited a sharp increase in phase content which coincided with a sharp decrease in rhombohedral phase content and a minor increase in cubic phase content. The monoclinic phase content peaked at ~540 °C and thereafter decreased on further heating and was no longer present by ~625 °C. At ~550 °C, there was a sharp decrease in the rhombohedral phase content and a corresponding sharp increase in cubic phase content. Additionally, above ~550 °C there was no longer tetragonal phase content detected and by 656 °C, the material was predominantly cubic with trace rhombohedral phase content.

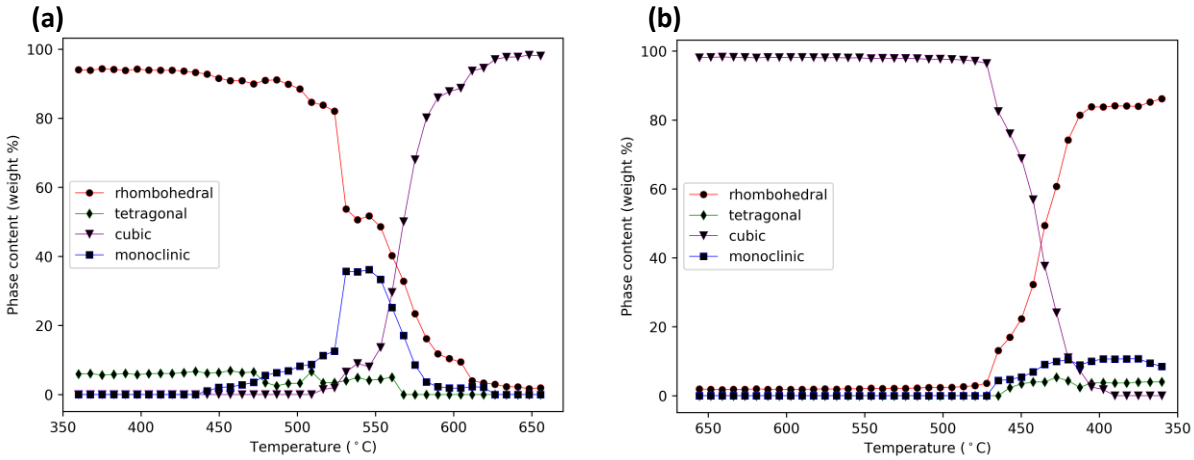

Figure 6.12. *In situ* phase content variation of the 2Y5.5LSB sample annealed at 750 °C over the temperature range of (a) 360-656 °C and (b) 656-360 °C.

During cooling between 656-360 °C (Figs. 6.12b and 6.13), the predominantly cubic material was maintained until ~460 °C. Thereafter, a sharp decrease in cubic phase content was observed which coincided with a sharp increase in rhombohedral phase content and the additional formation of the tetragonal and monoclinic polymorphs. The monoclinic polymorph was still present at 360 °C, however, the phase content was found to decrease between ~390-360 °C. Hence it is predicted that the monoclinic-rhombohedral phase transformation is sluggish during the cooling cycle and further cooling is expected to promote this transformation to completion.

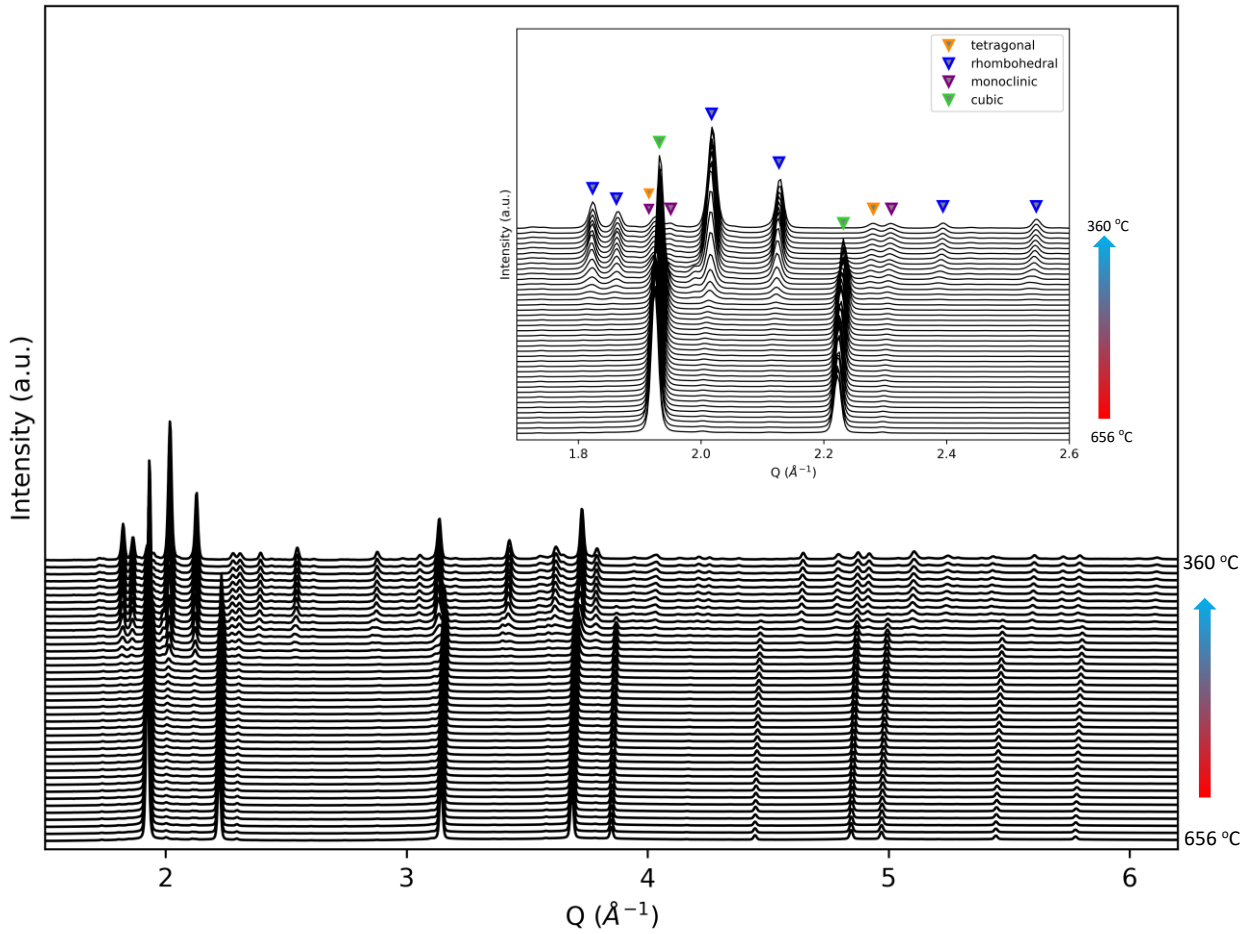

Figure 6.13. *In situ* diffractograms of the 2Y5.5LSB sample annealed at 750 °C collected at ~7 °C intervals over the temperature range of 656-360 °C.

For 2.5Y7.5LSB, similar phase transitions were evident during thermal cycle. During heating between 32-656 °C (Figs. 6.14 and 6.15a), the rhombohedral/tetragonal/cubic phase mixture was largely maintained until ~420 °C. Further heating resulted in minor tetragonal phase formation and a minor decrease in rhombohedral phase content, the latter continuing to gradually decrease until ~550 °C. At ~450 °C, a sharp decrease in tetragonal phase content was evident and by ~560 °C the tetragonal phase was no longer present. These changes coincided with the formation of the monoclinic phase at ~450 °C, which exhibited significantly increased phase content during further heating to ~550 °C. At 550 °C, the monoclinic phase content decreased sharply and was reduced to a trace quantity level at 656 °C (Fig. 6.15a). Additionally at ~550 °C there is an abrupt increase in cubic phase content and an abrupt decrease in rhombohedral phase content which represented the onset of the rhombohedral-cubic phase

transformation. Additionally, at the end of the heating cycle cubic, rhombohedral and monoclinic phase content was detected. This contrasts to the phase change behaviour exhibited by 2Y5.5LSB.

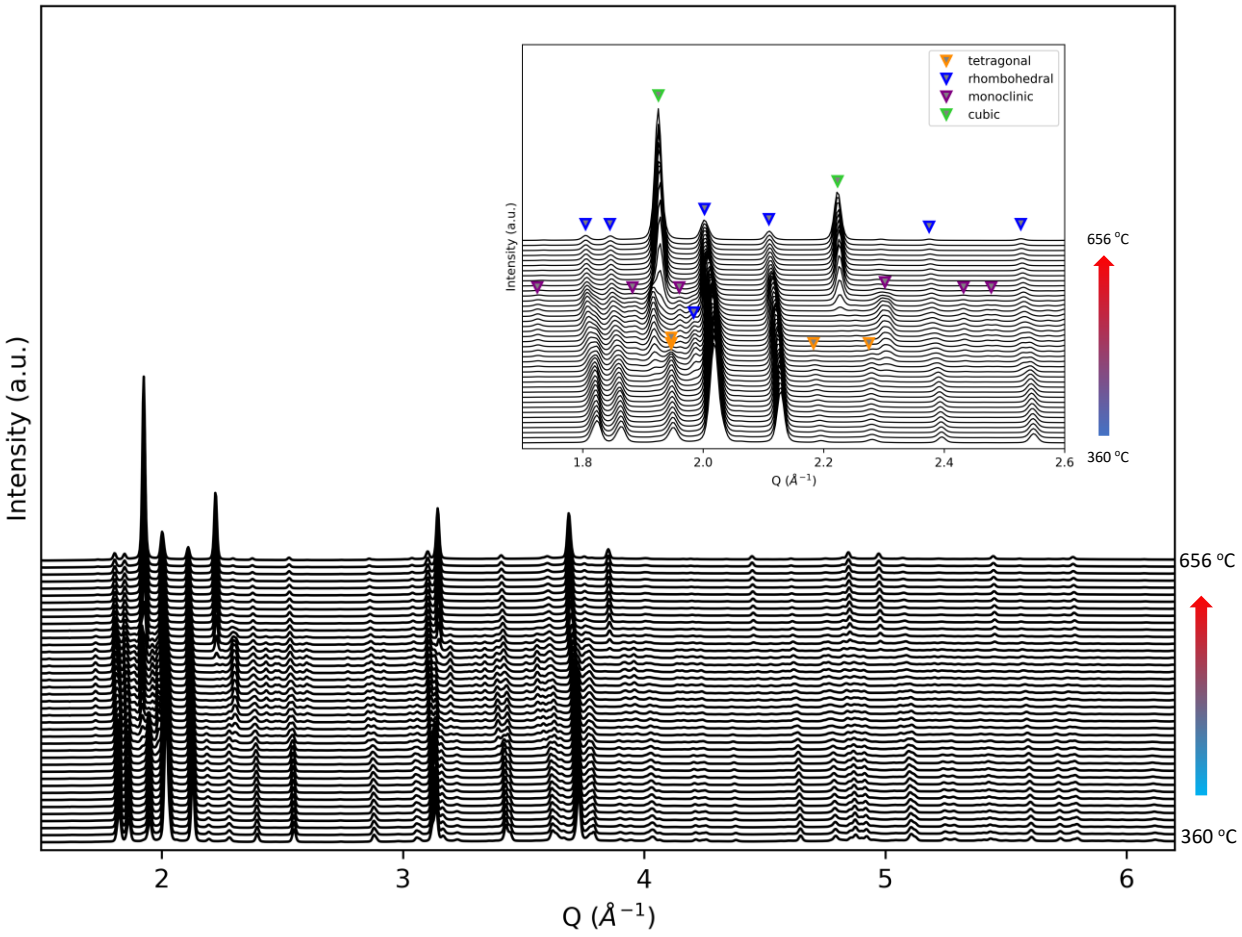

Figure 6.14. *In situ* diffractograms of the 2.5Y7.5LSB sample annealed at 750 °C collected at ~7 °C intervals over the temperature range of 360-656 °C.

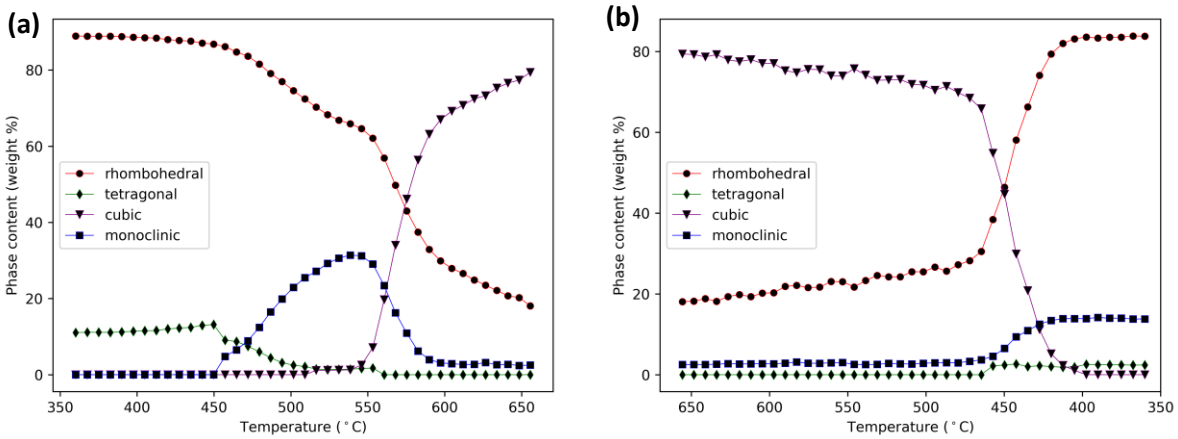

Figure 6.15. *In situ* phase content variation of the 2.5Y7.5LSB sample annealed at 750 °C over the temperature range of (a) 360-656 °C and (b) 656-360 °C.

During cooling between 656-360 °C (Figs. 6.15b and 6.16), the mixed phase nature of the 2.5Y7.5LSB material was maintained until ~460 °C with only a gradual changes in rhombohedral and cubic phase content between ~656-460 °C. Thereafter, a sharp decrease in cubic phase content was observed which coincided with a sharp increase in rhombohedral phase content and the additional formation of the tetragonal and monoclinic polymorphs. This phase change behaviour mirrors that which was observed for the 2Y5.5LSB material. However, for 2.5Y7.5LSB the monoclinic polymorph was still present at 360 °C and the phase content was stable. Hence it is predicted that the monoclinic-rhombohedral phase transformation is even more sluggish for 2.5Y7.5LSB in comparison to that exhibited for 2Y5.5LSB.

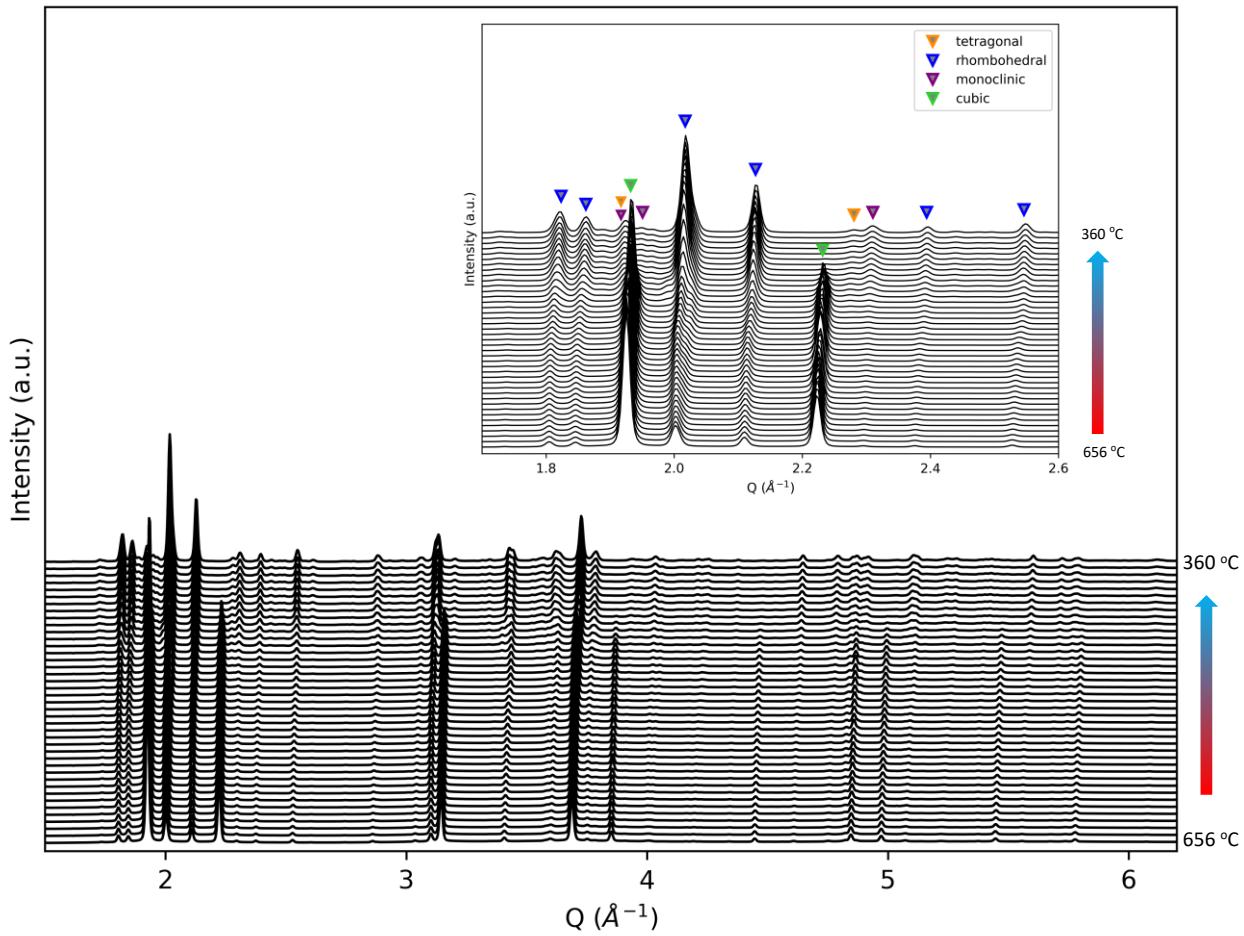

Figure 6.16. *In situ* diffractograms of the 2.5Y7.5LSB sample annealed at 750 °C collected at ~7 °C intervals over the temperature range of 656-360 °C.

6.3.3. Thermal expansion behaviour of 2Y5.5LSB and 2.5Y7.5LSB investigated using variable temperature powder X-ray diffraction

The thermal expansion behaviour of the cubic phase component in both the 2Y5.5LSB and 2.5Y7.5LSB compositions was monitored *in situ* during the thermal cycle (Fig. 6.17) over the temperature range of 531-656-427 °C where the cubic phase content present for both compositions was sufficient to allow for accurate lattice parameter refinements. The thermal expansion of the cubic phase fraction in both samples was nearly identical, with only a noteworthy discrepancy at temperatures above ~580 °C (Fig. 6.17 inset).

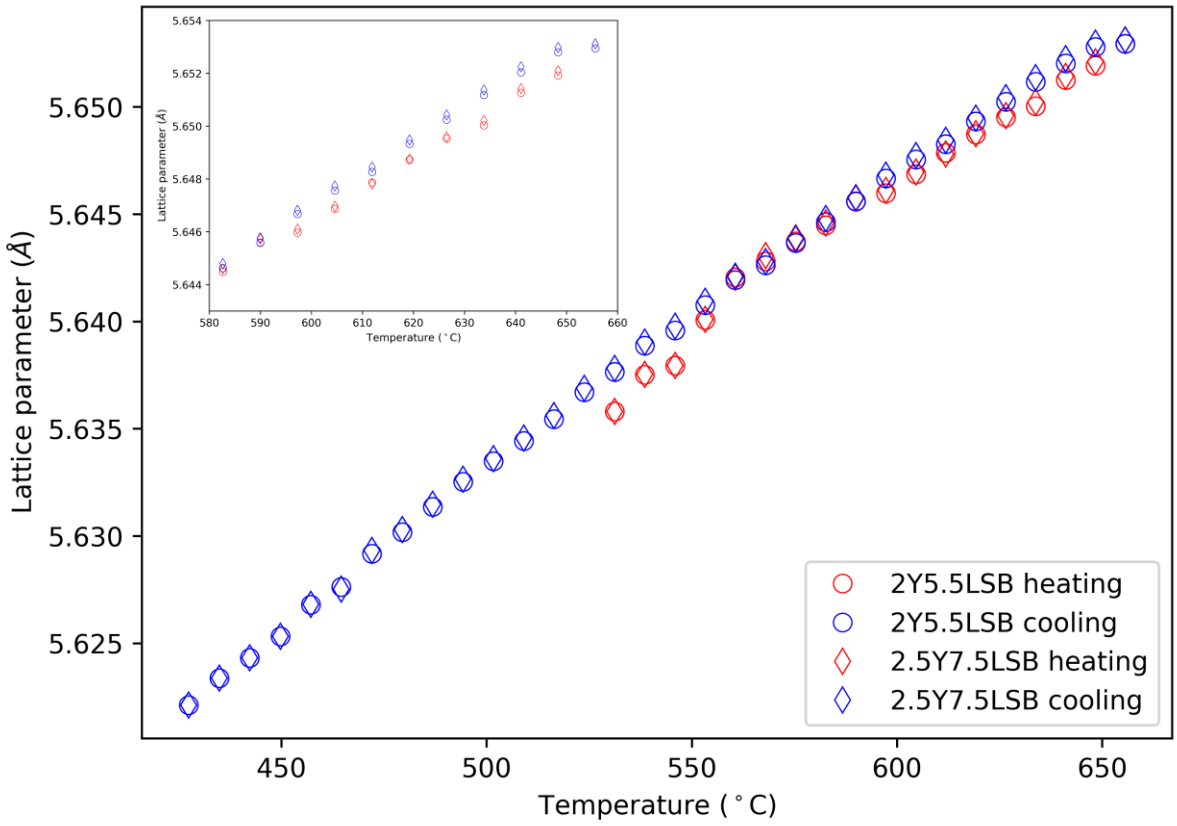

Figure 6.17. Cubic phase lattice parameter variation of 2Y5.5LSB (circle markers) and 2.5Y7.5LSB (diamond markers) materials over the temperature range of 531-656-427 °C. The inset accentuates the increased variation in lattice parameter values in the upper segment of the thermal cycle.

In our previous work we have shown that the total dopant content influences the observed coefficient of thermal expansion (CTE) of the cubic phase.[39–41] Higher dopant content resulted in decreased CTEs over similar temperature ranges to that investigated in this work (Table 6.2).[41] The CTEs derived for 2Y5.5LSB and 2.5Y7.5LSB are essentially equivalent within the calculated uncertainty (standard error) in the

measurements due to their similar the total dopant content. However, the CTEs for 2.5Y7.5LSB are greater than those for 10YSB even though the total dopant content is equivalent. This indicates that the nature of the dopant and the identity of the phases present in the phase mixture additionally influences the thermal expansion. The magnitude of the CTEs for the cubic phase reported in this work are significantly greater than those for components presently used in SOFCs.[39]

Table 6.2. Cubic phase CTE variation of 2Y5.5LSB and 2.5Y7.5LSB over the temperature range of 531-656-427 °C. CTEs determined for the cubic phase of various compositions are included for comparison.

Sample composition	Temperature range (°C)	CTE (10^{-6} K^{-1})	Ref.
2Y5.5LSB	531-656	130.8 ± 4.3	This work
	656-427	138.2 ± 1.3	This work
2.5Y7.5LSB	531-656	131.7 ± 4.5	This work
	656-427	139.0 ± 1.4	This work
10YSB	525-636	120.8 ± 5.1	[41]
	636-455	111.4 ± 4.4	[41]
10Y1AlSB	502-636	120.9 ± 7.1	[41]
	636-432	114.2 ± 3.4	[41]
27.5YSB	525-636	110.6 ± 1.7	[41]
	636-287	107.5 ± 1.0	[41]

The thermal expansion behaviour of the rhombohedral phase component of both the 2Y5.5LSB and 2.5Y7.5LSB compositions were also monitored *in situ* during the thermal cycle. For 2Y5.5LSB, the thermal expansion behaviour is reported over the 360-575 °C temperature range during heating and over the 457-360 temperature range during cooling. For 2.5Y7.5LSB the entire 360-656-360 °C temperature range was investigated. This was again due to the requirement of sufficient rhombohedral phase content over these temperature ranges to allow for accurate lattice parameter refinements. Due to the crystal structure of the rhombohedral phase, the thermal expansion behaviour was investigated by monitoring the change in the unit cell volume during the thermal cycle. For 2Y5.5LSB, the expansion of the rhombohedral lattice is uniform over ~360-450 °C during heating (Fig. 6.18a), with an abrupt increase in rhombohedral unit cell volume occurring at ~450 °C. Thereafter over ~460-575 °C the thermal expansion was again uniform. During the cooling cycle, an abrupt decrease in the unit cell volume was evident at ~440 °C. The correlation

between phase transformations and abrupt changes in unit cell parameters has been reported by Thrall *et al.*[42] for $BiFeO_3$, by Struzik *et al.*[43] for $Bi_{14}YO_{22.5}$, by Struzik *et al.*[43] for $Bi_{14}YO_{22.5}$ and by Borowska-Centkowska *et al.*[44] for $Bi_{14}WO_{24}$. This is reinforced here for 2Y5.5LSB where the temperature ranges during which the abrupt changes in the rhombohedral phase unit cell volume occurred coincided with the temperature ranges wherein significant phase changes occurred during the heating (Figs. 6.11 and 6.12a) and cooling (Figs. 6.12b and 6.13) cycles. Interestingly, during heating the rhombohedral phase lattice volume expansion results in the separation of the (009) and (104) peaks (Fig. 6.18b). This separation was prominent over the temperature range preceding the onset of the rhombohedral-cubic phase transformation and serves as an excellent visual marker for this process. During cooling the peak separation was less prominent, likely due to both the lower temperature range during which the cubic-rhombohedral transformation occurred and the decreased rhombohedral phase (Fig. 6.18c).

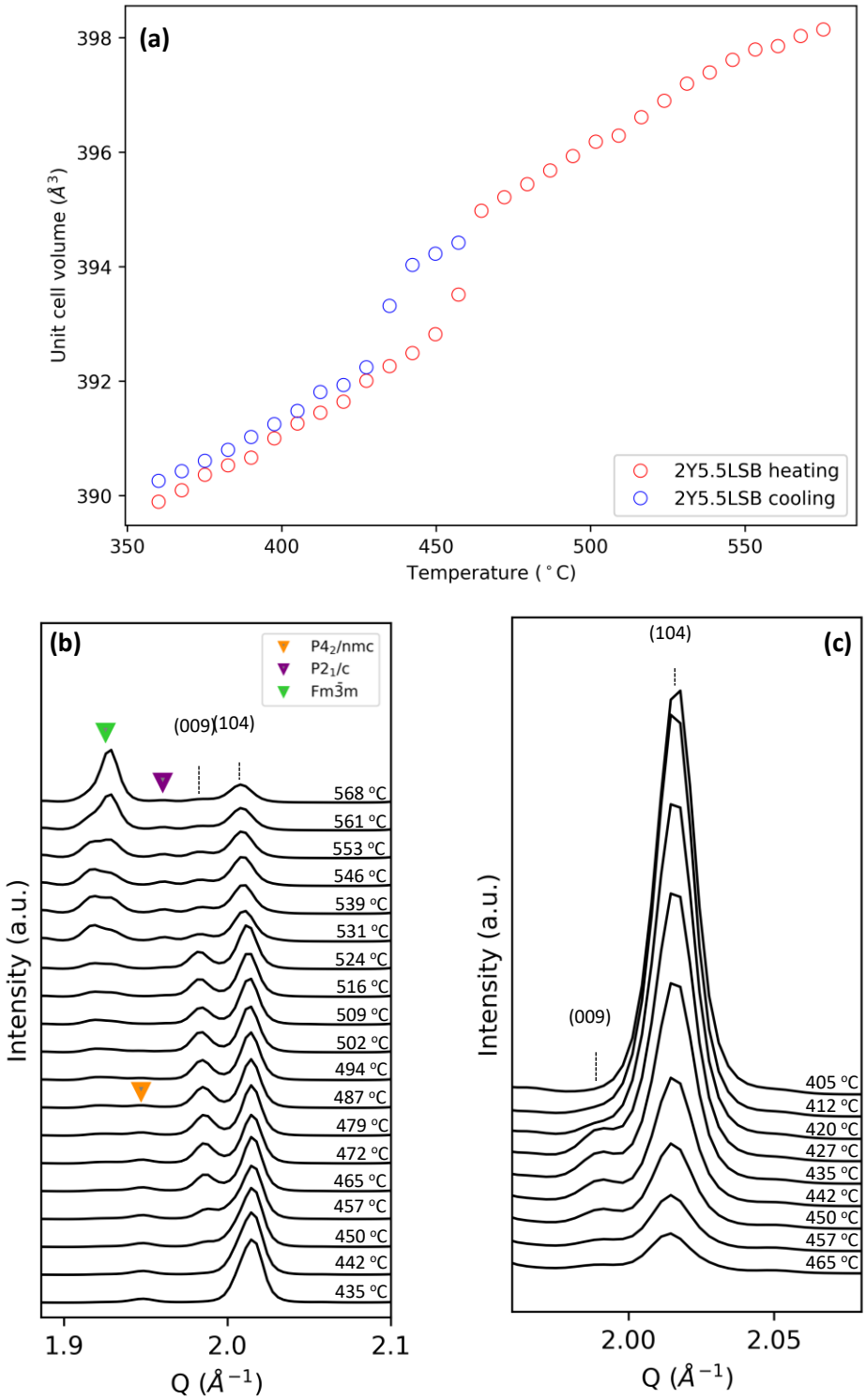

Figure 6.18. (a) Rhombohedral phase unit cell volume variation of the annealed 2Y5.5LSB material. Abrupt changes in unit cell volume during (b) heating and (c) cooling coincide with various phase changes observed and are highlighted by the separation of the rhombohedral phase (009) and (104) peaks.

A similar trend for 2.5Y7.5LSB was observed (Fig. 6.19a), where the expansion of the rhombohedral lattice was uniform over ~360-470 ^{o}C during heating. An abrupt increase in the unit cell volume occurred between ~470-550 ^{o}C, i.e. at a higher temperature range than that for 2Y5.5LSB. Thereafter (~550-656 ^{o}C) the rate of thermal expansion was again uniform. During the cooling cycle, a similar abrupt change in rhombohedral unit cell volume was evident over ~525-480 ^{o}C. As before, the temperature ranges during which these abrupt changes occurred coincided with that wherein significant phase changes occurred during the heating (Figs. 6.14 and 6.15a) and cooling (Figs. 6.15b and 6.16) cycles. Once again, the separation of the (009) and (104) peaks of the rhombohedral phase was evident and was prominent over the temperature range preceding the abrupt onset of the rhombohedral-cubic phase transformation during heating (Fig. 6.19b). Similarly, during cooling the peak separation was again less prominent but coincides with the onset of the cubic-rhombohedral phase transformation (Fig. 6.19c). The changes in rhombohedral unit cell volume during both the heating and cooling cycles for the 2.5Y7.5LSB material are less pronounced in comparison to that which was seen for the 2Y5.5LSB material. This is not surprising given that the rhombohedral-cubic transformation was almost driven to completion at 656 ^{o}C for the 2Y5.5LSB material whereas this was not the case for the 2.5Y7.5LSB material. This was also evident in the reduced separation of the (009) and (104) peaks for the rhombohedral phase in the temperature range in which significant phase transformation were observed (Figs. 6.19b and 6.19c).

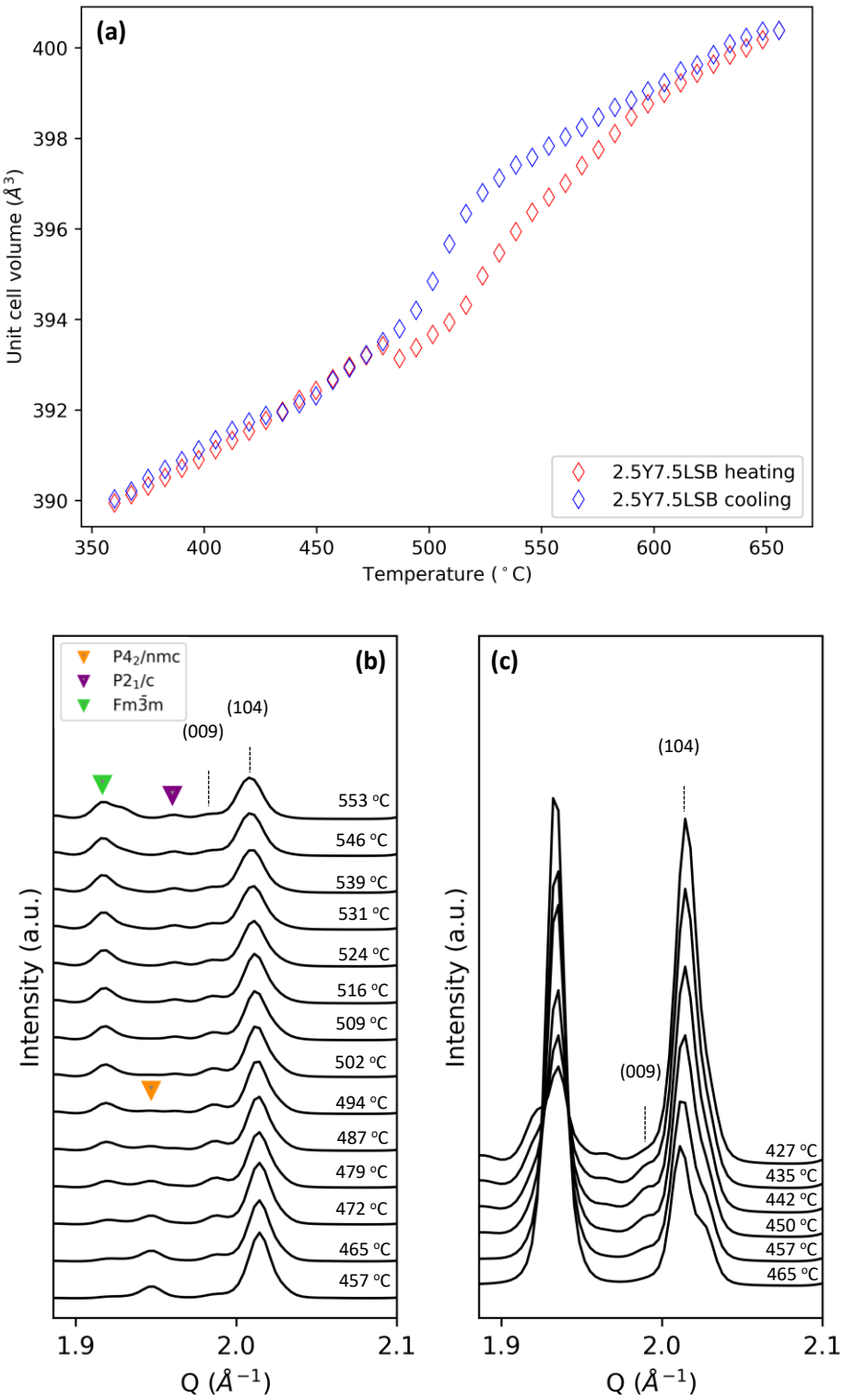

Figure 6.19. (a) Rhombohedral phase unit cell volume variation of the annealed 2.5Y7.5LSB material. Abrupt changes in unit cell volume during (b) heating and (c) cooling coincide with various phase changes observed and are highlighted by the separation of the rhombohedral phase (009) and (104) peaks.

6.4. Conclusion

Investigating the phase stability window of rhombohedral Bi_2O_3 is crucial to the optimization of this conductive phase for application as a SOFC electrolyte. The phase stability window of rhombohedral Bi_2O_3 was investigated in this work over a wide range of total dopant content and average dopant ionic radii. The phase stability window identified on this basis, although in agreement with previous results published by Iwahara *et al.*[16] was found to otherwise conflict the results published in literature.[14,24] This indicates that the nature of the dopant cation in addition to the synthetic methodology used also contribute significantly towards the stabilization of rhombohedral Bi_2O_3. The investigation of the *in situ* phase transformation behaviour illustrated for the first time the complex phase transformations that occur for rhombohedral-rich phase mixtures. Although these transformations are undesirable in materials for SOFC applications, the two compositions studied in this work provided insight into the rhombohedral-cubic phase transformation in addition to the formation of the monoclinic polymorph. The variation in both the cubic phase lattice parameter and rhombohedral phase unit cell volume proved to be indicative of the phase transformations observed. Additionally, the separation of the (009) and (104) peaks of the rhombohedral phase during the thermal cycle was identified as an excellent visual marker of the rhombohedral-cubic phase transformation.

6.5. Future work

To investigate the phase transformations in greater detail would be advantageous to enable more accurate quantitative phase analysis and thermal expansion behaviour investigations. For this, high resolution synchrotron X-ray diffraction measurements are sought. The effect of these phase transformations on the ionic conductivity are required to further probe the suitability of these materials as SOFC electrolytes. Additionally, measurements of both the thermal expansion behaviour and ionic conductivity of pure rhombohedral phase materials are sought to further determine if these materials are suitable for SOFC applications.

6.6. References

1. Sammes, N. M., Tompsett, G. A., Näfe, H. and Aldinger, F. Bismuth based oxide electrolytes—structure and ionic conductivity. *J. Eur. Ceram. Soc*. **19**, 1801–1826 (1999).

2. Shuk, P. Oxide ion conducting solid electrolytes based on Bi_2O_3. *Solid State Ion.* **89**, 179–196 (1996).

3. Azad, A. M., Larose, S. and Akbar, S. A. Bismuth oxide-based solid electrolytes for fuel cells. *J. Mater. Sci*. **29**, 4135–4151 (1994).

4. Levin, E. M. and Roth, R. S. Polymorphism of bismuth sesquioxide. I. Pure Bi_2O_3. *J. Res. Natl. Bur. Stand. Sect. A Phys. Chem*. **68A**, 189 (1964).

5. Levin, E. M. and Roth, R. S. Polymorphism of bismuth sesquioxide. II. Effect of oxide additions on the polymorphism of Bi_2O_3. *J. Res. Natl. Bur. Stand. Sect. A Phys. Chem*. **68A**, 197 (1964).

6. Battle, P. D., Catlow, C. R. A., Heap, J. W. and Moroney, L. M. Structural and dynamical studies of δ-Bi_2O_3 oxide ion conductors. I. The structure of $(Bi_2O_3)_{1-x}(Y_2O_3)_x$ as a function of x and temperature. *J. Solid State Chem*. **63**, 8–15 (1986).

7. Kale, K. V., Jadhav, K. M. and Bichile, G. K. Investigations on a high-conductivity solid electrolyte system, Bi_2O_3-Y_2O_3. *J. Mater. Sci. Lett*. **18**, 9–11 (1999).

8. Takahashi, T., Iwahara, H. and Arao, T. High Oxide Ion Conduction in Sintered Oxides of the System Bi_2O_3-Y_2O_3. *J. Appl. Electrochem*. **5**, 187–195 (1975).

9. Wang, C., Xu, X. and Li, B. Ionic and electronic conduction of oxygen ion conductors in the Bi_2O_3-Y_2O_3 system. *Solid State Ion.* **13**, 135–140 (1984).

10. Lee, J. G., Kim, S. H. and Yoon, H. H. Synthesis of yttria-doped bismuth oxide powder by carbonate coprecipitation for IT-SOFC electrolyte. *J. Nanosci. Nanotechnol*. **11**, 820–823 (2011).

11. Wang, S.-F., Hsu, Y.-F., Tsai, W.-C. and Lu, H.-C. The phase stability and electrical conductivity of Bi_2O_3 ceramics stabilized by Co-dopants. *J. Power Sources* **218**, 106–112 (2012).

12. Zhang, X. J., Jin, W. T., Hao, S. J., Zhao, Y. and Zhang, H. Study of the crystal structures of new buffer materials $Bi_{1-x}Y_xO_{1.5}$. *J. Supercond. Nov. Magn*. **23**, 1011–1014 (2010).

13. Wu, Y.-C., Chang, Y.-W. and Wang, S.-F. Electrical Properties and Microstructural Analysis of Aliovalent-Ion (Y^{3+}, Nb^{5+})–Doped Bismuth-Based Solid-Oxide Electrolyte. *Ferroelectrics* **455**, 123–128 (2013).

14. Jolley, A. G., Jayathilake, R. and Wachsman, E. D. Optimizing rhombohedral Bi_2O_3 conductivity for low temperature SOFC electrolytes. *Ionics (Kiel)*. **25**, 3531–3536 (2019).

15. Takahashi, T., Iwahara, H. and Nagai, Y. High oxide ion conduction in sintered Bi_2O_3 containing SrO, CaO or La_2O_3. *J. Appl. Electrochem*. **2**, 97–104 (1972).

16. Iwahara, H., Esaka, T., Sato, T. and Takahashi, T. Formation of high oxide ion conductive phases in the sintered oxides of the system Bi_2O_3-Ln_2O_3 (Ln = La-Yb). *J. Solid State Chem*. **39**, 173–180 (1981).

17. Watanabe, A. and Kikuchi, T. Cubic-hexagonal transformation of yttria-stabilized δ-bismuth sesquioxide, $Bi_{2-2x}Y_{2x}O_3$ (x=0.215-0.235). *Solid State Ion.* **21**, 287–291 (1986).

18. Cahen, H. T., Van Den Belt, T. G. M., De Wit, J. H. W. and Broers, G. H. J. The electrical conductivity of δ-Bi_2O_3 stabilized by isovalent rare-earth oxides R_2O_3. *Solid State Ion.* **1**, 411–423 (1980).

19. Obbade, S., Huve, M., Suard, E., Drache, M. and Conflant, P. Powder neutron diffraction and TEM investigations of $Bi_{0.775}Ln_{0.225}O_{1.5}$ oxide conductors (Ln=La, Pr, Nd, Sm, Tb, Dy) with rhombohedral Bi-Sr-O type: Structural relationships with monoclinic ε-$Bi_{4.86}La_{1.14}O_9$ form. *J. Solid State Chem*. **168**, 91–99 (2002).

20. Drache, M., Obbade, S., Wignacourt, J. P. and Conflant, P. Structural and Conductivity Properties of $Bi_{0.775}Ln_{0.225}O_{1.5}$ Oxide Conductors (Ln = La, Pr, Nd, Sm, Eu, Gd, Tb, Dy) with Rhombohedral Bi-Sr-O Type. *J. Solid State Chem*. **142**, 349–359 (1999).

21. Belik, A. A., Wuernisha, T., Kamiyama, T., Mori, K., Maie, M., Nagai, T., Matsui, Y. and Takayama-Muromachi, E. High-pressure synthesis, crystal structures, and properties of perovskite-like $BiAlO_3$ and pyroxene-like $BiGaO_3$. *Chem. Mater*. **18**, 133–139 (2006).

22. Zhang, X., Hu, W., Qi, X., Sun, G., Qi, J., Chen, H. and Zhong, R. Synthesis and characterization of $Bi_2Al_4O_9$ powders. *Adv. Mater. Res*. **624**, 34–37 (2013).

23. Bloom, I., Hash, M. C., Zebrowski, J. P., Myles, K. M. and Krumpelt, M. Oxide-ion conductivity of bismuth aluminates. *Solid State Ion.* **53–56**, 739–747 (1992).

24. Mercurio, D., Farissi, M. El, Frit, B., Reau, J. M. and Senegas, J. Fast ionic conduction in new oxide materials of the Bi_2O_3-Ln_2O_3-TeO_2 systems (Ln=La, Sm, Gd, Er). *Solid State Ion.* **39**, 297–304 (1990).

25. Danks, A. E., Hall, S. R. and Schnepp, Z. The evolution of 'sol-gel' chemistry as a technique for materials synthesis. *Mater. Horizons* **3**, 91–112 (2016).

26. Shi, X., Ghose, S. and Dooryhee, E. Performance calculations of the X-ray powder diffraction beamline at NSLS-II. *J. Synchrotron Radiat*. **20**, 234–242 (2013).

27. Hammersley, A. P. FIT2D: A multi-purpose data reduction, analysis and visualization program. *J. Appl. Crystallogr.* **49**, 646–652 (2016).

28. Kaiser, D. L. and Watters, R. L. SRM 640d - Silicon Powder - Line Position and Line Shape Standard for Powder Diffraction. *National Institute of Standards and Technology* 1–5 (2010). Available at: https://www-s.nist.gov/srmors/certificates/archives/640d.pdf. (Accessed: 2nd January 2021)

29. Lyon, K. G., Salinger, G. L., Swenson, C. A. and White, G. K. Linear thermal expansion measurements on silicon from 6 to 340 K. *J. Appl. Phys*. **48**, 865–868 (1977).

30. Okada, Y. and Tokumaru, Y. Precise determination of lattice parameter and thermal expansion coefficient of silicon between 300 and 1500 K. *J. Appl. Phys*. **56**, 314–320 (1984).

31. Coelho, A. A. TOPAS and TOPAS-Academic: An optimization program integrating computer algebra and crystallographic objects written in C++: An. *J. Appl. Crystallogr*. **51**, 210–218 (2018).

32. Dinnebier, R. E., Leineweber, A. and Evans, J. S. O. *Rietveld Refinement Practical Powder Diffraction Pattern Analysis Using Topas*. (Walter de Gruyter GmbH, Berlin/Boston, 2019).

33. Cheary, R. W., Coelho, A. A. and Cline, J. P. Fundamental parameters line profile fitting in laboratory diffractometers. *J. Res. Natl. Inst. Stand. Technol.* **109**, 1–25 (2004).

34. Cheary, R. W. and Coelho, A. A. Axial Divergence in a Conventional X-ray Powder Diffractometer. I. Theoretical Foundations. *J. Appl. Crystallogr.* **31**, 851–861 (1998).

35. Thompson, P., Cox, D. E. and Hastings, J. B. Rietveld Refinement of Debye-Scherrer Synchrotron X-ray Data from Al_2O_3. *J. Appl. Crystallogr.* **20**, 79–83 (1987).

36. Shannon, R. D. Revised Effective Ionic Radii and Systematic Studies of Interatomie Distances in Halides and Chalcogenides. *Acta Crystallogr*. **32**, 751–767 (1976).

37. Drache, M., Obbade, S., Wignacourt, J. P. and Conflant, P. Structural and Conductivity Properties of $Bi_{0.775}Ln_{0.225}O_{1.5}$ Oxide Conductors (Ln = La, Pr, Nd, Sm, Eu, Gd, Tb, Dy) with Rhombohedral Bi-Sr-O Type. *J. Solid State Chem*. **142**, 349–359 (1999).

38. Takahashi, T., Iwahara, H. and Nagai, Y. High oxide ion conduction in sintered Bi_2O_3 containing SrO, CaO or La_2O_3. *J. Appl. Electrochem.* **2**, 97–104 (1972).

39. Kiefer, M. A., Billing, C., Erasmus, R. M., Mogodi, W. M. and Billing, D. G. A detailed investigation of the structural stability, ionic conductivity and in situ δ-phase formation of $Y_xBi_{2-x}O_\delta$. *Submitted. Manuscr.* (2021).

40. Kiefer, M. A., Billing, C., Olds, D. and Billing, D. G. Investigating the ambient and in situ thermal phase stability of $Y_xBi_{2-x}O_3$ electrolytes. *Unpubl. Manuscr.* (2021).

41. Kiefer, M. A., Billing, C., Olds, D. and Billing, D. G. Investigating the thermal expansion behaviour of $Y_xBi_{2-x}O_3$ electrolytes using in situ total scattering studies. *Unpubl. Manuscr.* (2021).

42. Thrall, M., Freer, R., Martin, C., Azough, F., Patterson, B. and Cernik, R. J. An in situ study of the formation of multiferroic bismuth ferrite using high resolution synchrotron X-ray powder diffraction. *J. Eur. Ceram. Soc*. **28**, 2567–2572 (2008).

43. Struzik, M., Malys, M., Krynski, M., Wojcik, M., Dygas, J. R., Wrobel, W., Krok, F. and Abrahams, I. Structural and electrical behaviour in $Bi_{14}YO_{22.5}$. *RSC Adv*. **5**, 83471–83479 (2015).

44. Borowska-Centkowska, A., Krok, F., Abrahams, I., Wrobel, W., Dygas, J. R. and Hull, S. Thermal variation of structure and electrical conductivity in $Bi_{14}WO_{24}$. *Solid State Ion.* **202**, 14–21 (2011).

Chapter 7. General conclusions and future work

Bismuthate materials have immense potential as improved SOFC electrolytes due to their high ionic conductivity at lower operating temperatures, however, there are several issues due to the characteristics of these materials which make them unsuitable for this application at this stage. Investigating these characteristics in more detail, which was the focus of this thesis, is essential to build a better understanding of bismuthate materials in order to improve their characteristics or use them in combination with other materials, and hence eventually compete with the more popularized ceria and zirconia electrolytes. Throughout this thesis, several bismuthate materials were synthesized using the citrate-gel method and investigated using powder X-ray diffraction, Raman spectroscopy and impedance spectroscopy techniques, all as a function of temperature.

The δ-phase is the most studied phase of Bi_2O_3, and yttrium doping has been previously reported to stabilize this phase. However, the results across several publications were found to be inconsistent. To investigate these inconsistencies and to further explore the characteristics of yttrium-doped bismuthates, the structural stability, ionic conductivity and *in situ* δ-phase formation of several yttrium-doped bismuthates was explored. The δ-phase was found to be fully stabilized only with yttrium dopant content ≥ 25 mol%, whereas stabilization has been previously reported for yttrium content as low as 10 mol%. This emphasizes the need to identify subtle diffraction peak asymmetries, which are often overlooked in lab-based experiments, to correctly identify mixed phase bismuthates. Higher dopant content resulted in decreased CTEs observed for the δ-phase and decreased ionic conductivity. Sample preparation and measurement strategies were found to play a role in the measured conductivity values, thus values determined within this work are comparable, but comparisons become a bit more tenuous when extending this to similar work by others.

The phase stability of several yttrium-stabilized Bi_2O_3 materials was investigated over prolonged periods of time under ambient conditions. The 'stabilized' cubic and tetragonal phases were found to be metastable under these conditions and the spontaneous formation of both the rhombohedral and subcarbonate phases was observed. The formation of the latter is particularly remarkable as this was the first time that the sequestration of atmospheric carbon dioxide has been observed for bismuth oxide. Additionally, the thermal prehistory of the 'stabilized' materials was found to have a distinct effect on the long-term phase stability characteristics.

In attempts to enhance the ambient, long term stability of the δ-phase, pelletization and additional sintering as well as annealing under an inert atmosphere was found to significantly increase the phase stability. The annealing in a nitrogen atmosphere additionally resulted in a thermochromic response characterized by a colour change from brown to yellow, indicating a non-reversible change in the electronic structure of the material.

During a thermal cycle, a 15YSB material displayed abrupt changes in cubic unit cell volume which are thought to be due to an unidentified phase change and/or the order-disorder transition. Similarly, a 27.5YSB material exhibited non-linear thermal expansion during the thermal cycle, likely indicating the occurrence of changes in disorder and/or oxygen occupancy occurred during the thermal cycle. This behaviour was resolved, using synchrotron-based *in situ* total scattering, into two regions of approximate linear thermal expansion (i.e., a low temperature and a high temperature region). Over the high temperature region, the CTE was found to be increased in comparison to that observed over the low temperature region. By *direct analysis* and by monitoring changes in the cationic thermal displacement parameters, abrupt changes in disorder of the 27.5YSB material were observed during the thermal cycle. These changes coincided with the change observed in the CTE, indicating that the order-disorder transition contributed to the non-linear thermal expansion behaviour.

For 10YSB and 10Y1AlSB, abrupt changes in the cubic phase unit cell volume were observed during the thermal cycle, which coincided with the tetragonal-cubic phase transformation. A phase change mechanism was proposed to account for the abrupt change in unit cell volume and to substantiate the phase change mechanism, evidence was sought from local structure analysis. This showed that abrupt changes in disorder during the thermal cycle coincided with the phase transformation and with changes observed in the CTE. Importantly, *direct analysis* of selected PDF features showed the presence of a second cubic phase at elevated temperatures which substantiates the proposed phase change mechanism. Impedance measurements for 10YSB showed that abrupt increases in ionic conductivity coincide with the tetragonal-cubic phase transformation. Similar measurements for 27.5YSB showed that changes in conductivity occur, which coincide with changes in the CTE of the material. This indicates that changes in the disorder of the material, which are evident in the EIS data, contribute towards the changes observed in the CTE which substantiates the findings from the total scattering analyses.

The rhombohedral phase of Bi_2O_3 has recently emerged as a promising SOFC electrolyte material due to its high ionic conductivity. The phase stability window of the rhombohedral phase of Bi_2O_3 was found to differ somewhat from that reported in literature. This discrepancy highlights that the phase stability at a

particular dopant level and average dopant ionic radius is dependent on the synthetic method used and the nature of the dopant atoms. *In situ* phase stability investigations of rhombohedral-rich phase mixtures 2Y5.5LSB and 2.5Y7.5LSB exhibited complex phase transformations involving the reversible rhombohedral-cubic phase transformation along with the formation of the monoclinic and tetragonal phases. The CTEs derived for the cubic phase content of 2.5Y7.5LSB are larger than those derived for 10YSB although the total dopant content is equivalent. This indicates that the nature of the dopant and the identity of the phases present in the phase mixture additionally influences the observed thermal expansion behaviour. Abrupt changes in thermal expansion were observed for the rhombohedral phase of both 2Y5.5LSB and 2.5Y7.5LSB during the heating and cooling cycles, indicating the reversible rhombohedral-cubic phase transformation and the separation of the (009) and (104) peaks of the rhombohedral phase during the thermal cycle was identified as an excellent visual marker of the transformation.

The research undertaken in this thesis demonstrates both the immense potential and pitfalls of bismuthates as SOFC electrolytes. Future work is required to further unravel these complex materials further, the most critical of which would be:

- Variable temperature high resolution powder diffraction measurements are required to better resolve phase content to provide more confidence in the claim of a 'phase pure' material. Throughout this thesis, prominent diffraction peak overlap was identified, and this limited the accuracy to which phase compositions were determined.
- Variable temperature neutron powder diffraction (NPD) measurements are required to aid structure elucidation and to probe changes in the oxygen sublattice during the thermal cycle. These measurements are required to investigate the contribution from the oxygen sublattice to the non-linear thermal expansion behaviour exhibited for the stabilized bismuthates and to identify changes in the order of the anion sublattice.

Appendix A

A1. VT-PXRD collected at ID22 of the ESRF

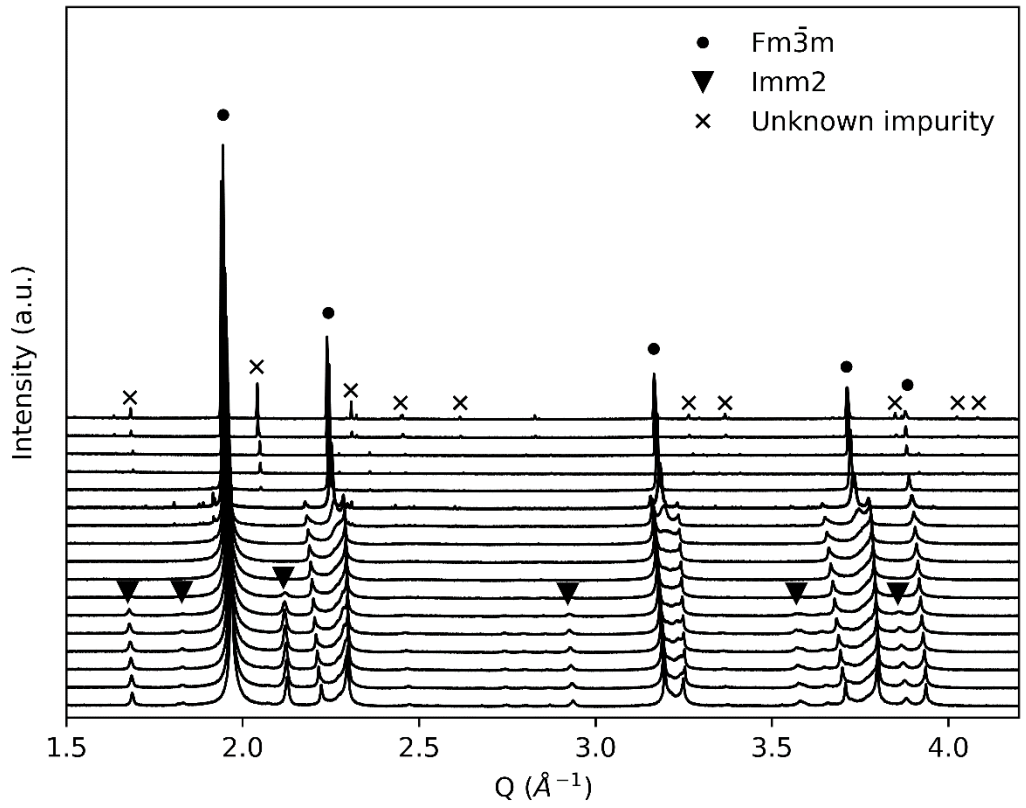

Figure A1. VT-PXRD data collected for 15YSB (calcined at 450 °C) over the temperature range of 123-769 °C.

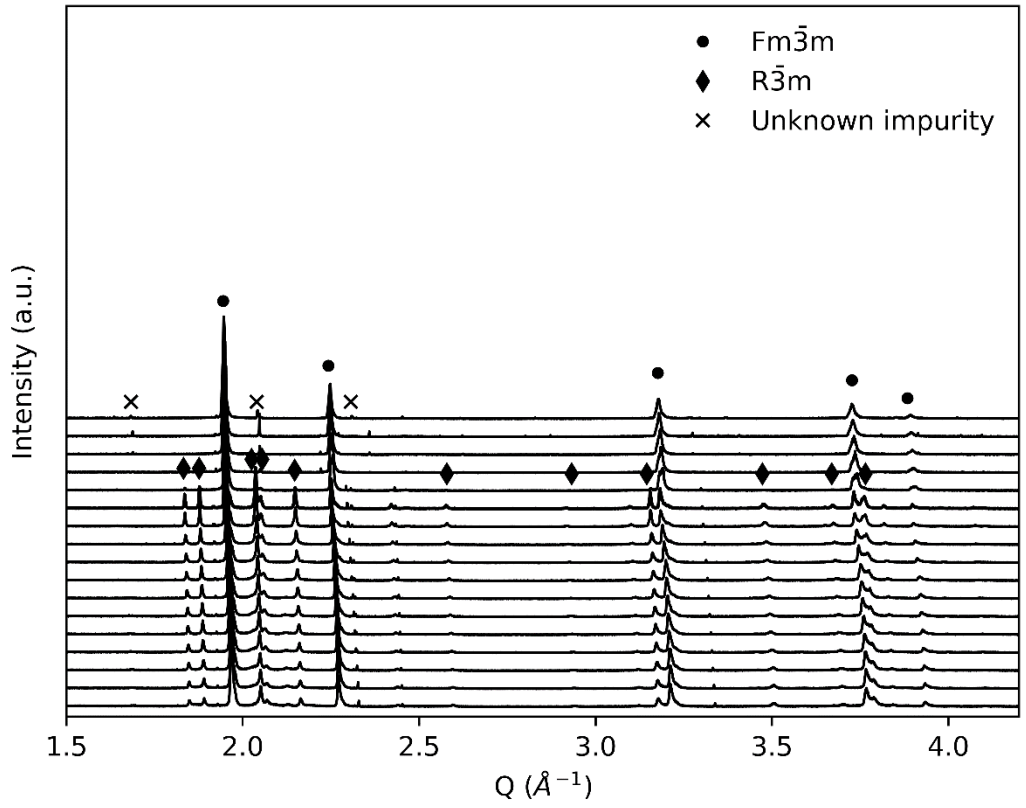

Figure A2. VT-PXRD data collected for 22.5YSB (calcined at 450 °C) over the temperature range of 123-769 °C.